ANNUAL REPORTS ON NMR SPECTROSCOPY

Volume 49

- Novel Applications of Dynamic NMR in Organic Chemistry
- Principles and Unconventional Aspects of NMR Diffusometry
- Density Functional Theory and its Application to Nuclear Magnetic Resonance Shielding Constants
- NMR Studies of *lac* Operator and *lac* Repressor
- Intramolecular Interactions of Polyethers and Polysulfides, Investigated by NMR, *Ab initio* Molecular Orbital Calculations, and Rotational Isomeric State Scheme: An Advanced Analysis of NMR Data

ACADEMIC PRESS

ANNUAL REPORTS ON

NMR SPECTROSCOPY

This Page Intentionally Left Blank

ANNUAL REPORTS ON

NMR SPECTROSCOPY

Edited by

G. A. WEBB

Royal Society of Chemistry, Burlington House, London, England

VOLUME 49

ACADEMIC PRESS

An imprint of Elsevier Science

Amsterdam – Boston – Heidelberg – London – New York
Oxford – Paris – San Diego – San Francisco – Singapore – Sydney – Tokyo

ELSEVIER SCIENCE Ltd
The Boulevard, Langford Lane
Kidlington, Oxford OX5 1GB, UK

First edition 2003

ISBN: 0-12-505449-1
ISSN: 0066-4103

♾ The paper used in this publication meets the requirements of ANSI/NISO Z39.48-1992 (Permanence of Paper).
Printed and bound in Great Britain.

List of Contributors

Erkki Kolehmainen, *Department of Chemistry, University of Jyväskylä, PO Box 35, 40251 Jyväskylä, Finland*

Ioan Ardelean, *Technical University, Physics Department, 3400 Cluj-Napoca, Romania and* Rainer Kimmich, *Universität Ulm, Sektion Kernresonanzspektroskopie, 89069 Ulm, Germany*

Philip J. Wilson, *Department of Chemistry, Joseph Black Building, The King's Buildings, University of Edinburgh, West Mains Road, Edinburgh, EH9 3JJ, UK*

Gérard Lancelot, *Centre de Biophysique Moléculaire, Rue Charles Sadron, 45071 Orléans cedex2, France and* Françoise Paquet, *Centre de Biophysique Moléculaire, Rue Charles Sadron, 45071 Orléans cedex2, France*

Yuji Sasanuma, *Department of Materials Technology, Faculty of Engineering, Chiba University, 1-33 Yayoi-cho, Inage-ku, Chiba 263-8522, Japan*

This Page Intentionally Left Blank

Preface

It is a pleasure for me to introduce Volume 49 of *Annual Reports on NMR Spectroscopy*. This volume contains accounts of the applications of NMR spectroscopy in five very interesting areas of molecular science.

The first chapter is on Novel Applications of Dynamic NMR in Organic Chemistry by E. Kolehmainen. This is followed by an account on Principles and Unconventional Aspects of NMR Diffusometry by I. Ardelean and R. Kimmich. The third contribution is by P.J. Wilson on Density Functional Theory and its Application to NMR Shielding Constants and the next contribution is on NMR Studies of *lac* Operator *lac* Repressor by G. Lancelot and F. Paquet. Finally Y. Sasanuma has reported on Intramolecular Interactions of Polyethers and Polysulphides, Investigated by NMR, *Ab Initio* Molecular Orbital Calculations and the Rotational Isomeric State Scheme.

I am very grateful to all of the authors for their stimulating accounts and to the staff at Elsevier for the production of this volume.

Royal Society of Chemistry
Burlington House
London
UK

G.A. WEBB
October 2002

This Page Intentionally Left Blank

Contents

Density Functional Theory and its Application to Nuclear Magnetic Resonance Shielding Constants
PHILIP J. WILSON

NMR Studies of *lac* Operator and *lac* Repressor
GÉRARD LANCELOT and FRANÇOISE PAQUET

Intramolecular Interactions of Polyethers and Polysulfides, Investigated by NMR, *Ab Initio* Molecular Orbital Calculations, and Rotational Isomeric State Scheme: An Advanced Analysis of NMR Data
YUJI SASANUMA

This Page Intentionally Left Blank

Novel Applications of Dynamic NMR in Organic Chemistry

ERKKI KOLEHMAINEN

Department of Chemistry, University of Jyväskylä, Finland

This review article is oriented on NMR applications in studying various dynamic processes of organic molecules. The topic as a whole is too large to be covered exhaustively in one article or by one author. Therefore, the literature searches are limited mainly for the years 1999–2001. Further, many interesting branches joined essentially with organic chemistry such as supramolecular and organometallic chemistry are left outside this article because there exist recent reviews on these topics. Similarly, the theoretical background of dynamic NMR is not included. The nature of dynamic NMR itself is changing with the recent progress in computational possibilities to estimate the different contributors involved in dynamic processes and in reproducing experimental NMR parameters, especially chemical shifts by density functional theory (DFT) approaches. This article tries to highlight these developments and future trends in organic chemistry, which hopefully forms a firm basis for the same progress in larger many electron systems such as organometallics and biological macromolecules.

ANNUAL REPORTS ON NMR SPECTROSCOPY
VOLUME 49 ISSN 0066-4103

1. INTRODUCTION

The available literature dealing with dynamic phenomena studied by various NMR techniques is enormous and too large to be covered in one review article. Even the subject itself "Dynamic NMR" is somewhat flexible and dependent on the phenomena studied, measuring techniques and nuclei involved. From 1985 when M. Oki's textbook "Applications of Dynamic NMR Spectroscopy to Organic Chemistry"[1] was published the variety of experimental NMR and calculational methods has enlarged remarkably. However, as it has been argued by Keith G. Orrell in his recent review on Dynamic NMR in Inorganic and Organometallic Chemistry[2] the basic one-dimensional band-shape analysis can be used over slow, intermediate and fast exchange regimes but it is most suited to intermediate rates (10–10^3/s). Exchange rates (typically 0.1–10/s) are most accurately measured by magnetization transfer experiments and especially by T_1-relaxation times while fast dynamic processes (rates $> 10^3$/s) can be obtained by spin–spin relaxation times, T_2, or via T_1-based estimates for molecular correlation times. In fact, all NMR data have always been more or less an average of time or frequency domains. Only the time scale of the dynamic processes involved determines whether we observe only one time averaged signal or two or more signals originating from different contributors participating in various dynamic equilibria. Traditionally it has been thought that a characteristic limiting factor in applying NMR to dynamic studies is its slow time scale when compared with some other techniques such as pulsed laser spectroscopy where the time resolution can be on the femtosecond (10^{-15} s) time scale. In order to adjust the time scale of a dynamic process suitable for NMR, variable temperature runs, solvent changes or some additives have been frequently used. All these techniques tend to slow down the dynamic processes and freeze some or all of their contributors to allow them to be observed separately. When we know the NMR parameters joint with the individual contributors it is often straightforward to calculate the statistical average of all signals which one can observe in the fast exchange regime. A more comprehensive approach can be obtained using various band shape simulators[3,4] developed for a two-site exchanging system, which can produce the observed spectra in slow, intermediate and fast exchange regimes. There exist also more sophisticated calculational procedures for multi-spin systems and random two-site exchange processes as reviewed by Orrell[2] but the detailed descriptions of those methods fall beyond the scope of this review. Similarly, dynamics in biological macromolecules, organometallics and inorganics as well as solid state NMR studies are not considered in this review.

Novel theoretical methods such as density functional theory (DFT)/gauge included atomic orbitals (GIAO) procedure which can reproduce experimental NMR chemical shifts in reasonable accuracy are, however, changing the role of NMR in dynamic studies remarkably. Now, it is possible to estimate by

reasonable computational time and resources the NMR parameters of all, or at least of the major, contributors involved in dynamic processes. As a very first example can be mentioned DFT/GIAO studies of the ^{1}H, ^{13}C and ^{15}N NMR chemical shifts in aminopyrimidines and aminobenzenes and their relationships to electron densities and amine group orientations.[5] It has been shown that in aniline the ring atom chemical shifts and $2p_z$ electron densities at *ortho* and *para* (but not *meta*) positions are quite sensitive to the orientations of the amine groups which are pyramidalized as the result of the balance between delocalization with the ring and the use of strongly directed sp^3-orbitals at the nitrogen. The calculated results show that the barriers to amine group torsional and inversion motions are low, but averaging the chemical shifts over these appears to be relatively unimportant.

In addition to the above mentioned review by Orrell and the books catalogued therein, there exist excellent new review articles such as ''Dynamic NMR Studies of Supramolecular Complexes'' by Pons and Millet,[6] ''Recent Advances in Studying Tautomerism in Solution and in the Solid State'' by Kleinpeter[7] and ''^{15}N NMR Spectroscopy in Structural Analysis'' by Marek and Lyčka.[8]

In the review on supramolecular complexes with 231 references by Pons and Millet[6] the investigations of the subject structures by 1D dynamic and 2D EXSY techniques are reported. The dynamic aspects of many supramolecular oligomers such as melamine-cyanuric acid rosettes, self-assembling glycoluril-based capsules, noncovalent calixarene-based capsules, cavitands, carcerands, hemicarcerands, helicates, catenanes and rotaxanes are discussed. The dynamic features associated with the binding of small guests (molecules or ions) to large hosts are also treated.

In Kleinpeter's review[7] on tautomerism with 88 references the various NMR methods are classified with respect to the rate constants of the present tautomeric equilibria. Detailed discussions on temperature dependencies of chemical shifts, heteronuclear coupling constants, NOEs, deuterium-induced ^{13}C and ^{15}N chemical shifts, and temperature dependent line shape variations due to tautomeric equilibria are included. For solid state studies, both the CP-MAS ^{13}C NMR spectroscopy and X-ray diffraction are considered. The review is completed by a critical survey on semiempirical and *ab initio* MO calculations relating to tautomerism; the calculation of chemical shifts and their application to estimate tautomeric equilibria is included as well.

In their very recent review from 2002 with 198 references Marek and Lyčka[8] discuss a variety of ^{15}N NMR studies on tautomerism such as azo–hydrazone equilibria, prototropic tautomerism with ring opening of nitrogen heterocycles, tautomerism of nitrazoles, natural chlorins, porphyrins, 2-phenacylpyridines and 1,8-bis(dimethylamino)naphtalenes. Further, they have included studies on conformational changes and rotational barriers for benzenediazonium salts with aliphatic nitro compounds, substituted triazines and *N*-acyl-*N*-alkyl-substituted amino acids.

2. NOVEL ROLE OF DYNAMIC NMR

As mentioned above novel calculational capabilities have changed the role of dynamic NMR studies because many dynamic processes can be simulated reliably with PC installed programs. One should remember that experimental dynamic NMR studies themselves (especially at natural abundance of ^{13}C and ^{15}N nuclei) often are spectrometer time invasive requiring measurements under different conditions (temperature, solvent etc.). In addition, owing to the complexity of the line shape equation derived even for the simplest nonbiased A $\rightleftarrows$ B-system, the interpretations of these data most often are based on heavy approximations. Although the sources of errors joined with these approximations has been discussed by Harald Günther in his well-known textbook[9] an organic chemist often is unsure of the validity limits of the method which he or she has used. This is true even in case of the most frequently used Eyring equation although it is recently familiarized for organic chemists by Goodman *et al.*[10] In spite of the fact that the calculations of NMR parameters at different levels of theory have been for a long time as one focus of research by NMR spectroscopists the reliability of the NMR chemical shift calculations (especially ^{13}C) using DFT/GIAO procedure has gained a special attention very recently as reported in 1999 by Smith *et al.*[11–13]

Although dynamic NMR studies cover almost all branches of chemistry and a huge variety of dynamic processes, in this review the main audience is thought to be organic chemists and only recent applications in prototropic tautomerism and conformational equilibria are included. In addition, especially novel calculational methods as an aid in the interpretation of dynamic NMR data are considered.

3. PROTOTROPIC TAUTOMERISM

Prototropic tautomerism such as its azo–hydrazone, imino–amino and keto–enol variants are very typical dynamic processes met with in organic chemistry for which NMR spectroscopy is a method of choice as reviewed by Kleinpeter in 2000.[7] Therefore, the present literature search performed by SciFinder from Chemical Abstracts using keywords ''prototropic tautomerism'' and ''NMR'' was limited to the years 1999–2002.

3.1. Nitrogen heterocycles

With regards to the tautomerism of nitrogen heterocycles calculations of ^{15}N NMR parameters are particularly useful as recently applied to purine bases.[14] Further, the effect of hydrogen bonding on ^{15}N NMR isotropic chemical shifts and the individual components of the shielding tensor in nucleic acid base pairs

has been recently reported by Sklenář and co-workers.[15] The calculated ^{15}N NMR parameters are especially useful in investigating tautomeric equilibria where data are not experimentally observable from model compounds or the exchange rate cannot be slowed down in the slow exchange regime on the NMR time scale.

As one of the most recent dynamic applications can be mentioned the ^{13}C NMR and *ab initio* study by Kleinpeter and Koch[16] on the tautomeric equilibria between the CH, OH and NH forms of 4-substituted 1-phenyl-3-methyl-pyrazolin-5-ones (**1**) (Fig. 1). On the NMR time scale the interconversion of **1a** $\rightleftarrows$ **1b**/**1c** is sufficiently slow whereas the equilibrium between the OH (**1b**) and NH-tautomers (**1c**) was found to be too fast even at low temperatures and only averaged signals were observed. In $CDCl_3$ the CH-form of 4-methylated derivative of **1** is predominant but in more polar solvents such as DMSO-d_6 the equilibrium is shifted towards the OH/NH-forms. Further, substitution at C-4 influences the relative stabilities of the tautomers. In 4-NO_2-, 4-SCN-, 4-$COCH_3$- and 4-$NHCOCH_3$-derivatives the intramolecular hydrogen bonds between the substituents and the adjacent OH-groups in the OH-forms make them the most stable tautomers, which are experimentally identified. However, minor proportions of the NH-forms contributing to the equilibrium cannot be totally excluded.

Since it was impossible to freeze out the OH- and NH-forms in the tautomeric equilibrium of **1**, high-level *ab initio* MO calculations were done. The influence of the solvent was included by employing various models of the self-consistent reaction field theory (SCRFT). First, the solvent was included in the calculations by applying a continuum of differing polarity over the surface of isolated tautomers (self-consistent isodensity polarized continuum model method), then by assuming formation of an adduct between the solute and the solvent (thereby simulating effectively the hydrogen bonding in the OH and NH tautomers) and finally by calculating dimeric or trimeric complexes of the various tautomers. By this relatively complex approach, a significant improvement between the theoretically calculated and experimentally detected tautomeric equilibria was achieved. The largest variation in the relative total energies of the tautomers was obtained by including electron correlation in the MO calculations. For the OH-form the stabilization was 4.7–7.3 kcal/mol while

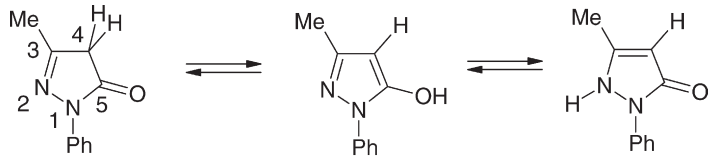

CH-form **1a** OH-form **1b** NH-form **1c**

Fig. 1. Tautomers of 3-methyl-1-phenylpyrazolin-5-one (**1**).

the CH-tautomer was stabilized by 0–2.2 kcal/mol when compared with the NH-form.

Also ^{15}N NMR and theoretical calculations have been used for tautomerism studies of ^{15}N5-labeled adenine **2** derivatives by Laxer *et al.*[17] (Fig. 2). ^{15}N NMR spectra (at 60.8 MHz) of fully ^{15}N-labeled adenine, ^{15}N5-2-hexylthioether-adenine and ^{15}N5-8-Br-adenine suggested the existence of the N3–H species in the tautomeric mixtures of these compounds in solution; in addition to the well-reported N9–H (major) and N7–H (minor) contributors. These observations were also supported by quantum mechanical calculations for the tautomeric equilibria in the gas phase (DFT and second-order perturbation theory). Also in this work solvent effects were included by both continuum and discrete solvation models. The observation of the existence of the N3–H tautomer has a clear impact on the possible H-bonding patterns of these adenine prototypes and on their molecular recognition by various biological macro-molecules such as proteins. These ^{15}N-labeled analogues are expected to find use as ^{15}N NMR probes for numerous biochemical studies.

Another recent work utilizing ^{15}N, ^{1}H and ^{13}C NMR on restricted rotation and degenerate tautomeric forms of ethenoadenosine **3** is reported by Mäki *et al.*[18] (Fig. 3). In the prototropic equilibrium and protonation of the resultant bi-imidazole nucleoside it was found that in the neutral form an intramolecular H-bond is formed between N3′ of the outer imidazole ring and the N6 protons of the inner imidazole ring, giving rise to degenerate tautomeric forms. In the protonated form it is the pyridine-type nitrogen (N3′) of the outer imidazole

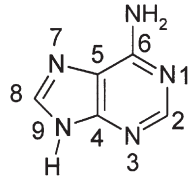

Fig. 2. Structure and numbering of adenine **2**.

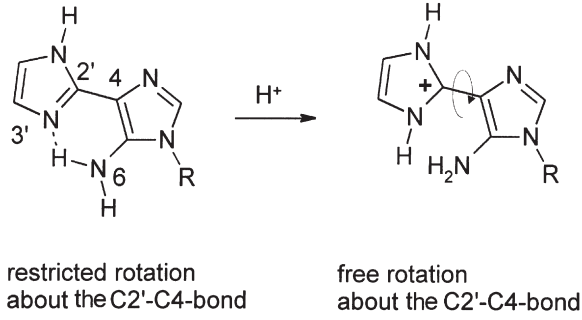

Fig. 3. Protonation of ethenoadenosine **3**.

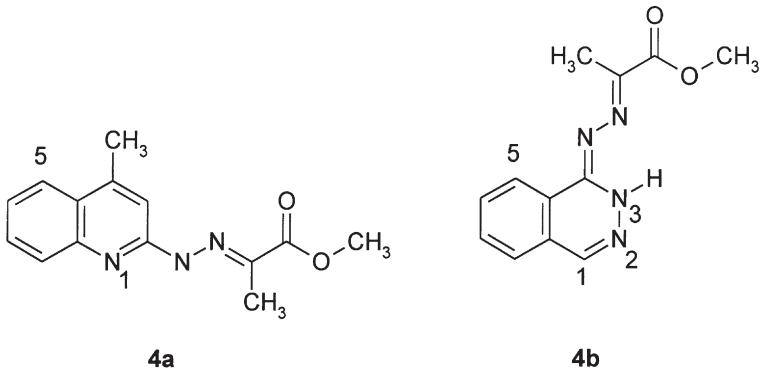

Fig. 4. Structures of the *N*-heterocyclic hydrazones **4a** and **4b**.

ring where the proton is predominately located and the reduced intramolecular H-bonding results in essentially unrestricted rotation of the imidazole rings with respect to one another. From the dynamic NMR point of view a very interesting detail in this work was a comparison between the 1D ^{13}C and 2D $^{1}H,^{15}N$ HMBC data upon protonation of the nucleoside. It was observed that due to the increased exchange rate of rotation around the C2′–C4-bond the dynamic effects are not visible in ^{13}C NMR while ^{15}N NMR still gives useful information.

Giorgi *et al.*[19] have studied by (dynamic) NMR and theoretical calculations isomerism and imino–amino tautomerism of α-*N*-heterocyclic hydrazone **4a** and **4b** (Fig. 4). Among possible *syn-Z*/*anti-E* isomers and different tautomeric structures, the molecular structures of the 4,8-dimethylquinolylhydrazone derivative of **4a** and its phthalazinyl analog **4b** have been shown to exist as *anti-E* isomers. Further, in **4a** the mobile proton resides on the hydrazone nitrogen while in the phthalazine derivative **4b** it is located on one of the endocyclic nitrogens. The same isomeric structures are also confirmed in solution by NMR experiments. For the 4,8-dimethylquinolylhydrazone derivative of **4a** no other isomer is detected while the 4,6- and 4,7-dimethylquinolylhydrazone derivatives of **4a** show chemical equilibrium between the imino and amino tautomers in the solution, the latter being present in a very high amount (>90%). In contrast, phthalazine derivative **4b** exist in the imino form both in the crystalline state and in chloroform solution and no coalescence was observed at −60 °C.

Tautomerism of 3(5)-methylpyrazole **5** has been studied by Jimenez *et al.*[20] (Fig. 5). Differential Scanning Calorimetric (DSC) and $^{13}C/^{15}N$ NMR spectroscopic studies at low temperatures (in supercooled liquid) show that 3(5)-methylpyrazole is a mixture of four trimers formed by the 3-Me and 5-Me tautomers.

Substituted pyridines have been a subject of several dynamic NMR studies. 2- and 4-Hydroxypyridines are known to exist mainly as pyridone tautomers.

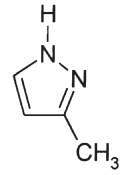

Fig. 5. 3-Methyl-1*H*-pyrazole (**5**).

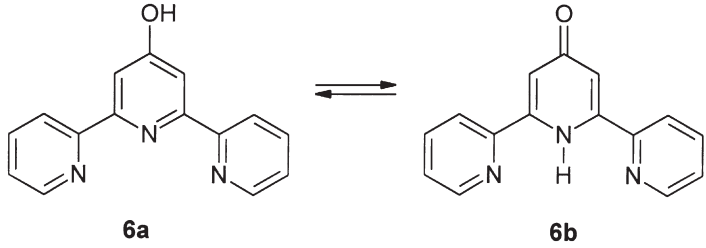

Fig. 6. Tautomerism of 2,6-bis(2′-pyridyl)-4-hydroxypyridine (**6a**) and 2,6-bis(2′-pyridyl)-4-pyridone (**6b**).

This phenomenon has been studied recently quantum mechanically using DFT(B3LYP and B3PW91)/6-31++G**) and *ab initio* (RHF/6-31++G**) methods by Dkhissi *et al.*[21] Also 2-mercaptopyridine exists predominantly as the 2-thiopyridone tautomer while in 2-aminopyridine the amino form is preferred.[7] Similarly 2-hydroxy- and 2-mercaptopyrazines have been shown to be predominantly in the 1,4-diazin-2-one and 1,4-diazin-2-thione forms.[22]

The tautomerism of nitraminopyridines has been studied using ^{1}H, ^{13}C and ^{15}N NMR by Gawinecki *et al.*[23] Especially informative was the ^{15}N NMR chemical shift of 2-nitraminopyridine (−18.6 ppm) which suggested the prevalence of a nitrimino tautomer for this compound. The above reasoning was based on the ^{15}N NMR chemical shifts of model compounds: nitro-(*N*-methyl-1*H*-pyridin-2-ylidene)amine (−14.9 ppm), nitro-(*N*-methyl-1*H*-pyridin-4-ylidene)amine (−9.0 ppm) and 3-niraminopyridine (−31.0 ppm).

Further, the tautomerism of 4-hydroxyterpyridine in the solid, solution and gas phases has been studied with X-ray, FT-IR and NMR techniques by Murguly *et al.*[24] (Fig. 6). The keto–enol equilibrium between 2,6-bis(2′-pyridyl)-4-hydroxypyridine (**6a**) and 2,6-bis(2′-pyridyl)-4-pyridone (**6b**) was evaluated using IR spectroscopy, VT ^{1}H and ^{13}C NMR spectroscopy and X-ray crystallography. These studies show that the less polar hydroxy tautomer **6a** is the predominant species in the gas phase. The solution-state studies show the more polar keto form **6b** to be predominant but not exclusive, the ratio of tautomers depends on the polarity and hydrogen-bonding ability of the solvent as well as temperature. In $CDCl_3$ the temperature did not effect remarkably the ^{1}H NMR spectra of the predominant form **6b** between 25 and −80 °C. In CD_2Cl_2 at 25 °C, however, both **6b** and **6a** were visible in a 6 : 1 molar ratio.

This ratio changed to 3 : 1 as the temperature was lowered shifting the tautomeric equilibrium towards the hydroxy form **6a**. In the solid state both species are present in a 1 : 1 ratio and form a dimeric structure held together by a strong C=O · · · H–O-hydrogen bond between the tautomers.

Kolehmainen *et al.* have studied systematically, by dynamic NMR and computational methods, the temperature and substituent effects on the tautomerism in 2-phenacylpyridines,[25] in 2-phenacylquinolines,[26] in 2-(acylmethyl)quinolines[27] and in (1*Z*,3*Z*)-1,4-di(pyridin-2-yl)buta-1,3-diene-2,3-diol.[28]

2-Phenacylpyridines **7a**[25] substituted in the benzene ring [R = 4-(1-pyrrolidinyl), 4-NMe_2, 4-NH_2, 4-MeO, 4-Me, 3-Me, H, 4-Cl, 4-CF_3, 4-NO_2, etc.] are in equilibrium with (*Z*)-2-(2-hydroxy-2-phenylvinyl)pyridines (**7b**) when dissolved in chloroform (Fig. 7). A significant substituent effect on the tautomeric equilibrium was observed: the amount of the enolimine form stabilized by the intramolecular hydrogen bond is 1% for R = 4-(1-pyrrolidinyl)- and 92% for 4-NO_2-derivative, respectively]. The negative logarithm of the tautomeric equilibrium constant, K_T, is linearly dependent on the Hammett σ substituent constants. The dependence of K_T vs. temperature is exponential in character: the more electron-withdrawing the substituent, the more distinct the influence of temperature. Unexpectedly, the tautomer present in the crystalline state is not the same for all of the compounds studied (it is the ketimine form for the compounds substituted with strong electron-donors). Among the different *ab initio* methods used to calculate the enthalpy of the proton transfer in chloroform solution, MP2/6-31G** gives the best results

The proton-transfer equilibria of twelve 2-phenacylquinolines **8a**[26] in $CDCl_3$ were studied by ^1H, ^{13}C and ^{15}N NMR spectroscopy (Fig. 8). The (*Z*)-enaminone form stabilized by an intramolecular hyrogen bond predominated

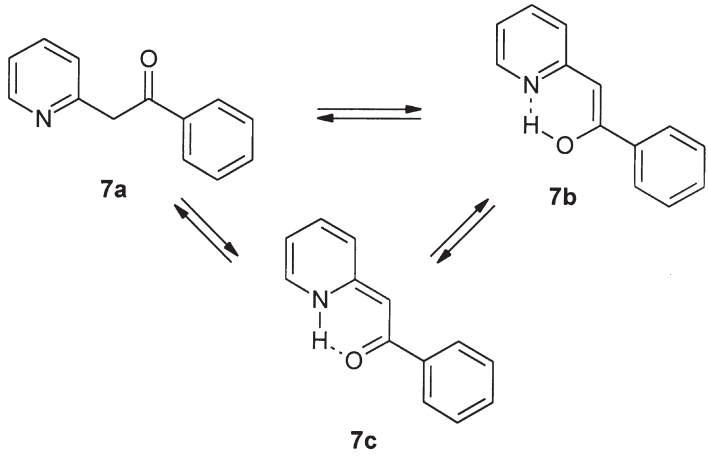

Fig. 7. Tautomeric forms of 2-phenacylpyridine **7**.

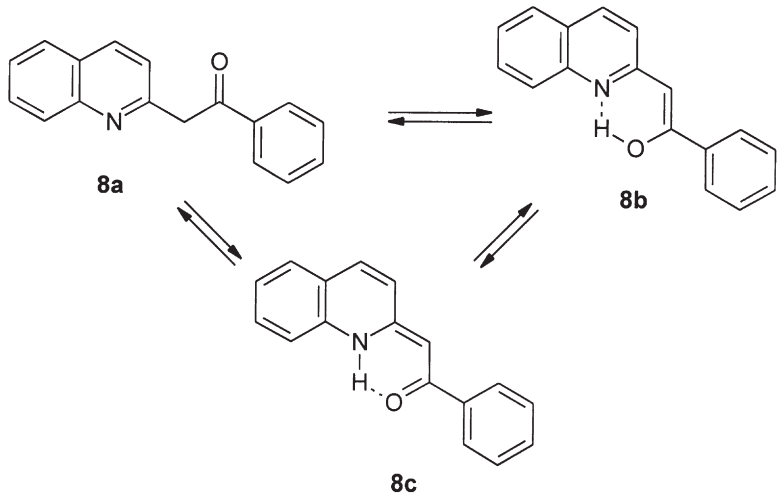

Fig. 8. Tautomeric forms of 2-phenacylquinoline **8**.

in all cases. Electron-donating substituents in the phenacyl part of the molecule lead to an increase of the ketimine form (up to 33% for *p*-NMe_2). VT ^{1}H NMR measurements show that higher temperatures have the same effect. The negative logarithm values of the equilibrium constant, pK_T, were linearly dependent on Hammett σ substituent constants as in the case of related pyridines. The pK_T vs. temperature correlation was also linear. In general, strong electron-withdrawing substituents cause transformation of the ketimine **8a** to the enaminone form **8c** to become more exothermic. X-ray data show that the strength of the internal hydrogen bond in the enaminone form increases when strongly electron-withdrawing substituents are present. An estimation shows this bond to be stronger in $CHCl_3$ solution than in the crystalline state. π-Electron delocalization in the six-membered quasi-ring involving the H···O bond is very strong. This effect is responsible for the predominance of the tautomeric enaminone form in 2-phenacylquinolines. On the other hand, semiempirical AM1 and PM3 calculations show that in the gas phase the ketimine tautomer is energetically favoured in most cases.

Tautomeric equilibrium between 2-(4-pyrrolidinylcinnamoylmethyl)quinoline (**9**), (*Z*)-1,2-dihydro-2-(cinnamoylmethylene)quinoline (**9a**) and (*Z*)-4-phenyl-1-(2-quinolyl)-1,3-butadien-2-ol (**9c**)[27] were studied by ^{1}H, ^{13}C and ^{15}N NMR methods (Fig. 9). The –CH=CH– fragment conjugated with phenyl and a strong electron donor 4-(1-pyrrolidinyl) substituent was found to favour the enolimine tautomer **9c**. This undergoes fast exchange (on the NMR time-scale) with the enaminone form **9a**. The amount of the latter tautomer was found to increase at low temperatures. In order to determine quantitatively the relative contributions of **9a** and **9c** VT NMR studies were performed in $CDCl_3$. The

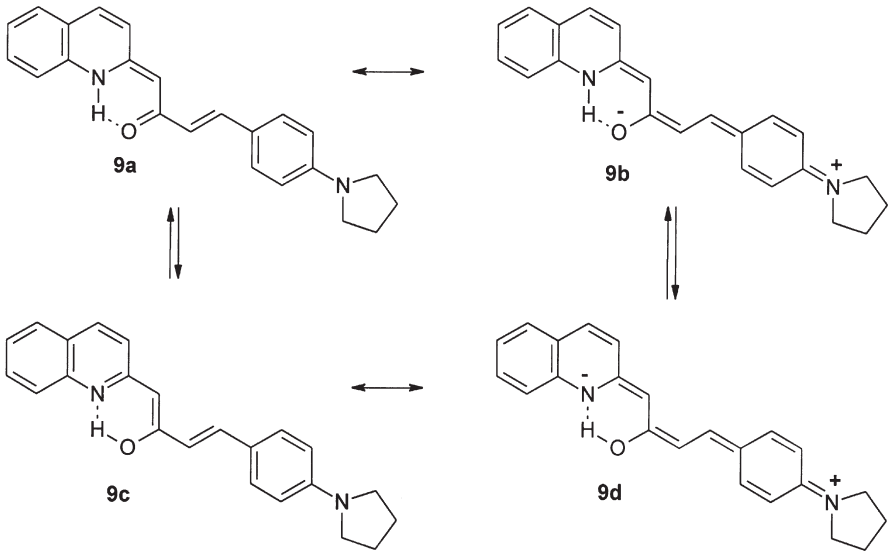

Fig. 9. Resonance and tautomerism in 2-(4-pyrrolidinylcinnamoylmethyl)quinoline.

frozen tautomers (in the slow exchange regime) could be assigned by their different heteronuclear *J*(H,N) coupling constants. Also the ^{15}N NMR chemical shift of the ketimino form at 30 °C (−74.7 ppm) is in the range of −68–−75 ppm observed for ketimino forms of 2-phenacylpyridines. The other observed ^{15}N NMR chemical shift at −184.5 ppm suggests that it is a time average (in the fast exchange regime) of enolimine **9c** and enaminone **9a** tautomers falling between the range of −120 and −126 ppm for enolimines of 2-phenacylpyridines and the range of −226 and −228.5 ppm of enaminones of 2-phenacylpyridines, respectively.

^{1}H, ^{13}C, and ^{15}N NMR spectral data show that in chloroform solution (1*Z*,3*Z*)-1,4-di(pyridin-2-yl)buta-1,3-diene-2,3-diol (**10a**) is in ca. 9 : 1 equilibrium with (3*Z*)-3-hydroxy-1,4-di(pyridin-2-yl)but-3-en-2-one (**10b**) while no 1,4-di(pyridin-2-yl)-2,3-butanedione (**10c**) was detected[28] (Fig. 10). The species present in the tautomeric mixture were identified by comparing their experimental chemical shifts with those known for similar compounds as well as with the theoretically calculated (GIAO-HF/DFT) values. *Ab initio* (MP2/6-31G**) calculations show that **10b** and especially the highly conjugated **10a** form are preferred in the tautomeric mixtures both *in vacuum* and in chloroform solution. There is one and two strong O–H · · · N hydrogen bonds present in the molecule of the former and latter tautomers, respectively. Other tautomeric forms, e.g., dienaminedione {(1*Z*,4*Z*)-1,4-di[pyridin-2(1*H*)-ylidene]butane-2,3-dione}, and their rotamers were found to have higher energies. The single crystal X-ray diffraction studies show that dienediol **10a** is the only tautomeric form

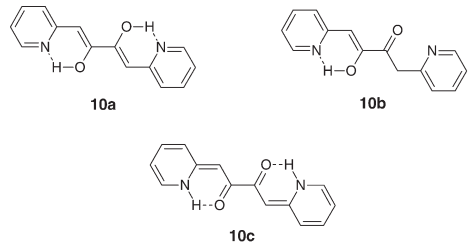

Fig. 10. Tautomers of 1,4-di(pyridin-2-yl)buta-1,3-diene-2,3-diol (**10**).

present in the crystal at 173 K. Its almost perfectly planar form is stabilized by two strong intramolecular O–H $\cdots$ N hydrogen bonds.

GIAO/DFT calculated chemical shifts of the tautomeric species of 2-phenacylpyridines and (*Z*)-2-(2-hydroxy-2-phenylvinyl)pyridines have been reported by Ośmiałowski *et al.*[29] ^{1}H, ^{13}C and ^{15}N NMR chemical shifts for 28 substituted 2-phenacylpyridines (ketimine forms) and their enol imine tautomers, (*Z*)-2-(2-hydroxy-2-phenylvinyl)pyridines, were calculated via the GIAO/DFT approach. Among four tested methods at the B3LYP level of theory, the 6-311G, 6-311++G and 6-311G** basis sets gave acceptable results for the ^{13}C NMR chemical shifts whereas the 6-311++G** basis set was the minimum needed for the reproduction of ^{15}N NMR chemical shifts. Satisfactory results for ^{13}C and ^{15}N NMR chemical shifts for different tautomers revealed that intramolecular hydrogen bonding could be modeled reliably by these calculations when the geometry optimizations were done with the HF/3-21G method. Agreements between theoretical and experimental ^{13}C and ^{15}N NMR chemical shifts and also HF/3-21G and HF/6-31G** optimized structural parameters with those obtained by X-ray crystallographic measurements suggest that it is not necessary to select too sophisticated and CPU time-intensive methods for geometry optimizations.

NH tautomerim in fully conjugated porphyrins has been studied extensively by NMR and IR as reviewed by Helaja *et al.*[30] Further, dynamic NMR studies reveal that all of the nonsymmetric free-base porphyrins exist in solution as a mixture of two distinct *trans*-NH-tautomers possessing different energies and different populations.[31,32] Helaja *et al.*[30] have investigated the NH tautomerization process in bonellin di-Me ester **11**, which is a natural derivative of chlorin (17,18-dihydroporphyrins) by NMR spectroscopy and molecular modeling (Fig. 11). The tautomerization was observed to occur between the two degenerate N21–H, N23–H *trans*-tautomers. The dynamic ^{1}H NMR measurements showed a coalescence temperature of 297 K for the total tautomeric exchange process. The free energy of activation $\Delta G^{\ddagger}_{297}$ was calculated to be 14.4 kcal/mol on the basis of the Eyring equation using values of $T_c = 297$ K and $\Delta\nu = 74$ Hz which was the line separation measured in the slow exchange regime ($T = 210$ K). The two-dimensional ^{1}H and ^{15}N

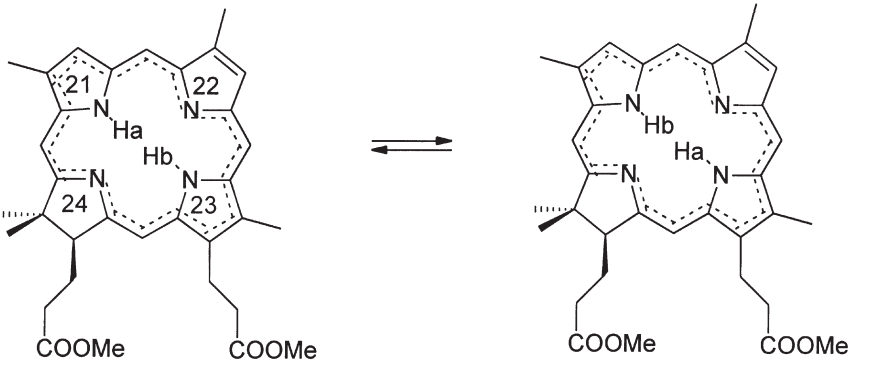

Fig. 11. Tautomers of the dimethyl ester of bonellin **11**.

heteronuclear single quantum coherence (HSQC) and heteronuclear multiple bond correlation (HMBC) techniques were used to assign the ^{15}N and NH proton resonances at natural abundance. In $^{1}H,^{15}N$ HMBC measured at 278 K correlation peaks of the chlorin *meso*-CH protons were found with three central nitrogens with different frequencies resonating at 131.5 (N21), 128.5 (N23) and 281.5 ppm (N24), respectively. These ^{15}N NMR chemical shifts are referenced to the internal DMF for which $\delta(^{15}N_{DMF}) = 103.8$ ppm. In addition to the strong ^{15}N–^{1}H one-bond correlations, the HSQC spectrum showed weak correlations between the diagonally opposite nitrogen and proton, thus providing clear evidence for the NH tautomeric exchange. These weak correlations arise from the exchange between the NH protons after the refocusing period of the HSQC pulse sequence. The semiempirical molecular modeling methods, AM1 and PM3, were used to estimate the energies of the possible tautomers. The AM1 and PM3 methods with a UHF (UHF) spin-pairing option both favour strongly the chlorin tautomers in which an aromatic 18-atom 18 π-electron delocalization pathway is possible without delocalizing the lone-pair electrons of N24 in the reduced sub-ring. In the proposed tautomerization pathway, the fully aromatic N21–H, N22–H and N22–H, N23–H *cis*-tautomers were found to be energetically more advantageous than the less aromatic N21–H, N24–H and N23–H, N24–H *cis*-tautomers. The stepwise tautomerization mechanism is concluded to be active for the proton transfer.

3.2. Miscellaneous cyclic compounds

In addition to nitrogen heterocycles other ring systems can possess interesting tautomeric properties. Ring-chain tautomerism in spiro-1,3-oxathianes **12** has been studied by Muntean *et al.*[33] (Fig. 12). The ring-chain tautomerism of

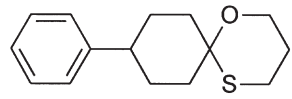

Fig. 12. 1-Oxa-9-phenyl-3-thia-spirocyclo[5.5]undecane (**12**).

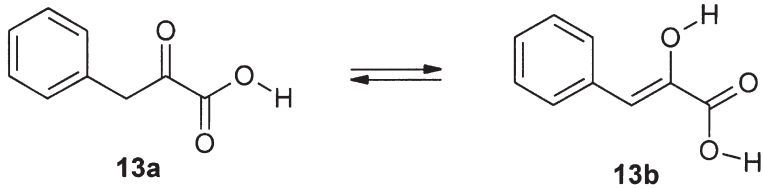

Fig. 13. Tautomerism of phenylpuryvic acid (**13**).

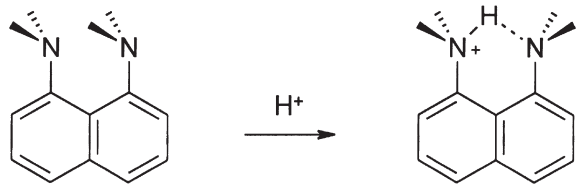

Fig. 14. Protonation of 1,8-bis(dimethylamino)naphthalene (**14**).

spiro-1,3-oxathiane derivatives was studied with **12** obtained as a mixture of *cis*- and *trans*-isomers in solution and in the solid phase. The phenyl group is in the equatorial position in both isomers, while the sulfur group occupies the axial position in the *cis*-isomer and the equatorial position in the *trans*-isomer. Both diastereoisomers have a semiflexible structure, the cyclohexane ring is anancomeric (phenyl is the holding group), whereas the heterocycle is flipping. NMR and flash chromatographic separation experiments show that the interconversion between the isomers takes place via the open-chain form. The isomerization kinetics were detected in slightly acidic $CDCl_3$ by NMR to be first-order with $k_1 = 8.71 \times 10^{-3}$/min and $k_{-1} = 1.20 \times 10^{-2}$/min.

Keto/enol tautomerism in phenylpyruvic acid **13** has been investigated by Carpy *et al.*[34] (Fig. 13). *o*-Nitrophenylpyruvic acid was formed on acid hydrolysis of the azlactone of *o*-nitrobenzaldehyde. The structures of the two tautomeric forms were assigned by NMR spectroscopy. X-ray diffraction of a single crystal revealed that the crystalline form corresponds to the keto tautomer. Quantum mechanical calculations (AM1, HF and DFT) in the gas phase confirmed the experimental findings in solution.

A ^1H, ^{13}C and ^{15}N NMR investigation of 3-substituted 1,8-bis(dimethylamino)naphthalene (DMAN) (**14**) derivatives and their monoprotonated salts has been reported by Pietrzak *et al.*[35] (Fig. 14). Based on the multinuclear magnetic resonance data of 2-chloro-, 4-bromo- and 2,7-dichloro-DMAN and

their protonated salts the authors conclude that the most sensitive parameters for investigating this kind of compound are a direct heteronuclear spin–spin coupling, $^{1}J(^{15}N,^{1}H)$, and ^{15}N and ^{1}H chemical shifts for the atoms in the [N8–H–N1]$^{+}$-bridge. A further significant NMR parameter is a homonuclear vicinal spin–spin coupling $^{3}J(^{1}H,^{1}H)$ for the bridging proton and the $N(CH_3)_2$ protons. An analysis of the $^{1}J(^{15}N,^{1}H)$-values is consistent with the view that, in the investigated system, equilibria between two tautomeric forms occurs. A VT study between 27 and −40 °C, and a change of solvent, show that the values of the ^{15}N chemical shifts and couplings $^{1}J(^{15}N,^{1}H)$ and $^{3}J(^{1}H,^{1}H)$ for the [N8–H–N1]$^{+}$-bridge are essentially unchanged. This shows that the bonding arrangements of the bridge atoms are stable under these experimental conditions.

Proton transfer equilibrium in Schiff bases **15**, derived from 5-nitrosalicylaldehyde, has been studied using deuterium isotope effects on ^{13}C NMR chemical shifts by Rozwadowski and Dziembowska[36] (Fig. 15). The proton transfer equilibrium in a series of Schiff bases derived from 5-nitrosalicylaldehyde and aliphatic amines (I; R = Et, Pr, *iso*-Pr, Bu) was investigated by means of VT NMR spectra and the deuterium isotope effect on ^{13}C NMR chemical shifts. The equilibrium constants K_{PT} for the proton transfer process in these Schiff bases were evaluated based on the equation derived by Alarcón *et al.*[37] (Eq. (1))

$$K_{PT} = [\delta(^{13}C_{2obs}) - \delta(^{13}C_{2OH})]/[\delta(^{13}C_{2NH}) - \delta(^{13}C_{2obs})], \quad (1)$$

where $\delta(^{13}C_{2OH})$ and $\delta(^{13}C_{2NH})$ are the chemical shifts of carbon-2 in the pure OH and NH tautomers. Further, a K_{PT} vs. T plot afforded the thermodynamic parameters ΔH° and ΔS°. From these it can be concluded that the entropy factor seems to be decisive in the stabilization of the NH form in $CDCl_3$. The dependence of the deuterium isotope effect $\Delta C_{2(OD)}$ on ΔG° is in agreement with statements that the large isotope effect $\Delta C_{2(OD)}$ (negative or positive) results from an isotopic perturbation of the tautomeric equilibrium which in turn depends on the free energy differences between these two tautomers.

Fig. 15. Tautomerism in the Schiff base derived from 5-nitrosalicylaldehyde **15**.

4. CONFORMATIONAL EQUILIBRIA

The majority of dynamic NMR studies are probably dealing with conformational equilibria in solution. There exist a huge number of variants under this topic such as conformational equilibria in cycloalkanes and various heterocycles, nitrogen inversion, substituent rotation in substituted aromatics and generally rotations about $C(sp^n)$–$C(sp^m)$-bonds (where $n = 2$, 3 and $m = 2$, 3) representing different degrees of conjugation etc. These various dynamic processes span a large range of rate constants and thermodynamic parameters offering real challenges for a variety of NMR techniques.

4.1. Nitrogen inversion

Huuskonen *et al.*[38] have studied photoresponsive piperazine macrocycles which show interesting dynamic phenomena when studied by ^{1}H NMR (Fig. 16). The piperazine moiety of **16** gave at $-65\,^\circ$C two pairs of resonance patterns (two doublets and two triplets) owing to a slow ring inversion of the piperazine moiety. Spectral coalescence of piperazine proton signals of **16** occurred at $-10\,^\circ$C which according to the Eyring equation corresponds to an energy barrier of 51.0 kJ/mol. For piperazine itself the coalescence temperature was $-50\,^\circ$C corresponding to an energy barrier of 45.0 kJ/mol. For 1,4-bis(1-methylpropyl)piperazine the corresponding energy barrier was 50.4 kJ/mol.

Another example for nitrogen inversion in heterocycles viz. ethyl 2-aroyl- and ethyl 2-arylcarbamaoyl-4,5-dimethyl-1,2,3,6-tetrahydropyridazine-1-carboxylates (**17**) has been given recently by Kolehmainen *et al.*[39] (Fig. 17). The dynamics of the tetrahydropyridazine ring has been studied by the 2D ^{1}H,^{1}H EXSY-technique. The diastereotopic protons of two CH_2-groups in the heterocycle of **17** are in dynamic equilibrium via simultaneous inversion of the adjacent nitrogens.

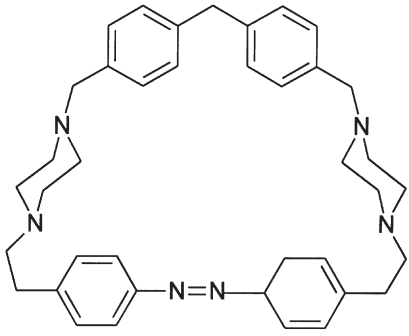

Fig. 16. 1,3,7,9(1,4)-Tetrabenzena-2-diazena-5,11(1,4)-dipiperazinacyclododecaphane (**16**).

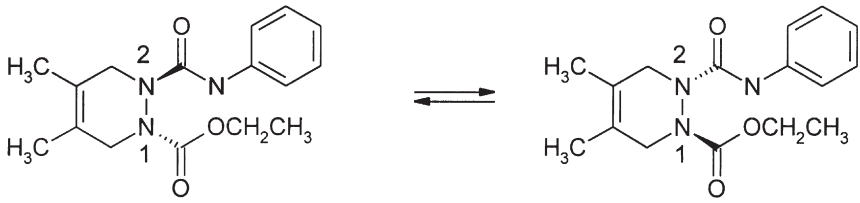

Fig. 17. Simultaneous two nitrogen inversions in ethyl 2-phenylcarbamaoyl-4,5-dimethyl-1,2,3,6-tetrahydropyridazine-1-carboxylate (**17**).

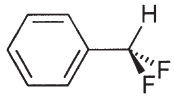

Fig. 18. Benzal fluoride **18**.

4.2. Rotation of substituents in aromatics

Conformational characteristics of substituted aromatics has been extensively studied by Ted Schaefer (Univ. Manitoba, Winnibeg). In a majority of his more than 180 papers (mostly published in *Can. J. Chem.*) rotational barriers of substituents in substituted aromatics have been studied by a variety of experimental NMR and theoretical methods. As one of his most recent works can be mentioned theoretical and experimental NMR approaches to the effects of solvation on the small internal rotational potential of benzal fluoride (α,α-difluorotoluene)[40] (Fig. 18). The internal rotational potential for benzal fluoride is computed at various levels of MO theory, including correlation-gradient, MP2 (frozen core) methods. The perturbations of the potential caused by solvents are calculated with the Onsager model (ellipsoidal cavity with $l=6$ in the multipole expansion) as well as with the self-consistent isodensity-polarizable continuum model (SCI-PCM). Analysis of the ^{1}H and ^{19}F NMR spectra in cyclohexane-d_{12} and acetone-d_6 solutions yields long-range spin–spin coupling constants from which the expectation values of the term $\sin^2\theta$ in the internal rotation potential can be derived. Reasonable agreement between the experimental and theoretical results is found for potentials obtained from MP2/6-31G* approaches in both solvent models. Long-range coupling constants $^{n}J(^{19}F,^{13}C)$ provide very rough checks of the $\sin^2\theta$-values. For the isolated molecules an additivity scheme based on the potential for benzyl fluoride (α-fluorotoluene) reproduces much of the potential for benzal fluoride except for a deviation caused by the rather larger relative magnitude of the fourfold potential component in the latter. The minimum in the potential for benzal fluoride occurs for a torsional angle, $\theta=90^{\circ}$, corresponding to a conformation in which the C–H bond of the side

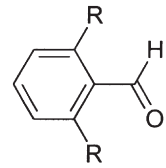

Fig. 19. 2,6-Disubstituted benzaldehyde, R = Cl (**19a**) and nitro (**19b**).

chain lies in a plane perpendicular to the aromatic plane and is rationalized on the basis of electrostatic forces.

A similar approach to the solvent dependence of the rotational energetics, and formyl-proton long-range spin–spin coupling behaviour of 2,6-dichloro- and 2,6-dinitrobenzaldehyde (**19a** and **19b**) using dipolar couplings and temperature dependence of long-range couplings, has been reported by Lounila *et al.*[41] (Fig. 19). The solvent effects on the rotational energetics of the formyl group and its proton spin–spin coupling behaviour of 2,6-dichloroenzaldehyde (**19a**) were studied by analysis of dipolar couplings and the temperature dependence of the spin–spin couplings. The general form of the rotational potential was taken from molecular mechanics and the conjugative $\sin^2\theta$-type component was then optimized using the dipolar couplings obtained by analyzing the ^{1}H NMR and ^{13}C proton satellite spectra in a liquid–crystal solvent. Optimization based on the dipolar couplings gave the following rotational free-energy potential (Eq. (2)) in kJ/mol:

$$V(\theta) = 4.5\cos^6\theta + 10.7(\pm 2.0)\sin^2\theta. \tag{2}$$

Analysis based on the temperature dependence of ^6J data allowed estimation of solvent effects on the potential, e.g., the potentials in acetone and in acetonitrile differ by $1.0\sin^2 2\theta$ (in kJ/mol). The $CHCl_3$ solvent effect was described by a term of $-1.0\cos^6\theta$. When the $^6J(\mathbf{CHO},\mathbf{H}_p)$ was fitted, assuming it obeyed the expression (Eq. (3))

$$^6J(\theta) = {}^6J_{90}\sin^2\theta + {}^6J_0 \tag{3}$$

and assuming $^6J_0 = 0.015$ Hz, the analysis yielded a $^6J_{90}$ value of -0.48 (± 0.03) Hz. The scalar-coupling temperature-dependence method was also applied to the conformational analysis of **19b**.

In addition to the conformational behaviour these studies give an estimate for the solvent effect on the rotational barrier of 1–2 kJ/mol. Together with previous studies[42–44] it is obvious that the solvent and temperature dependence of long-range spin–spin couplings offers a sensitive tool for the study of weak solvent–solute interactions. Estimates for rotational barriers using long-range spin–spin couplings have been derived also for some toluoic[45] and styrenoic[46] systems.

4.3. Atropoisomerism and related phenomena

Multiple internal motions form a real challenge for dynamic NMR studies. As a very recent example can be mentioned conformational studies by dynamic NMR on stereomutation processes in the diastereoisomers of an amino alcohol and related amide precursors by Bartoli *et al.*[47] The barriers for three internal motions (i.e., phenyl and *tert*-butyl rotations as well as nitrogen inversion) have been studied by dynamic NMR spectroscopy in the two diastereoisomeric forms (enantiomer pairs) **20a** and **20b** of a typical amino alcohol, *N*,*N*-dimethylamino-2,4,4-trimethyl-3-phenyl-3-pentanol (Fig. 20). The two structures were assigned by comparison with those of the corresponding amide precursors **20c** and **20d** (CH_2 substituted by C=O) detected by single-crystal X-ray diffraction. These amides were also found to undertake internal motions amenable to NMR observation, i.e., phenyl, *tert*-butyl, and N–CO rotations: the corresponding barriers were also measured. *Ab initio* molecular orbital calculations indicate that H-bonding makes all these molecules adopt six-membered cyclic conformations, a conclusion which agrees well with the X-ray crystal structure detected for the amide precursors (Table 1).

Another interesting dynamic problem studied by Dell'Erba *et al.*[48] is that dealing with the dynamics of the diastereoisomers of *o*-dinaphthylphenyl derivatives (Fig. 21). The static and dynamic stereochemistry of the hydrocarbon comprising a benzene ring, bearing two α-naphthyl substituents in the *ortho* positions, i.e., 1,2-di(4-methyl-naphth-1-yl)benzene (**21**), has been studied by a combination of VT NMR, cryogenic HPLC, and molecular mechanics calculations. In solution both *syn* (meso) **21a** and *anti* (chiral P,P′ and M,M′ enantiomers) **21b** forms were observed. Their interconversion (M,M′ → M,P′

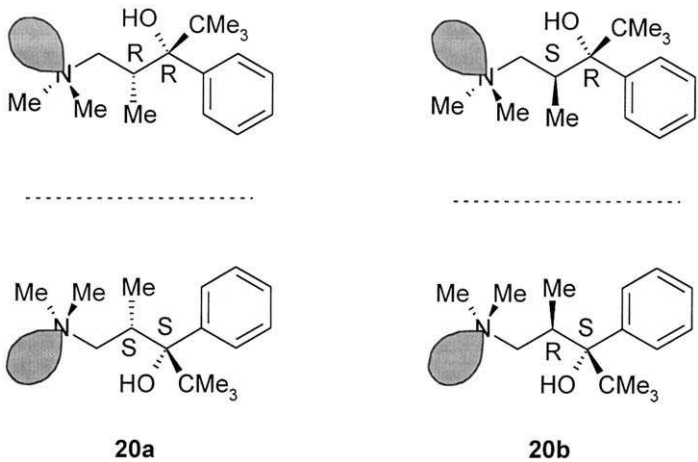

20a **20b**

Fig. 20. Stereoisomers of *N*,*N*-dimethylamino-2,4,4-trimethyl-3-phenyl-3-pentanol (**20**).

Table 1. Experimental free energy barriers (kcal/mol) and coalescence temperatures (°C) in parentheses for the internal motions of **20a**–**20d**

Compound	Phenyl rotation	*tert*-Butyl rotation	N-inversion or N–CO rotation
20a	12.3 (−4)	10.0 (−59)	11.3 (−26)
20b	11.9 (−15)	9.4 (−70)	9.3 (−75)
20c	15.8 (+70)	6.3 (−140)	19.7 (+118)
20d	17.9 (+104)	7.7 (−107)	18.5 (+114)

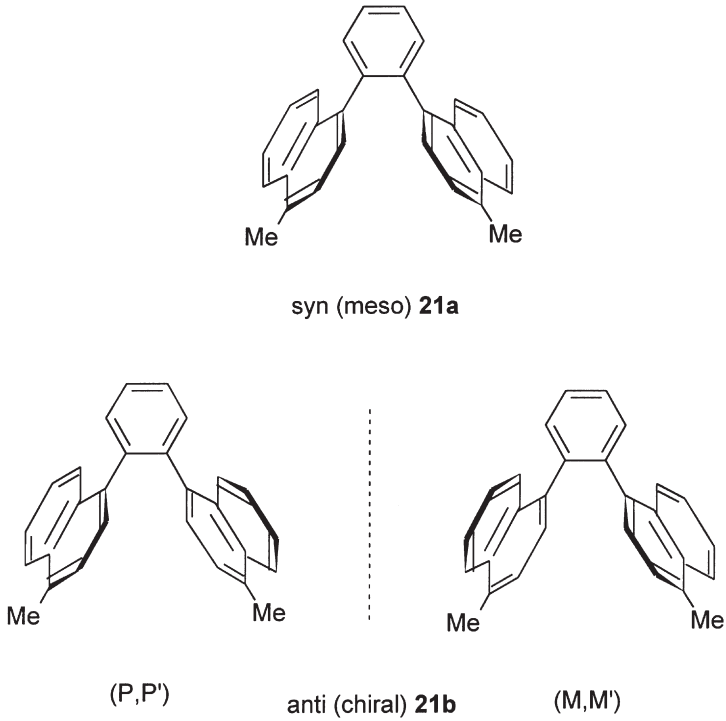

Fig. 21. Conformational diastereomers of 1,2-di(4-methylnaphth-1-yl)benzene (**21**).

or M,M′ → P,M′ mechanisms) barrier was $\Delta G^{\pm} = (19.5 \pm 0.2)$ kcal/mol. On the basis of the measured barrier the lifetime of the diastereoisomers is expected to be a few weeks at −50 °C. However, in the crystalline state (X-ray diffraction) only the *anti* diastereoisomer was found to be present. When the molecule is rendered asymmetrical by the introduction of a nitro group in the benzene ring, as in 1,2-di(4-methyl-naphth-1-yl)-4-nitrobenzene, the chiral *syn* and *anti* diastereoisomers are simultaneously present both in solution and in the solid state but in different proportions. The interconversion barriers of these stereolabile isomers independently determined by the two methods

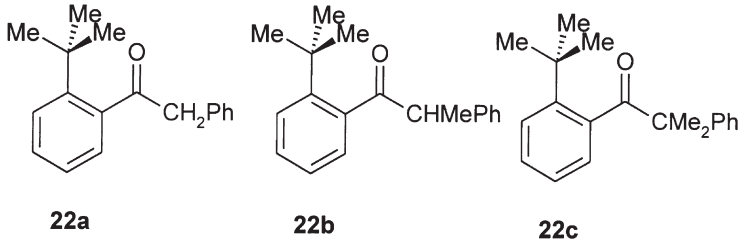

Fig. 22. Substituted *o-tert*-butylphenyl methyl ketones **22**.

essentially gave the same results: accordingly dynamic NMR and dynamic HPLC can be used as complementary techniques.

In sterically hindered aromatic ketones bearing bulky *ortho*-substituents the plane of the carbonyl group, C=O, is twisted from that of the aryl ring. Leardini *et al.*[49] have studied, by dynamic NMR, the stereomutation of the conformational atropisomers of *o-tert*-butylphenyl alkyl ketones **22** (Fig. 22). A prerequisite for using dynamic NMR is that the hindered ketones either have to adopt a propeller like chiral conformation, or the enantiotopic groups in the molecule can be transformed to diastereotopic by a proper chiral agent. At $-162\,^{\circ}C$ the protons of the CH_2-group in **22a** form an AB-spin system ($\Delta\nu = 70$ Hz, $^2J(^1H,^1H) = -17$ Hz) which means that these protons are now diastereotopic due to the slow Ar–CO-bond rotation. Line shape simulation gave the rate constants ($k = 25$/s at $-162\,^{\circ}C$) and further $\Delta G^{\pm} = (5.50 \pm 0.15)$ kcal/mol. In **22c** the corresponding value was 6.7 kcal/mol while in **22b** it was approximately the same as in **22a**.These experimental findings are complemented by molecular mechanics calculations.

Another example of dynamic NMR studies on atropoisomerism in *N*-aryl-1,4,5,6-tetrahydropyrimidines is based on the observation of the anisochronous NMR signals of the prochiral methylene groups as published by Garcia *et al.*[50] (Fig. 23). In hindered *N*-aryl-tetrahydropyrimidines the plane of the *ortho*-substituted benzene ring is significantly twisted, with respect to the time-averaged dynamic plane of the six-membered nitrogen heterocycle. The existence of such an Ar–N stereogenic axis produces a pair of stereolabile enantiomeric forms (atropoisomers) if the corresponding rotation rate is slow on the NMR time scale. For **23a** (X = Cl) at $-9\,^{\circ}C$ only one rotamer was observed (rotation was frozen, rate constant $k = 0$/s) giving AB-quartets for both of the geminal proton pairs at C-4 and C-4′ (the geminal protons at C-5 were decoupled). At $80\,^{\circ}C$ (where $k = 3000$/s) only single average signals for both of the geminal proton pairs were observed (fast exchange regime). From these data a $\Delta G^{\pm}$ value of 15.0 kcal/mol, for the interconversion of stereolabile atropoisomers for **23a**, is obtained. In **23b** (X = nitro) and **23c** (X = methyl) the corresponding free energy of activation values were 14.2 and 16.6 kcal/mol, respectively. In addition to the above mentioned enantiomerization of stereolabile atropoisomers, also the energy barriers for topomerization about

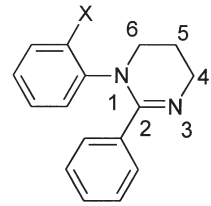

X = chloro (**23a**), nitro (**23b**) or methyl (**23c**)

Fig. 23. *N*-Aryl-2-phenyl-1,4,5,6-tetrahydropyrimidine (**23**).

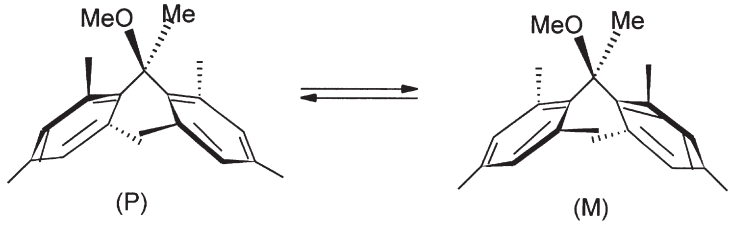

Fig. 24. Ring flip of the 1,1-dimesitylethyl methyl ether **24**.

the Ph–C-axis and for ring inversion in six-membered heterocycles were deteremined. Molecular mechanics modeling resulted in good agreement with these values. Further, a single-crystal X-ray diffraction study of **23a** yielded a molecular structure in good agreement with the results obtained by *ab initio* molecular orbital calculations.

Grilli *et al.*[51] have investigated, by dynamic NMR, the enantiomerization of stereolabile conformers of 2,4,6-trimethylphenyl (mesityl) substituted ethanol and ethers **24** (Fig. 24). Below $-100\,^{\circ}C$, in the NMR spectra of **24** both (M) and (P) propeller-like stereolabile enantiomers were visible. In principle, the enantiomerization of **24** from the (P) propeller antipode to the (M) form (reversion of helicity) can occur by three pathways. From these the conrotary motion characterized by the crowded transition state (coplanar mesityl rings) is not energetically favoured. Molecular mechanics modeling predicts that from the other two possible pathways: conrotary two-ring flip and disrotary one-ring flip, the latter pathway (representing a gear meshing mechanism) is the energetically favoured one. The computed energy barrier being 7.6 kcal/mol while for the former pathway (a gear clashing mechanism) the calculated barrier was 18.2 kcal/mol. The experimental energy barrier based on dynamic NMR studies is 7.45 kcal/mol, which is in agreement with the disrotary mechanism. Further, an introduction of a configurationally stable chiral center allowed two distinct NMR spectra to be detected for two stereolabile diastereoisomers.

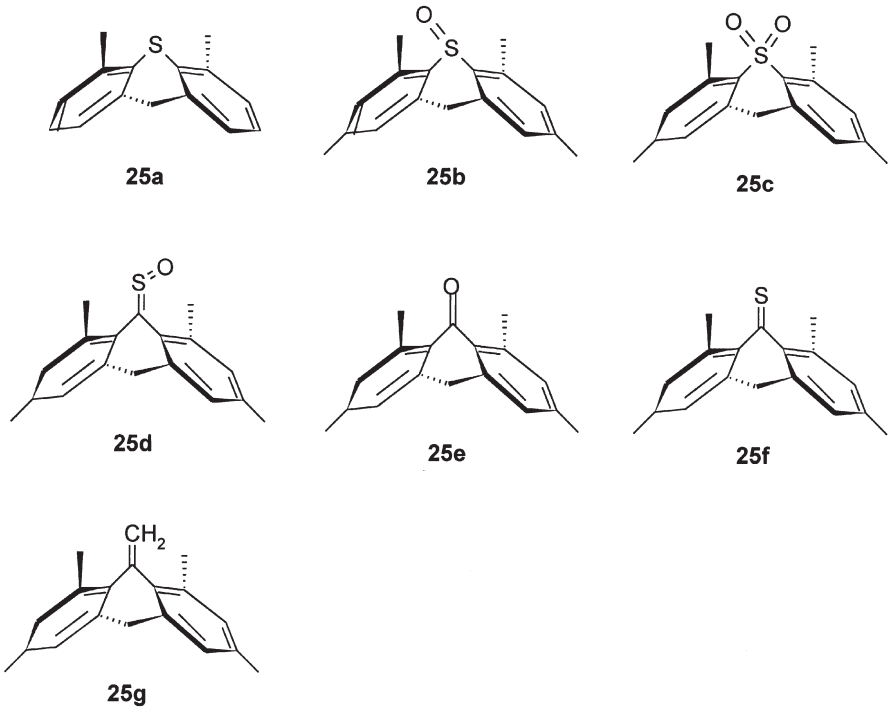

Fig. 25. 2,2′,6,6′-Tetramethyldiphenyl sulfide (**25a**), dimesityl sulfoxide (**25b**), dimesityl sulfone (**25c**), dimesityl sulfine (**25d**), dimesityl ketone (**25e**), dimesityl thioketone (**25f**) and 1,1-dimesityl ethene (**25g**).

The same correlated rotation (a cog wheeling circuit mechanism) for the enantiomerization of the propeller antipodes, as described above, is observed by Grilli *et al*. also for the 2,2′,6,6′-tetramethyldiphenyl sulfide **25a**,[52] dimesityl sulfoxide **25b** and dimesityl sulfone **25c**,[53] dimesityl sulfine **25d**,[54] dimesityl-ketone **25e**, dimesitylthioketone **25f**, and the 1,1-dimesitylethene **25g**[55] (Fig. 25).

Again the energy barriers explained by the one-ring flip mechanism (cog wheeling or gear meshing) equates generally better with the experimental ones based on dynamic NMR studies. Only in the case of **25g** (1,1-dimesitylethene) is the computed energy for the two-ring flip mechanism closer to the experimental value than is the barrier of the one-ring flip pathway. In Table 2 are collected the free energy barriers for the enantiomerizations of **25a**–**25g**.

As an example of how an achiral molecule, such as diphenyl sulfoxide (**26**) in the solid state, can possess two distinct rotation barriers about Ph–S-bonds is reported by Casarini *et al*.[56] (Fig. 26). The anisochronous signals in the solid state ^{13}C NMR spectrum of **26** at $-30\,^{\circ}C$ are due to the sulfur atom being a prochiral tetrahedral center (there is one electron lone pair pointing to one apex of the tetrahedron) with two enantiotopic phenyl groups in an isolated molecule. In the crystalline state these phenyls become diastereotopic (giving

Table 2. Experimental and calculated free energy barriers (kcal/mol) for the enantiomerizations of **25a**–**25g**

Compound	Experimental	Calculated (one-ring flip)
25a	< 4	4.8
25b	4.5	3.2
25c	5.0	Not available
25d	5.9 (Z-ring)	10.8
	13.8 (E-ring)	11.6
25e	4.6	5.4
25f	6.5	Not available
25g	9.2	12.3
		10.7 (conrotary two-ring flip)

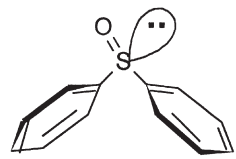

Fig. 26. Diphenyl sulfoxide (**26**).

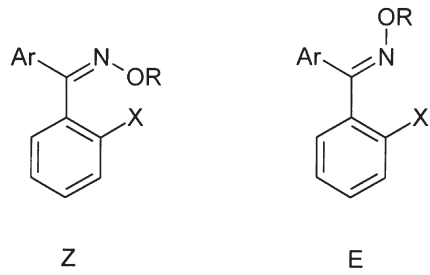

Fig. 27. *o*-Substituted diaryl ketone oximes **27**. X = PhS or Ph_2N, Ar = phenyl or benzyl.

rise to the anisochronous chemical shifts) because the crystal lattice forms a chiral extramolecular environment. Line shape simulations proved quantitatively that these experimental findings, which gave the values for distinct rate constants for both Ph–S-rotations, are correct. For example at 0 °C $k_1 = 200$/s and $k_2 = 0$/s (which means that one rotation is activated but the other one is still frozen), while at 25 °C both are activated the rate constants being $k_1 = 1200$/s and $k_2 = 350$/s, respectively. The fast exchange limit is achieved at 80 °C where both rate constants are $> 10^4$/s. In an achiral isotropic medium (solution) this phenomenon can be observed only if the formerly achiral molecule adopts a chiral conformation as described before.[51]

Leardini *et al.*[57] have studied stereomutation of the enantiomers of hindered O-substituted oximes (Fig. 27). Molecular mechanics calculations predict that

the (*E*)- and (*Z*)-isomers of diaryl ketone oximes **27** bearing a bulky substituent (PhS or Ph_2N) in the *ortho*-position of the phenyl ring, display different conformational preferences. Whereas the (*E*)-isomers exhibit a plane of symmetry at any accessible temperature, the (*Z*)-isomers exist as a pair of stereolabile enantiomers that were detected by low-temperature NMR spectroscopy in a chiral environment (Pirkle's alcohol). For example, in the (*Z*)-isomer of the X = PhS, R = CH_3 derivative of **27**, the methyl signal splits into a pair below −15 °C while the corresponding signal of the (*E*)-isomer does not split even at −100 °C. Another way to study these enantiomerization processes is to prepare derivatives containing two identical geminal substituents (such as hydrogens in a CH_2-group), which will give anisochronous signals (or display diastereotopic character) if the molecules are asymmetric. The free energy of activation for the enantiomerization process in (*Z*)-isomers of various O-substituted phenyl benzyl oximes varies between 14.2 and 14.9 kcal/mol. Further, when the O-substituent contains a configurationally stable stereogenic center (such as R = CHMeEt) all four stereoisomers (RM, RP, SM and SP) have been detected. The NMR results in solution were confirmed by X-ray diffraction measurements in the solid state.

It has been shown that even fairly strained bicyclic hydrocarbons can show some dynamic behaviour as modeled by molecular dynamics simulations for β-pinene.[58] In larger and more flexible hydrocarbons, and their derivatives, these phenomena are even more obvious. Grilli *et al.*[59] have investigated the stereodynamics of ring inversion of bicyclo[3.3.1]nonan-9-one (**28**) (Fig. 28). Molecular modeling of **28** suggests that the two most preferred conformers with the C_{2v}- and C_s-symmetries differ only by 0.95 kcal/mol in their relative energies while the third one characterized by C_2-symmetry has 4.92 kcal/mol higher energy than the first one. A ^{13}C NMR study (100.6 MHz) at −165 °C shows two separate signals for carbons 3 and 7 in a conformer with C_s-symmetry (in addition to the strong peak coming from the symmetrical C_{2v}-form where C-3 and C-7 are identical) pointing to an exchange between these two very biased conformers. Line shape simulations yielded rate constants $k = 130$ (at −148 °C) and 110/s (at −150 °C) for the inversion between these

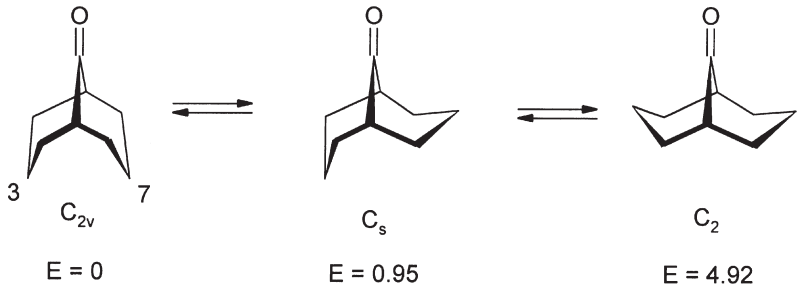

Fig. 28. Symmetry and ring inversion in bicyclo[3.3.1]nonan-9-one (**28**).

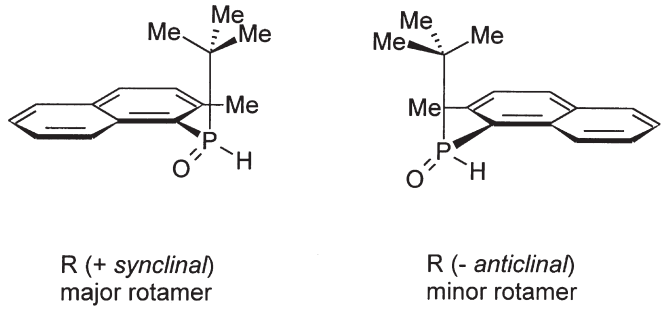

Fig. 29. Conformational rotamers of (*R*)-enantiomer of **29**.

two low energy conformers which corresponds to a free energy of activation of $\Delta G^{\ddagger} = 5.70 \pm 0.15$ kcal/mol. In contrast, the corresponding hydrocarbon, bicyclo[3.3.1]nonane, did not show any line broadening even at $-170\,^{\circ}C$ although in principle the calculated value of $\Delta G^{\circ} = 7.6$ kcal/mol for ring inversion should be accessible to NMR spectroscopy.

As an example of how stereolabile isomers of configurational enantiomers can be identified by dynamic NMR, and even separated by low temperature HPLC, is the case of *tert*-butyl-1-(2-methylnaphthyl)phosphine oxide (**29**) reported by Gasparrini *et al.*[60] (Fig. 29). Two unequally populated stereolabile isomers (*synclinal* and *anticlinal*) for both of the configurational enantiomers (*R* and *S*) of *tert*-butyl-1-(2-methylnaphthyl)phosphine oxide were assigned. The assignment was based on NOE experiments at $-65\,^{\circ}C$. The ^{1}H NMR chemical shifts of H-8 and the Me at C-2 in the naphthalene ring are sensitive to the conformation of the molecule and support the NOE results. In the *synclinal*-conformer δ(H-8) = 8.98 and $\delta(CH_3\text{-}2) = 2.65$ ppm whereas in the *antilinal*-form these values are 8.15 and 2.95 ppm, respectively. The integrated intensities of the ^{31}P NMR spectra are in agreement with the conformer ratio measured from the ^{1}H NMR spectra. The polarity of the solvent (CD_2Cl_2 vs. CD_3OD) did not influence significantly this conformer ratio. All of the four species of **29** [*R*(*sc*), *R*(*ac*), *S*(*sc*) and *S*(*ac*)] were physically separated and identified on a cryogenic HPLC enantioselective column at $-83\,^{\circ}C$. The interconversion barriers measured by dynamic NMR and by dynamic HPLC are in excellent agreement being 14.75 and 14.95 kcal/mol, respectively.

Another example of the conformational enantiomers in substituted naphthalenes is given by Lunazzi *et al.*[61] (Fig. 30). Peri-substituted acylnaphthalenes **30** give rise to a pair of enantiomers when the rotation of the acyl group is slow. Such enantiomers were observed by means of VT NMR spectra at low temperatures in chiral environments [(*R*)-(−)-1-(9-anthryl)-2,2,2-trifluoroethanol]. The barrier to rotation for the acyl substituents was demonstrated to be lower than that for the phenyl group. However, at $-100\,^{\circ}C$ the rotation of both the acyl and the phenyl groups of **30** is restricted; as revealed by four anisochronous ^{13}C NMR signals originated from the *ortho*- and *meta*-carbons

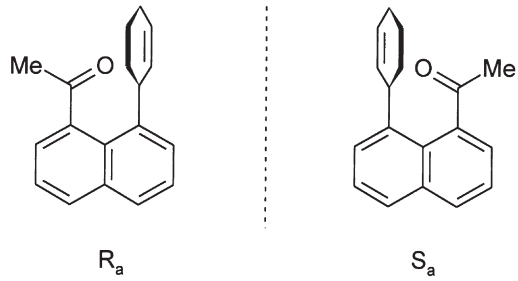

Fig. 30. Stereolabile (R_a)- and (S_a)-enantiomers of 1-(8-phenyl-1-naphthyl)-1-ethanone (**30**).

in the phenyl ring. In 1-[8-(3-ethylphenyl)-1-naphthyl]-1-ethanone it is possible to measure these two barriers that are found to be 10.4 and 15.9 kcal/mol, respectively. The barrier for the acyl group rotation increases regularly (from 9.5 to 13.2 kcal/mol) with an increase in the dimension of the alkyl part of the RCO-moiety (R = Me, Et, *iso*-Pr, *tert*-Bu). When the phenyl group is substituted by a bromine atom, the enantiomerization barriers for the corresponding RCO-derivatives (R = Et, *iso*-Pr, *tert*-Bu) are increased from 13.5 to 18.0 kcal/mol.

Lunazzi *et al.*[62] have studied the conformational dynamics of homochiral dicarvone **31** both in solution and in the solid state (Fig. 31). Dynamic NMR experiments show that **31** exists in the P- and M-helical forms (atropisomers) having a 99.5 : 0.5 molar ratio at −40 °C in CH_2Cl_2. The experimental interconversion barrier, 13.3 kcal/mol, is close to the computed value of 14.7 kcal/mol by molecular mechanics. A second stereomutation process has also been discovered, with a conformer having antiparallel exocyclic *iso*-propenyl groups interconverting into a second conformer (rotation around the C6–C7-bond) having these groups in a parallel orientation, in a 95.5 : 4.5 molar ratio at −135 °C. Also for this process the molecular mechanics computed barrier, 7.9 kcal/mol, equates satisfactorily with the experimental one, 8.4 kcal/mol. Low temperature solid state (CP-MAS) NMR studies show that the latter motion occurs also in the crystal but the corresponding barrier is significantly higher, 14.8 kcal/mol, due to the effects of the lattice forces. It is interesting that X-ray structural analysis gave solely the conformer where the *iso*-propenyl groups are in the antiparallel orientation.

As reported by Orrell[2] dynamic NMR has very interesting applications in organometallic and organoelement chemistry. As an example of that area Bonini *et al.*[63] have studied stereolabile enantiomers of acyl and thioacyl ferrocenes (Fig. 32). At −138 °C the ^{13}C NMR spectrum of **32** shows two conformational diastereomers in a 2:1 molar ratio. A line shape analysis gave the free energy of activation, $\Delta G^{\pm} = 7.5$ kcal/mol, for the interconversion of these diasteromers. For the thioacetyl derivative the corresponding value is 8.8 kcal/mol. Because the enthalpy difference between the *syn*- and *anti*-forms is

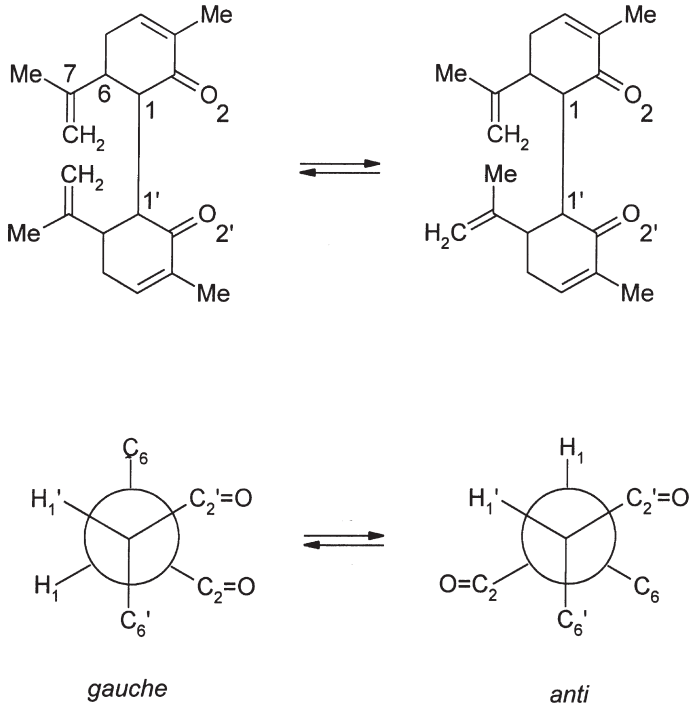

Fig. 31. Structures and Newman projections (along the C1′–C1-bond) of P- and M-helical atropoisomers for 6,6′-di-*iso*-propenyl-3,3′-dimethyl-bicyclohexyl-3,3′-diene-2,2′-dione (**31**).

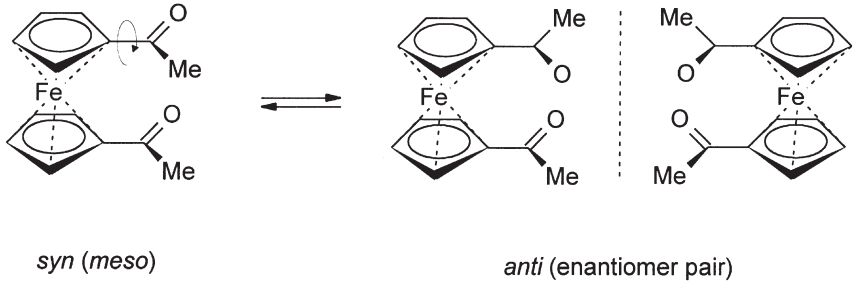

Fig. 32. *syn*- and *anti*-Conformers of 1,1′-dieacetylferrocene (**32**).

considered to be very small, the 2 : 1 molar ratio also predicts a value for the entropy factor in the free energy of activation of this interconversion process.

As an example of organoelement compounds Anderson *et al.*[64] have studied the conformations and stereodynamics of aliphatic tri-*iso*-propylsilanes in solution and in the solid state (Fig. 33). A dynamic process was detected in the solution by the ^{13}C NMR spectra of **33** taken over the temperature range

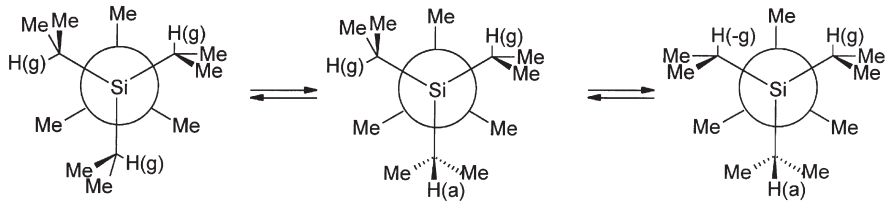

Fig. 33. Newman projections (along the **Si**–**C**$(CH_3)_3$-bond) of (*gauche*, *gauche*, *gauche*)-, (*gauche*, *anti*, *gauche*)- and (*gauche*, *anti*, −*gauche*)-conformers of *tert*-butyl(tri-*iso*-propyl)silane (**33**).

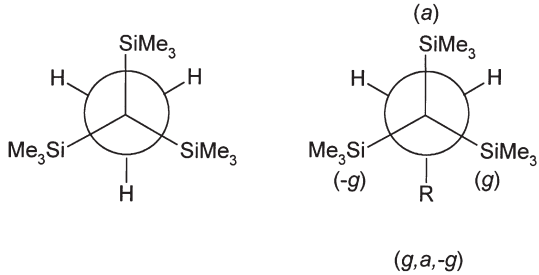

Fig. 34. Newman projections of 1,1,1-tris(trimethylsilyl)ethane (**34b**) and (*gauche*, *anti*, −*gauche*)-conformer of its derivative where R = CH_3 (**34C**), CH_2CH_3 (**34d**), and $CH_2C_6H_5$ (**34e**).

−145–−163 °C, $\Delta G^{\pm} = 5.5$ kcal/mol. Molecular mechanics calculations have identified three types of conformations that are markedly more stable than all of the others. However, the one with the highest symmetry (g, g, g-conformation) cannot be populated, as is evident from the appearance of the spectrum at low temperatures. The observed spectrum can be interpreted in terms of restricted rotation of the *tert*-butyl group and of the *iso*-propyl groups, leading to a structure centred around the ($g, -a, g$)-conformation. In (*iso*-Pr)$_3$SiCl, this dynamic process was not observed in solution, but an appropriate spectrum for the same ($g, a, -g$)-conformation was obtained by solid state CP-MAS NMR spectroscopy at −100 °C.

In sterically more crowded compounds such as tris(trimethylsilyl)methane (**34a**) correlated rotation of the Me_3S-groups is reported by Casarini *et al.*[65] (Fig. 34). Based on the low temperature NMR spectra of $(Me_3Si)_3CH$ (**34a**) the barrier for the restricted rotations of the Me_3Si-groups was calculated to be 5.1 kcal/mol. This motion was assigned (by molecular mechanics) to a correlated disrotatory process with an eclipsed, staggered, staggered (ESS) transition state. In a more crowded compound, $(Me_3Si)_3CMe$ (**34b**), both a correlated ESS disrotatory process and a correlated conrotatory SSS process

were distinguished with rotational barriers of 6.70 and 5.15 kcal/mol, respectively. Thus, **34b** appears to adopt a chiral conformation (point group C_3) at low temperature. In its homologues, $(Me_3Si)_3CCH_2CH_3$ (**34c**) and $(Me_3Si)_3CCH_2CH_2CH_3$ (**34d**), the ESS and SSS rotations around the Si–C bonds were also detected. Although in $(Me_3Si)_3CCH_2Ph$ (**34e**) the effects of restricted rotation about the C–CH_2Ph bond could not be observed. The same chiral conformation as adopted by **34c** and **34d** (point group C_1) was nonetheless assigned from molecular mechanics calculations and X-ray diffraction studies. An interesting novel application was to use ^{29}Si NMR to determine the barrier for the C–Et-rotation in **34c**. The effects of the ESS- and SSS-processes are not visible in the ^{29}Si NMR spectra, which makes their interpretation easy. At $-166\,^{\circ}$C the ^{29}Si NMR signal of **34c** was split into a doublet (intensity ratio 1 : 2) from which the free energy of activation of 5.55 ± 0.15 kcal/mol was calculated. This third process seems to be correlated with the SSS conrotatory process, since both have essentially the same energy barriers.

4.4. Dynamics of toxaphene congeners

In their recent review "Toxaphene. Analysis and Environmental Fate of Congeners" with 257 references Vetter and Oehme[66] write that in technical toxaphene mixtures there exist several hundreds of components consisting mainly of polychlorinated bornanes. This number is low, however, in comparison to the theoretically possible number of congeners, which exceeds 30,000. In the environment and particularly in higher organisms, most of the components of toxaphene are degraded, and only a few are accumulated. More than 40 individual polychlorinated bornanes were synthesized and isolated. Although the structural characterization of these congeners is reported, very little is known about their conformational characteristics, which can be of extreme importance for the correct assessment or prediction of their degradation or accumulation in the environment.

Among the very first systematic papers on this topic is that by Nikiforov *et al.*[67] who have utilized VT NMR studies in clarifying the internal rotations in three toxaphene congeners (Fig. 35). It is necessary to emphasize that prior to this study, for over 50 different toxaphene congeners known not more than one conformer was reported. This is surprising since already at ambient temperature, ^{1}H NMR spectra of the three toxaphene congeners, 2-*exo*,3-*endo*,6-*exo*,8,9,10,10-heptachlorobornane (**35a**), 2,2,3-*exo*,5-*endo*,6-*exo*,8,9,10,10-nonachlorobornane (**35b**) and 2-*exo*,3-*exo*,6,8,8,9,10,10-octachlorodihydrocamphene (**35c**) show broadening of several signals. At $-58\,^{\circ}$C, **35a** exists in two stable conformations in approximately a 1 : 5 molar ratio.

Compound **35b** was obtained as a 1 : 1 mixture with its close structural analogue, 2-*exo*,3,3,5-*exo*,6-*endo*,8,9,10,10-nonachlorobornane. These two

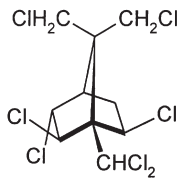

35a

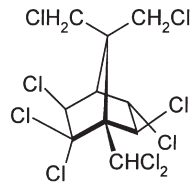

35b

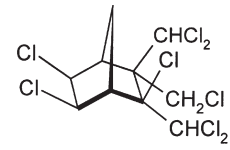

35c

Fig. 35. 2-*exo*,3-*endo*,6-*exo*,8,9,10,10-Heptachlorobornane (**35a**), 2,2,3-*exo*,5-*endo*,6-*exo*,8,9,10,10-nonachlorobornane (**35b**) and 2-*exo*,3-*exo*,6,8,8,9,10,10-octachlorodihydrocamphene (**35c**).

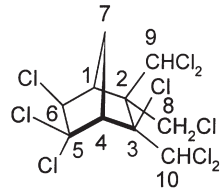

36

Fig. 36. 3-*exo*,5,5,6-*exo*,8,9,9,10,10-Nonachlorodihydrocamphene (**36**).

compounds always co-crystallize and all attempts to separate the pair were unsuccessful. At ambient temperature all three signals viz. dichloromethyl proton at 6.90 ppm, chloromethyl protons at 4.55 ppm and chloromethyl proton at 4.00 ppm of **35b** are broad. At −53 °C the broadening disappears, and fine structure becomes clearly visible. However, there are no signals for the second conformation. At the same time, at −53 °C two signals of the chloromethyl protons of another component of the mixture, 2-*exo*,3,3,5-*exo*,6-*endo*,8,9,10,10-nonachlorobornane, at 5.05 and 4.35 ppm become broader, and their fine structure disappears. This indicates, that the rotation of the chloromethyl-group in this compound gets slow enough to be detected at −53 °C.

In **35c**, at ambient temperature, one can see the most significant broadening of the signals of the dichloromethyl protons and of the 2-*endo* proton at 7.1, 6.65 and 5.70 ppm, respectively. This broadening disappears at −53 °C. However, no signs of another conformation appear which implies that this compound has a rotation behaviour like that of 2-*exo*,3-*endo*,6-*exo*,8,9,10,10-heptachlorobornane, but the most stable conformation is predominant (>90%) in the equilibration mixture. It also means, that the rotation behaviour of this compound is similar to that of 2,2,3-*exo*,5-*endo*,6-*exo*,8,9,10,10-nonachlorobornane (**35b**).

Another example of the conformational dynamics of toxaphene congeners, viz. in polychlorinated dihydrocamphenes, is given by Koivisto *et al.*[68,69] for 3-*exo*,5,5,6-*exo*,8,9,9,10,10-noachlorodihydrocamphene (**36**) (Fig. 36). As can be seen in Fig. 37 at 0 °C two conformers of **36** are clearly visible in 59.3 (a) and 40.7 (b) per cent molar ratios. These conformers are due to restricted rotation

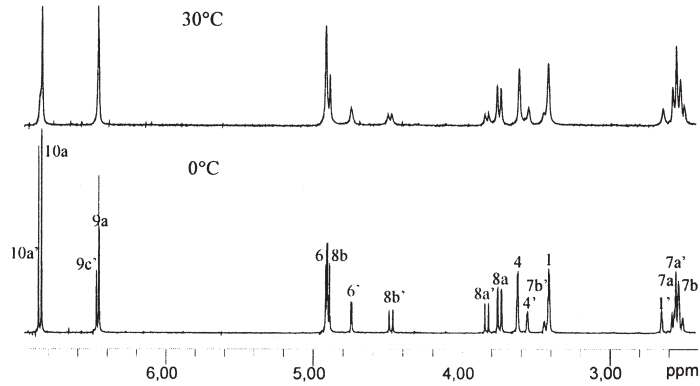

Fig. 37. ^{1}H NMR spectra of **36** at 0 and 30 °C.

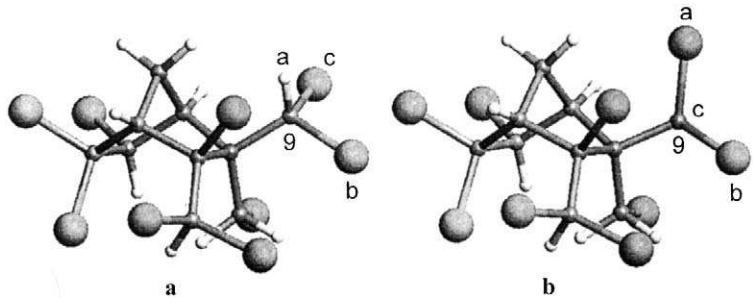

Fig. 38. The two most stable conformers of **36**.

around the C2–C9-bond (rotation of dichloromethyl-group at C2). In Fig. 38 are given the energetically optimized conformers (at the *ab initio* HF/6-31G* level) for **36**.

In contrast to the above mentioned compound, for a new toxaphene congener, 3-*endo*,5-*endo*-dichloro-4-dichloromethyl-7,7-bis-chloromethyl-tricyclo[2.2.1.0^{2,6}]heptane (**39**),[70] it is shown according to the rotation energy profile calculated at the HF/6-31G(d) level, that rotation of the chloromethyl and dichloromethyl groups are highly unlikely at room temperature (Fig. 39).

4.5. Conformational dynamics in cycles with multiple heteroatoms

Last but not least in this area can be mentioned many papers on the topic of configurational and conformationl studies of cyclopentane-, cyclohexane-, cycloheptane- and cyclooctane-fused 1,3-oxazines, 1,3-thiazines and pyrimidines published by Pihlaja *et al.*[71] Further, in their recent collective article[72] ^{1}H, ^{13}C and ^{17}O NMR spectral studies on monocyclic dioxolanes, dioxanes,

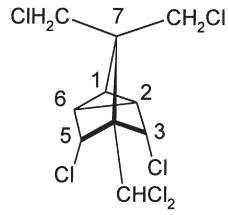

39

Fig. 39. 3-*endo*,5-*endo*-Dichloro-4-dichloromethyl-7,7-bis-chloromethyl-tricyclo[2.2.1.$0^{2,6}$] heptane (**39**).

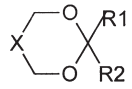

X = -$(CH_2)_0$- dioxolanes **40a**
X = -$(CH_2)_1$- dioxanes **40b**
X = -$(CH_2)_2$- dioxepanes **40c**
X = -$(CH_2)_3$- dioxocanes **40d**

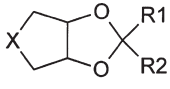

X = -$(CH_2)_1$- (*3ar,6ac*)-tetrahydrocyclopenta[d][1,3]dioxole **40e**
X = -$(CH_2)_2$- (*3ar,7ac*)-hexahydro-1,3-benzodioxole **40f**
X = -$(CH_2)_3$- (*3ar,8ac*)-hexahydrocyclohepta[d][1,3]dioxole **40g**
X = -$(CH_2)_4$- (*3ar,9ac*)-octahydrocycloocta[d][1,3]dioxole **40h**

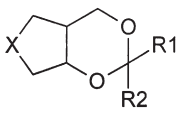

X = -$(CH_2)_1$- (*4ar,7ac*)-hexahydrocyclopenta[e][1,3]dioxine **40i**
X = -$(CH_2)_2$- (*4ar,8ac*)-hexahydro-1,3-benzodioxine **40j**
X = -$(CH_2)_3$- (*4ar,9ac*)-octahydrocyclohepta[e][1,3]dioxine **40k**
X = -$(CH_2)_4$- (*4ar,10ac*)-octahydrocycloocta[e][1,3]dioxane **40l**

Fig. 40. Nomenclature and structures of oxygen containing heterocycles **40**.

dioxepanes and dioxocanes and cycloalkane fused (5–8-membered) bicyclic 1,3-dioxolanes and 1,3-dioxanes (comprising 81 compounds in all) are reported (Fig. 40). These heterocycles possess a variety of very fascinating conformational dynamics related to the ring size as described in Figs. 41 and 42. As an example on the dynamics in the heterocyclic ring systems is the paper by Pihlaja *et al.*[73] on the synthesis and structural characterization of *cis*- and *trans*-fused 4a,5,6,7,8,8a-hexahydro-2*H*,4*H*-1,3-benzodithiines (**43**) and their 2-methyl and 2,2-dimethyl derivatives (Fig. 43). ^3J(H,H) spin–spin couplings of **43** reveal that both geometric isomers exist predominantly in chair–chair conformations: the *trans*-fused isomer is conformationally locked in this form. In contrast, the *cis*-isomer is more flexible and can potentially attain either the S-in or the S-out conformation. The interconversion of these conformers occurs in the fast exchange regime at ambient temperatures but at 213 K the *cis*-isomer freezes out into an 83 : 17 mixture of the S-in and S-out forms; the

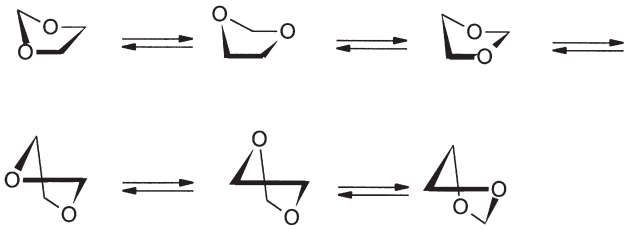

Pseudorotation of 1,3-dioxolanes **40a**

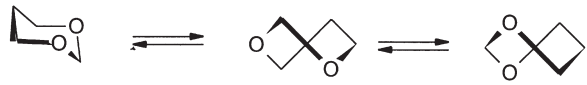

Chair, 2,5-twist- and 1,4-twist-boat conformers of 1,3-dioxane **40b**

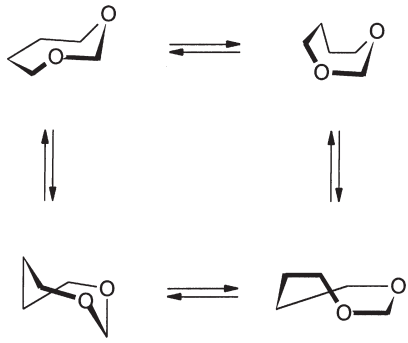

Chair, boat, twist-boat and twist-chair conformers of1,3-dioxepanes **40c**. In addition, there exists an internal dynamic equilibrium where oxygens are in different positions for each form

Fig. 41. Conformational dynamics in dioxolanes **40a**, dioxanes **40b** and dioxepanes **40c**.

S-in form is 2.8 kJ/mol more stable than the S-out form. Both 2-*cis*-methyl-4*ar*,5,6,7,8,8*ac*-hexahydro-1,3-dithiine and its 2,2-dimethyl derivative adopt almost exclusively the S-in conformer at ambient temperature (due to the intramolecular axial–axial interactions) whereas 2-*trans*-methyl-4*ar*,5,6,7,8,8*ac*-hexahydro-1,3-dithiine is in a 5 : 1 dynamic equilibrium between the S-out and S-in conformers.

cis-Fused 7a(8a)-methyl and 6-phenyl octa(hexa)hydrocyclopenta[*d*][1,3]oxazines and [3,1]benzoxazines also form an interesting topic for dynamic NMR studies as reported by Tähtinen *et al.*[74] (Fig. 44). In solution, the cyclopentane-fused 2-oxo derivatives and the 1,3-benzoxazinone were found to attain

Fig. 42. Chair–chair, boat–chair and boat–boat conformers of dioxocanes **40d**.

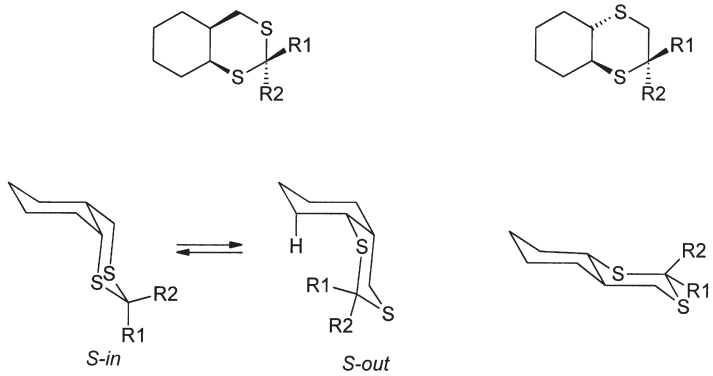

Fig. 43. *cis*- and *trans*-Fused 4a,5,6,7,8,8a-hexahydro-2*H*,4*H*-1,3-benzodithiines (**43**) and *S-in*/*S-out* conformational equilibrium in *cis*-fused isomer.

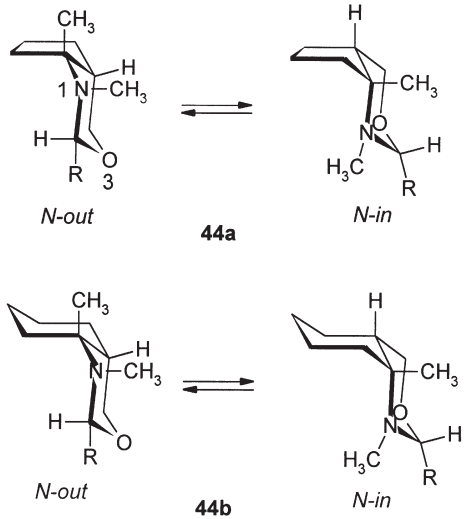

Fig. 44. Conformational equilibria in (4a*R*,7a*S*)-1,7a-dimethyl-1,2,4,4a,5,6,7,7a-octahydrocyclopenta[*d*][1,3]oxazine (**44a**) and (4a*R*,8a*S*)-1,8a-dimethyl-4*H*-1,2,4a,5,6,7,8,8a-octahydro[3.1]benzoxazine (**44b**).

exclusively the N-in/O-in conformation, whereas the 6-phenyl 2-oxo/thioxo derivatives were predominantly in the N-out conformation. The C-2 unsubstituted and the 2-oxo/thioxo 7a/8a-methyl derivatives were in solution as a rapidly interconverting equilibrium of the N-in and N-out conformations.

The positions of these conformational equilibria were estimated by the reproduction of experimental ^{3}J(H,H) spin–spin couplings from statistically weighed values for model compounds. The C-2 methyl derivatives were each found to be interconvertable mixtures of epimers (at C-2) with the N-in conformer predominating for one epimer and the N-out conformer predominating for the other; with both predominating conformers having the C-2 methyl group equatorially orientated. Based on selective NOE experiments the hydrogen or methyl group on the nitrogen was found to be always predominantly equatorial with respect to the heterocyclic ring, except for the epimeric 2-methyl derivatives with N-out conformations where steric constraints and the generalized anomeric effect favoured the axial orientation of the methyl substituent.

A related conformational study of N-substituted hexahydrocyclopent[*e*][1,3]-oxazin-4-ones and hexahydro-2*H*-1,3-benzoxazin-4-ones has been published by the same group[75] (Fig. 45). Dynamic ^{1}H and ^{13}C NMR studies of **45a** and **45b** revealed several dynamic conformational processes. These include a conformational equilibrium between the O-in (major conformer) and O-out ring forms in the hexahydro-2*H*-1,3-benzoxazin-4-ones, an equilibrium consisting of two intramolecularly hydrogen bonded forms between the hydroxyl proton (when R = CH_2OH) and the C4=O (major form) or the ethereal O1 (minor form) and a nonhydrogen bonded form in two congeners. In addition, the rotation about the amide C–N bond was restricted when R was sufficiently bulky, such as $CH_2OCONHC_6H_4X$-*p* (X = H, Cl). At 293 K in a 1 : 1

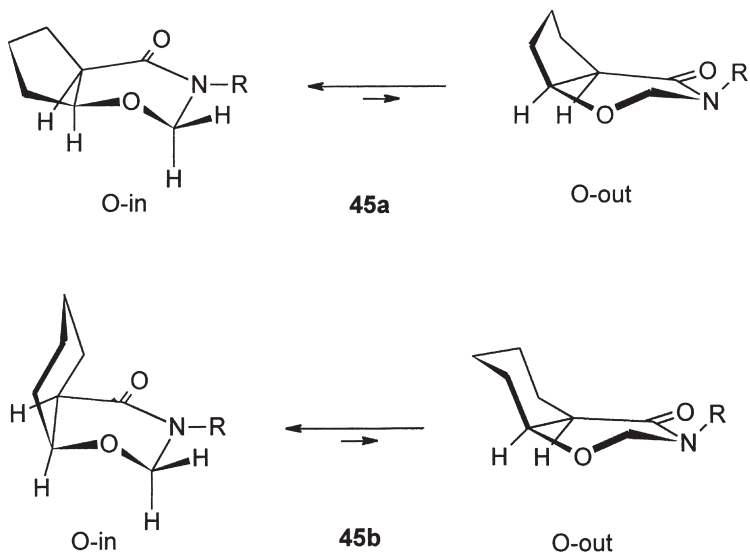

Fig. 45. Conformational equilibria in N-substituted hexahydrocyclopent[*e*]-[1,3]oxazin-4-ones (**45a**) and hexahydro-2*H*-1,3-benzoxazin-4-ones (**45b**).

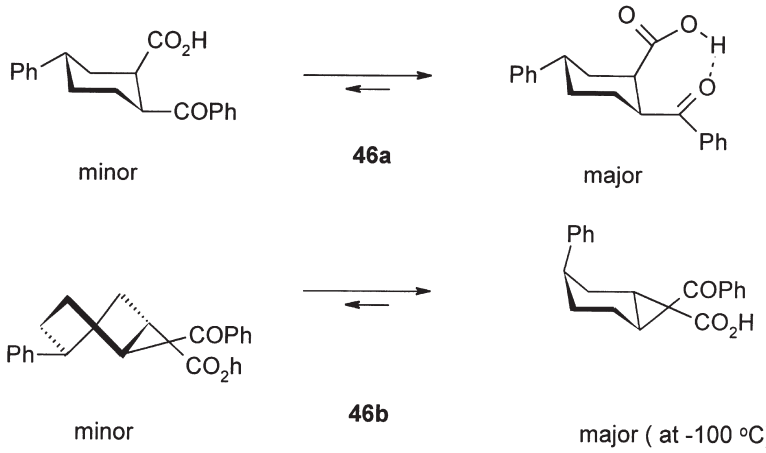

Fig. 46. Intramolecular hydrogen bonding and conformational equilibria in *t*-5-phenyl-*c*-benzoylcyclohexane-*r*-1-carboxylic acid (**46a**) and *t*-5-phenyl-*t*-2-benzoylcyclohexane-*r*-1-carboxylic acid (**46b**).

(v/v) CD_2Cl_2/CS_2-mixture the $K = [\text{O-in}]/[\text{O-out}]$ ratio was 2.0 for the parent **45a** (R = H) and 9.0 for **45b** (R = H) the corresponding free energy differences are $\Delta G^{\ddagger} = 1.7$ and 5.4 kJ/mol, respectively.

Substitution can significantly affect the conformational characteristics of cyclohexane derivatives as reported by Klika *et al.*[76] (Fig. 46). The conformational assignment of **46a**, its *trans*-4-phenyl positional isomer and both their *trans*-2-benzoyl epimers (**46b** and its *trans*-4-phenyl positional isomer) were elucidated by means of NMR spectroscopy. In fact, the previously postulated *trans–cis* transformation of **46b** to **46a** does not occur. All of the compounds show substantial intramolecular hydrogen bonding in $CDCl_3$. Furthermore, a dynamic equilibrium between the hydrogen bonded and nonhydrogen bonded forms is observed by NMR for **46a** the hydrogen bonded form is predominant. Based on low temperature NMR measurements at 173 K the ratio of the minor form to the major one in **46b**, $K = [\text{twist-boat}]/[\text{chair}] = 0.2$ corresponding to $\Delta G^{\ddagger} = 0.46$ kJ/mol.

In addition to the conformational dynamics of various fused heterocycles themselves, their substituents can show interesting dynamic properties such as high energy barriers for hindered rotation of bridgehead phenyl groups in *p*-(chlorophenyl)pyrrolo[1,2-*a*][3,1]benzoxazin-1-ones[77] (Fig. 47).

An unusually high free energy barrier for the restricted rotation around the $C(sp^3)$–$C(sp^2)$-bond of the bridgehead *p*-chlorophenyl group was measured for **47** (di-*endo* derivative) and its di-*exo* isomer. The average value for the free energy of activation based on both VT ^1H and ^{13}C NMR experiments is $\Delta G^{\ddagger} = 56.0 \pm 1.0$ kJ/mol.

Dynamic processes in *N*-acylated 1,2-dihydro-2,2,4-trimethylbenzo[*h*]quinoline have been investigated with NMR spectroscopic and quantum chemical

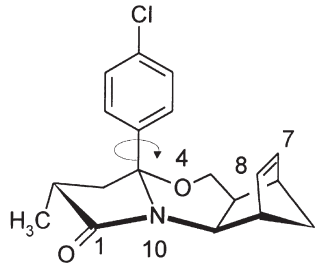

Fig. 47. (2*R**,3a*S**,5a*R**,9a*R**)-2-methyl-3a-(4-chlorophenyl)-6,9-methano-1,2,3,3a,5a,6,9a-octahydro-5*H*-pyrroli[1,2-*a*][3,1]benzoxazin-1-one (**47**).

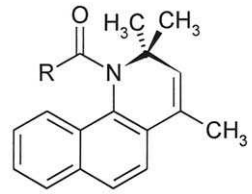

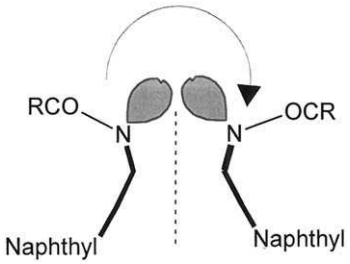

Fig. 48. Structure and nitrogen inversion of *N*-acylated 1,2-dihydro-2,2,4-trimethyl-benzo(*h*)benzoquinoline (**48**).

methods by Leis *et al.*[78] (Fig. 48). VT ^{1}H NMR signals of geminal methyls in **48** (R = methyl, ethyl, *iso*-propyl or phenyl) reveal the interconversion of a pair of enantiomers for with $\Delta G^{\ddagger} = 56.1$–$74.1$ kJ/mol. A good correlation exists between the experimental $\Delta G^{\ddagger}$ values and the energy barriers predicted by the semiempirical quantum chemical calculations using the AM1 SCF model.

5. CONCLUSIONS

The selected examples are limited to organic chemistry, as given above, and show that a large variety of dynamic processes are accessible by NMR studies. The limitations in time resolution of NMR can be overcome by rapidly

increasing computational power and by application of modern sophisticated calculational methods. Consequently, in the near future it is anticipated that quantum chemical methods will start a similar invasion to that found in organic chemistry, also in organometallic and biochemistry. These are areas which need much more computational resources than classic organic chemistry. On the other hand, the recent advancements of dynamic NMR in organic chemistry will certainly help and hasten those applications.

REFERENCES

1. M. Oki, *Applications of Dynamic NMR Spectroscopy to Organic Chemistry*, VCH, Deerfield Beach, 1985.
2. K. Orrell, *Annu. Rep. NMR Spectrosc.*, 1999, **37**, 2.
3. A. D. Bain and G. J. Duns, *J. Magn. Reson., A*, 1995, **112**, 258.
4. A. D. Bain and G. J. Duns, *Can. J. Chem.*, 1996, **74**, 819.
5. M. Barfield and P. Fagerness, *J. Am. Chem. Soc.*, 1997, **119**, 8699.
6. M. Pons and O. Millet, *Prog. Nucl. Magn. Reson. Spectrosc.*, 2001, **38**, 267.
7. E. Kleinpeter, *Adv. Mol. Struct. Res.*, 2000, **6**, 97.
8. R. Marek and A. Lyčka, *Curr. Org. Chem.*, 2002, **6**, 35.
9. H. Günther, *NMR Spectroscopy, Basic Principles, Concepts and Applications in Chemistry*, 2nd edn, John Wiley & Sons Ltd, Chichester, 1995, 339.
10. J. M. Goodman, P. D. Kirby and L. O. Haustedt, *Tetrahedron Lett.*, 2000, **41**, 9879.
11. W. B. Smith, *Magn. Reson. Chem.*, 1999, **37**, 103.
12. W. B. Smith, *Magn. Reson. Chem.*, 1999, **37**, 107.
13. W. B. Smith and C. A. Amezcua, *Magn. Reson. Chem.*, 1999, **37**, 110.
14. A. Dokalik, H. Kalchhauser, W. Mikenda and G. Schweng, *Magn. Reson. Chem.*, 1999, **37**, 895.
15. J. Czernek, R. Fiala and V. Sklenář, *J. Magn. Reson.*, 2000, **145**, 142.
16. E. Kleinpeter and A. Koch, *J. Phys. Org. Chem.*, 2001, **14**, 566.
17. A. Laxer, D. T. Major, H. E. Gottlieb and B. Fischer, *J. Org. Chem.*, 2001, **66**, 5463.
18. J. Mäki, K. D. Klika, R. Sjöholm and L. Kronberg, *J. Chem. Soc., Perkin Trans. 1*, 2001, 1216
19. G. Giorgi, F. Ponticelli, L. Savini, L. Chiasserini and C. Pellerano, *J. Chem. Soc., Perkin Trans. 2*, 2000, 2259
20. J. A. Jimenez, R. M. Claramunt, C. Escolastico and J. Elguero, *Struct. Chem.*, 2000, **11**, 7.
21. A. Dkhissi, L. Houben, J. Smets, L. Adamowicz and G. Maes, *J. Mol. Struct.*, 1999, **484**, 215.
22. S. Berger, S. Braun and H.-O. Kalinowski, *NMR Spectroscopy of the Non-Metallic Elements*, Wiley, New York, 1997, 195.
23. R. Gawinecki, E. Kolehmainen, D. Rasała and R. Suontamo, *J. Phys. Org. Chem.*, 1995, **8**, 689.
24. E. Murguly, T. B. Norsten and N. Branda, *J. Chem. Soc., Perkin Trans. 2*, 1999, 2789
25. E. Kolehmainen, B. Ośmiałowski, M. Nissinen, R. Kauppinen and R. Gawinecki, *J. Chem. Soc., Perkin Trans. 2*, 2000, 2185
26. E. Kolehmainen, B. Ośmiałowski, T. M. Krygowski, R. Kauppinen, M. Nissinen and R. Gawinecki, *J. Chem. Soc., Perkin Trans. 2*, 2000, 1259
27. R. Gawinecki, B. Ośmiałowski, E. Kolehmainen and R. Kauppinen, *J. Phys. Org. Chem.*, 2001, **14**, 201.
28. B. Ośmiałowski, E. Kolehmainen, M. Nissinen, T. M. Krygowski and R. Gawinecki, *J. Org. Chem.*, 2002, **67**, 3339.
29. B. Ośmiałowski, E. Kolehmainen and R. Gawinecki, *Magn. Reson. Chem.*, 2001, **39**, 334.
30. J. Helaja, F.-P. Montforts, I. Kilpeläinen and P. H. Hynninen, *J. Org. Chem.*, 1999, **64**, 432.

31. M. J. Crossley, L. D. Field, M. M. Harding and S. Sternhell, *J. Am. Chem. Soc*., 1987, **109**, 2335.
32. M. J. Crossley, M. M. Harding and S. Sternhell, *J. Org. Chem*., 1992, **57**, 1883.
33. L. Muntean, I. Grosu, S. Mager, G. Ple and M. Balog, *Tetrahedron Lett*., 2000, **41**, 1967.
34. A. J. M. Carpy, P. P. Haasbroek, J. Ouhabi and D. W. Oliver, *J. Mol. Struct*., 2000, **520**, 191.
35. M. Pietrzak, L. Stefaniak, A. F. Pozharskii, V. A. Ozeryanskii, J. Nowicka-Scheibe, E. Grech and G. A. Webb, *J. Phys. Org. Chem*., 2000, **13**, 35.
36. Z. Rozwadowski and T. Dziembowska, *Magn. Reson. Chem*., 1999, **37**, 274.
37. S. H. Alarcón, A. C. Olivieri and M. Conzáles-Sierra, *J. Chem. Soc., Perkin Trans. 2*, 1994, 1067
38. J. Huuskonen, J. Schulz, E. Kolehmainen and K. Rissanen, *Chem. Ber*., 1994, **127**, 2267.
39. E. Kolehmainen, K. Laihia, M. Nissinen, K. Pihlaja, A. Perjéssy, D. Loos, W.-D. Rudorf and P. Meyer, *J. Chem. Res., Synop*., 1999, **3**, 186.
40. T. Schaefer, G. M. Bernard, Y. Bekkali and D. M. McKinnon, *Can. J. Chem*., 1996, **74**, 1626.
41. J. Lounila, Y. Hiltunen, K. Tuppurainen, A. Pulkkinen and R. Laatikainen, *Can. J. Chem*., 1999, **77**, 1788.
42. R. Laatikainen, *Magn. Reson. Chem*., 1986, **24**, 588.
43. R. Laatikainen and K. Tuppurainen, *Magn. Reson. Chem*., 1986, **24**, 595.
44. R. Laatikainen, E. Kolehmainen, T. Kuokkanen and K. Tuppurainen, *J. Magn. Reson*., 1988, **78**, 9.
45. T. Scahefer and R. Laatikainen, *Can. J. Chem*., 1983, **61**, 2785.
46. E. Kolehmainen, R. Laatikainen and V. Král, *Magn. Reson. Chem*., 1986, **24**, 498.
47. G. Bartoli, S. Grilli, L. Lunazzi, M. Massaccesi, A. Mazzanti and S. Rinaldi, *J. Org. Chem*., 2002, **67**, 2659.
48. C. Dell'Erba, F. Gasparrini, S. Grilli, L. Lunazzi, A. Mazzanti, M. Novi, M. Pierini, C. Tavani and C. Villani, *J. Org. Chem*., 2002, **67**, 1663.
49. R. Leardini, L. Lunazzi, A. Mazzanti and D. Nanni, *J. Org. Chem*., 2001, **66**, 7879.
50. M. B. Garcia, S. Grilli, L. Lunazzi, A. Mazzanti and L. R. Orelli, *J. Org. Chem*., 2001, **66**, 6679.
51. S. Grilli, L. Lunazzi and A. Mazzanti, *J. Org. Chem*., 2001, **66**, 5853.
52. S. Grilli, L. Lunazzi and A. Mazzanti, *J. Org. Chem*., 2001, **66**, 4444.
53. D. Casarini, S. Grilli, L. Lunazzi and A. Mazzanti, *J. Org. Chem*., 2001, **66**, 2757.
54. S. Grilli, L. Lunazzi, A. Mazzanti and G. Mazzanti, *J. Org. Chem*., 2001, **66**, 748.
55. S. Grilli, L. Lunazzi, A. Mazzanti, D. Casarini and C. Femoni, *J. Org. Chem*., 2001, **66**, 488.
56. D. Casarini, L. Lunazzi and A. Mazzanti, *Angew. Chem., Int. Ed*., 2001, **40**, 2536.
57. R. Leardini, L. Lunazzi, A. Mazzanti, H. McNab and D. Nanni, *Eur. J. Org. Chem*., 2000, **20**, 3439.
58. E. Kolehmainen, K. Laihia, R. Laatikainen, J. Vepsäläinen, M. Niemitz and R. Suontamo, *Magn. Reson. Chem*., 1997, **35**, 463.
59. S. Grilli, L. Lunazzi and A. Mazzanti, *J. Org. Chem*., 2000, **65**, 3563.
60. F. Gasparrini, L. Lunazzi, A. Mazzanti, M. Pierini, K. M. Pietrusiewicz and C. Villani, *J. Am. Chem. Soc*., 2000, **122**, 4776.
61. L. Lunazzi, A. Mazzanti and A. M. Alvarez, *J. Org. Chem*., 2000, **65**, 3200.
62. L. Lunazzi, A. Mazzanti, D. Casarini, O. De Lucchi and F. Fabris, *J. Org. Chem*., 2000, **65**, 883.
63. B. F. Bonini, M. Fochi, L. Lunazzi and A. Mazzanti, *J. Org. Chem*., 2000, **65**, 2596.
64. J. E. Anderson, D. Casarini, L. Lunazzi and A. Mazzanti, *Eur. J. Org. Chem*., 2000, 479
65. D. Casarini, E. Foresti, L. Lunazzi and A. Mazzanti, *Chem. Eur. J*., 1999, **5**, 3501.
66. W. Vetter and M. Oehme, *Handbook of Environmental Chemistry, New Types of Persistent Halogenated Compounds*. In: "Anthropogenic Compounds, Part K", Vol. 3, J. Paasivirta, ed., Springer, Berlin, Germany, 2000, 237.
67. V. A. Nikiforov, V. G. Tribulovich, V. S. Karavan and S. A. Miltsov, *Organohalogen Comp*., 1997, **33**, 53.
68. J. Koivisto, E. Kolehmainen, V. Nikiforov, M. Nissinen, K. Tuppurainen, M. Peräkylä, S.A. Miltsov and V.S. Karavan, *ARKIVOC*, 2001, 95.

69. J. Koivisto, *Ph.D. Thesis, Structural Analysis of Selected Polychlorinated Persistent Organic Pollutants (POPs) and Related Compound*, Research Report no. 86, Department of Chemistry, University of Jyväskylä, 2001.
70. J. Koivisto, E. Kolehmainen, V. A. Nikiforov, M. Nissinen, J. Linnanto, M. Lahtiperä, S. A. Miltsov and V. S. Karavan, *Chemosphere*, 2001, **44**, 671.
71. K. Pihlaja, G. Bernáth and F. Fülöp, *Adv. Heterocycl. Chem*., 1998, **69**, 349.
72. K. Pihlaja, H. Nummelin, K. D. Klika and J. Czombos, *Magn. Reson. Chem*., 2001, **39**, 657.
73. K. Pihlaja, K. D. Klika, J. Sinkkonen, V. V. Ovcharenko, O. Maloshitskaya, R. Sillanpää and J. Czombos, *J. Org. Chem*., 2002, **67**, 1910.
74. P. Tähtinen, J. Sinkkonen, K. D. Klika, V. Nieminen, G. Stájer, Z. Szakonyi, F. Fülöp and K. Pihlaja, *Chirality*, 2002, **14**, 187.
75. R. A. Shaikhutdinov, K. D. Klika, F. Fülöp and K. Pihlaja, *Magn. Reson. Chem*., 2001, **39**, 141.
76. K. D. Klika, P. Tähtinen, M. Dahlqvist, J. A. Szabó, G. Stájer, J. Sinkkonen and K. Pihlaja, *J. Chem. Soc., Perkin Trans. 2*, 2000, 687
77. P. Tähtinen, R. Sillanpää, G. Stájer, A. E. Szabó and K. Pihlaja, *J. Chem. Soc., Perkin Trans. 2*, 1999, 2011
78. J. Leis, K. D. Klika, K. Pihlaja and M. Karelson, *Tetrahedron*, 1999, **55**, 5227.

This Page Intentionally Left Blank

Principles and Unconventional Aspects of NMR Diffusometry

IOAN ARDELEAN[1] and RAINER KIMMICH[2]

[1]*Physics Department, Technical University, 3400 Cluj-Napoca, Romania*
[2]*Universität Ulm, Sektion Kernresonanzspektroskopie, 89069 Ulm, Germany*

ANNUAL REPORTS ON NMR SPECTROSCOPY
VOLUME 49 ISSN 0066-4103

Starting from basic differential equations for the description of ordinary and anomalous diffusion the theory of the standard field gradient pulse sequences for diffusion studies with the aid of NMR is developed. Anomalous diffusion can be due to an "obstruction effect" or to a "trapping effect" depending on the geometry and nature of the system matrix confining the diffusing particles. The NMR methods under consideration refer both to pulsed and steady field gradients, and both to laboratory and rotating-frame variants. The advantages and disadvantages are weighed up. More recent results refer to the attenuation of so-called multiple (or nonlinear) echoes by diffusion, and the use of internal field gradients for diffusion studies in fluid filled porous media. The diffusion of ordinary or laser-polarized gases is discussed for applications to porous media again. On a much longer time scale, isotope interdiffusion can be used as a technique for the elucidation of anomalous diffusion on percolation networks. A further and very distinct example of anomalous displacement characteristics was predicted for entangled polymers. Corresponding studies are reviewed and discussed with respect to the experimental limits. Finally, spin diffusion by flip-flop processes of dipolar coupled spins is shown to be a competitive mechanism if Brownian diffusion is strongly hindered by obstacles.

1. INTRODUCTION

Molecular self-diffusion, interdiffusion and hydrodynamic dispersion are the most crucial processes by which thermodynamics in nature and technology manifests itself. Diffusion is a representative of randomness par excellence. It is ubiquitous in our world. NMR provides a number of most powerful tools adapted to diffusion studies under the dissimilar conditions that may be relevant for molecular displacement phenomena. The objective of this review article is to provide an introduction to the theoretical background of these techniques and to illustrate them by a series of typical examples of their widespread applications.

On the other hand, it is totally impossible to cover the vast literature on NMR diffusometry applications in a review article like the present one. The scope of this survey is rather to focus on selected physical aspects that are considered to be essential for future perspectives in this field. It should also be mentioned that several excellent reviews on field-gradient NMR already exist that may supplement the present treatise.[1–5] General introductions to the NMR framework needed in this context can be found in monographs such as Refs. [6–9], for instance.

Studies of particle displacements by diffusion are a matter of the length and time scales to be probed. The character of the diffusion process often changes

with the length scale of the displacements. This depends on the measuring interval allowed for sampling displacements. For example, the geometrical restrictions of the trajectories a fluid molecule can migrate on are only relevant on a length scale exceeding that of the pore size.

NMR provides the most versatile arsenal of diffusometry methods specifically adapted to all length and time scales of interest in the physics and chemistry of matter. This range from molecular dimensions up to length scales limited by magnet bore diameters or even laboratory room conditions.

Displacements by diffusion can be probed by NMR parameters directly or indirectly. Isotope interdiffusion between initially separated compartments containing molecules labeled with different isotopes such as deuterons versus protons can be directly monitored by spin-density mapping of the concentration profiles of one of the nuclear species as a function of time. An example will be described in Section 8. In principle there is no limitation of the time and length scale since the displacement distribution to be probed is already established when the actual NMR experiment is carried out.

The most popular principle of diffusion measurements by NMR is the attenuation of spin echoes due to incomplete refocusing of coherences. Attenuation of echoes on these grounds arises in the presence of pulsed or steady magnetic field gradients relative to which molecules are displaced in the diffusion interval of the pulse sequence. Any sort of spin echo can be employed. Examples are Hahn or stimulated echoes in the laboratory frame based on gradients of the external magnetic flux density B_0 (Section 3), rotating-frame echo phenomena based on the gradients of the amplitude of the radio frequency flux density B_1 (Section 4.2), nutation echoes on a mixed B_1 and B_0 gradient basis (Section 4.3), and nonlinear (''multiple'') echoes arising in the presence of a modulated demagnetizing field (Section 5).

With most of these techniques, a non-equilibrium magnetization distribution is first prepared in the form of a ''helix'' or as magnetization ''grid'' or ''grating''. Translational diffusion then tends to level the magnetization distribution during the diffusion time. That is, the leveling process can also be probed directly by imaging the magnetization profile across the sample. A corresponding method is the *ma*gnetization *g*rid *ro*tating-*f*rame *i*maging (MAGROFI) technique (Section 4.4).

The time and length scale limits of spin echo techniques are determined by the switching times and the strength of field gradients and, as a terminal limit, by spin-lattice relaxation. Typical diffusion times for liquids that can be probed with spin-echo experiments range from 10^{-4} to 10^{0} s corresponding to typical root mean squared displacements between 100 nm and 100 μm. Longer displacement length scales up to the mm range can be examined with the aid of gas diffusion (Section 7).

Diffusion length and time scales below 100 nm and shorter than 0.1 ms, respectively, cannot be probed by field gradient techniques for technical reasons. If this regime is of interest, spin-lattice relaxometry especially in the

field-cycling variant[7] may be utilized for diffusion studies in a more indirect way. Spin-lattice relaxation due to intramolecular spin interactions is normally caused by rotational diffusion processes. However, in strongly anisotropic systems such as liquid crystals and melts of long polymer chains, isotropic rotational diffusion is no longer possible. Molecular orientations tend rather to be determined by the local environment in the system. Complete loss of the correlation to the initial orientation of a molecule is then only possible by translations to positions of uncorrelated local orientation. That is, reorientations are mediated by translational displacements.

As a typical example where this sort of translational diffusion mechanism matters, melts of linear polymers in a solid porous matrix will be discussed in Section 9.3. This is a situation where field-gradient and -cycling techniques supplement each other in a perfect way. The theoretical limits predicted for the so-called reptation model are available both for segment mean square displacements and spin-lattice relaxation on the very same basis. So, direct comparisons and combined conclusions can be drawn from two experimentally totally different techniques.

An important issue of the present review will be the distinction of "normal" and "anomalous" diffusion (Section 2). In principle, any restriction of translational displacements to finite spaces leads to some deviations from the ordinary diffusion behavior, that is, a Gaussian propagator and a linear time dependence of its second moment. Here we will distinguish effects by confinements of a certain geometrical shape and more random topological constraints.

There are numerous papers in literature dealing with the attenuation of echoes by diffusion of molecules confined to cavities of simple and well-defined geometries with and without wall relaxation. Corresponding echo attenuation features or time dependent diffusion coefficients may be observable under favorable conditions.[8,10–15] A complete analogy between the echo attenuation curves and the light intensity distribution faced with Fraunhofer diffraction at apertures of different shape was figured out by Callaghan.[8] A spectacular manifestation of such "diffraction-like" patterns of echo attenuation curves were published by Kuchel *et al*. for diffusion of liquids in red blood cells.[16,17]

The restricted diffusion effects mainly under consideration in the present review are focusing on situations where either random geometrical confinements and/or mutual obstruction of molecules play a role. That is, emphasis will be laid on mechanisms leading to scaling laws of a potentially fractal nature (Section 8.1).

2. DIFFUSION EQUATIONS AND PROPAGATORS

2.1. Definitions

Diffusion and hydrodynamic dispersion always has to do with more or less random displacements of molecules. The random character arises from the

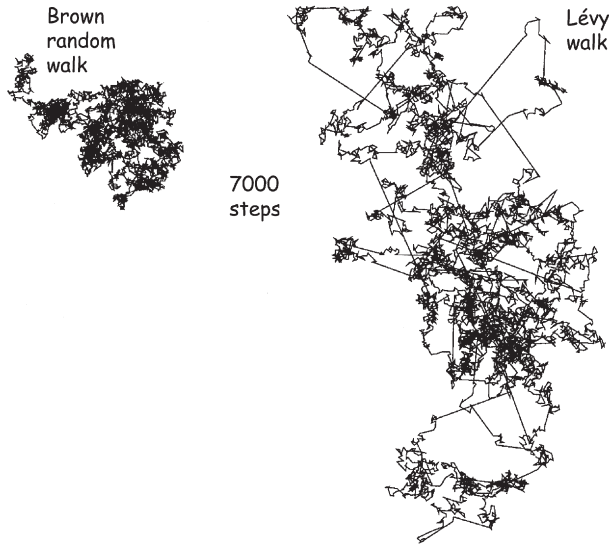

Fig. 1. Computer simulated trajectories of a random walker in two dimensions after ca. 7000 steps. *Left:* Brownian motion. *Right:* Lévy walk (adapted from Ref. 20).

multi-particle nature of thermal motion and/or from the random nature of the geometry of the confining medium. The latter, topological origin of randomness matters in particular in the case of hydrodynamic dispersion in connection with tortuous flow in a more or less random pore network.[18] However, the random topology may also influence Brownian motions without any superimposed coherent flow. An example is reptation of polymers in a randomly coiled tube[19,135] as will be outlined below.

Depending on the mutual interaction of molecules, the interaction with confining pore walls, and the topology of the pore space random-walk trajectories of a particle can be very different. Figure 1 shows examples for illustration obtained by Monte Carlo simulations of a Brownian random walk and a Lévy walk.[20] So the question arises, how to characterize the trajectories analytically.

An adequate way is to find the *propagator* $P(\vec{r}, t)$ which is a probability density by nature. Synonymous expressions are "probability distribution", "probability density function", or "van Hove self-correlation function". The probability that a particle is displaced into the volume element $\mathrm{d}^3 r$ in a distance $\vec{r}$ in a time interval t is given by $P(\vec{r}, t)\,\mathrm{d}^3 r$.

The stochastic processes usually under consideration are *stationary*, that is, the time t can represent any arbitrary interval of that length. Other conditions often assumed for stochastic mechanisms, namely *homogeneity* and *isotropy* of the medium in which the random walk takes place are more critical. In complex materials such as porous systems the propagator $P(\vec{r}, t)$ in principle refers to a

certain starting position relative to the pore space geometry. The trajectory is thought to start at a given position $\vec{r} = 0$ and ends in the volume element d^3r around a given position $\vec{r}$.

Since such detailed considerations are of little tractability one refers often to the *mean propagator* which is the average over all possible starting positions in a complex medium.[3,21,22] In the following we will tacitly adopt this approach when dealing with porous media. The mean propagator will be indicated by a scalar representation of the displacement as a position independent magnitude instead of the vector $\vec{r}$ in the argument. The mean propagator thus simply reads $P(r, t)$.

The full propagator given as an analytical function may contain more information than needed for the characterization and classification of random walk trajectories. It is then convenient to consider merely the *mean squared displacement* defined by

$$\langle r^2 \rangle = \int r^2 P(r, t)\, d^3r, \tag{1}$$

where the integral covers the whole space. Synonymous expressions for the mean squared displacement are "*variance*" or "*second moment*" of the propagator $P(r, t)$.

2.2. Diffusion equations

Under certain circumstances, the analytical forms of propagators can be obtained as solutions of diffusion differential equations for the initial condition $P(r, 0) \propto \delta(0)$. Fick's second law, the ordinary diffusion equation,

$$\frac{\partial P(r, t)}{\partial t} = D\nabla^2 P(r, t), \tag{2}$$

is valid for isotropic, homogeneous, and infinite media without any geometrical restrictions. The quantity D is the diffusion coefficient which is assumed to be constant in space (but not necessarily with respect to time). The solution of Eq. (2) for the above initial condition is the Gaussian propagator

$$P(r, t) = \frac{1}{(4\pi Dt)^{d/2}} \exp\left\{-\frac{r^2}{4Dt}\right\} \tag{3}$$

with the second moment given by the Einstein relation

$$\langle r^2 \rangle = 2dDt. \tag{4}$$

The Euclidean dimension is represented by d ($=1, 2, 3$). The mean squared displacement is a linear function of time provided that D is a constant in time. The linear time dependence in Eq. (4) represents "*normal diffusion*" as will be discussed below in more detail.

A generalization of Eq. (2) for propagators with second moments non-linearly depending on time is the fractional diffusion equation for one dimension[20]

$$\frac{\partial P(x, t)}{\partial t} = {}_0R_t^{1-\kappa} D_\kappa \frac{\partial^2}{\partial x^2} P(x, t). \tag{5}$$

The propagator solution reads

$$P(x, t) = \frac{1}{\sqrt{4\pi D_\kappa t^\kappa}} H_{1,2}^{2,0}\left[\frac{x^2}{4D_\kappa t^\kappa}\middle| \begin{matrix}\left(1-\frac{\kappa}{2}, \kappa\right) \\ (0, 1), \left(\frac{1}{2}, 1\right)\end{matrix}\right]. \tag{6}$$

${}_0R_t^{1-\kappa}$ is the Riemann/Liouville operator and D_κ is the generalized diffusion coefficient which is of dimension m^2/s^κ. $H_{1,2}^{2,0}$ represents the Fox function.[20] In the limit $|x| \gg \sqrt{D_\kappa t^\kappa}$ this propagator can be expressed by the stretched Gaussian

$$P(x, t) \propto \frac{1}{\sqrt{4\pi D_\kappa t^\kappa}} \sqrt{\frac{1}{2-\kappa}} \left(\frac{2}{\kappa}\right)^{[(1-\kappa)/(2-\kappa)]} \left(\frac{|x|}{\sqrt{D_\kappa t^\kappa}}\right)^{-[(1-\kappa)/(2-\kappa)]} \times \exp\left[-\frac{2-\kappa}{2}\left(\frac{\kappa}{2}\right)^{\kappa/(2-\kappa)} \left(\frac{|x|}{\sqrt{D_\kappa t^\kappa}}\right)^{1/[(1-\kappa)/2]}\right].$$

The mean squared displacement is given by

$$\langle x^2 \rangle \propto D_\kappa t^\kappa. \tag{8}$$

That is, anticipating a given value for the so-called diffusion exponent κ permits one to extend the propagator representation to "*anomalous diffusion*" as classified in the following section. Note however that the second moment does not converge for all propagators. Examples are Lévy flights (in contrast to Lévy walks).[23]

2.3. Classification of normal and anomalous diffusion

Displacements of molecules are called "*normal*" if the propagator has a Gaussian form *and* if the mean squared displacement is a linear function of time. The conditions are: (i) the particle trajectories correspond to purely random walks. There are no correlations or memory effects between elementary

steps with respect to probability (no waiting time distribution) and direction (the system is isotropic in the frame of its dimensionality). (ii) The particle displacements are unrestricted on the time scale of the experiment. There are no walls, geometrical confinements, obstacles or heterogeneities of the medium. The medium in which the molecules are diffusing is homogeneous and "infinite" in principle. Any possible particle trajectory in space is permitted. (iii) There is no mutual obstruction of the diffusing particles. (iv) There is no superimposed flow. A typical example of normal displacement behavior is self-diffusion of small molecules in homogeneous bulk liquids provided that the root mean square displacement in the measuring time is much shorter than the sample dimensions.

Most systems of interest in nature and technology are more complex. If any of the above conditions is violated, the consequence will be "*anomalous particle transport*" which can often be classified with the aid of the exponent of the time dependent mean squared displacement,

$$\langle r^2 \rangle \sim t^{\kappa}. \tag{9}$$

In particular one distinguishes the cases $\kappa = 0$, "*localized*"; $0 < \kappa < 1$, "*subdiffusive*"; $\kappa = 1$, "*normal*"; $\kappa > 1$, "*superdiffusive*"; $\kappa = 2$, "*ballistic*"; and $\kappa = 3$, "*turbulent*". Note that the term "diffusion" is used here in a more generalized sense including particle transport phenomena other than displacements by Brownian molecular motions. Rather, transport by flow, hydrodynamic dispersion, and thermal convection in more or less random porous media or even in bulk are to be discussed as well in this context.

2.3.1. *Obstruction effect*

Apart from the exponent based classification, two principally different categories of anomalous particle transport must be distinguished with respect to the origin of the anomalies. Let us first consider *Gaussian propagators* as they come out as solutions of Fick's diffusion equation for a homogeneous medium. Assuming a time dependent diffusion coefficient according to

$$\langle r^2(t) \rangle = 6D(t)t, \tag{10}$$

renders the mean square displacement anomalous in spite of the (spatially) Gaussian propagator and the "normal" diffusion equation the solution of which it still is. Replacing the diffusion coefficient in the Gaussian propagator given in Eq. (3) by a coefficient with a certain time dependence $D = D(t)$ and inserting this propagator in Eq. (2), readily demonstrates that this generalization is inherent to Fick's diffusion equation.

As examples of this sort of diffusive anomalies we will discuss Rouse modes of polymers confined in pores in Section 9. Another example is single-file diffusion of molecules in straight and tight cylindrical channels not permitting

molecules to pass each other. This scenario was found and described for zeolites[24,25] and molecular sieves.[26]

On a certain length scale zeolites and molecular sieves are homogeneous systems. The sole source of anomalies is then the mutual obstruction of molecules or polymer segments. The consequence is a subdiffusive behavior,[27]

$$\langle r^2 \rangle \propto \alpha l (Dt)^{1/2}, \tag{11}$$

where D is the diffusion constant of the basic particle motion, α is a factor characteristic for the molecular jump process, l is the "free volume" per particle along the axis of the cylindrical pore. This is a manifestation of the *obstruction effect*. With increasing pore diameter, a crossover to Fickian diffusion is expected as demonstrated with the aid of computer simulations.[27]

2.3.2. *Trapping effect*

On the other hand, displacements can become anomalous if geometrical restrictions matter in the dimensions in which displacements are considered. This scenario is often circumscribed by *waiting time distributions* due to "traps" where the particles are temporarily kept back or slowed down. The source of diffusion anomalies on this basis will be called *trapping effect*. The consequences are *non-Gaussian propagators* (and nonlinear time dependences of the mean squared displacement). This was verified in studies of hydrated protein aerogels and silica fineparticle agglomerates.[28–30] In Sections 8 and 9 we will discuss diffusion and hydrodynamic dispersion of particles on percolation clusters and the diffusion of polymer segments in randomly coiled tubes showing trapping anomalies as well.

3. LABORATORY FRAME DIFFUSOMETRY BASED ON HAHN AND STIMULATED SPIN ECHOES

The standard *pulsed gradient spin echo* (PGSE) and *steady gradient spin echo* (SGSE) methods are based on spatially constant field gradients $\vec{G} = \vec{\nabla} B_0 = \text{const}$, where B_0 is the magnitude of the main magnetic field. In the following, all main field gradients are assumed along the z direction so that the total magnetic flux density at a position z is given by $B(z) = B_0 + Gz$. The spin echoes to be considered in this section are understood as the result of ordinary coherence refocusing of the Hahn type. This is in contrast to methods using nonlinear ("multiple") echoes which will be discussed in Section 5.

3.1. Ordinary spin echoes and pulsed B_0 gradients

In this section we review a number of possible combinations of radio frequency (RF) and field gradient pulse schemes that are usually employed in ordinary NMR diffusion studies. In all cases, Hahn or stimulated spin echoes are produced and evaluated with respect to the echo amplitude.

We focus on the attenuation factor of the echo amplitude due to translational diffusion which is given by

$$A_{\mathrm{diff}}(T_{\mathrm{E}}) = \left\langle \mathrm{e}^{\mathrm{i}\varphi(T_{\mathrm{E}})} \right\rangle. \tag{12}$$

T_{E} is the echo time and φ is the (precession) phase a spin possesses at time $t = T_{\mathrm{E}}$. The brackets represent an ensemble average over all spins in the sample. In the following, this expression will be analyzed for different pulse sequences.

Any echo attenuation by relaxation occurs independently of diffusive attenuation and is of marginal interest in this context. It can readily be separated by either keeping all pulse intervals constant (and varying the gradient strength) or by compensating for relaxation losses in experimental protocols especially designed for this purpose.

3.1.1. *Hahn spin echo in the short gradient pulse limit* ($\delta \ll \Delta$)

We consider the coherence evolution of uncoupled spins $I = 1/2$ during the pulsed gradient Hahn spin echo sequence schematically shown in Fig. 2a. A suitable basis for the treatment is the spherical product operator formalism.

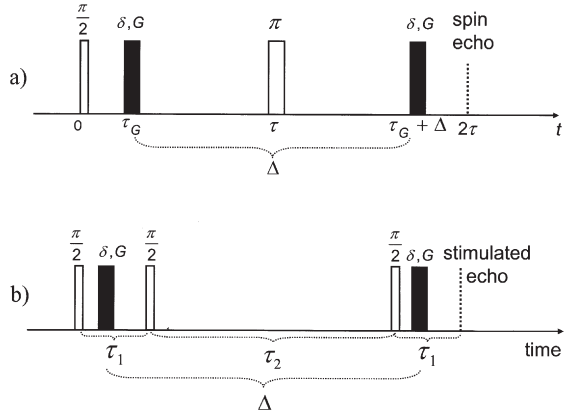

Fig. 2. Hahn spin echo (a) and stimulated spin echo (b) RF pulse sequences combined with magnetic field gradient pulses (black). Echoes other than the stimulated echo are not indicated in sequence (b). The stimulated echo variant of the PGSE method is of interest in viscous systems with small diffusion coefficients and, often as a related consequence, transverse relaxation times much shorter than the spin-lattice relaxation time. Note that in order to obtain distinct echoes at the indicated positions a finite background gradient is necessary.

All definitions and rules of this spin operator formalism needed in this context can be found in Ref. [7], for instance. Everywhere in the paper time moments just before and immediately after RF and field gradient pulses will be indicated by minus and plus signs, respectively.

The initial reduced density operator is given by the equilibrium density operator,

$$\sigma(0-) = \sigma_0 = I^{(0)}. \tag{13}$$

The sequence begins with a 90° pulse of width τ_{90} and a rotating-frame phase direction assumed along the x axis. The rotating-frame Hamiltonian during this RF pulse is defined by $\mathcal{H}_{90} = -\hbar\gamma B_1 I_x$, where B_1 is the amplitude of the rotating flux density component of the RF field. The reduced density operator immediately after this pulse reads

$$\sigma(0+) = \mathrm{e}^{-(\mathrm{i}/\hbar)\mathcal{H}_{90}\tau_{90}}\sigma(0-)\,\mathrm{e}^{+(\mathrm{i}/\hbar)\mathcal{H}_{90}\tau_{90}} = \frac{\mathrm{i}}{\sqrt{2}}\left(I^{(+1)} + I^{(-1)}\right) = \sigma(\tau_{\mathrm{G}}-). \tag{14}$$

During the field gradient pulses, the coherences evolve under the action of the rotating-frame Hamiltonian defined by $\mathcal{H}_{\mathrm{G}} = -\hbar\gamma G z_j I_z$, where z_j is the position coordinate of the spin bearing particle on the gradient axis during the jth gradient pulse. This produces

$$\sigma(\tau_{\mathrm{G}}+) = \mathrm{e}^{-(\mathrm{i}/\hbar)\mathcal{H}_{\mathrm{G}}\delta}\sigma(\tau_{\mathrm{G}}-)\,\mathrm{e}^{+(\mathrm{i}/\hbar)\mathcal{H}_{\mathrm{G}}\delta} = \frac{\mathrm{i}}{\sqrt{2}}\left(I^{(+1)}\mathrm{e}^{\mathrm{i}\varphi_1} + I^{(-1)}\mathrm{e}^{-\mathrm{i}\varphi_1}\right) = \sigma(\tau-), \tag{15}$$

where $\varphi_1 = \gamma G z_1 \delta$. The subsequent 180° RF pulse of length τ_{180} and a rotating-frame phase direction assumed along the y direction produces

$$\begin{aligned}\sigma(\tau+) &= \mathrm{e}^{-(\mathrm{i}/\hbar)\mathcal{H}_{180}\tau_{180}}\sigma(\tau-)\,\mathrm{e}^{+(\mathrm{i}/\hbar)\mathcal{H}_{180}\tau_{180}} \\ &= \frac{\mathrm{i}}{\sqrt{2}}\left(I^{(-1)}\mathrm{e}^{\mathrm{i}\varphi_1} + I^{(+1)}\mathrm{e}^{-\mathrm{i}\varphi_1}\right) = \sigma(\tau_{\mathrm{G}} + \Delta-)\end{aligned} \tag{16}$$

with $\mathcal{H}_{180} = -\hbar\gamma B_1 I_y$. The second gradient pulse causes further phase shifts according to

$$\begin{aligned}\sigma(\tau_{\mathrm{G}} + \Delta+) &= \mathrm{e}^{-(\mathrm{i}/\hbar)\mathcal{H}_{\mathrm{G}}\delta}\sigma(\tau_{\mathrm{G}} + \Delta-)\,\mathrm{e}^{+(\mathrm{i}/\hbar)\mathcal{H}_{\mathrm{G}}\delta} \\ &= \frac{\mathrm{i}}{\sqrt{2}}\left(I^{(-1)}\mathrm{e}^{\mathrm{i}(\varphi_1-\varphi_2)} + I^{(+1)}\mathrm{e}^{-\mathrm{i}(\varphi_1-\varphi_2)}\right) = \sigma(2\tau),\end{aligned} \tag{17}$$

where $\varphi_2 = \gamma G z_2 \delta$.

Coherence evolution in the presence of a field gradient winds the transverse magnetization up along the gradient direction in the form of a helix of pitch

$2\pi/(\gamma G\delta)$. The periodicity implied in this helix may be characterized by a "wave number"

$$k = \gamma G\delta. \tag{18}$$

The spin echo amplitude of a spin ensemble being at z_1 during the first gradient pulse and at z_2 during the second is thus represented by the reduced density operator

$$\sigma(2\tau) = \frac{\mathrm{i}}{\sqrt{2}}\left(I^{(-1)}\mathrm{e}^{\mathrm{i}k(z_1-z_2)} + I^{(+1)}\mathrm{e}^{-\mathrm{i}k(z_1-z_2)}\right). \tag{19}$$

The phase factors depend on the particle displacement $Z = z_1 - z_2$ which is distributed after the gradient pulse interval Δ according to the propagator $P(Z, \Delta)$. The average over all particles is given by

$$\left\langle \mathrm{e}^{\pm \mathrm{i}kZ}\right\rangle = \int_{-\infty}^{+\infty} P(Z, \Delta)\exp\{\pm \mathrm{i}kZ\}\,\mathrm{d}Z = \int_{-\infty}^{+\infty} P(Z, \Delta)\cos\{kZ\}\,\mathrm{d}Z, \tag{20}$$

where we have anticipated that $P(Z, \Delta)$ is an even function of Z and that k is constant within the sample.

(a) *Gaussian propagators*

The propagator for normal displacements, Z, along the gradient direction with the diffusion coefficient D is given by the Gaussian function

$$P(Z, \Delta) = \frac{1}{(4\pi D\Delta)^{1/2}}\exp\left\{-\frac{Z^2}{4D\Delta}\right\}. \tag{21}$$

Note that Eq. (21) is the one-dimensional version of Eq. (3): we are considering displacement components along only one space direction, namely that of the field gradient. Displacements along other space directions are not directly probed in this experiment and are therefore irrelevant.

Using the propagator given in Eq. (21) results in $\langle \mathrm{e}^{\pm \mathrm{i}kZ}\rangle = \exp\{-k^2 D\Delta\}$, so that Eq. (19) becomes

$$\sigma(2\tau) = I_y\,\mathrm{e}^{-k^2 D\Delta}. \tag{22}$$

That is, the echo attenuation factor, Eq. (12), takes the form

$$A_{\mathrm{diff}}(T_{\mathrm{E}}) = \left\langle \mathrm{e}^{\mathrm{i}\varphi(T_{\mathrm{E}})}\right\rangle \equiv A_{\mathrm{diff}}(k, \Delta) = \exp\{-k^2 D\Delta\}. \tag{23}$$

Note that this expression is also valid for time dependent diffusion coefficients, $D = D(\Delta)$, as far as the propagator is Gaussian (see the obstruction effect discussed above). Inserting $\langle Z^2\rangle = 2D\Delta$ in Eq. (23) provides a direct relation

between echo attenuation and the mean squared displacement in the diffusion time Δ:

$$A_{\mathrm{diff}}(T_{\mathrm{E}}) = \exp\{-\tfrac{1}{2}k^2\langle Z^2\rangle\} \overset{\text{isotropic}}{\underset{\text{system}}{=}} \exp\{-\tfrac{1}{6}k^2\langle r^2\rangle\}, \tag{24}$$

which refers to both normal and anomalous displacements provided the propagator is Gaussian.

(b) *Non-Gaussian propagators*

In some special cases it is possible to evaluate the echo attenuation factor Eq. (12) for non-Gaussian propagators. As an example the reptation mechanism of polymers in a tube will be considered below.

If such an analytical formalism is not available, the second moment of the propagator can be evaluated approximately from the experimental echo attenuation function by restricting oneself to the low wave number limit. The phase factor given in Eq. (20) can be expanded according to

$$A_{\mathrm{diff}} = \langle \mathrm{e}^{\pm \mathrm{i}kZ}\rangle = \left\langle 1 \pm \frac{\mathrm{i}kZ}{1!} - \frac{k^2Z^2}{2!} \mp \frac{\mathrm{i}k^3Z^3}{3!} + \cdots \right\rangle. \tag{25}$$

Keeping in mind that in the absence of flow the propagator is an even function of Z, one finds in the lowest non-trivial approximation for small wave numbers

$$A_{\mathrm{diff}} = \langle \mathrm{e}^{\pm \mathrm{i}kZ}\rangle \overbrace{\approx}^{k^2\langle Z^2\rangle \ll 1} 1 - \tfrac{1}{2}k^2\langle Z^2\rangle \overset{\text{isotropy}}{=} 1 - \tfrac{1}{6}k^2\langle r^2\rangle \approx \exp\{-\tfrac{1}{6}k^2\langle r^2\rangle\}, \tag{26}$$

where $\langle r^2\rangle$ is the three-dimensional mean squared displacement in the gradient pulse interval Δ. Plotting the echo amplitude as a function of k^2 and evaluating the initial slope of the decay curve thus provides the diffusion time dependence of the mean squared displacement, $\langle r^2\rangle = \langle r^2(\Delta)\rangle$.

3.1.2. *Hahn spin echo for long gradient pulses*

We are again referring to the pulse scheme shown in Fig. 2a. The gradient pulse width, δ, is now assumed to be comparable to the interval Δ. Displacements during the gradient pulses are therefore no longer negligible. That is, the phase shift accumulated by a spin depends on the trajectory of the spin bearing particle during the gradient pulse. For constant gradients along the z axis, this can be expressed by

$$\varphi_j(\delta) = \gamma G \int_0^{\delta} z_j(t')\,\mathrm{d}t', \tag{27}$$

where the subscript $j = 1, 2$ indicates the first or the second gradient pulse. The attenuation factor, Eq. (12), thus becomes

$$A_{\mathrm{diff}}(T_{\mathrm{E}}) = \langle \exp\{\mathrm{i}\varphi(T_{\mathrm{E}})\} \rangle = \left\langle \exp\left\{ \mathrm{i}\gamma G \left[\int_0^{\delta} z_1(t')\, \mathrm{d}t' - \int_0^{\delta} z_2(t')\, \mathrm{d}t' \right] \right\} \right\rangle \quad (28)$$

in analogy to the treatment in Section 3.1.1. The analytical form of this attenuation function is best obtained by solving the Bloch/Torrey equation,[31] that is Bloch's equations supplemented by a diffusion term according to

$$\frac{\mathrm{d}M_+(z, t)}{\mathrm{d}t} = -\mathrm{i}\gamma G z M_+(z, t) - \frac{M_+(z, t)}{T_2} + D\, \frac{\mathrm{d}^2}{\mathrm{d}z^2}\, M_+(z, t), \quad (29)$$

where $M_+ = M_x + \mathrm{i}M_y$ is the local complex transverse magnetization. The resulting attenuation factor by ordinary diffusion is[32]

$$A_{\mathrm{diff}}(k, \Delta) = \exp\{-k^2 D(\Delta - \delta/3)\}, \quad (30)$$

which takes the form of the short pulse limit given in Eq. (23) for $\delta \ll \Delta$. Equation (30) can also elegantly be obtained with the aid of computer algebra solutions of Eq. (29).[5]

3.1.3. *Stimulated echo*

The longest diffusion time (which is essentially given by Δ) that can be probed with the Hahn echo methods is limited by the transverse relaxation time T_2. As a consequence, the echo attenuation achievable in this time limit may not be sufficient for very slow diffusion even for the strongest field gradients technically feasible. Also, in the case of anomalous diffusion it may be desirable to probe a diffusion time range as wide as possible in order to acquire the time dependence of the mean square displacement on the basis of Eq. (24) or Eq. (26). Since the spin-lattice relaxation time T_1 tends to be much longer than T_2 in viscous or surface interacting systems, it is of interest to employ echo signals the relaxation decay of which is partly governed by T_1. The stimulated echo is a favorable example of this sort although a factor of two in the signal strength is sacrificed relative to the Hahn echo.[33]

Figure 2b shows a typical RF pulse sequence combined with field gradient pulses for probing diffusion with the aid of the stimulated echo. In the first RF pulse interval the transverse magnetization is attenuated by transverse relaxation, and the spin coherences evolve under the action of the magnetic field gradient. The second RF pulse "stores" half of the magnetization in z direction in spatially modulated form (often called "magnetization grid" or "grating" in complete analogy of the optical "forced Rayleigh scattering" technique[34]). The modulation degree of the grating is levelled off by diffusion and spin-lattice relaxation. The third RF pulse converts the z magnetization

back to spin coherences which then evolve into the stimulated echo. A detailed description of the spin coherence evolution can be found in Ref. [7], for instance.

The total attenuation of the stimulated echo in liquids after two free-evolution intervals τ_1 and the grating storage interval τ_2 is given by

$$A_{\text{stim.echo}} = A_{\text{relax}} A_{\text{diff}}, \tag{31}$$

where (anticipating monoexponential relaxation curves)

$$A_{\text{relax}} = \exp\{-2\tau_1/T_2\} \exp\{-\tau_2/T_1\}. \tag{32}$$

A_{diff} represents any of the formulas given in Eqs. (23), (24), (26) and (30) for the respective limits. If $\tau_1 \ll T_2 \ll T_1 > \tau_2$, the maximum diffusion time can be adjusted much longer than in the Hahn echo case. Note that, as an additional attenuation factor, the dipolar correlation effect[7] matters in systems anisotropic on the experimental time scale.

3.2. Spin echoes and steady B_0 gradients

The efficiency of spatial encoding by field gradients depends on the wave-number given in Eq. (18), that is the "area" $G\delta$ of the gradient pulses in the free-evolution intervals of the pulse sequences shown in Fig. 2. To generate short and intense gradient pulses with extremely short rise and decay times is technically difficult and, even worse, is susceptible to motional artefacts due to pulsed magnetic forces on the gradient coil system. For very short transverse relaxation times (which are usually accompanying slow translational diffusion) it may therefore be advisable to use steady gradients instead of pulsed ones: any gradient switching is then avoided and the gradient encoding efficiency in the coherence free-evolution intervals is optimal.

Figure 3a shows the steady-gradient RF pulse scheme for the Hahn echo. The pulsed-gradient parameters δ and Δ defined in Fig. 2a now take identical values and are equal to the RF pulse spacing,

$$\delta = \Delta = \tau. \tag{33}$$

Equation (30) thus becomes

$$A_{\text{diff}}(\tau) = \exp\left\{-\tfrac{2}{3} k^2 D\tau\right\} = \exp\left\{-\tfrac{2}{3} \gamma^2 G^2 D\tau^3\right\}, \tag{34}$$

where we have anticipated Gaussian propagators as above. If the propagator does not have a Gaussian form and if no special analytical formalism is available for the evaluation of experimental attenuation data, the low-wave-number limit given in Eq. (26) can again be employed as an approach.

Figure 3b shows the analogous variant for the stimulated echo. This is the preferential method for extremely short transverse relaxation times. In this case

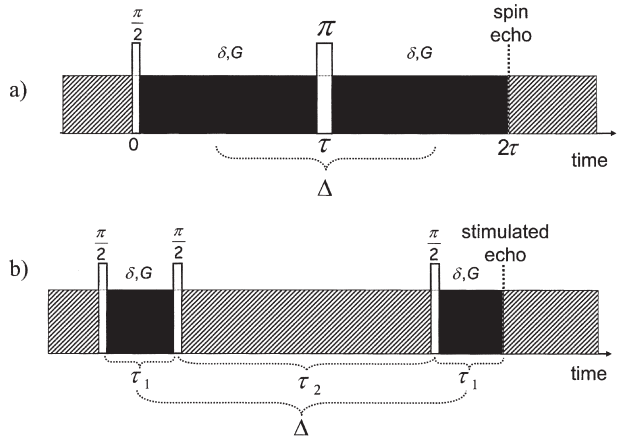

Fig. 3. Hahn spin echo (a) and stimulated spin echo (b) RF pulse sequences combined with a steady magnetic field gradient. The hatched areas are irrelevant for diffusion measurements. The echo attenuation by diffusive displacements is based on the black sections of the gradient cut out by the RF pulses and the echo time. As a stable and strong steady gradient, the fringe field gradient of superconducting magnets turned out to be particularly favorable.

the pulsed-gradient parameters turn into $\delta = \tau_1$ and $\Delta = \tau_1 + \tau_2$, so that Eq. (30) for Gaussian propagators becomes

$$A_{\text{diff}}(\tau_1, \tau_2) = \exp\left\{-\gamma^2 G^2 D \tau_1^3 \left(\frac{2}{3} + \frac{\tau_2}{\tau_1}\right)\right\}. \tag{35}$$

In the limit $\tau_1 \ll \tau_2$, this expression takes a form analogous to Eq. (26),

$$A_{\text{diff}}(\tau_1 \ll \tau_2) \approx \exp\{-k^2 D \tau_2\} = \exp\left\{-\tfrac{1}{6} k^2 \langle r^2(\tau_2)\rangle\right\}, \tag{36}$$

where $k = \gamma G \tau_1$.

Steady gradients of considerable strength (e.g., up to 60 T/m with a conventional 9.4 T wide-bore magnet) are readily available in the fringe field of superconducting magnets.[35] Applications to diffusion studies with molecular sieves and polymers have been reported in Refs. [26, 36, 37], respectively. Even stronger steady gradients can be produced with a special Maxwell coil design for superconducting magnets.[38]

Since the fringe field gradient has a fixed strength at the position of the probehead, the only experimental parameters of the pulse schemes shown in Fig. 3 that can be varied are the time intervals between the RF pulses. That is, the echo attenuation by relaxation must be considered and compensated for.

This can conveniently be done with the aid of self-compensating pulse schemes as described in Ref. [40].

Some care must be taken with fringe field methods if motional averaging of dipolar interactions is incomplete. Echoes then tend to be modulated by the so-called dipolar correlation effect.[41,42] One can account for this phenomenon by dividing the (normalized) echo amplitudes recorded with and without gradient at the same Larmor frequency and at the same pulse intervals.[36,37] Any influence by relaxation and dipolar correlation effect can be eliminated this way.

3.3. Coherent-flow compensation

Hydrodynamic dispersion is a transport phenomenon combining laminar flow and self-diffusion.[18] In this case the action of coherent and incoherent transport is superimposed. "Coherent" means here that the particle velocity vectors are stationary during the experimental time in contrast to "incoherent" processes where these vectors are randomized with respect to magnitude and/or direction.

The coherent and incoherent displacement contributions can easily be distinguished in experiments by eliminating all phase shifts due to velocities that are constant in the measuring interval by appropriate choice of the field gradient pulses:[7] echo attenuation by coherent transport components can be compensated for by using gradient sequels $G(t)$ (including all field gradients applied) with vanishing zeroth, first and, possibly, higher moments. For example, if all z gradient pulses occurring in the experimental time t are adjusted in such a way that,

$$\int_0^t G(t')(z + v_z t' + \cdots)\,\mathrm{d}t' = 0, \tag{37}$$

there will be no attenuation effect for particle trajectories starting at an initial position component z with a velocity component v_z stationary during t. What remains is attenuation by motions incoherent *on this particular time scale*.

Figure 4 shows a typical RF and field gradient pulse sequence for measurements of spin echo attenuation by incoherent displacements while the coherent part is compensated for. We assume the short gradient pulse limit again, i.e., $\delta \ll \Delta_a, \Delta_b, \Delta_c$, where $\Delta_a, \Delta_b, \Delta_c$ are the gradient pulse intervals defined in Fig. 4.

The reduced density operator after the first gradient pulse is given in Eq. (15). From this we deduce

$$\sigma(\tau_G+) = \sigma(\tau_G + \Delta_a-) = \frac{\mathrm{i}}{\sqrt{2}}\left[I^{(+1)}\mathrm{e}^{+\mathrm{i}\varphi_1} + I^{(-1)}\mathrm{e}^{-\mathrm{i}\varphi_1}\right], \tag{38}$$

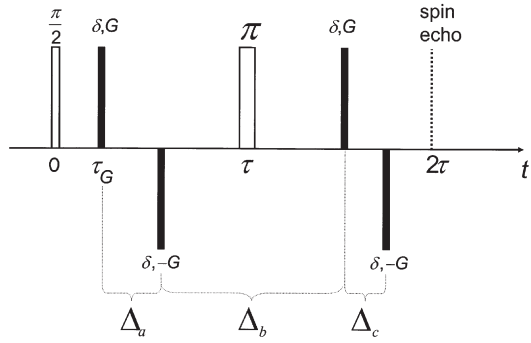

Fig. 4. Hahn spin echo RF pulse sequence combined with bipolar magnetic field gradient pulses (black) for diffusion or hydrodynamic-dispersion measurements while coherent-flow phase shifts are compensated on the time scale of the experiment.

where $\varphi_1 = \gamma G z_1 \delta$ and z_1 is the z position of the spin bearing particle during the first gradient pulse. After the second gradient pulse, this expression becomes

$$\sigma(\tau_G + \Delta_a +) = \sigma(\tau -) = \frac{i}{\sqrt{2}}\left[I^{(+1)} e^{+i\varphi_1} e^{-i\varphi_2} + I^{(-1)} e^{-i\varphi_1} e^{+i\varphi_2}\right], \tag{39}$$

where $\varphi_2 = \gamma G z_2 \delta$ and z_2 is the z position of the spin bearing particle during the second gradient pulse.

The π pulse converts this into

$$\sigma(\tau +) = \sigma(\tau_G + \Delta_a + \Delta_b -) = \frac{i}{\sqrt{2}}\left[I^{(-1)} e^{+i\varphi_1} e^{-i\varphi_2} + I^{(+1)} e^{-i\varphi_1} e^{+i\varphi_2}\right]. \tag{40}$$

The effect of the third gradient pulse is

$$\begin{aligned} \sigma(\tau_G + \Delta_a + \Delta_b +) &= \sigma(\tau_G + \Delta_a + \Delta_b + \Delta_c -) \\ &= \frac{i}{\sqrt{2}}\left[I^{(-1)} e^{+i\varphi_1} e^{-i\varphi_2} e^{-i\varphi_3} + I^{(+1)} e^{-i\varphi_1} e^{+i\varphi_2} e^{+i\varphi_3}\right], \end{aligned} \tag{41}$$

where $\varphi_3 = \gamma G z_3 \delta$ and z_3 is the z position of the spin bearing particle during the third gradient pulse. Finally, after the fourth gradient pulse we have

$$\sigma(\tau_G + \Delta_a + \Delta_b + \Delta_c +) = \sigma(2\tau) = \frac{i}{\sqrt{2}}\left[\begin{array}{l} I^{(-1)} e^{+i\varphi_1} e^{-i\varphi_2} e^{-i\varphi_3} e^{+i\varphi_4} \\ \quad + I^{(+1)} e^{-i\varphi_1} e^{+i\varphi_2} e^{+i\varphi_3} e^{-i\varphi_4} \end{array}\right], \tag{42}$$

where $\varphi_4 = \gamma G z_4 \delta$ and z_4 is the z position of the spin bearing particle during the fourth gradient pulse.

The total phase shifts at the echo time $2\tau = T_E$ in Eq. (42) are

$$\pm\varphi = \pm(\varphi_1 - \varphi_2 - \varphi_3 + \varphi_4) = \pm\gamma G\delta[(z_1 - z_2) - (z_3 - z_4)], \tag{43}$$

where $z_1 - z_2 \equiv Z_a$ and $z_3 - z_4 \equiv Z_c$ are the particle displacements in the gradient pulse intervals Δ_a and Δ_c, respectively, which are actually adjusted to be equal, $\Delta_a = \Delta_c$. The reduced density operator at the echo time thus reads

$$\sigma(T_E) = \frac{i}{\sqrt{2}}\left[I^{(-1)}e^{+ik(Z_a - Z_c)} + I^{(+1)}e^{-ik(Z_a - Z_c)}\right]. \tag{44}$$

The wave number k is the same as given in Eq. (18).

For completely coherent flow (that is, there is no random motion, and the z component of the velocity is constant, $v_z = \text{const}$) the displacements in the intervals $\Delta_a = \Delta_c$ are equal, $Z_a = Z_c$. As a consequence no phase shift remains at the echo time:

$$A_{flow} = 1. \tag{45}$$

On the other hand, if the motion is completely incoherent as expected in the pure self-diffusion limit, Z_a and Z_c will take uncorrelated values. Forming the ensemble average then gives the diffusive attenuation factor

$$A_{diff} = \left\langle e^{\pm ik(Z_a - Z_c)}\right\rangle = \left\langle e^{\pm ikZ_a}\right\rangle\left\langle e^{\mp ikZ_c}\right\rangle = \exp\{-2k^2 D\Delta_a\} = \exp\left\{-\tfrac{1}{3}k^2\langle r^2\rangle_{\Delta_a \text{ or } \Delta_c}\right\}, \tag{46}$$

where we have assumed a Gaussian propagator.

The intermediate case applies to hydrodynamic dispersion to be discussed in more detail in Section 8. Depending on the middle gradient pulse spacing, Δ_b, the correlation between the displacements Z_a and Z_c in the first and third gradient pulse intervals will be more or less strong:

$$A_{disp} = \left\langle e^{\pm ik(Z_a - Z_c)}\right\rangle \equiv \left\langle e^{\pm ikZ_{eff}}\right\rangle. \tag{47}$$

Here we have defined an effective displacement $Z_{eff} \equiv Z_a - Z_c$ for which a Gaussian distribution may be assumed again. In that case, Eq. (47) can be written as

$$A_{disp} = \begin{cases} \exp\{-k^2 D_{disp}\Delta_b\} & \text{for } \Delta_b \gg \Delta_a = \Delta_c \\ \exp\{-k^2 D_{disp}\Delta_a\} & \text{for } \Delta_b \ll \Delta_a = \Delta_c. \end{cases} \tag{48}$$

In both cases the dispersion coefficient D_{disp} defined in this way is a function of the displacement intervals Δ_b and Δ_a, that is $D_{disp} = D_{disp}(\Delta_b)$ and $D_{disp} = D_{disp}(\Delta_a)$, respectively. This time dependence reflects the loss of flow coherence with increasing displacement time.[42]

If the distribution of the effective displacement Z_{eff} is not a Gaussian function, an expansion of Eq. (47) can be performed analogous to Eq. (26). In the low wave-number limit, $k^2\langle Z_{\mathrm{eff}}^2\rangle \ll 1$, again a dispersion coefficient can be evaluated from experimental data according to

$$A_{\mathrm{disp}} = \left\langle \mathrm{e}^{\pm \mathrm{i}kZ_{\mathrm{eff}}} \right\rangle \overbrace{\approx}^{k^2\langle Z_{\mathrm{eff}}^2\rangle \ll 1} 1 - \tfrac{1}{2}k^2\left\langle Z_{\mathrm{eff}}^2\right\rangle = \begin{cases} 1 - k^2 D_{\mathrm{disp}}\Delta_{\mathrm{b}} & \text{for } \Delta_{\mathrm{b}} \gg \Delta_{\mathrm{a}} = \Delta_{\mathrm{c}} \\ 1 - k^2 D_{\mathrm{disp}}\Delta_{\mathrm{a}} & \text{for } \Delta_{\mathrm{b}} \ll \Delta_{\mathrm{a}} = \Delta_{\mathrm{c}}. \end{cases} \tag{49}$$

4. ROTATING-FRAME DIFFUSOMETRY BASED ON B_1 GRADIENTS

In the previous section we have outlined the principles of laboratory frame diffusometry techniques. In the following we will show that there is a number of rotating-frame techniques for probing diffusion analogous to the laboratory frame methods. That is, gradients of the RF amplitude B_1 are employed instead of or in addition to B_0 gradients.[43–48]

In the following we will describe three different diffusometry techniques based on B_1 gradients. The first method suggested in the literature is based on the "rotary stimulated echo".[43] This method requires both B_1 gradient pulses and homogeneous RF pulses, which makes the hardware set-up consisting of a combination of two different RF coils a bit demanding.

Diffusometry based on "nutation echoes" avoids this complication. Nutation echoes arise under coherence evolution in the presence of B_1 gradient pulses and steady or pulsed B_0 gradients in a combined way.[49–51] No homogeneous RF pulses are needed in this case.

Finally, diffusion measurements based on B_1 gradients can be combined with rotating-frame imaging. The B_1 gradient no longer needs then to be spatially constant (MAGROFI technique[44,52]). With the MAGROFI method again no RF pulses producing homogeneous B_1 fields are required.

One of the common features of all three variants is their insensitivity to inhomogeneities of the magnetic susceptibility in heterogeneous samples such as porous media. The appreciable internal B_0 gradients that can arise in high fields on these grounds do not affect B_1 gradient based diffusion measurements (see Section 6).

Furthermore, one of the major sources of experimental artifacts with pulsed gradient laboratory-frame techniques, namely magnetic susceptibility forces on the sample arising during the gradient pulses are safely avoided with B_1 gradient diffusometry.

4.1. Generation of B_1 gradients

The hardware requirements for the generation of B_1 gradient pulses are moderate. In particular, rise and fall times intrinsically are very short (typically in the order of only 1 μs). On the other hand, the gradient strengths reached with RF coils optimized for this purpose are limited to a few T/m compared with the 10–100 T/m range typical for laboratory frame techniques. It is also difficult to generate spatially constant B_1 gradients across the sample, although this problem can be solved by the combination with rotating-frame imaging.[44,52]

B_1 gradient pulses can be produced in different ways. A fairly constant gradient can be obtained by simply positioning the sample at a distance larger than $0.5R$ and smaller than $0.9R$ from the center of a single-turn coil of radius R.[43,44,53,54] For a single-turn coil and a transmitter output of ≈ 300 W gradient strengths lying between 200 mT/m at 100 MHz and 40 mT/m at 400 MHz[46] can be obtained. Larger gradients of up to 3 T/m were produced by Simon *et al.*[45] in the fringe field of a 5 mm solenoid coil at 200 MHz proton resonance.

Another possibility to produce large gradients is the use of toroid cavity detectors[55–57] but the gradient in this case is strongly non-uniform. The magnitude of the RF field strength is then proportional to $1/r$, with r the distance to the cylindrical-cavity axis. This is a situation where the spatially resolved measurements turn out to be particularly favorable (see the MAGROFI technique[44,52] discussed below).

An RF coil shape particularly suited for the generation of constant B_1 gradients is the conic geometry shown in Fig. 5b.[50] A B_1 gradient of about 300 mT/m at 400 MHz was realized this way. The filling factor of conic coils is much better than that of single-turn coils or solenoid coils in the fringe field.

4.2. Stimulated rotary echo

Figure 5a shows the basic pulse sequence for the generation of the stimulated rotary echo.[46] It consists of two B_1 gradient pulses of duration δ and strength G_1. The B_1 gradients are assumed to be aligned along the x axis of the laboratory frame. The rotating-frame phase direction of the RF pulses is arbitrarily chosen to be x_{rot}. The diffusion interval is denoted by Δ'. As we will see later, a 90° reading pulse is needed in order to convert the longitudinal magnetization into an observable signal. This pulse is normally "hard", that is, it excites the whole sample homogeneously. However, a composite pulse compensating for the spatial variation of the tip angle can be used as well.[58,59] In the latter case no extra RF coil producing homogeneous B_1 fields is required.

In order to understand the principle of the method let us consider uncoupled spins $I = 1/2$. The spin-bearing particle is assumed to be at the laboratory-frame position x at the first B_1 gradient pulse and at x' after the diffusion

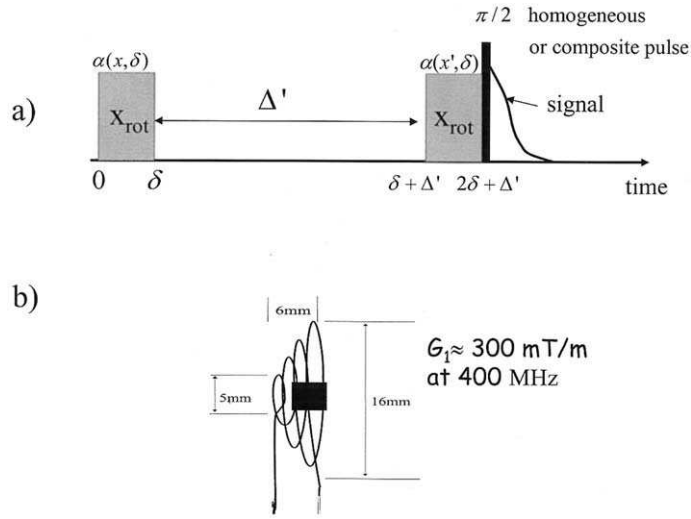

Fig. 5. (a) RF pulse sequence used in stimulated rotary echo experiments. The first two RF pulses of width δ have amplitudes subject to a gradient G_1. The phase direction of the RF pulses is assumed along the X_{rot} direction of the rotating frame. The B_1 gradient direction is assumed along the x axis of the laboratory frame, so that the local flip angle α is a function of the position x and the pulse width δ. The stimulated rotary echo reaches its maximum amplitude when the z component of the magnetization is refocused. It is read out with the aid of a 90° pulse with homogeneous B_1 distribution. (b) The conic coil geometry that permits the generation of reasonably constant B_1 gradients of about 300 mT/m. The version shown is designed for 400 MHz proton resonance.

interval $\Delta' \gg \delta$. The B_1 gradient pulses are assumed to be short enough to permit the neglect of any displacements and transverse relaxation losses during the RF pulses of duration δ.

The first B_1 gradient pulse splits the equilibrium magnetization into longitudinal and transverse components that are modulated along the B_1 gradient direction in the form of a helix wound around the gradient direction. The reduced density operator deprived from all constant terms and factors then takes the Cartesian spin operator form[50]

$$\sigma(x, \delta) = I_y \sin[\alpha(x, \delta)] + I_z \cos[\alpha(x, \delta)]. \tag{50}$$

For spatially constant B_1 gradient the tip angle is a linear function of the lab frame position and of the RF pulse length:

$$\alpha(x, \delta) = \gamma G_1 x \delta, \tag{51}$$

where γ is the magnetogyric ratio of the considered nucleus. If the transverse magnetization components are completely spoiled during the diffusion interval

Δ', the reduced density operator, just before the second B_1 gradient pulse, can be written as

$$\sigma(x, \delta + \Delta' -) = I_z\left[\left(1 - e^{-(\Delta'/T_1)}\right) + \cos\alpha(x, \delta)\, e^{-(\Delta'/T_1)}\right], \tag{52}$$

where T_1 is the longitudinal relaxation time.

Since the spin-bearing particle under consideration diffuses to a position x' during the diffusion interval Δ', the tip angle its spin is subjected by the second B_1 gradient pulse will consequently be a function of this new position. The density operator immediately after the second B_1 gradient pulse reads

$$\begin{aligned}\sigma(x, x', 2\delta + \Delta' +) = &\left[I_y \sin\alpha(x', \delta) + I_z \cos\alpha(x', \delta)\right] \\ &\times \left[\left(1 - e^{-(\Delta'/T_1)}\right) + \cos\alpha(x, \delta)\, e^{-(\Delta'/T_1)}\right].\end{aligned} \tag{53}$$

Note that the local tip angles produced by the two RF pulses are different due to the displacement of the spin in the pulse interval.

For unrestricted self-diffusion a Gaussian propagator applies as given in Eq. (21). Consequently, the tip angle difference between the two RF pulses will also be distributed according to a Gaussian function. Expressing the initial lab frame position, x, as a function of the final position, x', the reduced density operator can be rewritten as an average over all possible displacements:

$$\begin{aligned}\left\langle\sigma(x, x', 2\delta + \Delta')\right\rangle = &\left[I_y \sin\alpha(x', \delta) + I_z \cos\alpha(x', \delta)\right] \\ &\times \left[\left(1 - e^{-(\Delta'/T_1)}\right) + \cos\alpha(x', \delta)\, e^{-(\Delta'/T_1)}\left\langle e^{i\gamma G_1(x-x')\delta}\right\rangle\right].\end{aligned} \tag{54}$$

The attenuation factor $\langle e^{i\gamma G_1(x-x')\delta}\rangle$ is formed as an ensemble average over all spins in the sample. Using the propagator given in Eq. (21) the attenuation factor is found to be

$$\left\langle e^{i\gamma G_1(x-x')\delta}\right\rangle = e^{-D(\gamma G_1)^2\delta^2\Delta'} \tag{55}$$

in analogy to Eq. (23).

Applying now a 90° reading pulse along the x_{rot} direction (of homogeneous action) transfers the reduced density operator to

$$\begin{aligned}\left\langle\sigma(x, x', 2\delta + \Delta')\right\rangle &= \left\langle\sigma(x', 2\delta + \Delta')\right\rangle \\ &= \left[-I_z \sin\alpha(x', \delta) + I_y \cos\alpha(x', \delta)\right] \\ &\quad \times \left[\left(1 - e^{-(\Delta'/T_1)}\right) + \cos\alpha(x', \delta)\, e^{-(\Delta'/T_1)}\, e^{-D(\gamma G_1)^2\delta^2\Delta'}\right],\end{aligned} \tag{56}$$

where we have inserted Eq. (55). Note that this expression is no longer a function of the initial position x.

Only the transverse component of the magnetization can induce a signal voltage in the receiver coil. This signal is the average over all spin positions x' relevant at that time. It can be calculated as

$$\begin{aligned} S(\delta, \Delta') \propto M_y(\delta, \Delta') &= 2M_0 \overline{\mathrm{Tr}\{\langle \sigma(x', 2\delta + \Delta') \rangle I_y\}} \\ &= M_0 \left[\begin{array}{l} \left(1 - \mathrm{e}^{-(\Delta'/T_1)}\right) \overline{\cos \alpha(x', \delta)} \\ + \overline{\cos^2 \alpha(x', \delta)}\ \mathrm{e}^{-(\Delta'/T_1)}\ \mathrm{e}^{-D(\gamma G_1)^2 \delta^2 \Delta'} \end{array} \right], \end{aligned} \quad (57)$$

where the bar indicates the average over all x' lab frame positions in the sample.

Anticipating that the B_1 gradient pulses are long and strong enough to completely defocus the macroscopic magnetization of the sample,[43] permits us to set

$$\begin{aligned} &\overline{\cos \alpha(x', \delta)} = \overline{\sin \alpha(x', \delta)} = 0, \\ &\overline{\cos \alpha^2(x', \delta)} = \tfrac{1}{2}. \end{aligned} \quad (58)$$

The amplitude of the detected signal (the rotary echo) is then proportional to

$$A(\delta, \Delta') = \frac{M_0}{2}\ \mathrm{e}^{-(\Delta'/T_1)}\ \mathrm{e}^{-D(\gamma G_1)^2 \delta^2 \Delta'}. \quad (59)$$

The above formalism is valid for the short-pulse limit $\delta \ll \Delta'$. In the case of long B_1 gradient pulses the stimulated rotary echo amplitude was found to be[60]

$$A(\delta, \Delta') = \frac{M_0}{2}\ \mathrm{e}^{-(2\delta/T_2)}\ \mathrm{e}^{-(\Delta'/T_1)}\ \mathrm{e}^{-D(\gamma G_1)^2 \delta^2 (\Delta' + (2/3)\delta)}, \quad (60)$$

where T_2 represents the transverse relaxation time (assuming mono-exponential relaxation curves). The analogy to the lab frame result Eq. (30) becomes obvious when taking into account the somewhat different definition of the diffusion interval, i.e., $\Delta' = \Delta - \delta$.

According to Eq. (60), self-diffusion coefficients can be determined by varying either the B_1 gradient strength, G_1, or the duration δ of the RF pulse. For a given diffusion time, Δ', an exponential decay in the amplitude of the stimulated rotary echo is expected as a function of G_1^2 or δ^2.

Occasionally experimental artifacts in the form of oscillations or data scattering beyond the noise level may occur as reported by Humbert *et al.*[61] These distortions depend on the sample dimension, the gradient strength and the gradient pulse duration. The explanation is that the defocusing of the transverse magnetization assumed as a prerequisite of Eq. (58) is not very well fulfilled in this case. The magnetization vector helix then consists only of a few

turns, and the average cosine and sine functions in Eq. (58) do not vanish anymore:[61]

$$\begin{aligned}\overline{\cos\alpha(x',\delta)} &= \frac{1}{L}\int_{-L/2}^{L/2}\cos(\gamma G_1\delta(x''+x_0))\,\mathrm{d}x'' \quad \text{with } x''=x'-x_0\\ &= \cos(\gamma G_1 x_0\delta)\,\mathrm{sinc}\left(\frac{\gamma G_1 L\delta}{2}\right),\\ \overline{\cos^2\alpha(x',\delta)} &= \frac{1}{2}[1+\cos(2\gamma G_1 x_0\delta)\,\mathrm{sinc}(\gamma G_1 L\delta)].\end{aligned} \tag{61}$$

where $\mathrm{sinc}(x)=\sin(\pi x)/\pi x$. The sample length along the B_1 gradient direction is denoted by L and the middle of the sample is given by the lab frame coordinate x_0. The amplitude of the stimulated rotary echo consequently obeys

$$A(\delta,\Delta') = M_0\left\{\begin{array}{l}\left(1-\mathrm{e}^{-(\Delta'/T_1)}\right)\cos(\gamma G_1 x_0\delta)\,\mathrm{sinc}\left(\dfrac{\gamma G_1 L\delta}{2}\right)\\ +\frac{1}{2}[1+\cos(2\gamma G_1 x_0\delta)\,\mathrm{sinc}(\gamma G_1 L\delta)]\,\mathrm{e}^{-(\Delta'/T_1)}\,\mathrm{e}^{-D(\gamma G_1)^2\delta^2\Delta'}\end{array}\right\}. \tag{62}$$

The above expression suggests modulations of the echo attenuation versus G_1^2 or δ^2 due to the sinc functions in the parentheses. In the limit of very long samples or strong B_1 gradients, these oscillations vanish and Eq. (62) approaches Eq. (60).

The sinc function oscillations inherent to Eq. (62) can be eliminated experimentally by inserting appropriate homogeneous RF pulses in the basic pulse sequence together with the using of an appropriate phase cycling scheme.[61] This however requires an extra RF coil for the homogeneous pulses the set-up of which may be technically difficult.

4.3. Nutation echo

The nutation echo is the result of combined laboratory frame and rotating-frame coherence evolution.[49,50,62] That is, corresponding pulse sequences consist both of B_1 gradient pulses and B_0 gradients. The ordinary nutation echo pulse sequence consists of one B_1 gradient and one B_0 gradient pulse only.[49] A two-RF-pulse variant suitable for diffusometry is shown in Fig. 6.

The two B_1 gradient pulses have a duration δ and a gradient strength G_1. The pulses are separated by an interval Δ' in which the dominating part of the diffusive displacements takes place. In this version, the B_1 gradient pulses are applied in the presence of a steady gradient G_0 of the main magnetic field. One can apply G_0 also in pulsed form as it was suggested in context with an imaging experiment.[62]

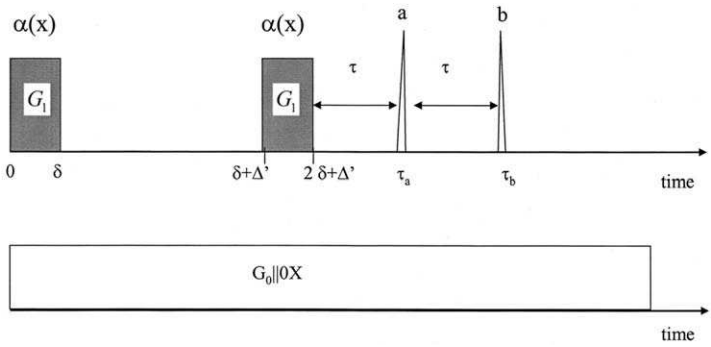

Fig. 6. Two-RF-pulse variant for the generation of nutation echoes. The B_1 gradient as well as the (steady) B_0 gradient are assumed to be aligned along the x axis of the laboratory frame. The first echo (a) originates from magnetization reestablished by spin-lattice relaxation. The second echo (b) is attenuated both by diffusion and relaxation.

The first B_1 gradient pulse in Fig. 6 splits the equilibrium magnetization into longitudinal and transverse components that are spatially modulated along the gradient direction. If the B_1 gradient is uniform in the sample, the magnetization vector forms a helix with a pitch $p = 2\pi/(\gamma G\delta)$. The transverse magnetization may be assumed to be completely spoiled during the interval Δ' due to the cumulative action of the B_0 gradient and by transverse relaxation.

At the end of the Δ' interval, the magnetization is therefore aligned in spatially modulated form along the z direction. The modulation tends to be balanced out by translational diffusion and spin-lattice relaxation. Note that the B_0 background gradient so far merely serves the defocusing of the transverse magnetization, but does not give rise to any attenuation by diffusion.

The second B_1 gradient pulse of the same "area" (width times strength) converts the longitudinal magnetization into spatially modulated transverse and spatially modulated longitudinal magnetization components. The longitudinal component does not matter for the further free evolution of the spin coherences as long as nonlinear echo phenomena (see Section 5) are not considered. The transverse magnetization evolves in the presence of the B_0 gradient and results in two distinct nutation echo signals.

For density operator treatment let us again assume uncoupled spins $I = 1/2$. The coherence evolution during the B_1 gradient pulse sequel is identical to that already described above in context with the stimulated rotary echo. After the second B_1 gradient pulse, the (initially dephased) coherences evolve in the presence of the spatially constant gradient $\vec{G}_0$ oriented along the same direction as $\vec{G}_1$. The effect of the main field gradient is to refocus the coherences resulting in two nutation echoes. The first nutation echo, appears at

$$\tau_a = 2\delta + \Delta' + \frac{G_1}{G_0}\,\delta \quad \text{(echo a)} \tag{63}$$

and can be traced back to the unmodulated term in Eq. (52). It has an amplitude given by[51]

$$A_a = \frac{M_0}{2}\left(1 - e^{-(\Delta'/T_1)}\right) e^{-\tau/T_2}, \tag{64}$$

where $\tau = (G_1/G_0)\delta$ is the time after the second B_1 gradient pulse at which the first echo reaches its maximum.

The second nutation echo originates from the modulated term in Eq. (52). Its maximum is reached at

$$\tau_b = 2\delta + \Delta' + 2\,\frac{G_1}{G_0}\,\delta \quad \text{(echo b)} \tag{65}$$

with an amplitude[51]

$$A_b = \frac{M_0}{4}\, e^{-(\Delta'/T_1)}\, e^{-(2\tau/T_2)}\, e^{-D(\gamma G_1)^2\delta^2\Delta'}. \tag{66}$$

The second echo amplitude is attenuated both by diffusion and relaxation whereas the first echo is subject only to relaxation losses. Thus, recording the amplitudes of the two echoes as a function of the interval Δ' permits one to measure the longitudinal relaxation time, T_1, and self diffusion coefficient D at a time. The technique was tested by Scharfenecker *et al.*[51] with water and cyclohexane in good agreement with results obtained with conventional B_0 gradient methods.

The attenuation term due to diffusion in Eq. (66) depends on G_1 but not on G_0. That is, neither G_0 nor any internal B_0 gradient arising from magnetic susceptibility inhomogeneities affects the amplitude of the second nutation echo. This unique feature of this sort of echo led to the suggestion to combine any sort of diffusometry measurement with localization[62] or high-resolution chemical shift spectroscopy in inhomogeneous fields as they occur in *ex situ* NMR for instance.[63]

4.4. MAGROFI

The third rotating-frame diffusometry technique to be discussed here is the MAGROFI technique.[44,45] This is again a method purely based on B_1 gradients. Neither B_0 gradients nor homogeneously acting RF pulses are needed. Rather it is a pure magnetization pattern generation/imaging procedure where, as a unique feature, transverse relaxation does not matter in principle since echoes are not evaluated in their basic version.[7]

Another unique feature of this method is that the B_1 gradients may vary within the sample. That is, quite general RF coil geometries can be used

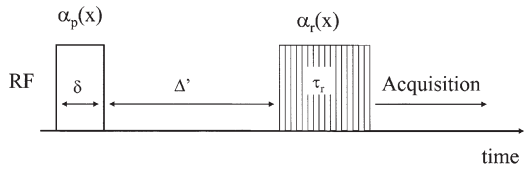

Fig. 7. RF-pulse sequence of the MAGROFI technique. The second (reading) pulse images the z-magnetization grid produced by the first one (preparation pulse). The image can be obtained by the "rotating frame zeugmatography" technique.[65] The flip angles of the pulses α_p and α_r depend on the x position. The reading pulse is incremented in length or equivalently in amplitude.

(surface coils, anti-Helmholtz coils, conic coils, solenoids, etc.). A device producing extremely inhomogeneous B_1 gradients is the toroid cavity which nevertheless turned out to be suitable for MAGROFI diffusometry.[52,64]

Figure 7 shows the pulse sequence which consists of two B_1 gradient pulses only. The first RF pulse prepares a z magnetization grating along the B_1 gradient direction. This magnetization grid is then more or less balanced off in the subsequent interval Δ' by diffusion and spin-lattice relaxation. The second B_1 gradient pulse serves then the acquisition of a rotating-frame image[7,65] of the more or less leveled z magnetization grid.

The first RF pulse (the "preparation pulse") with a gradient strength G_1 and a width δ is arbitrarily applied along the x_{rot} axis of the rotating frame. The B_1 gradient causes an inhomogeneous excitation of the sample, and the flip angle varies along the B_1 gradient direction. This preparation RF pulse thus produces a z-magnetization grid apart from transverse magnetization. The longitudinal magnetization component immediately after the first pulse is given by

$$M_z(x, \delta+) = M_0 \cos(k_p x), \tag{67}$$

where $k_p = \gamma G_1 \delta$ is the wavenumber of the preparation pulse.

The simultaneously excited transverse magnetization is of no further interest here. It decays by transverse relaxation or is spoiled by the B_0 field inhomogeneities of the magnet (which can be deliberately increased using the shimming coils if needed).

In the interval $\Delta' \gg \delta$ between the RF pulses, displacements by diffusion (or flow) tend to level (or shift) the longitudinal magnetization grid. Spin-lattice relaxation also tends to fade the grid away. The z magnetization at the end of this interval is given by

$$M_0 - M_z(x, \delta + \Delta'-) = \left[M_0 - \left\langle M_z(x, \delta+)\right\rangle_{\Delta'}\right] \mathrm{e}^{-\Delta'/T_1}, \tag{68}$$

where $\langle M_z(x, \delta+)\rangle_{\Delta'}$ is spatially modulated z magnetization at the end of the Δ' interval as averaged by translational diffusion. Here we have assumed homogeneous and monoexponential spin-lattice relaxation throughout the

sample. Assuming furthermore a Gaussian propagator for diffusion gives the average of Eq. (67):

$$\left\langle M_z(x, \delta+)\right\rangle_{\Delta'} = M_0 \cos(k_p x)\, e^{-Dk_p^2\Delta'}. \tag{69}$$

Inserting this expression in Eq. (68) leads to

$$M_z(x, \delta + \Delta'-) = M_0\left(1 - e^{-\Delta'/T_1}\right) + M_0 \cos(k_p x)\, e^{-Dk_p^2\Delta'}\, e^{-\Delta'/T_1}. \tag{70}$$

The first (unmodulated) term on the right-hand side of Eq. (70) arises from longitudinal relaxation during the pulse interval. It provides information about the longitudinal relaxation time T_1. The second (spatially modulated) term represents the magnetization grid more or less balanced out by spin-lattice relaxation and diffusion.

The distribution of the longitudinal magnetization, Eq. (70), is then rendered as a one-dimensional image with the aid of the rotating frame imaging technique[65] using the same RF gradient coil, that is, the same B_1 gradient. The second B_1 gradient pulse (the "read pulse") with the local flip angle $\alpha_r(x) = \gamma G_1 x \tau_r = k_r x$ is incremented in a series of transients. τ_r is the width of the reading pulse, and $k_r = \gamma G_1 \tau_r$ is the corresponding wavenumber.

We assume a rotating-frame phase along the $-y_{rot}$ axis for the read pulse. The free-induction signal at a time t_{aq} after this pulse is then represented by

$$\begin{aligned} &S(k_p, k_r, \Delta', t_{aq}) \\ &\quad \propto M_0\, e^{-i\omega_0 t_{aq} - t_{aq}/T_2} \\ &\qquad \times \int \left[\left(1 - e^{-\Delta'/T_1}\right) + \cos(k_p x)\, e^{-Dk_p^2\Delta'}\, e^{-\Delta'/T_1}\right] F(x_r) \sin(k_r x)\, dx, \end{aligned} \tag{71}$$

where $F(x_r)$ is a detection sensitivity factor that takes into account the detection sensitivity on the voxel to coil distance, and ω_0 is the Larmor angular frequency. The transverse relaxation time T_2 matters merely in the acquisition interval.

The magnetization-grid shape function is then reproduced by the Fourier transform from the k_r to the x_r space, i.e.,

$$\begin{aligned} \tilde{S}(k_p, x_r, \Delta', t_{aq}) = M_0 F(x_r)\, &e^{-i\omega_0 t_{aq} - t_{aq}/T_2} \\ &\times \left[\left(1 - e^{-\Delta'/T_1}\right) + \cos(k_p x_r)\, e^{-Dk_p^2\Delta'}\, e^{-\Delta'/T_1}\right]. \end{aligned} \tag{72}$$

The square bracket expression on the right-hand side consists of two terms. The first term solely refers to spin-lattice relaxation during the evolution interval. The second term represents the magnetization grid modified by diffusion and spin lattice relaxation. Both contributions can be unambiguously distinguished and determined in experimental evaluations.

The baseline of the magnetization grid is determined by the first term. This allows us to determine the spin-lattice relaxation time T_1 independently of any influence of diffusion. The diffusion coefficient D can be evaluated by plotting the amplitude of the grid function (second term) versus k_p^2 for a given diffusion time Δ'. Alternatively one can vary Δ' for a given k_p^2.

Note that the evaluations are carried out with a certain spatial resolution. As one images the whole grid, the information is available for all positions along the B_1 gradient direction. That is, one is referring to the local gradient. The B_1 gradient therefore needs not to be spatially constant.[52]

Since the signal amplitude (see Eq. (71)) can be acquired in an extremely short acquisition time t_{aq} without perceptible transverse relaxation losses, one can say that the MAGROFI technique is not affected by this sort of diffusometry limitation. On the other hand, relaxation losses during the B_1 gradient pulses can play a role if the pulse width is too long.

It should also be mentioned that the MAGROFI technique can be combined with a multipulse variant producing a pseudo-FID in a single scan.[54] In the absence of any frequency offset such pulse sequences are suitable for rapid data acquisition.[45]

5. LABORATORY FRAME DIFFUSOMETRY BASED ON NONLINEAR ("MULTIPLE") ECHOES

Long-range dipolar interactions manifest themselves collectively by a mean field traditionally called the ''demagnetizing field''. ''Long-range'' means a length scale beyond that on which intermolecular dipolar couplings are subject to motional averaging on the time scale of NMR experiments. This range is characterized by the root mean square molecular displacement by translational diffusion. In liquids of low viscosity this is typically in the order of a few micrometers. Because interactions over such long distances involve many particles by nature, the couplings can be considered globally in the continuum limit analogous to the magnetic flux density B_0 generated by the magnetic dipoles in the poles of a permanent magnet.

Multiple echoes arise after nonlinear evolution of coherences in the presence of spatially modulated demagnetizing fields or any other sinusoidal modulated magnetic field irrespective of how it is produced.[49] Echoes of this sort were first observed in solid ^{3}He by Deville *et al.*[66] Later it was shown that the same sort of echo phenomena can be also produced in ordinary liquids like water using two[67,68] or three[69–71] homogeneous radiofrequency pulses. Moreover, it has been shown that the demagnetizing field to some degree influences even ordinary spin echoes produced by two RF pulses with tip angles of typically 90°.[72] Stimulated echoes are affected likewise.[70]

The prerequisite for such demagnetizing-field effects and nonlinear echoes is a sufficiently long coherence evolution time and a high magnetization in the

sample to create a sufficiently strong demagnetizing field. The evolution of coherences in the presence of a spatially modulated demagnetizing field can be suitably carried out with the aid of the modified Bloch equations[66] or with the product spin operator formalism adapted to the problem,[7] where long-range dipolar couplings are correctly taken into account in the form of the demagnetizing field.

In general, the demagnetizing field has a non-local form depending on the shape of the sample. Under spherical or ellipsoidal symmetries of homogeneous samples the demagnetizing field disappears or is constant. However, if the symmetry of the spatial magnetization distribution is broken as a consequence of coherence evolution, in a field gradient for instance, a spatially modulated demagnetizing field arises. In this case and, if the transverse magnetization components are rapidly dephased by background field gradients, the demagnetizing field takes a local form.[66] In the case of a homonuclear spin system it is given by

$$\boldsymbol{B}_{\mathrm{d}}(\boldsymbol{r}) = \mu_0 \varepsilon \left[M_z(s)\boldsymbol{u}_z - \tfrac{1}{3}\boldsymbol{M}(s) \right], \tag{73}$$

where

$$\varepsilon = \frac{3(\boldsymbol{u}_s \cdot \boldsymbol{u}_z)^2 - 1}{2}. \tag{74}$$

Here μ_0 is the magnetic field constant (permeability of vacuum) and $\boldsymbol{M}(s)$ the magnetization at a position $s = \boldsymbol{r} \cdot \boldsymbol{u}_s$ along the gradient direction defined by the unit vector $\boldsymbol{u}_s$. The direction of the magnetic flux density relevant for the coherence evolution (i.e., $\boldsymbol{B}_0$ in laboratory-frame experiments) is given by the unit vector $\boldsymbol{u}_z$. If the modulation direction and the quantization direction coincide we have $\varepsilon = 1$, and the demagnetizing field flux density takes its strongest values (see Eq. (73)).

Nonlinear echoes arise after evolution in spatially modulated magnetic fields irrespective of the origin of the modulation. The standard way of producing a sinusoidal modulation is a sequence of two (or more) homogeneously acting RF pulses in the presence of a pulsed or steady B_0 gradient. Transferring components of dephased transverse magnetizations by an RF pulse into the z direction results in a spatially modulated z magnetization, and hence in a spatially modulated demagnetizing field according to Eq. (73). A spatially modulated demagnetizing field (and hence nonlinear echoes) can be likewise generated with the aid of a B_1 gradient pulse[49,50,73] or any other suitable spin coherence preparation technique.

Spin echoes of any sort arising after some coherence evolution period can generally be subject to attenuation by translational diffusion. In the following it will be shown that nonlinear echoes can suitably be used for NMR

diffusometry applications. Several variants for homo- and heteronuclear spin systems have been reported in the literature.[67,74–76]

5.1. Homonuclear nonlinear spin echoes

Figure 8 shows the standard pulse sequences used for the generation of nonlinear echoes. They consist of two 90° RF pulses and a steady or a pulsed B_0 gradient. Unlike the ordinary Hahn echo, nonlinear echoes appear after asymmetric free-evolution intervals with respect to evolution times and or gradient pulse "areas". An experimental echo train is shown in Fig. 8a.

5.1.1. *Steady gradients*

In the pulse scheme shown in Fig. 8a, a constant and steady magnetic field gradient, G, is assumed along the z direction determined by the external magnetic flux density $\vec{B}_0$. We consider an ensemble of spins $I = 1/2$ without indirect (or J) coupling or short-range dipolar coupling. If radiation damping[77] and corresponding feedback effects by the transverse magnetization are negligible (which is normally the case), the evolution of the rotating-frame

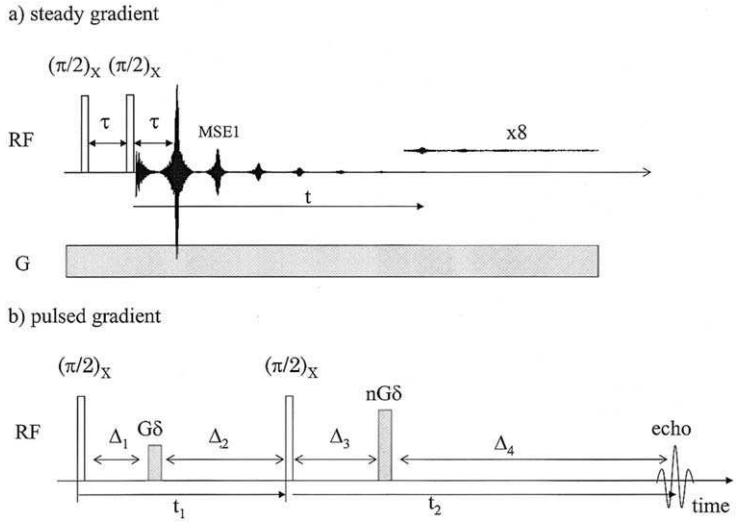

Fig. 8. Typical RF and B_0 gradient pulse sequences producing nonlinear ("multiple") echoes. (a) Steady gradient version. Echoes are generated at times $t = n\tau$ after the second RF pulse where n is a natural number. The first nonlinear echo (marked as MSE1) appears for $n = 2$. The ordinary Hahn echo (which is affected by nonlinear effects anyway[72]) shows up for $n = 1$. The echo signal trace showing nonlinear echoes up to the eighth order was experimentally recorded. (b) Pulsed gradient version. The nonlinear echo order n is selected by the ratio of the gradient pulse "areas".

magnetization in the intervals between (and after) RF pulses can be described by the modified Bloch/Torrey equation[66]

$$\frac{\mathrm{d}\boldsymbol{M}(z,\,t)}{\mathrm{d}t} = \gamma \boldsymbol{M}(z,\,t) \times [(B_0 + Gz)\hat{\boldsymbol{z}} + \boldsymbol{B}_\mathrm{d}(z)] - \left(\frac{M_z - M_0}{T_1}\right)\hat{\boldsymbol{z}} - \left(\frac{M_x\hat{\boldsymbol{x}} + M_y\hat{\boldsymbol{y}}}{T_2}\right)\hat{\boldsymbol{z}} + D\,\frac{\partial^2}{\partial z^2}\,\boldsymbol{M}(z), \tag{75}$$

where $\boldsymbol{M}(z)$ is the local magnetization and $\boldsymbol{B}_\mathrm{d}(z)$ the spatially modulated demagnetizing field.

In the present case the demagnetizing field is prepared after the second RF pulse in spatially modulated form so that only the longitudinal part of Eq. (73) is relevant for the coherence evolution.[67] That is,

$$\boldsymbol{B}_\mathrm{d}(z) = \mu_0 \boldsymbol{M}_z(z). \tag{76}$$

Equation (75) cannot be solved exactly. However, an approximate solution can be obtained in the limit of small demagnetizing fields, i.e., for

$$\mu_0 \gamma M_0 \tau \ll 1. \tag{77}$$

Neglecting relaxation losses and assuming ordinary diffusion, the amplitude of the first nonlinear echo that arises at the time $t = 2\tau$ after the second RF pulse was found to obey[67]

$$A_\mathrm{MSE1} = \frac{\sqrt{\pi}}{4}\,\gamma\mu_0 M_0^2 \tau \exp\left(-\tfrac{7}{3}\,D(\gamma G)^2\tau^3\right) \frac{\mathrm{erf}\left(\sqrt{D(\gamma G)^2\tau^3}\right)}{\sqrt{D(\gamma G)^2\tau^3}}, \tag{78}$$

where $\mathrm{erf}(x) = (2/\sqrt{\pi})\int_0^x \exp(-y^2)\,\mathrm{d}y$ represents the *error* function. The attenuation effect of the diffusion coefficient D is obviously stronger than in the Hahn echo case (compare Eq. (34)). Diffusometry applications on this basis may therefore be favorable.

5.1.2. *Pulsed gradients*

Figure 8b represents the *p*ulsed *g*radient *n*onlinear *s*pin *e*cho method (PGNSE) for diffusion measurements. It consists of two 90° RF pulses and two B_0 gradient pulses. The nonlinear-echo order, n, is selected by the "area" ratio of the second and first gradient pulse. If the first gradient pulse has an area δG, that of the second one is chosen to be $n\delta G$. In the following we will refer to the second order echo, $n = 2$.

During the pulse intervals Δ_1, Δ_2 (see Fig. 8b) no modulation of the demagnetizing field is expected so that the coherence evolution is conventional (see, for instance, Ref. [7]). The spatial modulation of the demagnetizing field is

generated by the second RF pulse and hence is relevant for the intervals Δ_3, Δ_4. This means that attenuation by diffusion in these intervals does no longer originate from a uniform field gradient. Unfortunately, no exact theory is known that accounts for diffusion effects in spatially varying gradients. That is, approximations are unavoidable to some degree in order to make the formalism tractable.[76]

If the condition

$$\gamma\mu_0 \frac{M_0}{2} \Delta_3 e^{-(\Delta_1+\Delta_2)/T_2} e^{-\Delta_3/T_1} e^{-D(\gamma G\delta)^2(\Delta_2+\Delta_3)} \ll 1 \tag{79}$$

is fulfilled, that is for small demagnetizing fields, the Bloch/Torrey equation (75) can be solved.[76] In this approximation, the amplitude of the first nonlinear echo ($n=2$) arising after the pulse sequence displayed in Fig. 8b reads

$$A_{n=2}(\Delta_1, \Delta_2, \Delta_3, \Delta_4) = \gamma\mu_0 \frac{M_0^2}{4} e^{-[(2(\Delta_1+\Delta_2)+\Delta_3+\Delta_4)/T_2]} e^{-(\Delta_3/T_1)} \times e^{-2D(\gamma G)^2\delta^2(\Delta_2+\Delta_3)} \left[\frac{1 - e^{-[2D(\gamma G)^2\delta^2 - 1/T_1]\Delta_3}}{2D(\gamma G)^2\delta^2 - 1/T_1} + \frac{1 - e^{-[2D(\gamma G)^2\delta^2 + 1/T_1]\Delta_4}}{2D(\gamma G)^2\delta^2 + 1/T_1} \right]. \tag{80}$$

This result is quite general and holds for any combination of the free evolution intervals $\Delta_1, \Delta_2, \Delta_3$ and Δ_4 and reproduces the expression obtained for $\Delta_3 = 0$ using a product operator formalism approach.[78]

Equation (80) interestingly suggests that the nonlinear echo is attenuated by diffusion even if the interval between the gradient pulses reduces to zero, that is $\Delta_2+\Delta_3 = 0$. This finding indicates that the echo attenuation is subject to processes other than conventionally anticipated. There are three mechanisms in addition to the incomplete-rephasing process normally considered in spin-echo diffusometry applications. Additional attenuation of nonlinear echoes arises from: (i) leveling of the magnetization helix before the z magnetization grid is formed, (ii) leveling of the z magnetization grid after it was formed, and (iii) displacements of the spin-bearing particles relative to the z magnetization grid. Note that the latter two mechanisms are related to each other because the displacement of spins both levels the magnetization grating (i.e., the spin-up and -down state modulation) and disturbs the coherence evolution by fluctuating demagnetizing fields "seen" by the transverse spin operators.

5.2. Heteronuclear nonlinear spin echoes

The same attenuation principles and mechanisms as mentioned above apply also to heteronuclear spin systems with spins $I = S = 1/2$ and gyromagnetic ratios γ_I and γ_S, respectively. The two nuclear spin species may populate the

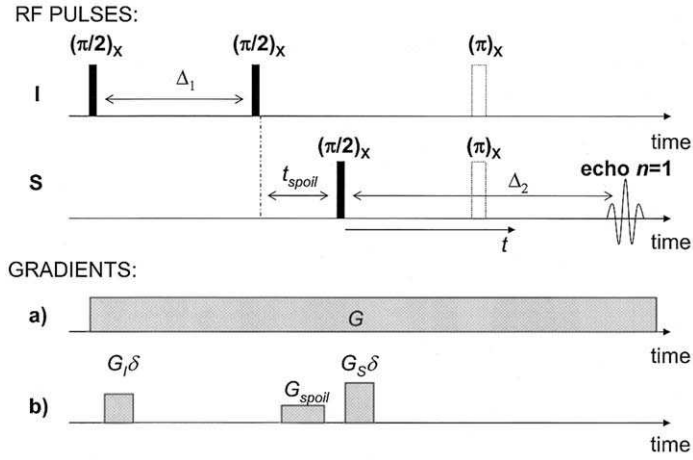

Fig. 9. RF pulse and B_0 gradient schemes for generating heteronuclear nonlinear spin echoes. The field gradient can be applied in a steady (a) or pulsed version (b). In the pulsed variant the gradient pulse width, δ, is chosen short enough to permit the neglect of diffusion during the pulses. Extra π pulses in the middle of the evolution interval Δ_2 ensure echoes in distinct form. Note that the echo order number $n = 1$ here refers to the first nonlinear echo and not to a Hahn type echo.

same (homomolecular case) or different (heteromolecular case) molecular species (with potentially different diffusivities). Corresponding pulse sequences are represented by Fig. 9 for steady (a) or pulsed gradients (b). As I spins one can typically take those of ^{1}H nuclei whereas ^{13}C is the standard example for an S spin bearing species.

5.2.1. *Steady gradients*

The equilibrium magnetizations, the longitudinal and transverse relaxation times and the diffusion coefficients of the two spin species are denoted by M_0^I, M_0^S, T_1^I, T_1^S, T_2^I, T_2^S, D^I and D^S, respectively. Indirect (or J) couplings and short-range (i.e., motional averaged) dipolar interactions will be neglected in the following. The only couplings under consideration are long-range dipolar interactions represented by the demagnetizing field.

The S spins are considered to be "rare", so that their contribution to the demagnetizing field can be neglected. The evolution of the single quantum coherences of the S spins in the spatially modulated demagnetizing field, B_d^I, produced by the "abundant" I spins leads then to heteronuclear nonlinear echoes.

Irrespective of whether the transverse magnetization of the I spins is spoiled by gradients or not, it will not contribute to the demagnetizing field because the corresponding precession frequency $(\gamma_S - \gamma_S)B_0$ in the frame rotating with the S spins is off-resonance. Consequently, no secular effect can arise.

The relevant I spin magnetization component therefore is the longitudinal one. For a gradient oriented along the z-direction, the z component of the demagnetizing field produced by the I spins reads[79]

$$B_{\mathrm{d}}^{I}(z) = \tfrac{2}{3}\,\mu_0 M_z^I(z). \tag{81}$$

Figure 9a shows the pulse sequence to be considered in the following. The modified Bloch/Torrey equation (75) adapted to the heteronuclear case can be treated analogous to the homonuclear version.[76] It turns out that nonlinear S spin echoes occur at times $t = n(\gamma_I/\gamma_S)\Delta_1$ ($n = 1, 2, \ldots$) after the S spin RF pulse. In the limit of small demagnetizing fields, the amplitude of the first nonlinear echo ($n = 1$) that matters for diffusion experiments is given by

$$\begin{aligned} A(\Delta_1, \Delta_2) = {} & \tfrac{1}{6}\,\gamma_S \mu_0 M_0^I M_0^S\, \mathrm{e}^{-(\Delta_1/T_2^I)} \mathrm{e}^{-(\Delta_2/T_2^S)} \mathrm{e}^{-(t_{\mathrm{spoil}}/T_1^I)} \mathrm{e}^{-D^I(\gamma_S G)^2 \Delta_2^2 (t_{\mathrm{spoil}} + \Delta_1/3)} \\ & \times \mathrm{e}^{-(1/3) D^S (\gamma_S G)^2 \Delta_2^3}\, \mathrm{e}^{[(D^I - D^S)(\gamma_S G)^2 \Delta_2^2 + 1/T_1^I]^2 / 4 D^S (\gamma_S G)^2 \Delta_2} \sqrt{\frac{\pi}{D^S (\gamma_S G)^2 \Delta_2}} \\ & \times \left[\begin{array}{l} \mathrm{erf}\left(\dfrac{1}{2}\, \dfrac{(D^I + D^S)(\gamma_S G)^2 \Delta_2^2 + 1/T_1^I}{\sqrt{D^S (\gamma_S G)^2 \Delta_2}} \right) \\ -\mathrm{erf}\left(\dfrac{1}{2}\, \dfrac{(D^I - D^S)(\gamma_S G)^2 \Delta_2^2 + 1/T_1^I}{\sqrt{D^S (\gamma_S G)^2 \Delta_2}} \right) \end{array} \right]. \end{aligned} \tag{82}$$

This expression reflects the complex attenuation mechanisms that determine heteronuclear diffusion experiments. The situation simplifies somewhat if one spin species (the I spins, for instance) is assumed to be spatially immobilized as one would expect it for protons of long polymer chains dissolved in a ^{13}C containing solvent, for example.

5.2.2. *Pulsed gradients*

The pulsed gradient version of the heteronuclear nonlinear echo sequence is represented in Fig. 9b. The steady gradient is now replaced by two gradient pulses of strength G_I and G_S, respectively. Similarly to the homonuclear case the duration δ of the gradient pulses is assumed to be short enough to neglect both relaxation and diffusion effects during the pulses. The evolution of the magnetization can be calculated again with the modified Bloch/Torrey equations. The condition to be fulfilled by the gradient pulses for the appearance of heteronuclear nonlinear echoes reads

$$\gamma_I G_I = n \gamma_S G_S \quad (n = 1, 2, \ldots). \tag{83}$$

In the small demagnetizing-field limit, the amplitude of the first nonlinear echo is found to be proportional to[76]

$$A(\Delta_1, \Delta_2) = \tfrac{1}{6}\,\gamma_S \mu_0 M_0^I M_0^S\, \mathrm{e}^{-(\Delta_1/T_2^I)}\, \mathrm{e}^{-(\Delta_2/T_2^S)}\, \mathrm{e}^{-(t_{\mathrm{spoil}}/T_1^I)}\, \mathrm{e}^{-D^I(\gamma_I G_I)^2\delta^2(t_{\mathrm{spoil}}+\Delta_1)} \times \frac{1-\mathrm{e}^{-[(D^I+D^S)(\gamma_I G_I)^2\delta^2+1/T_1^I]\Delta_2}}{(D^I+D^S)(\gamma_I G_I)^2\delta^2+1/T_1^I}. \tag{84}$$

The above expression suggests that the cumulative D_I+D_S can be measured if the decay of the nonlinear echo versus the diffusion interval Δ_2 is examined.

5.3. Nonlinear stimulated echoes

*No*nlinear *s*timulated *e*choes (NOSE) are generated by a sequence of three RF pulses in high magnetic fields in the presence of steady or pulsed field gradients.[69,70] Figure 10 shows typical pulse schemes. Note that the first two RF pulses have tip angles of preferably 90°, whereas the third RF pulse flips the magnetization only by preferably 45°. The value of the latter angle may not be 90° as in the conventional stimulated-echo sequence (see Figs. 2 and 3) because a finite z magnetization must remain during the free-evolution interval after the third RF pulse. As a consequence of the field gradients in the RF pulse interval, this z magnetization will be spatially modulated and consequently cause a correspondingly modulated demagnetizing field.

In the steady-gradient case (Fig. 10a), the ordinary stimulated echo (STE) appears at a time τ_1 after the third RF pulse, whereas the NOSE are refocused at times $2\tau_1, 3\tau_1, \ldots$, with varying amplitude. With pulsed gradients (Fig. 10b), the echo order n is selected by the ratio of the two gradient areas. Note that coherence echoes other than those originating from z magnetization intermittently stored in the τ_2 interval are not considered here. Compare Ref. [7] for a complete discussion of different echo types.

Using the modified Bloch/Torrey equations, the coherence evolution leading to the NOSE phenomena can be described under equivalent conditions as assumed above. If intramolecular spin–spin coupling (or J coupling) is to be accounted for, the standard product operator formalism can be employed as described in Refs. [70,71].

The spatial distribution of the demagnetizing field is given by Eq. (76) for gradients applied along the z direction. The first NOSE, that appears at a time $t=2\tau_1$ after the third RF pulse. For steady gradients its amplitude obeys[75]

$$A(\tau_1, \tau_2) = \tfrac{1}{4}\,\gamma \mu_0 M_0^2 \tau_1\, \mathrm{e}^{-(4\tau_1/T_2)}\, \mathrm{e}^{-(\tau_2/T_1)}\, \mathrm{e}^{-2D(\gamma G)^2\tau_1^2\tau_2}. \tag{85}$$

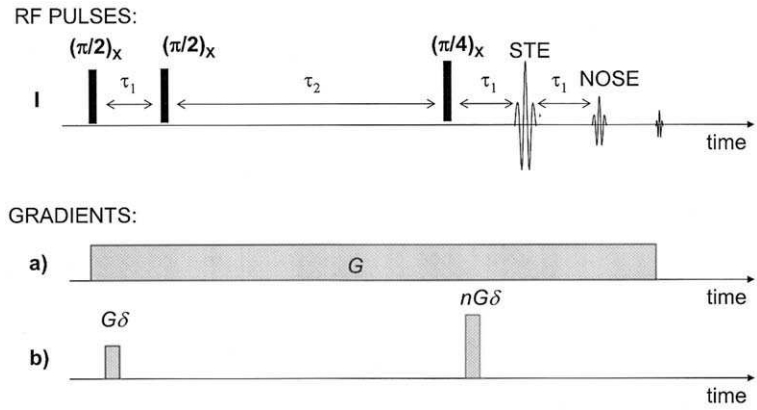

Fig. 10. RF pulse and B_0 gradient schemes producing NOSE. (a) Steady gradient version. The ordinary stimulated echo (STE) and a series of NOSE appear after intervals τ_1 and $n\tau_1$ after the third RF pulse, respectively, where n is a natural number beginning with 2. (b) Pulsed gradient version. The ratio of the gradient "areas" determines the echo order selected. The first NOSE is selected for $n = 2$.

The pulsed-gradient variant shown in Fig. 10b leads to

$$A(\tau_1, \tau_2) = \tfrac{1}{4}\,\gamma\mu_0 M_0^2 \tau_1\, \mathrm{e}^{-(4\tau_1/T_2)}\, \mathrm{e}^{-(\tau_2/T_1)}\, \mathrm{e}^{-2D(\gamma G)^2\delta^2\tau_2}, \tag{86}$$

where the second gradient pulse is assumed to have twice the strength (for equal pulse width) or twice the width (for equal gradient strength) in order to select the first NOSE. The above expressions indicate that the NOSE is more efficiently attenuated by diffusion than the ordinary stimulated echo (see Eq. (36), for instance). It can be favorably used for diffusion measurements provided that the transverse relaxation time is long enough to allow for the extended echo time.

6. MAGNETIC SUSCEPTIBILITY INDUCED FIELD GRADIENTS

In the pulse sequences considered so far we have assumed that the gradients responsible for spin echo attenuation by diffusion are of an external origin. In the following, we will also consider the effect of gradients produced by the sample itself. Such internal field gradients arise in an external magnetic field if the magnetic susceptibility is heterogeneously distributed. This situation occurs with fluid filled porous media, for instance. Porous materials like rocks, cement gels, ceramics, etc., are ubiquitous in nature and technology. The solid matrix and the fluid tend to have different magnetic susceptibilities, so that the fluid in

the pore space is subject to inhomogeneities even if the external field is perfectly homogeneous.

The strength of the local internal gradients depends on the magnetic susceptibility difference, $\Delta\chi$, between the two phases, on the applied external magnetic flux density, B_0, and on the pore space geometry.[80] In the case of spherical pores of radius r, the gradient at the pore surface is[81]

$$G_{iz} \approx \frac{\pi}{r} \Delta\chi B_0. \tag{87}$$

In more complex structures such as a periodic array of cubic pores the local magnetic field gradient must be estimated numerically.[82,83] The general conclusions drawn from such calculations are: (i) the average local magnetic field gradient increases with decreasing pore size, (ii) it is strongest at the solid/liquid interfaces, (iii) it increases with the curvature of the surface.[84] Due to the heterogeneity of the sample the internal gradients tend to be widely distributed with respect to magnitude and orientation.[85,86] However, unlike externally applied gradients, internal gradients are bounded in magnitude, and the field variation occurs on the length scale of the pore size.

Hürlimann[86] suggested that the internal gradients relevant for NMR measurements are to be taken as effective ones. The effective gradient is related to the local field inhomogeneities averaged over the dephasing length. The dephasing length, that is the typical length over which the spins diffuse until they are dephased relative to each other, depends on the diffusion properties.

Leventis *et al.*[165] have proposed a method for the evaluation of the mean square of the internal gradients. The effect of random internal gradients on NMR signals generated by stimulated echo and saturation recovery pulse sequences have been considered. Extreme root mean square internal gradients as large as 90 T/m have been estimated in this way in cement samples at 200 MHz proton resonance frequency.

Diffusion measurements in fluids in porous media are best done with external field gradients exceeding internal gradients by far. The 60 T/m fringe field gradient used by Fischer *et al.*[36] for the study of polymer diffusion in pores of a solid polymer matrix is certainly large enough in order to avoid experimental artifacts by internal gradients in this particular sample.

A good indication of a potential influence of internal gradients is the occurrence of unusually short effective transverse relaxation times T_2^*. If the internal gradients become comparable to the externally applied gradient, strong misinterpretations of experimental data are not excluded.[87] It is therefore of interest to employ diffusometry pulse sequences compensating internal-gradient effects.

6.1. Compensation of internal-gradient effects

The safest ways to avoid influences of internal field gradients is to use either rotating-frame diffusometry techniques (see Section 4) or to employ low-field magnets and external field gradients ensuring an encoding effect much stronger than expected by internal gradients. If this is technically not possible, pulse sequences specifically designed to compensate for internal field gradient offsets may be useful.

Figure 11a shows the usual pulsed field gradient stimulated echo sequence in a slightly modified form of the one already rendered in Fig. 2b. Assume now a superposition of an external gradient G and, for simplicity, a spatially constant internal gradient G_0. The attenuation of the stimulated-echo amplitude follows then[87]

$$\ln\left(\frac{A}{A_0}\right) = -\gamma^2 D\Big[\delta^2(\Delta + \tau - \delta/3)G^2 + \delta(2\tau\Delta + 2\tau^2 - 2\delta^2/3 - \delta(\delta_1 + \delta_2) - (\delta_1^2 + \delta_2^2))GG_0 + \tau^2(\Delta + 2\tau/3)G_0^2\Big], \tag{88}$$

where the time intervals are defined in Fig. 11a.

Equation (88) contains a gradient cross term, GG_0, that prevents any simple separation of the contributions of the two gradients to the attenuation of the echo while varying the area of the external gradient as usual. Without that cross term, the effect of the internal gradient could be simply taken apart by

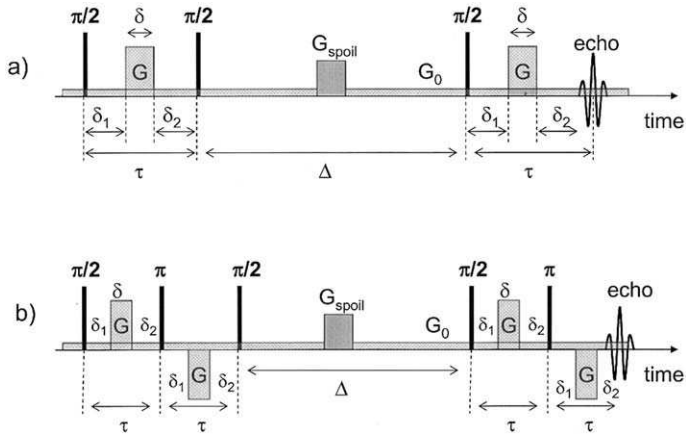

Fig. 11. Ordinary pulsed field gradient stimulated echo sequence (a) in comparison to a variant designed for the compensation of internal gradients (b). In contrast to the methods considered above, a background gradient G_0 is assumed to produce undesired diffusion attenuation effects. The spoiling gradient G_{spoil} is to make sure that all coherences in the Δ interval are dephased.

normalization the attenuation function for a vanishing area of the external gradient.

A remedy for the elimination of the gradient cross term is the application of bipolar external gradient pulses as shown in Fig. 11b.[88–90] Assuming again that the internal gradients are constant during the diffusion time leads to the modified attenuation function[87]

$$\ln\left(\frac{A}{A_0}\right) = -\gamma^2 D\left[\delta^2(4\Delta + 6\tau - 2\delta/3)G^2 + 2\delta\tau(\delta_1 - \delta_2)GG_0 + \frac{4\tau^3}{3}\,G_0^2\right]. \quad (89)$$

Choosing $\delta_1 = \delta_2$ eliminates the cross term, so that diffusion coefficients can be accurately measured by varying the external gradient pulse strength, $\mathcal{G}$, under such conditions.

The assumption that the spins are subject to a spatially constant internal gradient during the diffusion time is a critical one, of course. It conflicts with the fact that translational displacements by diffusion takes the molecules to different positions within the heterogeneous structure connected with different local field gradients. That is, this compensation attempt will only work in the short-time limit and in large pores, where more sophisticated 17-interval bipolar pulse sequences may help a bit.[88] The introduction of additional RF pulses may lead to additional echo phenomena interfering with the stimulated echo. In order to remove these unwanted echoes, phase cycles,[91] orthogonal spoiler gradients[92] or bipolar gradients of different strength[90] have been suggested.

6.2. Determination of the pore size using internal gradients

Internal gradients seen in a more positive light permit one to deduce information on the pore space structure as suggested by Song *et al.*[93–95] and Lisitza and Song.[96,97] This method does it without any external gradient. Merely the effect of the internal gradients is examined. In order to discriminate the signal attenuation by diffusion in the internal gradients from relaxation losses, the outcome of two RF pulse sequences shown in Fig. 12a and b is compared.

Figure 12a represents the standard stimulated-echo sequel. The amplitude $E(t_d)$ of the stimulated echo produced by this sequence is attenuated by transverse relaxation in a total interval $2t_e$, by spin-lattice relaxation in the interval t_d, and by translational diffusion in the internal gradients during the echo time $T_E = 2t_e + t_d$. In the limit $t_e \ll t_d$ the effective diffusion time may be identified with t_d as an approximation.

Relaxation losses can separately be determined with the aid of the modified pulse sequence shown in Fig. 12b. We note that the total interval relevant for transverse relaxation is again $2t_e$. Also the period t_d during which spin-lattice

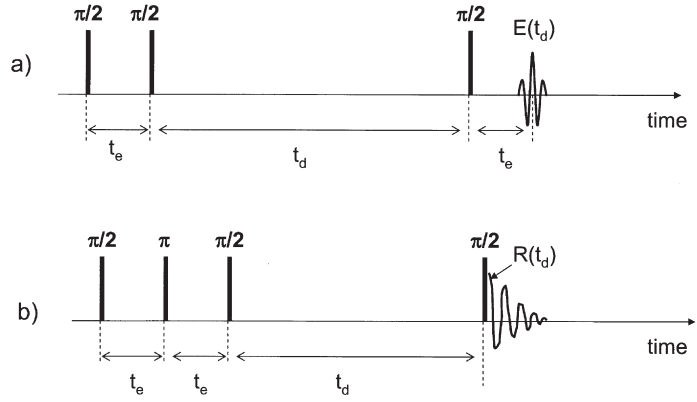

Fig. 12. Internal gradient method for the determination of the pore size in porous media.[94,96] This is a two-step experiment: first the amplitude of the ordinary stimulated echo, $E(t_d)$, is measured as a function of the diffusion interval t_d for a given encoding time t_e (RF pulse sequence a). Then a reference FID signal is recorded with pulse sequence (b) in order to eliminate attenuation by relaxation losses.

relaxation is active has the same length as in sequence version (a). That is, the attenuation of the acquired signals by relaxation is identical in both cases.

This is in contrast to attenuation by translational diffusion. In version (a) we have phase encoding of the position and subsequent storage in z direction in the form of magnetization "gratings" corresponding to the wave-numbers of the local gradients. Since the internal gradients are not uniform, the term "grating" is to be understood more in the sense of a spatial variation of the z magnetization corresponding to the spatial distribution of the local gradients. In version (b) the intermittent π pulse prevents any phase encoding in the first free-evolution interval and, hence, any spatial variation of the z magnetization in the t_d interval on these grounds.

Translational diffusion tends to level the spatial variation of the z magnetization in version (a), and the stimulated echo will be attenuated correspondingly (compare Eq. (36) derived for uniform gradients). Version (b), on the other hand, is insensitive to this sort of attenuation whereas the relaxation losses are the same. Dividing the stimulated-echo amplitude, $E(t_d)$, recorded with pulse sequence (a) by the amplitude of the free-induction signal, $R(t_d)$, acquired with version (b) under otherwise equivalent conditions thus eliminates the influence of relaxation. The only prerequisite of this technique is that the internal gradients "seen" by the spins remain temporally constant during the free-evolution intervals t_e.

The decay of the ratio $E(t_d)/R(t_d)$ as a function of the diffusion time t_d thus reflects diffusion effects in internal gradients. At large t_d, above a critical time t_{cr}, the ratio $E(t_d)/R(t_d)$ approaches a constant value as demonstrated in Fig. 13. The critical time t_{cr} is defined by Song *et al.*[94] as the time it takes a molecule to

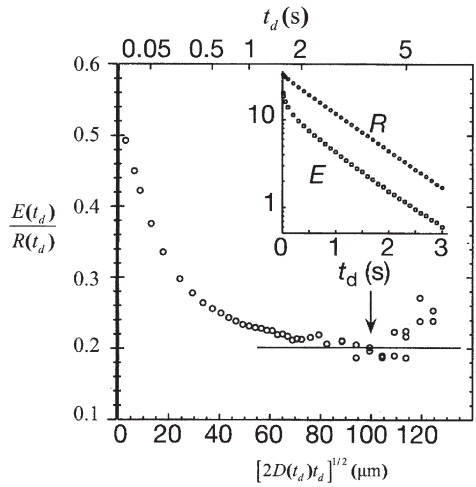

Fig. 13. Stimulated echo and FID amplitude attenuation curves acquired in water in a random pack of glass beads with a diameter of 105 μm with the method shown in Fig. 12. The inset shows the amplitudes of the echo (E) and the reference signal (R) versus the diffusion time. The ratio of these amplitudes is attenuated by diffusion relative to internal field gradients and is a function of the root mean squared displacement $(2D(t_d)t_d)^{1/2}$ of the water molecules (adapted from Ref. [94]).

experience all local flux densities, B_i. It is related to the length scale L of the field variation and the bulk diffusion coefficient D_0 by the relation

$$L \approx \sqrt{2D_0 t_{cr}}. \tag{90}$$

Determining the critical time, t_{cr}, based on the ratio $E(t_d)/R(t_d)$ as described above permits one to estimate the length L which is a measure of the pore dimension. This method was successfully applied and tested with water in random bead pack samples with varying bead diameters and sedimentary rocks.[93,94] Song[95] and Lisitza and Song[96,97] also managed it to analyze diffusion eigenmodes, i.e., the mode solutions of the Bloch/Torrey equation given in Eq. (29),[98,99] from corresponding spin echo experiments.

7. GAS DIFFUSION AND VAPOR-ENHANCED DIFFUSION IN POROUS MEDIA

7.1. Probing into the structure of porous media by gas diffusion

In nanoporous materials, translational diffusion of solvents depends on the interaction with the pore walls ('adsorption effect') and/or the restriction on the diffusion pathways due to the pore network ('geometry effect'). NMR

relaxation and diffusion measurements are commonly used for getting information about the mobility restrictions which porous media impose on molecular dynamics.[100,101]

Time dependent diffusion coefficients can be analyzed in terms of the tortuosity, the porosity and the surface-to-volume ratio. For an interconnected pore space, the time dependent diffusion coefficient is given in the limit of long observation times by:[102]

$$\frac{D(t)}{D_0} = \frac{1}{\alpha} + \frac{\beta_1}{t} - \frac{\beta_2}{t^{3/2}}, \tag{91}$$

where α is the tortuosity of the medium, and β_1 and β_2 are constants which depend on the microgeometry of the pore space. D_0 is the self-diffusion coefficient in bulk. The porosity is given as the ratio of the pore space volume and the total sample volume. If diffusion in the pore space is slowed down on a predominantly geometrical basis, the tortuosity may be defined as the ratio of the mean squared displacement in bulk and in the pore space in the long-time limit, where the time-dependent diffusion coefficient becomes a constant, $D(t \to \infty) \equiv D_\infty$. That is,[167]

$$\frac{D_0}{D_\infty} \longrightarrow \alpha. \tag{92}$$

For random bead packs, this diffusivity ratio depends on the porosity ϕ of the medium in such a way that $1/\alpha \approx \sqrt{\phi}$. For short diffusion times, t, the fraction of fluid spins with displacements restricted by pore walls is $\sim (S/V_p)\sqrt{D_0 t}$, where S/V_p is the pore surface-to-volume ratio. Mitra and Sen[11] and Mitra *et al.*[168] have shown that the time-dependent diffusion coefficient, $D(t)$, is given by

$$D(t)/D_0 = 1 - \frac{4}{9\pi}\,\frac{S}{V_p}\,\sqrt{D_0 t} + \mathcal{O}(D_0 t). \tag{93}$$

NMR self-diffusion measurements of liquids confined in porous media provide information on the sample structure for length scales below 100 μm.[89,103] This upper limit is given by the relatively short root mean squared displacements of molecules on the time scale of spin-lattice relaxation. In systems with larger pores, confined-liquid NMR may accurately probe the porosity and the pore surface-to-volume ratio but is not able to determine physical properties associated with the interconnectivity and tortuosity.

Gas diffusion is three to four orders of magnitude faster than in liquids of the same molecular species. The root mean square displacements are correspondingly longer. Therefore, gas diffusion was suggested to probe porous systems with large pores. The sensitivity problem arising from the low gas spin density which is three orders of magnitude lower than that in the liquid state can

convincingly be solved by employing hyperpolarized spin-1/2 noble gases such as ^{3}He and ^{129}Xe.[104,105] In recent investigations diffusion coefficients of both laser-polarized and thermally polarized xenon gas were examined with the objective to determine tortuosities on a length scale extended up to 2 mm.[106–108] More recently it was shown that the tortuosities measured in the Knudsen and bulk regimes of diffusion are different.[109]

The main problem encountered in the case of laser polarized noble gas diffusion measurements is the finite, non-renewable longitudinal magnetization during the experiment. Since the noble gas magnetization is induced by optical pumping, there is no recovery of magnetization possible within a T_1 time after the RF pulse. The magnetization is lost once used and must be replaced by that of freshly hyperpolarized gas. This requires modifications of standard NMR pulse sequences. In particular, low flip angle experiments such as FLASH (see Ref. [7], for instance) have been used for rendering spin density maps in this context.[110]

However, since each pulse consumes a certain fraction of the magnetization, the continued application of the same flip angle will deliver progressively less magnetization into the transverse plane. This effect can be compensated for by using a variable angle approach progressively increasing the pulse angle in the course of the pulse sequel.[110]

Low flip angle excitation techniques are very sensitive to miss-adjusted or spatially non-uniform 180° RF pulses. Ordinary PGSE experiments combined with low flip angle excitation of laser polarized noble gases are therefore impractical. The spurious signals from non-uniform 180° RF pulses could exceed the signals produced by the excitation pulses.

Two variants of the PGSE technique have been suggested to overcome this problem.[106] The pulse sequences are shown in Fig. 14. The sequel represented by Fig. 14a is a *p*ulsed *g*radient *e*cho (PGE) method where the refocusing of the signal is obtained by reversing the sign of the second gradient pulse so that 180° pulses are avoided for refocusing of coherences. The difference here in comparison to other similar pulse sequences[111,112] is that the diffusion interval is not fixed but can be varied. A total number of N RF pulses is applied. The tip angle α of the nth pulse is adjusted according to[112]

$$(\sin^2 \alpha_n)^{-1} = N - n + 1, \tag{94}$$

so that the tip angle increases from the first RF pulse ($n = 1$),

$$\alpha_1 = \arcsin\left(1/\sqrt{N}\right) \tag{95}$$

to the Nth RF pulse,

$$\alpha_N = \pi/2. \tag{96}$$

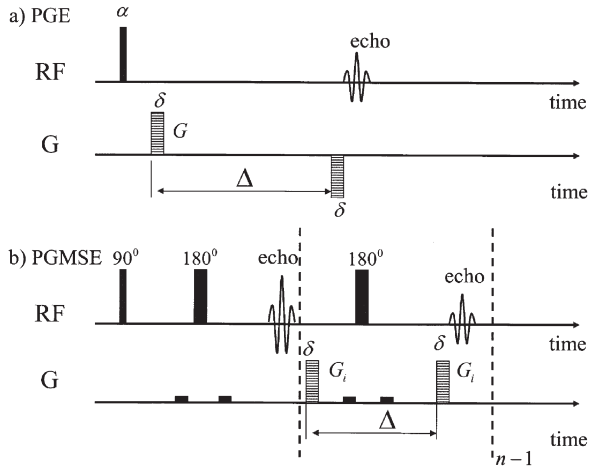

Fig. 14. RF and field gradient pulse sequences for NMR diffusometry in hyperpolarized noble gases.[106] (a) PGE method with variable excitation flip angle α. (b) PGMSE sequence (not to be confused with the multiple (nonlinear) echoes discussed in Section 5).

A deficiency of such gradient echo sequences is that they are limited by the T_2^* decay instead of the longer T_2 periods relevant for Hahn spin echo methods. As a consequence only moderate diffusion times (< 100 ms) can be probed even in systems with unrestricted diffusion.

This limitation can be circumvented by manipulating the transverse magnetization with fully refocusing RF pulses similarly to the standard spin echo or stimulated echo techniques. However, the magnetization of laser polarized noble gases is finite and cannot be recovered by spin-lattice relaxation. The attenuation information can be only obtained for a single diffusion encoding gradient value in each experiment. That is, time dependent diffusion coefficients cannot be studied this way.

Mair *et al.*[106] therefore proposed a single-shot diffusion technique that provides a series of echoes with differing diffusion attenuation after a single RF excitation pulse. This method was adapted from a sequence suggested by Li and Sotak.[113,114] The RF and gradient pulse scheme of this "*p*ulsed *g*radient *m*ultiple *s*pin *e*cho (PGMSE) technique" (not to be confused with the nonlinear (or "multiple") echoes treated in Section 5) is shown in Fig. 14b.

With this technique the echo attenuation curve can be probed with a single 90° RF excitation pulse. The transverse magnetization is repeatedly refocused by 180° pulses. A gradient pulse pair is applied during each echo cycle so that subsequent echoes are more and more attenuated by diffusion. Consequently, the diffusion encoding gradient effects are cumulative. The echoes are additionally attenuated by T_2 relaxation, of course. In order to remove the spurious signals from imperfect 180° pulses, small spoiling gradients can be

applied along an axis orthogonal to the diffusion-encoding direction. The amplitude of the nth echo is given by[106]

$$A_n(G, t) = \exp\left[-\left(\sum_{i=1}^{n} G_i^2\right)\delta^2\gamma^2 D(\delta + \Delta/3)\right] e^{-t/T_2}, \tag{97}$$

where D is the free gas diffusion coefficient, and G_i is the strength of the gradient pulse applied during the ith echo.

The data acquisition and analysis differs from the standard PGSE experiment. In the study by Mair *et al.*[106] two sets of PGMSE experiments were performed. In one experiment the echo train was recorded without gradient pulses and then the experiment was repeated with gradient pulses. This permits one to eliminate the transverse relaxation decay. The resulting normalized data can then be analyzed using Eq. (97) without the relaxation decay factor. The maximum diffusion time probed in PGMSE experiments is limited by T_2 which tends to be longer than T_2^* relevant for the PGE experiment.

As a general problem remains, that even at magnetic fields as low as 1 T large local magnetic fields are produced by the spatially varying magnetic susceptibility of porous media. The consequence is that T_2 and T_2^* of the noble gas are shortened. For example, the relaxation times of hyperpolarized xenon gas in a glass bead pack range between only 20 and 30 ms for T_2 and 5 and 10 ms for T_2^* in a magnetic field of 4.7 T.[106] It is therefore recommendable to perform such experiments at moderate magnetic fields.

In the case of thermally polarized noble gases it was shown that the conventional PGSE techniques can be applied successfully.[106–108] In order to avoid excessive recovery times of the longitudinal magnetization, paramagnetic oxygen can be added to the gas as a relaxation agent. It was also shown that reasonable sensitivity can be achieved with fluorine containing gases at moderate temperatures.[115]

Note that the narrow-pulse approximation $\delta \ll \Delta$ (see Section 3) tends to break down with gas diffusion experiments. It has been shown[116] that this is the case when $\sqrt{\delta D}$ exceeds $\sim 0.14a$, where a is the average pore diameter of the porous medium. Assuming gas self-diffusion coefficient in the order of $D \sim 10^{-6}\,\mathrm{m^2/s}$ gradient pulse widths in the order of 1 ms, the narrow-pulse approximation breaks down for pore diameters smaller than 0.2 mm.

7.2. Vapor diffusion contribution to the molecular mobility in porous media

If a macroscopic sample contains a two- or more-phase system formed of a liquid in thermal equilibrium with its vapor, the acquired NMR signals are normally entirely dominated by the magnetization of the liquid phases. The reason is that the density of the vapor phase at normal conditions is three

orders of magnitude less. Consequently, the vapor phase signal can be neglected normally.

On the other hand, diffusion coefficients measured in partially liquid filled porous media showed enhanced values coefficient compared to completely filled pores.[30,39,117,119] An explanation is the fast (relative to the NMR time scale) exchange between the liquid and gaseous phases so that an average diffusion coefficient is measured. The consequence is that, although the signal is dominated by spins in the liquid phase, the effective diffusion coefficient is substantially affected by the intermittent intervals a spin spends in the vapor phase where the diffusion coefficient is three to four orders of magnitude larger than in bulk liquids.

PGSE measurements of the effective diffusion coefficient of water filled into porous sol–gel glasses[117] showed this diffusion enhancement for filling degrees below 30% of the saturation value. Above that value the effective diffusion coefficient is practically independent of the filling factor. Diffusion coefficients exceeding three times the bulk value were found this way.

The dependence on the filling degree was interpreted in terms of a two-phase fast-exchange model. Water being a polar species is confined in adsorption layers on the surface with a thickness depending on the pore filling degree. The remaining free space of the pores then contains saturated vapor. The effective self-diffusion coefficient then is a sum of vapor and liquid contributions:[117]

$$D_{\mathrm{eff}} = \frac{V\rho_{\mathrm{l}}}{V\rho_{\mathrm{l}} + (V_0 - V)\rho_{\mathrm{v}}}\, D_{\mathrm{l}} + \frac{(V_0 - V)\rho_{\mathrm{v}}}{V\rho_{\mathrm{l}} + (V_0 - V)\rho_{\mathrm{v}}}\, D_{\mathrm{v}}, \tag{98}$$

where V_0 is the pore space volume, V the liquid phase volume, and ρ_{l}, ρ_{v} represent the mass densities of the liquid and vapor phases, respectively. The self diffusion coefficients D_{l} and D_{v} in the liquid and vapor, respectively, are reduced relative to the bulk values D_{l}^0 and D_{v}^0 because of the pore space tortuosity (which again depends on the filling degree). D'Orazio *et al.*[117] suggested tentatively that the diffusion coefficient in the liquid phase is reduced by a factor $\phi^{m'}$ on these grounds, i.e.,

$$D_{\mathrm{l}} = \phi^{m'} D_{\mathrm{l}}^0, \tag{99}$$

where ϕ is the porosity of the liquid phase and m' is an exponent to be determined experimentally.

Taking into account the Knudsen effect[120] at the vapor/liquid interface, the diffusion coefficient in the vapor phase can be written as:

$$D_{\mathrm{v}} = \phi^m (1 - V/V_0)^m \Big/ \left(\frac{1}{D_{\mathrm{v}}^0} + \frac{1}{D_{\mathrm{K}}}\right). \tag{100}$$

In the above expression $D_K = (2a/3)(8k_BT/\pi M)^{1/2}$ represents the Knudsen diffusion coefficient which depends on the absolute temperature (T), the molecular mass (M) and the size of the vapor phase domains (a). k_B is the Boltzmann constant. The exponent m is a parameter to be fitted to experimental data.

Kimmich *et al.*[39] corroborated the influence of the vapor on the effective diffusion coefficient by varying the available gas phase volume. The initially powdery silica fine particle samples were saturated with water corresponding to the water uptake in a moist atmosphere at equilibrium. In this initial state the effective diffusion coefficient exceeds that of bulk water by up to one order of magnitude. Compressing the powder down to 16% of the initial sample volume reduces the volume accessible to the vapor phase correspondingly. As a consequence the effective diffusion coefficient is diminished and finally approaches the value of bulk water. This demonstrates the role the vapor phase volume plays for the effective displacement of water molecules by diffusion.

The expression for the effective diffusion coefficient as a function of the filling degree, Eq. (98), describes the experimental data only for porous sample with big pore dimensions (bigger than 10 nm). Recent observations by Wonorahardjo *et al.*[121] apparently contradict these results. The effective diffusion coefficient for water filled into Vycor porous glass with approximately 4 nm pore diameter did not show this vapor enhancement effect. A conclusion may be that the vapor enhancement phenomenon depends on the pore size. However, further studies in this respect will be needed before final statements can be made.

8. ISOTOPE INTERDIFFUSION AND HYDRODYNAMIC DISPERSION IN PERCOLATION MODEL OBJECTS

8.1. Isotope interdiffusion

The main objective of gas diffusion studies in porous media is to probe pore spaces on length scales much larger than possible by ordinary gradient spin echo techniques (see Section 7.1). Another way of probing extended diffusion length (or time) scales is to examine isotope interdiffusion. Bringing two compartments filled with H_2O and D_2O gels in contact with each other at time 0 provides a well-defined initial condition for the subsequent interdiffusion process. The proton spin density is then recorded as a function of position and time. That is, magnetic imaging techniques[122] are employed in this case. The proton spin density profiles across the sample rendered in this way directly reflect the interdiffusion displacements. Note that there is no limitation of the diffusion time in principle because the samples need not reside inside the NMR spectrometer all the time.

The technique was demonstrated with porous objects fabricated for modeling randomly disordered porous media on the basis of the percolation

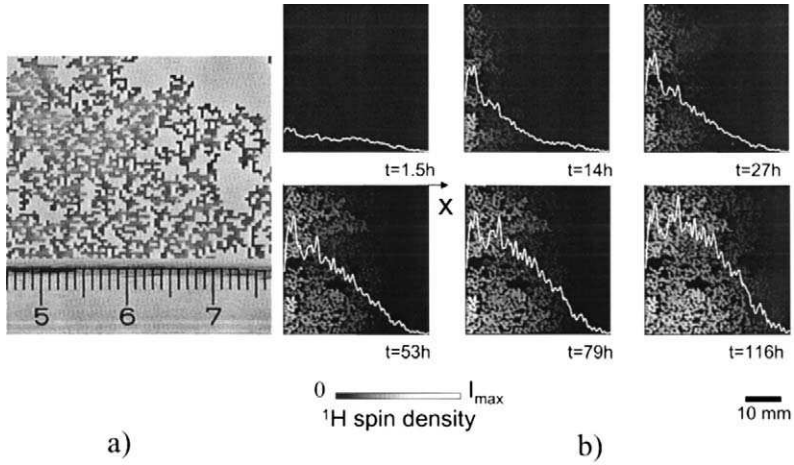

Fig. 15. (a) Photograph of a quasi-two-dimensional random site percolation model object.[122] The object was milled into polystyrene plates with a mechanical resolution of 400 μm and a milling depth of 2 mm. The length scale at the bottom is in centimetres. (b) Evolution of two-dimensional proton spin density maps (256×256 pixels) in the random-site percolation model object. The initial condition is illustrated in the inset of Fig. 16. The white lines represent the mean proton concentration profiles, i.e., projections of the diffusion front on the main diffusion direction.

theory.[122] The percolation theory[123] helps to relate the dynamic behavior of the confined liquids to geometrical parameters of a porous medium of a well-defined geometry. The long-term objective is to relate geometrical parameters of the topological constraints with dynamic transport quantities.

Figure 15a shows a typical quasi two-dimensional random-site percolation model object with a pore dimension > 300 μm. The object structure is based on randomly occupied lattice points of a square lattice. The occupation probability p is chosen in the vicinity of the (two-dimensional) percolation threshold $p_c = 0.592746$. Neighboring occupied sites are connected by pores with a cross section corresponding to the lattice constant or integer multiples of it. The total subset of connected lattice sites forms a so-called "cluster". For an occupation probability, $p \geq p_c$, sample spanning clusters occur that can be examined with respect to transport properties.

The pore space structure generated by the random-site percolation model can be characterized by four parameters. These are: the lattice constant a, the fractal dimension d_f, the correlation length ξ and the percolation probability P_∞.[124] The latter quantity is defined as the probability that a site belongs to a infinite cluster traversing the whole sample.[125] The correlation length is defined as the mean distance between two sites of a finite cluster or the mean holes diameter in an infinite cluster.

Random-site percolation clusters are known to display fractal properties on a length scale $a < r < \xi$.[124,126] The consequence is that a random walker on the

percolation cluster is subject to a waiting time distribution. That means the walker is frequently and temporarily trapped in "dead end" pores and its movement becomes anomalous (subdiffusive regime). That is, the dynamic parameters of the fluid in the pore space and the structural properties of the matrix confining the fluid are interrelated.

Alexander and Orbach[127] suggested that the anomalous diffusion exponent and the fractal dimension of the percolation cluster should be inversely proportional to each other with a fixed proportionality constant. The purely structural relationship between the volume averaged porosity and the probe volume radius is opposed by the dynamic property for the mean squared displacement of a random walker,

$$\langle r_{\mathrm{d}}^2 \rangle \propto \begin{cases} t^{2/d_{\mathrm{w}}} & \text{for } t \ll t_\xi \\ D_{\mathrm{eff}} t & \text{for } t \gg t_\xi, \end{cases} \tag{101}$$

where $t_\xi \propto \xi^{d_{\mathrm{w}}}$ is the time a random walker needs to explore the correlation length ξ and d_{w} is the fractal dimension of the random walk. Strictly speaking anomalous diffusion is only expected in the scaling range $a < \langle r_{\mathrm{d}}^2 \rangle^{1/2} < \xi$. The diffusion coefficient becoming effective in the long-time limit, $t \gg t_\xi$, is denoted by D_{eff}. According to the Alexander and Orbach[127] conjecture, the quantity d_{w} is assumed to be related to the fractal dimension d_{f} by

$$d_{\mathrm{w}} \approx \tfrac{3}{2} d_{\mathrm{f}} \quad (\text{for } d_{\mathrm{E}} \geq 2). \tag{102}$$

That is, the structural parameter d_{f}, characteristic for the volume-averaged porosity is linked to the dynamic parameter d_{w} specifying anomalous diffusion. The evaluations of both quantities have been carried out by Klemm *et al.*[122] based on NMR tomography experiments so that a comparison with the conjecture given in Eq. (102) was possible.

The displacement of the isotope diffusion front was measured as a function of time in the form of repeatedly recorded proton spin density maps (Fig. 15b). Since there is no limitation of the diffusion time by the proton relaxation times in these experiments, water diffusion can be probed on a length scale much larger than the pore dimension, so that any geometry induced anomalies become detectable.

Tests with bulk H_2O and D_2O compartments, that is in the absence of obstacles due to the matrix showed that neither the gel formation nor the isotope exchange perceptively affect the water diffusion behavior in the frame of accuracy of the experiments. In the test experiments the known solution of the Fickian diffusion equation of the proton concentration $C(\vec{r}, t)$,[128]

$$C(x, t) = \tfrac{1}{2} C_0 \operatorname{erfc}\left\{ \frac{x}{2\sqrt{Dt}} \right\}. \tag{103}$$

The one-dimensional initial condition anticipated for this solution,

$$C(x, 0) = \begin{cases} C_0 & \text{for } x \leq 0 \\ 0 & \text{for } x > 0, \end{cases} \tag{104}$$

was reasonably well realized in the experiment. The agreement between the theoretical solution and the experimental results proves that the measuring technique based on imaging of proton concentration profiles is a reliable method for the detection of the isotope interdiffusion processes.

Interdiffusion in random-site percolation model objects was examined in an analogous way. The inset in Fig. 16 schematically shows the experimental setup. The bulk H_2O reservoir was chosen large enough so that the proton concentration at the interface to the initially D_2O filled percolation object (Fig. 15a) can be treated to be practically constant. Using the two-dimensional proton spin density maps of the proton diffusion front in the compartment that was initially filled completely with D_2O, Klemm *et al.*[122] evaluated the half-height positions $x_{1/2}$ of the proton concentration profiles. The square of the half-height positions plotted versus the diffusion time are shown in Fig. 16.

At long times, when the imperfections of the initial isotope distribution, the finite lateral size of the compartment interface, and the finite time resolution of 26′ do not matter anymore, the data can be described by a power law as suggested by Eq. (102) for $t \ll t_\xi$. Fitting the exponent of this equation to the long-time data leads to a value $d_w = 2.85$. According to the Alexander/Orbach conjecture, given in Eq. (102), this suggests a fractal dimension of $d_f = 1.9$, i.e.,

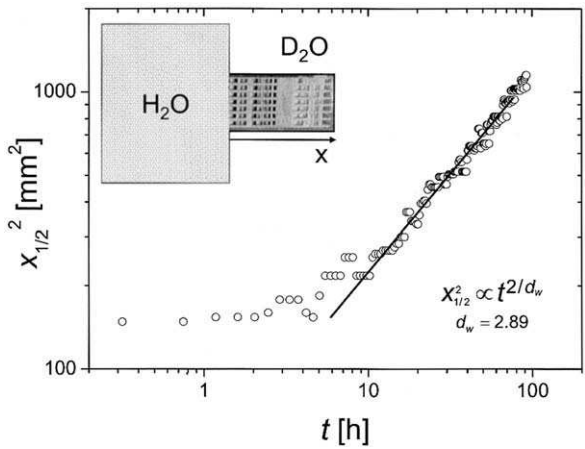

Fig. 16. Square of the position at half height of the proton concentration profile in the percolation cluster shown in Fig. 15a versus diffusion time.[122] The inset shows the experimental setup at time 0. The concentration profiles were obtained as projections of two-dimensional spin density maps (see Fig. 15b). The solid line was fitted according to Eq. (101) for $t \ll t_\xi$. The resulting exponent is $d_w = 2.89$.

a value close to the fractal dimension directly evaluated from the volume averaged porosity of a spin density map of the same object. The two values coincide in the limits of the experimental accuracy. The anomalous diffusion data are thus in accordance with the Alexander/Orbach conjecture which is of particular interest as an example linking geometrical with dynamical parameters.

Interestingly, anomalous diffusion was found even for displacements considerably exceeding the correlation length contrary to the expectation according to Eq. (101). That is, the crossover to normal diffusion occurs only for times much longer than t_ξ or for root mean squared displacements much larger than ξ. The experimental findings of Klemm *et al.*[122] have been proved to be in agreement with Monte Carlo simulations done by Poole and Salt.[129]

Apart from the mean square displacement considered here, one can compare[122] the whole concentration profile with theoretical predictions based on fractional diffusion equation.[20] The measured concentration profile in principle contains all information of the propagator effectively determining the diffusion properties and thus can be compared with the analytical derivations from fractional diffusion equation.

8.2. Hydrodynamic dispersion

In this section we are again referring to the percolation model objects discussed above. In the situation to be considered now a pressure gradient is exerted to the object so that the fluid filled into the pore space starts to percolate through the object. The consequence is hydrodynamic dispersion (see Section 3.3).

Hydrodynamic dispersion in principle represents the simultaneous random displacement of molecules by flow and self-diffusion. As a consequence the propagator will contain features of self-diffusion as well as of coherent transport by flow. The "weight" of the influence of the two phenomena relative to each other is characterized by the Péclet number,[18,130]

$$P_e = \frac{\bar{u}R}{D}, \tag{105}$$

where R is a typical length scale on which the two transport processes are to be compared, $\bar{u}$ is the mean flow velocity corresponding to that length scale. For example, in the case of hydrodynamic dispersion through a capillary[131] this length would be just the radius of the capillary.

In random porous media, the tortuosity of flow streamlines comes into play in addition. The characteristic length scale is then defined in the macroscopic sense by the correlation length ξ indicating the distance on which diffusion effectively becomes normal. The diffusion coefficient in Eq. (105) is then to be interpreted as an effective one.

At large Péclet numbers, $P_e \gg 1$, that is, if displacements by flow are larger than displacements by Brownian diffusion, the dominating source of the

dispersion of the particle trajectories is the tortuosity determined by the pore space geometry. Incoherent displacements by tortuous flow dominate then over Brownian displacements, and particle transport tends to be superdiffusive according to the definition given in Section 2.3. Corresponding computer simulations[130,132] and NMR experiments[42,133] have been reported in literature.

The attenuation of spin echo amplitudes in pulsed gradient NMR experiments is due to phase shifts in the field gradient pulse intervals. With tortuous flow through porous media, the question whether the velocity of a particle is constant depends on the length of the sensitive interval t adjusted. In the limit of small measuring intervals, that is, for displacements shorter than the mean pore dimension, $\sqrt{\langle z^2 \rangle} < a$, flow velocities tend to be constant so that the only incoherent displacement contribution can arise from Brownian diffusion. Intervals permitting displacements in the range $a < \sqrt{\langle z^2 \rangle} < \xi$ are connected with more or less random velocity changes so that the compensation for coherent flow becomes incomplete (see the discussion in Section 3.3).

In this case, random phase shifts by tortuous flow lead to the attenuation of the echo amplitude indicating incoherent displacements. The influence of such motions will be the larger the longer the sensitive interval is, i.e., the more randomly the particle trajectories develop.

Finally, for displacements $\sqrt{\langle z^2 \rangle} \gg \xi$ reached in the sensitive interval, we have a superposition of a constant drift velocity and randomized displacements due to the tortuosity of the percolation cluster. In coherent velocity compensation experiments, the drift contribution can completely be eliminated so that attenuation by incoherent tortuous flow governs the echo amplitude.

From the echo attenuation curves the mean squared displacement can be evaluated analogously to the right-hand side of Eq. (26),

$$\langle z^2 \rangle = 2D_{\mathrm{disp}}(t)t, \tag{106}$$

where t is the relevant gradient pulse interval, and D_{disp} is the dispersion coefficient. In the limit $\sqrt{\langle z^2 \rangle} < a$, the dispersion coefficient approaches the ordinary Brownian diffusion coefficient,

$$D_{\mathrm{disp}} \approx D_{\mathrm{Brown}} = \mathrm{const.} \tag{107}$$

For $\sqrt{\langle z^2 \rangle} \gg \xi$, the dispersion coefficient is again stationary and adopts an effective value,

$$D_{\mathrm{disp}} \approx D_{\mathrm{eff}} = \mathrm{const} \gg D_{\mathrm{Brown}}. \tag{108}$$

However, in the scaling window $a < \sqrt{\langle z^2 \rangle} < \xi$, a time dependent diffusion coefficient is expected for flow through random percolation clusters at large Péclet numbers, $P_e \gg 1$,

$$D_{\mathrm{disp}} = D_{\mathrm{disp}}(t) \propto t^f \quad \text{with } 0 < f < 1 \quad \text{and} \quad D_{\mathrm{Brown}} < D_{\mathrm{disp}} < D_{\mathrm{eff}}. \tag{109}$$

9. POLYMER DIFFUSION

9.1. The tube/reptation model

In his famous 1971 paper, de Gennes[134] treated the dynamics of a polymer chain in the presence of fixed obstacles that cannot be crossed by the chain. These topological constraints merely permit the chain to move in a "reptile" manner, for which the term "reptation" became popular. Effectively the chain is thought to be encaged in a randomly coiled "tube" restricting the dynamic modes possible under the circumstances.

In a more elaborated form, Doi and Edwards[135] defined a number of limits for which predictions of dynamic features of the reptation model are possible. These limits are based on four different dynamic time constants for a Kuhn (or statistical) segment chain as illustrated in Fig. 17.

The shortest time constant, the "segment fluctuation time"

$$\tau_s = \frac{\zeta b^2}{3\pi^2 k_B T}, \tag{110}$$

characterizes local fluctuations on the length scale of a Kuhn segment. The friction coefficient and the length of a Kuhn segment are denoted by ζ and b, respectively. $k_B T$ is the Boltzmann constant times the absolute temperature. This time constant may also be regarded as the shortest Rouse relaxation time compatible with a chain of discrete Kuhn segments.

The next longer length scale refers to the width of the tube, $a = N_e b$, where N_e is the number of Kuhn segments on a chain section of length a. The relaxation time of Rouse modes corresponding to this length is the so-called "entanglement time",

$$\tau_e = \frac{\zeta a^2}{3\pi^2 k_B T} = N_e^2 \tau_s, \tag{111}$$

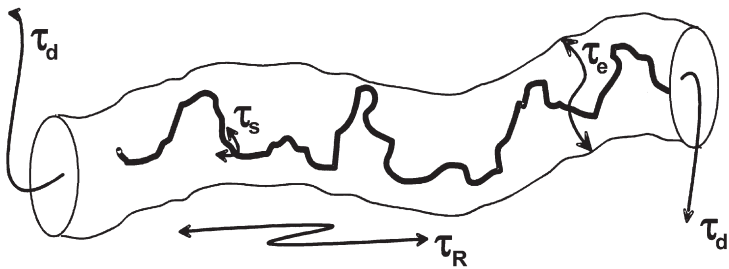

Fig. 17. Schematic representation of a polymer chain in a randomly coiled tube. The arrows illustrate the four types of dynamic modes that are mattering for polymer segment motions under topological constraints. The characteristic time constants are indicated.

alluding to the notion that in bulk systems of entangled polymers the entanglements might act as a sort of fixed obstacles and thus determine the tube diameter.[135] Below we will reason that this picture is too crude a model to account for experimental findings, but will anyway make use of the quantity τ_e as a characteristic time constant for the definition of limiting cases.

The chain length L defines the length scale of the longest Rouse relaxation modes with the "Rouse relaxation time" as such,

$$\tau_R = \frac{\zeta L^2}{3\pi^2 k_B T} = N^2 \tau_s, \tag{112}$$

where N is the number of Kuhn segments per chain. The longest characteristic time constant in this context is the "disengagement time", τ_d, indicating how long it takes a chain to leave its initial tube conformation. In the original tube model referring to bulk liquids of entangled polymers, the tube length is intimately related with the chain length, which is the length of the so-called primitive path.[135] In this case the disengagement time is given by

$$\tau_d = \frac{N^3}{N_e}\ \tau_s. \tag{113}$$

Beyond this time scale, the chain can be considered to diffuse as a whole with the center-of-mass self diffusion coefficient D. Any extra displacements of segments due to Rouse modes relative to the center-of-mass ("segment diffusion") become negligible on this time scale, whereas intracoil segment diffusion tends to dominate at shorter times. Note however that the disengagement time of polymers confined in artificial "tubes" to be considered in Section 9.2 can be very different and tends to be much longer.

Based on these characteristic time constants, Doi and Edwards[135] have defined four dynamic cases. In limit $(I)_{DE}$, $\tau_s < t < \tau_e$, chain dynamics is governed by free Rouse modes. That is, on this time scale (and the corresponding length scale) chain modes are not yet affected by the topological constraints imposed by the tube. The first constraint effect in lateral direction arises in limit $(II)_{DE}$, $\tau_e < t < \tau_R$, when Rouse modes can occur in an unconstraint fashion only along the tube contour. The length scale corresponding to this regime is still shorter than the chain length, so that the pertinent chain modes refer to chain internal dynamics. Global chain displacements along the tube contour, i.e., reptation in the proper sense, start to become relevant in limit $(III)_{DE}$, $\tau_R < t < \tau_d$. Unrestricted displacements by center-of-mass diffusion become possible only after the chain has migrated out of its initial tube conformation, that is in limit $(IV)_{DE}$, $t > \tau_d$.

Relationships of particular interest are the time and molecular weight dependences of the mean square segment displacement and the frequency and molecular weight dependences of the spin-lattice relaxation time. There are

predictions for all four limits. Table 1 shows the laws expected in the corresponding regimes. Some of the power laws are of particular interest in connection with NMR experiments,[36,37,136–138] and will be discussed in more detail in the following sections.

The theoretical laws given in Table 1 for the mean squared segment displacement on the one hand and for spin-lattice relaxation on the other are intimately related with each other. The behavior predicted for one phenomenon of the two unambiguously anticipates the law predicted for the other. Also, the time, frequency and molecular weight dependences entail each other compellingly and cannot be considered independently.

We note that the limiting laws $(I)_{DE}$ to $(III)_{DE}$ predicted for short times refer to *subdiffusive* transport of polymer segments. This general feature is grounded in different facts acting in a more or less combined way. In Section 2 we have generally distinguished "mutual obstruction of molecules" from "waiting time distributions due to traps" as potential sources of molecular transport anomalies. The Doi/Edwards limits can be discussed in this particular respect.

Free Rouse diffusion (limit $(I)_{DE}$) reflects the chain connectivity property, which may be allocated to the "mutual obstruction" category. The same applies to limit $(II)_{DE}$, but now the "trapping effect" owing to the randomly coiled tube contour additionally comes into play in addition. Segment displacements must follow the tube contour in a curvilinear way (see Fig. 18 and the discussion in the following section). The diffusion of the whole polymer along the tube contour as the dominating process in limit $(III)_{DE}$ follows the normal Einstein relation if displacements are measured in curvilinear coordinates s. However, when displacements are measured along a coordinate axis of the laboratory frame (such as the field gradient direction), the trapping effect mentioned before comes into play again. That is, the anomaly is of a purely topological nature in this limit. Finally, center-of-mass diffusion governing limit $(IV)_{DE}$ is completely unrestricted and therefore normal.

9.2. Polymer diffusion in artificial "tubes"

In a real "entangled" polymer systems, there is no such thing as rigid tubes as anticipated by the model situation illustrated in Fig. 17. Actually all attempts to experimentally verify the predictions given in Table 1 with polymer melts or concentrated polymer solutions either failed or could not really convince. It may therefore be helpful to consider chain dynamics in tubelike pores of a physically real nature.

Segment diffusion in tubes with a harmonic radial potential were treated analytically by Denissov *et al.*[19] Fig. 19 shows the resulting mean squared segment displacement as a function of time and tube diameter. The tube confinement effect relative to free Rouse chains ("infinite" tube diameter) and the crossover between the Doi/Edwards limits $(I)_{DE}$, $(II)_{DE}$ and $(III)_{DE}$ are

Table 1. Theoretical time (t), angular frequency (ω), and molecular mass (M), dependences predicted by the tube/reptation model for the mean squared segment displacement and the spin-lattice relaxation time in the four Doi/Edwards limits

	Limit	Mean squared segment displacement	References	Spin-lattice relaxation time	References
$(I)_{DE}$	$\tau_s \ll (t, 1/\omega) \ll \tau_e$	$\langle r^2 \rangle \propto M^0 t^{1/2}$	Doi and Edwards[135]	$T_1 \propto -M^0/\ln(\omega\tau_s)$	Khazanovich, 1963; Fatkullin *et al.*[166]
$(II)_{DE}$	$\tau_e \ll (t, 1/\omega) \ll \tau_R$	$\langle r^2 \rangle \propto M^0 t^{1/4}$	de Gennes[134]; Doi and Edwards[135]	$T_1 \propto M^0 \omega^{3/4}$	de Gennes[134]; Dennissov *et al.*, 2002
$(III)_{DE}$	$\tau_R \ll (t, 1/\omega) \ll \tau_d$	$\langle r^2 \rangle \propto M^{-1/2} t^{1/2}$	de Gennes[134]; Doi and Edwards[135]	$T_1 \propto M^{-1/2} \omega^{1/2}$	de Gennes[134]
$(IV)_{DE}$	$\tau_d \ll (t, 1/\omega)$	$\langle r^2 \rangle \propto M^{-2} t^1$	de Gennes[134]; Doi and Edwards[135]		

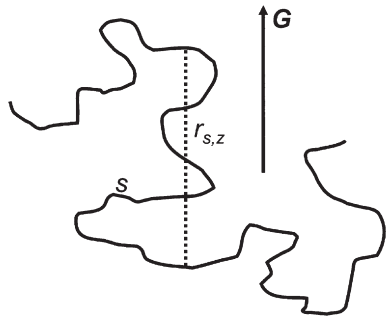

Fig. 18. Polymer segments in a "tube" are displaced along the randomly coiled contour line resulting in the "curvilinear displacement" s. Field gradient NMR diffusometry measures displacements $r_{s,z}$ along the gradient direction (***G***). Contour loops act as "traps" for segments the displacements of which are monitored along ***G***.

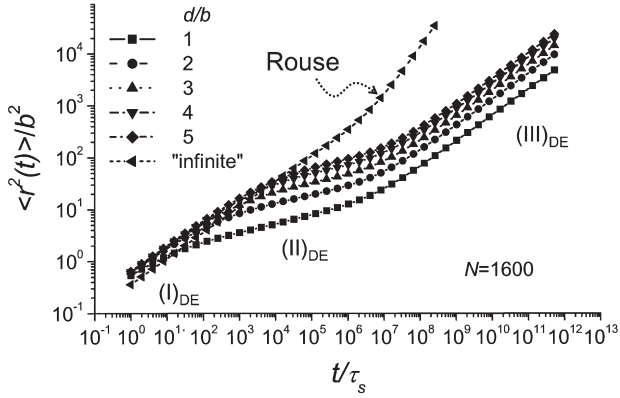

Fig. 19. Mean squared segment displacement versus time according to the harmonic radial potential theory.[19] The tube diameter d is given in multiples of the Kuhn segment length b. The crossover tendency to free, unconfined Rouse chain dynamics with increasing tube diameter is obvious. The mean squared displacement is given in units b^2, the diffusion time t in units of the segmental fluctuation time τ_s. The chain length was assumed to be $N = 1600$ Kuhn segments. The three "anomalous" Doi–Edwards limits (see Table 1) are reproduced with finite tube diameters.

demonstrated. The data suggest that any direct verification of a crossover between two of these limits will be experimentally extremely difficult, because the transition regimes are extended over four or five orders of magnitude of time.

For experimental investigations, polymers can be encaged in narrow pores of a solid matrix. Fig. 20 shows a so-called semi-interpenetrating network as an example. The matrix consisted of cross-linked polyhydroxyethylmethacrylate (PHEMA). In the 10 nm pores, linear polyethylene oxide (PEO) was incorporated. The molecular weights of the PEO samples used in experiment were chosen large enough to ensure that the root mean squared random coil

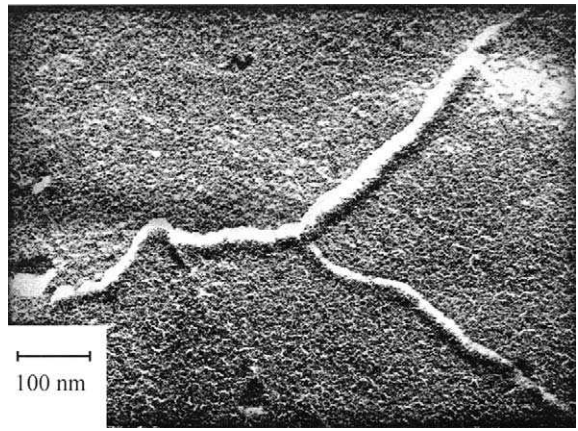

Fig. 20. Electron micrograph (TEM, replica) of pores in a matrix of solid cross-linked PHEMA.[36] The pore width is about 10 nm. The pores are filled with linear PEO with a narrow molecular weight distribution. The molecular weights of the PEO samples used in the experiments were chosen large enough to ensure that the root mean squared random coil diameter in bulk exceeded the pore diameter.

diameter in bulk exceeded the pore diameter. Diffusion of the PEO segments was examined with the aid of the fringe field NMR diffusometry technique.[36]

The evaluation formula given in Eq. (36) for the stimulated echo attenuation anticipates Gaussian propagators. As illustrated in Fig. 18 and discussed in the previous section, waiting time delays are mattering in NMR diffusion measurements with polymers subject to reptation. This follows from the fact that segments diffusing along the curvilinear path of the randomly coiled tube contour are intermittently ''trapped'' in loops that contribute little to displacements along the field gradient direction. Effectively non-Gaussian propagators are the consequence in the Doi/Edwards limits $(II)_{DE}$ and $(III)_{DE}$. One may try an approximate evaluation according to Eq. (26). However, it turned out to be more indicative for the characteristic reptation features to consider a special formalism specifically developed for the reptation problem.[139]

In the short gradient ''pulse'' limit of the fringe field NMR diffusometry technique (see Figs. 3 and 4), the effective diffusion time is given by $t \approx \Delta = \tau_2$. Under this prerequisite the stimulated-echo attenuation factor can be analyzed according to

$$A_{\mathrm{diff}}(k,t) = \left\langle \mathrm{e}^{\mathrm{i}\vec{k}\cdot\vec{r}(t)} \right\rangle_r = \underbrace{\left\langle \mathrm{e}^{\mathrm{i}\vec{k}\cdot\vec{r}_{\mathrm{s}}(t)} \right\rangle_{r_{\mathrm{s}}}}_{\text{segments; } A_{\mathrm{s}}(k,t)} \quad \underbrace{\left\langle \mathrm{e}^{\mathrm{i}\vec{k}\cdot\vec{r}_{\mathrm{c}}(t)} \right\rangle_{r_{\mathrm{c}}}}_{\text{center-of-mass; } A_{\mathrm{c}}(k,t)} , \tag{114}$$

where we have anticipated that segment and center-of-mass displacements can be taken to be independent of each other because of the different time scales on which these processes take place.

The ensemble averages indicated by the brackets refer to displacements along the field gradient direction. The subscripts of the ensemble averages indicate displacements r in general, displacements r_s relative to the center-of-mass by segment diffusion (limits $(I)_{DE}$, $(II)_{DE}$ and $(III)_{DE}$), and displacements of the center-of-mass, r_c (limit $(IV)_{DE}$), respectively.

Attenuation by center-of-mass diffusion (limit $(IV)_{DE}$) is described by the standard expression given in Eq. (36)

$$A_c(k, t) = \exp\{-k^2 D_c t\}, \tag{115}$$

where D_c is the center-of-mass diffusion coefficient of the whole chain. Since ordinary center-of-mass diffusion is of no interest in the frame of this consideration and since it is unlikely to matter in experiments with polymer chains confined in pore channels such as those displayed in Fig. 20, we will focus in the following on the spin echo attenuation factor due to segment diffusion. Features such as the inversely quadratic molecular weight dependence of the diffusion coefficient predicted by limit $(IV)_{DE}$ were however observed in experiments with bulk melts of polymers with relatively low molecular weights.[35]

The experimentally relevant time scale refers to limits $(II)_{DE}$ and $(III)_{DE}$, where displacements achieved in the interval of limit $(I)_{DE}$ due to free Rouse modes are relatively small and can safely be neglected. The spin-echo attenuation factor is then dominated[139] by

$$\begin{aligned} A_s(k, t) &= \underbrace{\left\langle \underbrace{\int \left(\frac{4\pi}{3}\, a|s|\right)^{-3/2} e^{r_s^2/a|s|}\, e^{i\vec{k}\cdot\vec{r}_s(t)}\, d^3\vec{r}_s}_{\text{average over all } r_s \text{ for a given } s} \right\rangle}_{\text{average over all } s} \\ &= \exp\left\{\frac{k^4 a^2 \langle s^2(t)\rangle}{72}\right\} \operatorname{erfc}\left\{\frac{k^2 a \sqrt{\langle s^2(t)\rangle}}{6\sqrt{2}}\right\}, \end{aligned} \tag{116}$$

where the mean squared *curvilinear* segment displacement,

$$\langle s^2(t)\rangle = \frac{2D_0 t}{N + (12a^2 D_0 t/N^2 b^4)} + \frac{2b\sqrt{D_0 t}}{\sqrt{3\pi} + (18\sqrt{D_0 t}/Nb)} \tag{117}$$

combines the expressions given in Doi and Edwards[135] for limits $(II)_{DE}$ and $(III)_{DE}$. The step length of the so-called primitive path is denoted by $a = b\sqrt{N_e}$. The quantity $D_0 = k_B T/\zeta$ is the (fictitious) diffusivity of a Kuhn segment in the absence of chain connectivity.

Figure 21 shows typical echo attenuation curves recorded with PEO in a solid PHEMA matrix.[36] The good coincidence of the theoretical curves calculated on the basis of Eqs. (116) and (117) for all k and t values, which was

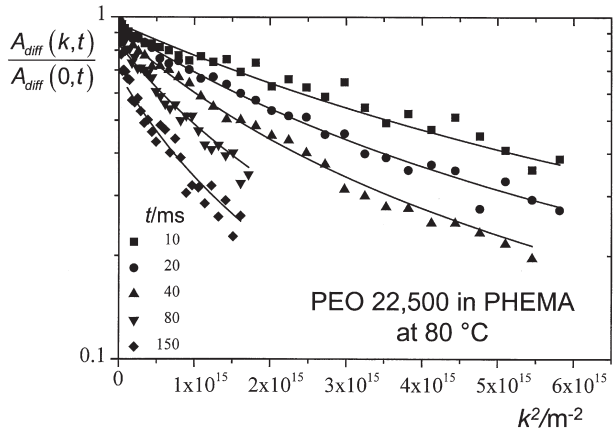

Fig. 21. Spin echo attenuation curves for linear PEO (weight average molecular weight $M_w = 22{,}500$) confined in 10 nm wide pores of a solid PHEMA matrix.[36] The solid lines correspond to a fit based on Eqs. (116) and (117). The data were recorded at 200 MHz proton resonance frequency in a field gradient of 60 T/m using the fringe-field NMR diffusometry technique.

also found with different molecular weights, corroborates the validity of the tube/reptation model for the case of linear polymers confined in artificial nanopores in a solid matrix.

9.3. Spin-lattice relaxation dispersion in artificial "tubes"

Field-gradient NMR diffusometry experiments such as the one represented by Fig. 21 tend to be largely dominated by the time and length scales of limit $(III)_{DE}$ (compare Fig. 19). On the other hand, the much shorter time scale of limit $(II)_{DE}$ can specifically be examined by NMR relaxometry, which under suitable conditions can indirectly probe translational diffusion of polymer segments. The laws predicted in Table 1 for anomalous diffusion on the one hand and spin-lattice relaxation on the other are based on the very same translational segment displacement mechanisms. They stipulate each other in a stringently compelling way. Spin-lattice relaxation at low frequencies as they can be covered with the aid of field-cycling NMR relaxometry[7] is therefore suitable to extend the range of field-gradient NMR diffusometry toward much shorter times. The total proton frequency range that can be probed by NMR spin-lattice relaxation techniques is $10^3 < \nu < 10^9$ Hz. For deuterons, this range is shifted by a factor of 0.15 to lower frequencies. This frequency window largely matches the time scale of chain modes of polymers with medium molecular masses.

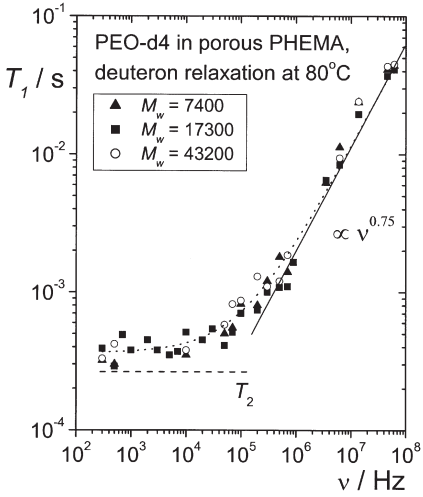

Fig. 22. Frequency dependence of the deuteron spin-lattice relaxation time of perdeuterated PEO confined in 10 nm pores of solid PHEMA at 80 °C.[140] No molecular weight dependence shows up, and the dispersion at high frequencies verifies the law $T_1 \propto M_w^0 \omega^{0.75}$ predicted for limit $(II)_{DE}$ (see Table 1). The low-frequency plateau indicates that the correlation function implies components decaying more slowly than the magnetization relaxation curves, so that the Bloch/Wangsness/Redfield relaxation theory is no longer valid in this regime. The plateau value corresponds to the transverse relaxation time, T_2, extrapolated from the high-field value measured at 9.4 T.

The exceptional frequency and molecular weight dependence for the spin-lattice relaxation time expected for limit $(II)_{DE}$,

$$T_1 \propto M^0 \omega^{3/4} \quad (\omega\tau_s \ll 1 \ll \omega\tau_e), \tag{118}$$

is particularly indicative for the combined "obstruction" and "trapping" effects making reptational segment diffusion in this limit anomalous. Fig. 22 shows the frequency dependence of the deuteron spin-lattice relaxation time of perdeuterated PEO of different molecular weights in a solid PHEMA matrix.[140] In the frequency regime, where the standard Bloch/Wangsness/Redfield relaxation theory is applicable, the law given in Eq. (118) is reproduced as

$$T_1 \propto M_w^{0\pm0.05} \nu^{0.75\pm0.02} \tag{119}$$

where M_w is the weight average molecular weight. The experimental deuteron frequency range in which the dependence given by Eq. (119) was observed as $5 \times 10^5\,\text{Hz} < \nu < 6 \times 10^7\,\text{Hz}$. De Gennes' prediction for limit $(II)_{DE}$ has thus

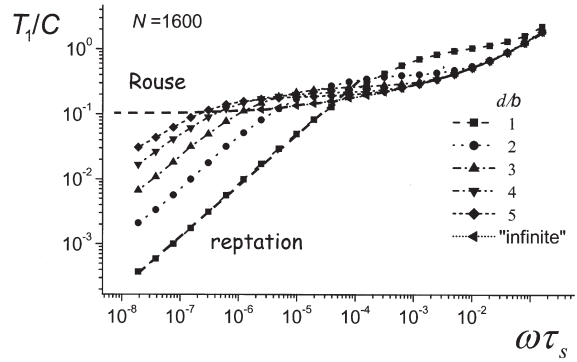

Fig. 23. Spin-lattice relaxation dispersion for a chain of $N = 1600$ Kuhn segments (of length b) confined in randomly coiled tubes with a harmonic radial potential with varying effective diameters d.[19] C is a constant. At low frequencies the curves visualize the crossover from Rouse dynamics depending on the effective tube diameter. The latter case is characterized by a T_1 dispersion proportional to $\omega^{3/4}$.

been verified for polymers confined in artificial tubes in full accordance with the theory. This peculiar frequency dependence characteristically reflects the tube confinement effect as demonstrated analytically by the harmonic radial potential theory and numerically with the aid of Monte Carlo computer simulations.[19] Fig. 23 shows the frequency dependence of the spin-lattice relaxation time for different tube diameters in clear contrast to unconfined Rouse chains.

It can be concluded that polymers confined in randomly coiled pores with diameters less than the Flory radius are governed in the frame of the experimentally accessible ranges by the combined time/frequency/molecular weight dependences given in Table 1 for the tube/reptation model. On the other hand, apart from limit $(IV)_{DE}$[35] none of these combined dependences was ever verified consistently for bulk melts of ''entangled'' polymers in the limits indicated. The term ''entangled'' refers here to molecular weights above the critical value M_c, where free Rouse chain dynamics is supposed to be prevented by strong obstruction of lateral displacements.

10. SPIN DIFFUSION

Immaterial spin diffusion based on Zeeman energy conserving flip-flop processes, that is interchange of spin-up and -down states of dipolar coupled spins, is normally negligible compared to molecular self-diffusion in liquids. However, with viscous systems with little motional averaging of dipolar coupling and with the aid of very strong field gradients, NMR diffusometry is

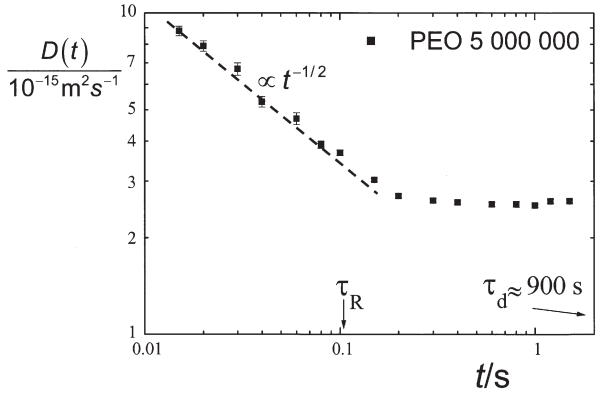

Fig. 24. Time dependent diffusion coefficient of a PEO melt with a weight average molecular weight of 5,000,000.[37] The data were evaluated from the spin echo attenuation curves according to Eq. (26) using $\langle z^2(t)\rangle = 2D(t)t$, where $t \approx \Delta$. Estimated values for the longest Rouse relaxation time τ_R and for the tube disengagement time τ_d are indicated.

able to detect this competing transport mechanism. Spin echoes can be attenuated on this basis just as with any other incoherent displacement process.

Employing the strong fringe-field gradient of a superconducting magnet, it was possible to demonstrate the influence of flip-flop spin diffusion on the echo attenuation of polymer melts indeed.[141] A typical data set is displayed in Fig. 24. In this study, a PEO melt with an extremely large molecular weight, $M_w = 5{,}000{,}000$, was examined. The time dependent diffusion coefficient was evaluated in the low wave number limit, Eq. (36), according to $\langle r^2(t)\rangle = 6D(t)t$. The data plotted in Fig. 24 indicate a regime $D(t) \propto t^{-1/2}$ for $t < \tau_R$ and a plateau for $t \gg \tau_R$. The Rouse relaxation time, τ_R, was evaluated from Eq. (112) using data for the Kuhn segment length and the segment friction coefficient derived from viscoelasticity studies.[142] The plateau appearing for $t > \tau_R$ was shown to be due to flip-flop spin diffusion in Ref. [141]. In this paper, it was demonstrated that the flip-flop spin diffusion effect is reduced by isotopic dilution of the proton spin density, i.e., when intermolecular dipolar coupling is weakened.

As a consequence, the proper evaluation of segment diffusion at long diffusion times turned out to be more complicated than often anticipated. However, even with flip-flop spin diffusion theoretically taken into account, it is not possible to fit the formulas predicted by the tube/reptation model to the experimental data with respect to both the time and molecular weight dependences in a consistent way and without assuming unrealistic parameters.[37]

Flip-flop spin diffusion was also directly detected in a CaF_2 single crystal.[143] In this case, a modified pulsed gradient technique was employed. The

coherence evolution time in solids is strongly limited by extremely short T_2 values due to the absence of motional averaging of dipolar interactions. Unaveraged dipolar interaction, on the other hand, is the prerequisite for flip-flop spin diffusion. The problem was solved by reversing the evolution under dipolar couplings during the free-evolution intervals with the aid of a magic sandwich pulse sequence.[7,144] Two magic sandwiches were placed in the free evolution intervals of a stimulated-echo sequence (i.e., the two τ_1 intervals shown in Fig. 2b). Field gradient pulses were then applied in gaps between the RF pulses and the magic sandwiches. As a result, a modulation grating of the z magnetization arises in the storage interval τ_2 (see Fig. 2) in complete analogy to the ordinary stimulated-echo techniques and the MAGROFI rotating-frame method described in Sections 3.2 and 4.3, respectively. Spin diffusion then tends to blur the grating during the τ_2 interval. The echo signal read out from the grating after evolution in a symmetric magic-sandwich/gradient pulse sequence is then attenuated according to flip-flop spin diffusion (and spin-lattice relaxation) during τ_2.

11. CONCLUDING REMARKS AND OUTLOOK

NMR techniques for diffusion measurements are well established tools for studying molecular motion non-invasively without disturbing the system under investigation. The main principle is to prepare first a non-equilibrium magnetization distribution in the sample and then to follow its evolution. As has been pointed out in Sections 3 and 4, non-equilibrium magnetization distributions can be created in a controlled way either by using gradients of the main magnetic field (B_0 gradients) or of the radiofrequency amplitude (B_1 gradients), respectively.

The time evolution of the magnetization distribution toward equilibrium can be then followed either indirectly by recording spin echoes (Hahn echo, stimulated echo, nonlinear echoes, rotary echo, nutation echo, etc.) or by directly imaging the magnetization distribution after a certain evolution interval. The latter principle can be applied with the MAGROFI technique in the rotating frame (Section 4.4) or as an isotope interdiffusion experiment by laboratory frame imaging as described in Section 8.

The strength of the field gradient is crucial for probing slow diffusion. With pulsed B_0 gradient techniques, strong currents are switched in gradient coils in the magnet. The consequence is a mechanical impulse on the gradient coil each time the current is switched on or off. This may lead to vibrations of the whole probe. Such motions of the sample relative to the gradient coils must be carefully avoided in order to prevent motional artifacts.

Forces are also produced by the magnetic susceptibility of the sample in the presence of a magnetic field gradient. That is, pulsed gradients generate pulsed forces directly on the sample. In order to avoid global sample displacements on

these grounds, the whole system including gradient coil, sample holder and sample must be kept at mechanically fixed positions.[145] This may be difficult in heterogeneous samples with compartments of different magnetic susceptibility. Relative motions are then unavoidable. An example is a granular system loosely filled into a sample tube where field gradient pulses tend to whirl the particles around.

Complications of this sort can be avoided by steady gradients produced by superconducting magnets.[35,38,137] Extremely stable and homogeneous gradients up to 200 T/m have been reported with systems of this sort. There is still the problem to screen off building vibrations from the magnet which might shift the sample relative to the gradient during the measuring intervals. The accuracy required for the position stability may be estimated by the root mean square displacement to be measured during the diffusion time. Assuming a diffusion coefficient of $10^{-15}\,m^2/s$ and a diffusion time of 1 s suggest a root mean square displacement along the field gradient of 45 nm. That is, the material to be studied in this case must be kept fixed relative to the field gradient with a precision much better than 45 nm during 1 s.

It has also been suggested to increase the efficiency of gradient encoding with the aid of multiple-quantum coherences. Corresponding pulse sequences and applications have been published for homonuclear[146,147] as well as heteronuclear spin systems.[148,149] The principle is that n-quantum coherences are dephased by a given gradient n times faster than single quantum coherences. The attenuation exponent of n-quantum coherence transfer echoes[7] is consequently enhanced by a factor of n^2 relative to single quantum coherences.

The use of the B_1 gradient diffusometry methods described in Section 4 has the advantage that mechanical ringing by pulsing of the gradients does not arise, that switching times in the order of microseconds can be readily achieved, and that background gradients due to susceptibility inhomogeneities do not matter. The gradient strengths achieved with special probe geometries can be comparably strong as with pulsed B_0 gradient methods.[52,57] On the other hand, the gradients produced with probe devices such as the toroid cavity is strongly inhomogeneous. This suggests the combination with imaging techniques such as MAGROFI (Section 4.4) where the measurement is carried out with spatial resolution. In principle, even a substantial wave-number range corresponding to different positions in the cavity can be recorded at a time with this technique.

At least from the experimental point of view, the so-called "electrophoretic NMR"[150–152] is a technique closely related with PGSE NMR diffusometry. During RF and field gradients such as those shown in Fig. 2 or Fig. 3, electrostatic potential gradient pulses are applied to ion solution containing samples. One then distinguish incoherent displacements by spin echo attenuation and coherent electrophoretic drift displacements by signal phase shifts. From the drift velocity, the ionic mobility can be deduced, which is of considerable interest because it is characteristic for the ionic species in its

particular environment. Exploiting the chemical-shift selectivity all ionic components can be detected simultaneously.

In porous media saturated with an electrolyte solution the self-diffusion coefficient as well as the electrophoretic ion mobility can be analyzed into short-time (''anomalous'') and long-time ''effective'') components (compare Ref. 153) with the aid of the ordinary PGSE technique and its electrophoretic variant.[154] In this way, the Nernst/Einstein relation which predicts a proportionality of the diffusivity and the ionic mobility was verified for the effective values of these quantities. Moreover, the evaluation of the tortuosity (Eq. (92)) both from time dependent diffusion and mobility measurements yielded the same result.

The electrophoretic drift of ions is to be understood to take place in a static solvent environment. This is to be distinguished from electroosmosis which arises in porous media in the presence of polar surfaces.[155] The result is coherent flow of the solvent driven by the ionic drag. Using the same pulse technique as for ordinary electrophoretic NMR, Ise *et al.*[156] have studied Nafion membranes as they are used in fuel cell technology.

In soft heterogeneous systems such as emulsions the problem arises often how to selectively study a certain component of the system. In this case, the combination of chemical shift selective techniques such as the cyclic cross polarization (CYCLCROP) method[157] with PGSE diffusometry turned out to be most useful. A corresponding study of oil-in-water emulsions using the CYCLCROP–PGSE technique was published by McDonald *et al.*[158]

The NMR diffusometry techniques described above are particularly powerful tools to study anomalous diffusion as defined in Section 2. This in particular refers to the trapping effect occurring with diffusion of particles in random porous media. Examples have been demonstrated in random-site percolation model objects,[122] protein aerogels,[29] and silica fineparticle agglomerates.[28,30] All these studies refer to the relatively long time and length scales of field-gradient NMR diffusometry or even isotope interdiffusion imaging experiments.

On much shorter length and time scales than accessible by these methods anomalous diffusion processes occur that may be even more pronounced. An example is Lévy walks (see Fig. 1b and Ref. [23]) probed by field-cycling NMR relaxometry in the form of ''reorientations mediated by translational displacement'' (RMTD) processes.[159,160] Bychuk and O'Shaughnessy[161] predicted this sort of anomaly for adsorbate diffusion along pore surfaces in the so-called strong-adsorption limit. Very interestingly this peculiar reaction–diffusion problem is connected with a superdiffusive behavior as it was demonstrated in a Monte Carlo computer simulation by Valiullin *et al.*[162]

The utilization of magnetic resonance imaging for diffusion studies has been exemplified above with the MAGROFI technique (rotating-frame imaging; Section 4.4) and with isotope two-compartment interdiffusion measurements (spin density mapping; Section 8.1). There is a third imaging variant that can

be used for the visualization the diffusive displacements. If the diffusing species is paramagnetic or strongly changes the magnetic susceptibility otherwise, the diffusion front is accompanied with a frequency offset of the nuclear magnetic resonance frequency of the solvent nuclei. That is, frequency offset mapping (in a different context also called chemical-shift mapping[7]) can be employed for monitoring the propagation of diffusion fronts. In this way, it was possible to study the uptake of heavy metal ions in alginate gels and other biomaterials in the form of an ion exchange process.[163,164]

Acknowledgements

Financial support by the Alexander von Humboldt foundation and the Deutsche Forschungsgemeinschaft is gratefully acknowledged.

REFERENCES

1. P. T. Callaghan, *Aust. J. Phys.*, 1984, **37**, 359.
2. P. Stilbs, *Prog. Nucl. Magn. Reson. Spectrosc.*, 1987, **19**, 1.
3. J. Kärger, H. Pfeifer and W. Heink, *Adv. Magn. Reson.*, 1988, **12**, 1.
4. W. S. Price, *Annual Reports on NMR Spectroscopy*, G. A. Webb, ed., Academic Press, London, 1996, 51–142.
5. W. S. Price, *Concepts Magn. Reson.*, 1997, **9**, 299.
6. B. Blümich, *NMR Imaging of Materials*, Clarendon Press, Oxford, 2000.
7. R. Kimmich, *NMR Tomography, Diffusometry, Relaxometry*, Springer-Verlag, Berlin, 1997.
8. P. T. Callaghan, *Principles of Nuclear Magnetic Resonance Microscopy*, Clarendon Press, Oxford, 1991.
9. E. Fukushima and S. B. W. Roeder, *Experimental Pulse NMR. A Nuts and Bolts Approach*, Addison-Wesley, Reading, 1981.
10. D. G. Cory and A. N. Garroway, *Magn. Reson. Med.*, 1990, **14**, 435.
11. P. P. Mitra and P. Sen, *Phys. Rev. B*, 1992, **45**, 143.
12. J. E. M. Snaar and H. Van As, *J. Magn. Reson. A*, 1993, **102**, 318.
13. P. T. Callaghan, *J. Magn. Reson. A*, 1995, **113**, 53.
14. O. Södermann and B. Jönsson, *J. Magn. Reson. A*, 1995, **117**, 94.
15. R. Valiullin and V. D. Skirda, *J. Chem. Phys.*, 2001, **114**, 452.
16. P. W. Kuchel, A. Coy and P. Stilbs, *Magn. Reson. Med.*, 1997, **37**, 637.
17. A. M. Torres, A. T. Taurins, D. G. Regan, B. E. Chapman and P. W. Kuchel, *J. Magn. Reson.*, 1999, **138**, 135.
18. M. Sahimi, *Flow and Transport in Porous Media and Fractured Rock*, VCH, Weinheim, 1995.
19. A. Denissov, M. Kroutieva, N. Fatkullin and R. Kimmich, *J. Chem. Phys.*, 2002, **116**, 5217.
20. R. Metzler and J. Klafter, *Phys. Rep.*, 2000, **339**, 1.
21. J. Kärger and D. M. Ruthven, *Diffusion in Zeolites*, John Wiley, New York, 1992.
22. J. Kärger, P. Heitjans, and R. Haberlandt, eds. *Diffusion in Condensed Matter*, Vieweg, Braunschweig, 1998.
23. J. Klafter, M. F. Shlesinger and G. Zumofen, *Physics Today*, 1996, February, 33.
24. J. Kärger, *Phys. Rev. E*, 1993, **47**, 1427.

25. K. Hahn, J. Kärger and V. Kukla, *Phys. Rev. Lett.*, 1996, **76**, 2762.
26. M. Ylihautala, J. Jokisaari, E. Fischer and R. Kimmich, *Phys. Rev. E*, 1998, **57**, 6844.
27. K. K. Mon and J. K. Percus, *J. Chem. Phys.*, 2002, **117**, 2289.
28. F. Klammler and R. Kimmich, *Croatica Chemica Acta*, 1992, **65**, 455.
29. R. Kimmich, F. Klammler, V. D. Skirda, I. A. Serebrennikova, A. I. Maklakov and N. Fatkullin, *Appl. Magn. Reson.*, 1993, **4**, 425.
30. R. Kimmich, S. Stapf, R.-O. Seitter, P. T. Callaghan and E. Khozina, *Mater. Res. Soc. Symp. Proc.*, 1995, **366**, 189.
31. H. C. Torrey, *Phys. Rev.*, 1956, **104**, 563.
32. E. O. Stejskal and J. E. Tanner, *J. Chem. Phys.*, 1965, **42**, 288.
33. J. E. Tanner and E. O. Stejskal, *J. Chem. Phys.*, 1968, **49**, 1768.
34. T. R. Saarinen and C. S. Johnson, *J. Magn. Reson.*, 1988, **78**, 257.
35. R. Kimmich, W. Unrath, G. Schnur and E. Rommel, *J. Magn. Reson.*, 1991, **91**, 136.
36. E. Fischer, R. Kimmich, U. Beginn, M. Möller and N. Fatkullin, *Phys. Rev. E*, 1999, **59**, 4079.
37. E. Fischer, R. Kimmich, N. Fatkullin and G. Yatsenko, *Phys. Rev. E*, 2000, **62**, 775.
38. F. Fujara, B. Geil, H. Sillescu and G. Fleischer, *Z. Phys. B*, 1992, **88**, 195.
39. R. Kimmich, S. Stapf, P. Callaghan and A. Coy, *Magn. Reson. Imaging*, 1994, **12**, 339.
40. R. Kimmich, E. Fischer, P. Callaghan and N. Fatkullin, *J. Magn. Reson. A*, 1995, **117**, 53.
41. F. Grinberg and R. Kimmich, *J. Chem. Phys.*, 1995, **103**, 365.
42. F. Klammler and R. Kimmich, *Phys. Med. Biol.*, 1990, **35**, 67.
43. D. Canet, B. Diter, A. Belmajdoub, J. Brondeau, J. C. Boubel and K. Elbayed, *J. Magn. Reson.*, 1989, **81**, 1.
44. R. Kimmich, B. Simon and H. Köstler, *J. Magn. Reson. A*, 1995, **112**, 7.
45. B. Simon, R. Kimmich and H. Köstler, *J. Magn. Reson. A*, 1996, **118**, 78.
46. D. Canet, *Prog. Nucl. Magn. Reson. Spectrosc.*, 1997, **30**, 101.
47. C. Malveau, B. Diter, F. Humbert and D. Canet, *J. Magn. Reson.*, 1998, **130**, 131.
48. M. Valtier, F. Humbert and D. Canet, *J. Magn. Reson.*, 1999, **141**, 7.
49. R. Kimmich, I. Ardelean, Y.Ya Lin, S. Ahn and W. S. Warren, *J. Chem. Phys.*, 1999, **110**, 3708.
50. I. Ardelean, A. Scharfenecker and R. Kimmich, *J. Magn. Reson.*, 2000, **144**, 45.
51. A. Scharfenecker, I. Ardelean and R. Kimmich, *J. Magn. Reson.*, 2001, **148**, 363.
52. K. Woelk, B. L. J. Zwank, P. Trautner, E. Lehnhof, J. Bargon, R. J. Klingler, Gerald, R. E., II and J. W. Rathke, *J. Magn. Reson.*, 2000, **145**, 276.
53. A. Haase, C. Malloy and G. K. Radda, *J. Magn. Reson.*, 1983, **55**, 164.
54. P. Mafei, P. Mutzenhardt, A. Retournard, B. Diter, R. Raulet, J. Brondeau and D. Canet, *J. Magn. Reson. A*, 1994, **107**, 239.
55. K. Woelk, J. W. Rathke and R. J. Klingler, *J. Magn. Reson. A*, 1993, **105**, 113.
56. K. Woelk, J. W. Rathke and R. J. Klingler, *J. Magn. Reson. A*, 1994, **109**, 132.
57. K. Woelk, *J. Magn. Reson.*, 2000, **146**, 157.
58. M. H. Levitt, *J. Magn. Reson.*, 1982, **48**, 234.
59. K. Woelk and J. W. Rathke, *J. Magn. Reson. A*, 1995, **115**, 106.
60. R. Dupeyre, Ph. Devoulon, D. Bourgeois and M. Decorps, *J. Magn. Reson.*, 1991, **95**, 589.
61. F. Humbert, M. Valtier, A. Retournard and D. Canet, *J. Magn. Reson.*, 1998, **134**, 245.
62. I. Ardelean, R. Kimmich and A. Klemm, *J. Magn. Reson.*, 2000, **146**, 43.
63. C. A. Meriles, D. Sakellariou, H. Heise, A. J. Moulé and A. Pines, *Science*, 2001, **293**, 82.
64. K. Woelk, R. E. Gerald, R. J. Klinger and J. W. Rathke, *J. Magn. Reson. A*, 1996, **121**, 74.
65. D. I. Hoult, *J. Magn. Reson.*, 1979, **33**, 183.
66. G. Deville, M. Bernier and J. M. Delrieux, *Phys. Rev. B*, 1979, **19**, 5666.
67. R. Bowtell, R. M. Bowley and P. Glover, *J. Magn. Reson.*, 1990, **88**, 643.
68. A. S. Bedford, R. Bowtell and R. M. Bowley, *J. Magn. Reson.*, 1991, **93**, 516.
69. I. Ardelean, S. Stapf, D. E. Demco and R. Kimmich, *J. Magn. Reson.*, 1997, **124**, 506.
70. I. Ardelean, R. Kimmich, S. Stapf and D. E. Demco, *J. Magn. Reson.*, 1997, **127**, 217.
71. I. Ardelean, R. Kimmich, S. Stapf and D. E. Demco, *J. Magn. Reson.*, 1998, **132**, 138.

72. I. Ardelean and R. Kimmich, *Chem. Phys. Lett*., 2000, **320**, 81.
73. A. Jerschow, *Chem. Phys. Lett*., 1998, **296**, 466.
74. P. Robyr and R. Bowtell, *J. Magn. Reson. A*, 1996, **121**, 206.
75. I. Ardelean and R. Kimmich, *J. Magn. Reson*., 2000, **143**, 101.
76. I. Ardelean, E. Kossel and R. Kimmich, *J. Chem. Phys*., 2001, **114**, 8520.
77. A. Abragam, *The Principles of Nuclear Magnetism*, Clarendon Press, Oxford, 1961.
78. I. Ardelean and R. Kimmich, *J. Chem. Phys*., 2000, **112**, 5275.
79. R. Bowtell, *J. Magn. Reson*., 1992, **100**, 1.
80. L. E. Drain, *Proc. Phys. Soc*., 1962, **80**, 1380.
81. R. Blinc, J. Dolinsek, G. Lahajnar, A. Sepe, I. Zupancic, S. Zumer, F. Mila and M. M. Pintar, *Z. Naturforsch. Teil A*, 1988, **43a**, 1026.
82. J. C. Ford, F. W. Wehrli and H. W. Chung, *Magn. Reson. Med*., 1993, **30**, 373.
83. J. A. Bertolina, C. H. Durney, D. C. Ailion, A. G. Cuttilo, A. H. Morris and K. C. Goodrich, *J. Magn. Reson*., 1992, **99**, 161.
84. M. E. Smith and S. N. Stuart, *J. Phys. D: Appl. Phys*., 1995, **28**, 229.
85. J. Zhong, R. P. Kennan and J. C. Gore, *J. Magn. Reson*., 1991, **95**, 267.
86. M. D. Hürlimann, *J. Magn. Reson*., 1998, **131**, 232.
87. J. G. Seland, G. H. Sørland, K. Zick and B. Hafskjold, *J. Magn. Reson*., 2000, **146**, 14.
88. R. M. Cotts, M. J. R. Hoch, T. Sun and J. T. Markert, *J. Magn. Reson*., 1989, **83**, 252.
89. L. L. Latour, P. Mitra, R. L. Kleinberg and C. H. Sotak, *J. Magn. Reson. A*, 1993, **101**, 342.
90. G. H. Sørland, B. Hafskjold and O. Herrstad, *J. Magn. Reson*., 1997, **124**, 172.
91. E. J. Fordham, S. J. Gibbs and L. D. Hall, *Magn. Reson. Imaging*, 1994, **12**, 279.
92. L. L. Latour, L. Li and C. H. Sotak, *J. Magn. Reson. B*, 1993, **101**, 72.
93. Y.-Q. Song, *J. Magn. Reson*., 2000, **143**, 397.
94. Y.-Q. Song, S. Ryu and P. N. Sen, *Nature*, 2000, **406**, 178.
95. Y.-Q. Song, *Phys. Rev. Lett*., 2000, **85**, 3878.
96. N. V. Lisitza and Y.-Q. Song, *J. Chem. Phys*., 2001, **114**, 9120.
97. N. V. Lisitza and Y.-Q. Song, *Phys. Rev. B*, 2002, **65**, 1724061.
98. K. R. Brownstein and C. E. Tarr, *J. Magn. Reson*., 1977, **26**, 17.
99. K. R. Brownstein and C. E. Tarr, *Phys. Rev. A*, 1979, **19**, 2446.
100. R. Kimmich, S. Stapf, A. I. Maklakov, V. D. Skirda and E. V. Khozina, *Magn. Reson. Imaging*, 1996, **14**, 793.
101. P. Barie, *Annu. Rep. NMR Spectrosc*., 2000, **41**, 265.
102. J. W. Haus and K. W. Kehr, *Phys. Rep*., 1987, **150**, 263.
103. M. D. Hürlimann, K. G. Helmer, L. L. Latour and C. H. Sotak, *J. Magn. Reson. A*, 1994, **111**, 169.
104. G. Navon, Y.-Q. Song, T. Room, S. Appelt, R. E. Taylor and A. Pines, *Science*, 1996, **271**, 1848.
105. B. M. Goodson, *J. Magn. Reson*., 2002, **155**, 157.
106. R. W. Mair, D. G. Cory, S. Peled, C. H. Tseng, S. Patz and R. L. Walsworth, *J. Magn. Reson*., 1998, **135**, 478.
107. R. W. Mair, G. P. Wong, D. Hoffmann, M. D. Hürlimann, S. Patz, L. M. Schwartz and R. L. Walsworth, *Phys. Rev. Lett*., 1999, **83**, 3324.
108. R. W. Mair, M. D. Hürlimann, P. N. Sen, L. M. Schwartz, S. Patz and R. L. Walsworth, *Magn. Reson. Imaging*, 2001, **19**, 345.
109. O. Geier, S. Vasenkov and J. Kärger, *J. Chem. Phys*., 2002, **117**, 1935.
110. L. Zhao, R. Mulkern, C. Tseng, D. Williamson, S. Patz, R. Kraft, R. L. Walsworth, F. A. Jolesz and M. S. Albert, *J. Magn. Reson. B*, 1996, **113**, 179.
111. M. Bock, *Magn. Reson. Med*., 1997, **38**, 890.
112. B. R. Patyal, J. H. Gao, R. F. Williams, J. Roby, B. Saam, B. A. Rockwell, R. J. Thomas, D. J. Stolarski and P. T. Fox, *J. Magn. Reson*., 1997, **126**, 58.
113. L. Li and C. H. Sotak, *J. Magn. Reson*., 1991, **92**, 411.
114. L. Li and C. H. Sotak, *J. Magn. Reson. B*, 1993, **101**, 8.

115. D. O. Kuethe, A. Caprihan, E. Fukushima and R. A. Waggoner, *Magn. Reson. Med.*, 1998, **39**, 85.
116. L. Z. Wang, A. Caprihan and E. Fukushima, *J. Magn. Reson.*, 1995, **117**, 209.
117. F. D'Orazio, S. Bhattacharja, P. Halperin and R. Gerhardt, *Phys. Rev. Lett.*, 1989, **63**, 43.
118. R. Kimmich and E. Fischer, *J. Magn. Reson. A*, 1994, **106**, 229.
119. R. Valiullin, V. D. Skirda, S. Stapf and R. Kimmich, *Phys. Rev. E*, 1997, **55**, 2664.
120. J. M. Smith, *Chemical Engineering Kinetics*, McGraw-Hill, New York, 1970.
121. S. Wonorahardjo, I. Ardelean and R. Kimmich, in preparation.
122. A. Klemm, R. Metzler and R. Kimmich, *Phys. Rev. E*, 2002, **65**, 021112.
123. M. Sahimi, *Application of Percolation Theory*, Taylor and Francis, London, 1993.
124. D. Stauffer and A. Aharony, *Introduction to Percolation Theory*, Taylor and Francis, London, 1992.
125. A. Kapitulnik, A. Aharony, G. Deutscher and D. Stauffer, *J. Phys. A*, 1983, **16**, L269.
126. R. Orbach, *Science*, 1986, **231**, 814.
127. S. Alexander and R. Orbach, *J. Phys.-Lett. (Paris)*, 1982, **43**, L-625.
128. J. Crank, *The Mathematics of Diffusion*, Clarendon Press, Oxford, 1975.
129. O. J. Poole and D. W. Salt, *J. Phys. A; Math. Gen.*, 1996, **29**, 7959.
130. H. A. Makse, J. S. Andrade and H. E. Stanley, *Phys. Rev. E*, 2000, **61**, 583.
131. S. L. Codd, B. Manz, J. D. Seymour and P. T. Callaghan, *Phys. Rev. E*, 1999, **60**, R3491.
132. J. Koplik, S. Redner and D. Wilkinson, *Phys. Rev. A*, 1988, **37**, 2619.
133. R. Kimmich, A. Klemm, M. Weber and J. Seymour, *Mater. Res. Soc. Symp. Proc.*, 2001, **951**, T2.7.1.
134. P. G. de Gennes, *J. Chem. Phys.*, 1971, **55**, 571.
135. M. Doi and S. F. Edwards, *The Theory of Polymer Dynamics*, Clarendon Press, Oxford, 1986.
136. M. Appel and G. Fleischer, *Macromolecules*, 1993, **26**, 5520.
137. E. Fischer, R. Kimmich and N. Fatkullin, *J. Chem. Phys.*, 1996, **104**, 9174.
138. M. E. Komlosh and P. T. Callaghan, *J. Chem. Phys.*, 1998, **109**, 10,053.
139. N. Fatkullin and R. Kimmich, *Phys. Rev. E*, 1995, **52**, 3273.
140. R. Kimmich, R.-O. Seitter, U. Beginn, M. Möller and N. Fatkullin, *Chem. Phys. Lett.*, 1999, **307**, 147.
141. E. Fischer, R. Kimmich and N. Fatkullin, *J. Chem. Phys.*, 1997, **106**, 9883.
142. W. W. Graessley and S. F. Edwards, *Polymer*, 1981, **22**, 1329.
143. W. Zhang and D. G. Cory, *Phys. Rev. Lett.*, 1998, **80**, 1324.
144. S. Hafner, D. E. Demco and R. Kimmich, *Solid State NMR*, 1996, **6**, 275.
145. N. K. Bär, J. Kärger, C. Krause, W. Schmitz and G. Seiffert, *J. Magn. Reson. A*, 1995, **113**, 278.
146. J. F. Martin, L. S. Selwyn, R. R. Vold and R. L. Vold, *J. Chem. Phys.*, 1982, **76**, 2632.
147. P. Mutzenhardt and D. Canet, *J. Chem. Phys.*, 1996, **105**, 4405.
148. B. E. Chapman and P. W. Kuchel, *J. Magn. Reson. A*, 1993, **102**, 105.
149. M. Liu, Xi-An Mao, C. Ye, J. K. Nicholson and J. C. Lindon, *Mol. Phys.*, 1998, **93**, 913.
150. M. Holz and C. Müller, *Ber. Bunsenges. Phys. Chem.*, 1982, **86**, 141.
151. F. M. Coveney, J. H. Strange, A. L. Smith and E. G. Smith, *Colloids Surf.*, 1989, **36**, 193.
152. C. S. Johnson, Jr., *Encyclopedia of NMR*, D. M. Grant and R. K. Harris, eds., John Wiley, Chichester, 1995, 1886.
153. T. M. de Swiet and P. N. Sen, *J. Chem. Phys.*, 1996, **104**, 206.
154. S. R. Heil and M. Holz, *J. Magn. Reson.*, 1998, **135**, 17.
155. R. F. Probstein, *Physicochemical Hydrodynamics*, Wiley, New York, 1994.
156. M. Ise, K. D. Kreuer and J. Maier, *Solid State Ionics*, 1999, **125**, 213.
157. C. Kunze, R. Kimmich and D. E. Demco, *J. Magn. Reson. A*, 1993, **101**, 277.
158. P. J. McDonald, E. Ciampi, J. L. Keddie, M. Heidenreich and R. Kimmich, *Phys. Rev. E*, 1999, **59**, 874.
159. S. Stapf, R. Kimmich and R.-O. Seitter, *Phys. Rev. Lett.*, 1995, **75**, 2855.
160. T. Zavada and R. Kimmich, *J. Chem. Phys.*, 1998, **109**, 6929.

161. O. V. Bychuk and B. O'Shaughnessy, *J. Phys. II*, 1994, **4**, 1135.
162. R. Valiullin, R. Kimmich and N. Fatkullin, *Phys. Rev. E*, 1997, **56**, 4371.
163. N. Nestle and R. Kimmich, *Colloids Surf. A*, 1996, **115**, 141.
164. N. Nestle and R. Kimmich, *Biotechnol. Bioeng.*, 1996, **51**, 538.
165. A. Leventis, G. Papavassiliou, M. Fardis, F. Milia, E. Chaniotakis, J. Dolinsek and T. Apih, *J. Chem. Phys.*, 2000, **113**, 7621.
166. N. Fatkullin, R. Kimmich and H. W. Weber, *Phys. Rev. E*, 1993, **47**, 4600.
167. P. N. Sen, L. M. Schwartz, P. P. Mitra and B. J. Halperin, *Phys. Rev. B*, 1994, **49**, 215.
168. P. P. Mitra, P. N. Sen and L. M. Schwartz, *Phys. Rev. B*, 1993, **47**, 8565.

This Page Intentionally Left Blank

Density Functional Theory and its Application to Nuclear Magnetic Resonance Shielding Constants

PHILIP J. WILSON

Department of Chemistry, University of Edinburgh, West Mains Road, Edinburgh EH9 3JJ, UK

ANNUAL REPORTS ON NMR SPECTROSCOPY
VOLUME 49 ISSN 0066-4103

An overview of the key methodological developments within the framework of density functional theory that have led to an improved description of NMR shielding constants is presented. The performances of standard exchange–correlation functionals are assessed, and possible causes for their shortcomings and promising new routes for their improvement are discussed. In particular, the role of the current density, self-interaction, exact orbital exchange, and the exchange–correlation potential are highlighted. Relativistic, rovibrational and intermolecular effects are also important factors that must be taken into account in order to provide a more meaningful comparison with experiment. Density functional approaches for the inclusion of these important effects in the NMR shielding calculations are also presented. Recent developments in wavefunction-based ab initio methods and applications are also highlighted.

1. INTRODUCTION

Since its discovery in 1945, nuclear magnetic resonance (NMR) spectroscopy[1,2] has become one of the most powerful instrumental techniques for the characterisation of the structure and dynamics of molecular systems. It has had a major impact in many aspects of science, especially in the areas of chemistry, biology, the materials and food sciences, as well as medical physics. As well as providing a viable alternative to X-ray methods in providing important structural information, the experimental NMR shielding data also offers a critical test for the quality of the NMR theoretical methods. An increasing library of shielding tensor data is becoming available as a result of new advances in high-resolution NMR technology, especially in the solid phase through the combination of techniques such as cross-polarisation, magic angle spinning, and homonuclear decoupling. Since the assignment of the NMR spectrum is often non-trivial (especially for larger and more complex systems), theoretical predictions of the spectral parameters of NMR spectroscopy have proved invaluable in aiding the assignment of problematic resonances in experimental NMR spectra. Theoretical information about the NMR shielding constants as well as the NMR indirect spin–spin coupling constants[3] would provide a more complete description of the NMR spectra. In this review, only the shielding constants are discussed.

The routine and efficient computation of NMR shielding constants has only been viable in the last decade even though the theoretical framework for determining these properties has been available since its fundamental formulation.[4] This has arisen from the new advances in computer power and continuing progress in the development and application of more accurate and reliable quantum-chemical methodologies. The wider availability of these methods in commercial and academic electronic structure software

packages is now proving beneficial in a wide range of NMR related applications.

For the quantum chemist, the accurate determination of NMR shielding constants represents a difficult and important challenge. Apart from the problem of gauge-origin dependence for magnetic properties, and the importance of relativistic effects in heavy nuclei, the development of cost-effective approaches to accurately describe electron-correlation effects in computationally demanding systems remains key. Hartree–Fock theory is known to be unreliable and fails to predict accurate shielding constants for systems containing significant electron-correlation effects. Since an accurate description of electron-correlation effects is crucially important for the accurate determination of NMR shielding constants, this article will review those important methodological developments that go beyond the single determinant Hartree–Fock level of theory. Wavefunction-based *ab initio* methods and density functional theory (DFT) represent the most widely used quantum chemical methods for describing these important effects. However, the high computational cost of the high-level correlated *ab initio* methods restricts their application to small systems only (at most 5–10 heavy atoms). Although medium-sized molecules are accessible by Moller–Plesset perturbation theory, it has been shown to be unreliable for systems containing significant electron-correlation effects and low-lying excited states. DFT methods represent an efficient alternative to these conventional *ab initio* methods because electron-correlation is implicitly included via the exchange–correlation functional.

In contrast to conventional wavefunction-based methods where there is a well-defined route for the systematic improvement in describing electron-correlation, in DFT no similar route is available because the form of exact exchange–correlation density functional remains unknown. To meet this challenge, the DFT community is constantly evolving new methodologies and as a result the central role of DFT in quantum chemistry is now well established for ground state properties. More recently it has also been shown to be a useful tool for the determination of a variety of electric and magnetic properties. For the latter, most progress has been made towards the accurate determination of NMR shielding constants. This review will discuss the key methodological developments within the framework of DFT that have led to an improved description of NMR shielding constants. Several articles have appeared in recent years that review DFT related NMR studies.[5–11] Recent methodological developments and applications in wavefunction-based *ab initio* calculations for the prediction of NMR shielding constants will also be included. It is not intended to be an exhaustive review but instead will highlight those studies that are most likely to have an impact on the theoretical DFT-NMR community. Several comprehensive reviews in this area have been published in recent years.[8,9,11]

2. NMR SHIELDING CONSTANTS AND EXPERIMENT

2.1. The resonance condition

For an atom or molecule in the presence of an applied static external magnetic field, B_0, the energy levels measured in NMR spectroscopy for nucleus K are the spin eigenstates of the nuclear magnetic moment μ_K

$$E = -\mu_K \cdot B_0 \tag{1}$$

Due to the shielding of nucleus K by the surrounding electrons, the magnetic field experienced by this nucleus, B_{loc}, is different to B_0

$$B_{loc} = B_0 + B_{ind} \tag{2}$$

where the induced field is defined as

$$B_{ind} = -\sigma_K \cdot B_0 \tag{3}$$

The energy correction and the splitting of the energy levels in the presence of B_0 is

$$E = -\mu_K \cdot B_{loc} - \mu_K(1 - \sigma_K)B_0 \tag{4}$$

2.2. The NMR shielding tensor

The magnitude and orientation dependence of σ_K, is described by a second-rank tensor (a 3×3 matrix). It is a molecular electronic property that describes the difference in shielding between the bare nucleus K and the same nucleus in the species of interest. Within the framework of a principal axis system, where all the off-diagonal elements vanish, the six independent components describing the magnitude of the diagonal tensor elements and their orientations (represented as eigenvalues or Euler angles) will vary as a function of the orientation of the molecular system with respect to the external magnetic field (relative to an arbitrary frame). The principal tensor components, σ_{ii} can be combined in several ways—although there is still no clear 'standard convention' amongst NMR experimentalists—in this review the following definitions will be used. For σ_{ii} such that $\sigma_{\alpha\alpha} > \sigma_{\beta\beta} > \sigma_{\gamma\gamma}$, the general definition of the isotropic shielding constant is

$$\sigma_{iso} = \tfrac{1}{3}\,\mathrm{tr}(\sigma_{ii}) \tag{5}$$

or for a linear or symmetric top molecule it can be more conveniently defined as

$$\sigma_{\mathrm{iso}} = \tfrac{1}{3}(\sigma_{\parallel} + 2\sigma_{\perp}) \tag{6}$$

where $\sigma_{\parallel}$ and $\sigma_{\perp}$ are the shielding tensor components parallel and perpendicular to the principal molecular axis, respectively. In this review, a more positive absolute isotropic shielding means a greater shielding (i.e., the resonances are more upfield). The general definition for the anisotropic shielding constant is

$$\Delta\sigma = \sigma_{\alpha\alpha} - \tfrac{1}{2}(\sigma_{\gamma\gamma} + \sigma_{\beta\beta}) \tag{7}$$

or for a linear or symmetric top molecule the definition reduces to

$$\Delta\sigma = \sigma_{\parallel} - \sigma_{\perp} \tag{8}$$

2.3. Absolute shielding scales and chemical shifts

The existence of an experimental absolute shielding scale for nucleus K provides the most rigorous and thorough assessment of the theoretical method for predicting σ_{K}. This is possible when at least one molecule containing the nucleus of interest has had its absolute shielding measured.[12] The most accurate way to obtain absolute shielding scales is to combine spin–rotation constant data (determined from microwave experiments[13,14] and molecular beam experiments[15,16]) with theoretically determined diamagnetic shieldings.[14] The accuracy of these scales critically depends on the quality of both the experimental and theoretical data supplied. Although accurate absolute shielding scales have been determined for a range of lighter nuclei,[17–24] for heavier elements,[25,26] particularly transition metals, accurate absolute shielding scales are still rare. In these systems, the theoretical approximations used to describe relativistic corrections to the diamagnetic shielding can significantly affect the accuracy of the absolute shielding scales.[27]

Since it is not possible to measure the absolute magnetic shielding directly, experimentalists instead use a quantity called the chemical shift defined as the difference in shielding between the nucleus K in the species under investigation σ_{K}, and the shielding of the same nucleus in a reference compound $\sigma_{\mathrm{K}}(\mathrm{ref.})$:

$$\delta_{\mathrm{K}} = \sigma_{\mathrm{K}}(\mathrm{ref.}) - \sigma_{\mathrm{K}} \tag{9}$$

Although most calculations are performed on gas-phase (*in vacuo*) species, relatively little gas-phase experimental data is available (especially for heavier

nuclei). In reality, the bulk of experimental NMR data correspond to chemical shifts determined in solution and solid state. The theoretical determination of chemical shifts rather than absolute shieldings provides a less rigorous way of quantifying the calculated shielding constants. It can only really be expected to reproduce the observed experimental *trends* in carefully chosen series of molecules where many of the factors influencing the absolute shieldings will cancel. In reality, for a meaningful comparison between theory and experimental condensed phase NMR data, rovibrational and intermolecular effects must be taken into consideration. These important effects will be discussed in more detail in Sections 7 and 8. A common, although from a rigorous theoretical viewpoint unsatisfactory approach is the use of linear scaling methods to convert the calculated absolute shieldings into chemical shift predictions.[28–30] In several instances, correlation with experiment remains disappointing even after scaling.[28,31,32]

3. THEORETICAL BACKGROUND

In DFT, the ground electronic state of a system is represented as a functional of the electronic density. In principle, a knowledge of this density is all that is required to determine *all* the properties of the system.[33] The most important quantity in DFT is the exchange–correlation energy E_{XC} that describes all the non-classical contributions to the electronic energy. Since the exact exchange–correlation energy functional is unknown, approximations to it can be obtained by solving the Kohn–Sham equations. They represent the most popular approach in DFT and involve solving the Schrödinger equation within the framework of Hartree–Fock theory but replacing the *orbital* exchange potential term with the exchange–correlation potential (which is now a function of the density).

3.1. Kohn–Sham density functional theory

In Kohn–Sham DFT[33,34] the non-interacting N-electron reference system, whose wavefunction is a single Slater determinant formed from a set of one-particle Kohn–Sham orbitals $\{\varphi_p\}$, and whose density

$$\rho(\boldsymbol{r}) = \sum_{j}^{N} \varphi_j^2(\boldsymbol{r}) \tag{10}$$

is the same as that of the real interacting system. In most implementations, the one-electron Kohn–Sham equations are derived by minimising the total

electronic energy with respect to the Kohn–Sham orbitals, giving in the general case

$$\left(T_s + \upsilon_{ext}(\boldsymbol{r}) + \upsilon_J(\boldsymbol{r}) + \upsilon_{XC}(\boldsymbol{r}) - \xi/2 \int \mathrm{d}\boldsymbol{r}' \, \frac{\rho^1(\boldsymbol{r}, \boldsymbol{r}')}{|\boldsymbol{r} - \boldsymbol{r}'|} \, P_{\boldsymbol{r}\boldsymbol{r}'} - \varepsilon_p\right)\varphi_p(\boldsymbol{r}) = 0 \quad (11)$$

T_s is the exact kinetic energy of the non-interacting reference system

$$T_s = -\tfrac{1}{2}\sum_j^N \langle\varphi_j(\boldsymbol{r})|\nabla^2|\varphi_j(\boldsymbol{r})\rangle \quad (12)$$

$\upsilon_{ext}(\boldsymbol{r})$ and $\upsilon_J(\boldsymbol{r})$, denote the external, and coulomb (Hartree) potentials, respectively. The orbital exchange ξ is written in terms of the one density $\rho^1(\boldsymbol{r}, \boldsymbol{r}')$ and the electron interchange operator $P_{\boldsymbol{r}\boldsymbol{r}'}$. $\upsilon_{XC}(\boldsymbol{r})$ is the multiplicative potential associated with $E_{XC}[\rho]$

$$E_{XC}[\rho] = \int \rho(\boldsymbol{r})[F_{XC}(\rho(\boldsymbol{r}); \nabla\rho(\boldsymbol{r}); \ldots)] \, \mathrm{d}\boldsymbol{r} \quad (13)$$

The exchange–correlation energy is the fundamental quantity in Kohn–Sham DFT. It contains not only the non-classical effects of self-interaction correction (SIC), exchange and correlation, but also the residual part of the true kinetic energy not included in T_s. The quantities $\{\varepsilon_p\}$ are the corresponding one-particle Kohn–Sham eigenvalues, or orbital energies.

3.2. The NMR shielding equations

The shielding tensor σ_K is a second-order response property involving magnetic field and nuclear magnetic moment perturbations. The energy correction equation (4) corresponds to the quadratic term in a Taylor expansion of the molecular energy with respect to B_0 and μ_K

$$E(B_0, \mu_K) = E(0) + \sum_j \sum_i (\mathrm{d}^2E/\mathrm{d}B_j \, \mathrm{d}\mu_{Ki})_{B,\,\mu_{Ki}=0} B_j \mu_{Ki} + \cdots \quad (14)$$

The shielding for nucleus K is the second derivative of the electronic energy with respect to a static external magnetic field and nuclear magnetic moment, and is expressed by the second-rank tensor σ_k

$$\sigma_k = (\mathrm{d}^2E/\mathrm{d}B_j \, \mathrm{d}\mu_{Ki})_{B,\,\mu_A=0} \quad (15)$$

For a magnetic field B

$$B = \nabla \times A \quad (16)$$

$\boldsymbol{A}$ is the vector potential associated with the nucleus K defined as

$$\boldsymbol{A} = \tfrac{1}{2}(B \times \boldsymbol{r}) \tag{17}$$

and the perturbed one-electron Hamiltonians are

$$h_1 = B \cdot m \tag{18}$$

$m = -\frac{1}{2}\, l$, where l is the angular momentum operator,

$$h_2 = \tfrac{1}{8}|B \times \boldsymbol{r}|^2 \tag{19}$$

This response is determined from a set of coupled-perturbed equations

$$\sum_{bj} (\mathbf{H}_2)_{ai,bj} \cdot C^{\alpha}_{bj} = -l^{\alpha}_{bj} \tag{20}$$

where C^{α}_{bj} represents the linear response of the Kohn–Sham orbitals to the applied magnetic field

$$\psi_j = \psi^0_j + iB^{\alpha} \sum C^{\alpha}_{bj}\psi^0_b \tag{21}$$

where $(\mathbf{H}_2)_{ai,bj}$ is the magnetic hessian matrix

$$(\mathbf{H}_2)_{ai,bj} = (\varepsilon_b - \varepsilon_j)\delta_{ai,bj} + \xi[(bj|ai) - (bi|aj)] \tag{22}$$

and

$$l^{\alpha}_{bj} = (b|l^{\alpha}|\, j) \tag{23}$$

is the angular momentum integral matrix. When $\xi \neq 0$ the functional in Eq. (11) is a hybrid functional. In this case the Kohn–Sham operator is non-multiplicative due to the operator $P_{\boldsymbol{rr}'}$, and the magnetic hessian matrix (22) is non-diagonal. It follows that the coupled-perturbed equations must be solved and so the approach is commonly known as 'coupled'. When $\xi = 0$ the functional (11) reduces to a non-hybrid functional (i.e., LDA, GGA). In this case the Kohn–Sham operator is multiplicative (there is a well-defined exchange–correlation potential at each point in space) and the magnetic hessian is diagonal. In this case the linear response of the Kohn–Sham orbitals is simply given by

$$C^{\alpha}_{bj} = \frac{-l^{\alpha}_{bj}}{(\varepsilon_b - \varepsilon_j)} \tag{24}$$

and the approach is commonly referred to as 'uncoupled'.

The expressions for the NMR shielding tensors (in atomic units) for the diamagnetic shielding term are

$$\sigma_{\mathrm{d}}^{\mathrm{K}\alpha\beta} = \sum_{j} (\, j|(\boldsymbol{r}\cdot\boldsymbol{r}_{\mathrm{K}}\delta^{\alpha\beta} - r^{\alpha}r_{\mathrm{K}}^{\beta})r_{\mathrm{A}}^{-3}|\, j) \tag{25}$$

and for the paramagnetic shielding tensors

$$\sigma_{\mathrm{p}}^{\mathrm{K}\alpha\beta} = -\sum_{bj} C_{bj}^{\alpha}((\, j|l_{\mathrm{K}}^{\beta}r_{\mathrm{A}}^{-3}|b) + (b|l_{\mathrm{K}}^{\alpha}r_{\mathrm{A}}^{-3}|j)) \tag{26}$$

or in the uncoupled approximation

$$\sigma_{\mathrm{p}}^{\mathrm{K}\alpha\beta} = -\sum_{bj} \frac{(b|l^{\alpha}|\, j)(\, j|l_{\mathrm{K}}^{\beta}r_{\mathrm{A}}^{-3}|b) + (b|l_{\mathrm{K}}^{\alpha}r_{\mathrm{A}}^{-3}|\, j)(\, j|l^{\beta}|b)}{(\varepsilon_b - \varepsilon_j)} \tag{27}$$

Within DFT, the determination of NMR shielding constants is particularly attractive because there is no explicit dependence on the exchange–correlation integrand F_{XC} (unlike other response properties such as polarisabilities, excitation energies, etc.). Instead, the shielding equations simply depend only upon the Kohn–Sham orbitals and eigenvalues. However, in the presence of a magnetic field (with an associated vector potential) the original Hohenburg–Kohn theorem (with an associated scalar potential) is no longer valid and therefore must be generalised.

3.3. The current-density in DFT

In the presence of a static magnetic field, the exchange–correlation energy is a universal functional that now explicitly depends both on the density and the magnetic field (the local magnetic fields induced by the orbital currents cannot be described by the density alone). This generalisation of the original Hohenburg–Kohn theorem is known as current-density DFT (CDFT).[35]

For a closed-shell system the Kohn–Sham energy expression (13) now depends on the exchange–correlation energy defined as

$$E_{\mathrm{XC}}[\rho, \boldsymbol{j}_{\mathrm{p}}] = \int F_{\mathrm{XC}}(\rho(\boldsymbol{r}), \nabla\rho(\boldsymbol{r}), \ldots, \boldsymbol{j}_{\mathrm{p}}(\boldsymbol{r}), \ldots)\, \mathrm{d}\boldsymbol{r} \tag{28}$$

where ρ is the density and $\boldsymbol{j}_{\mathrm{p}}$ is the paramagnetic current density defined as

$$\boldsymbol{j}_{\mathrm{p}}(\boldsymbol{r}) = \frac{-i\hbar}{m_{\mathrm{e}}} \sum_{j} (\varphi_j^{*}(\boldsymbol{r})\nabla\varphi_j(\boldsymbol{r}) - \nabla\varphi_j^{*}(\boldsymbol{r})\varphi_j(\boldsymbol{r})) \tag{29}$$

On a rigorous theoretical basis, within Kohn–Sham DFT, the exact density functional appropriately generalised to include the vector potential, would yield the exact current and electron densities.[36,37] However, for a functional depending locally on $\rho(\boldsymbol{r})$ and $\boldsymbol{j}_{\mathrm{p}}(\boldsymbol{r})$, the theory is not gauge-invariant (only the total current density $\boldsymbol{j}$ is gauge-invariant). The exchange–correlation functional was formulated to give gauge-invariant VRG theory expressed as a functional of $\rho(\boldsymbol{r})$ and the gauge-invariant variable $\upsilon(\boldsymbol{r})$,

$$E_{\mathrm{XC}}[\rho, \boldsymbol{j}_{\mathrm{p}}] = E_{\mathrm{XC}}[\rho, \upsilon] \tag{30}$$

with

$$\upsilon(\boldsymbol{r}) = \nabla \times (\boldsymbol{j}_{\mathrm{p}}/\rho(\boldsymbol{r})) \tag{31}$$

An approximate expression for the current-dependent exchange–correlation energy $E_{\mathrm{XC}}[\rho, \upsilon]$ was used:

$$E_{\mathrm{XC}}^{\mathrm{VRG}}[\rho, \upsilon] = E_{\mathrm{XC}}[\rho] + \int g(\rho)|\upsilon(\boldsymbol{r})|^2 \, \mathrm{d}\boldsymbol{r} \tag{32}$$

and

$$g(\rho) = \frac{m_{\mathrm{e}} k_{\mathrm{f}}(\boldsymbol{r})}{24\pi^2}((\chi_{\mathrm{L}}/\chi_{\mathrm{L}}^0) - 1) \tag{33}$$

χ_{L} is the Landau orbital magnetic susceptibility, χ_{L}^0 the Landau non-interacting orbital susceptibilty, and $k_{\mathrm{f}}(\boldsymbol{r}) = (3\pi^2\rho(\boldsymbol{r}))^{1/3}$ represents the Fermi momentum.

The local form of $g(\boldsymbol{r})$ and $\rho(\boldsymbol{r})$ means the VRG current-density functional is only really applicable for systems where there is a slowly varying current in regions of high uniform density (i.e., the homogeneous electron gas). For molecular systems, where high and low density regions are present, the VRG current-density functional represents an even cruder approximation.

Within the VRG-CDFT approximation, a local exchange–correlation functional which depends on both the electron density $\rho(\boldsymbol{r})$ and the paramagnetic current density $\boldsymbol{j}_{\mathrm{p}}(\boldsymbol{r})$ has been implemented.[38] CDFT-GIAO-NMR shieldings in several small molecules containing first-row atoms (HF, H_2O, F_2, CH_4, N_2, and CO) were calculated. Overall, the current-dependence provided a deshielding effect on the calculated shieldings, thus worsening their accuracy with experiment. Whilst this deshielding effect was observed to be negligible in the singly bonded species (HF, H_2O, etc.), more significant deshielding resulted from stronger paramagnetic currents induced by the magnetic field perpendicular to the bond axes in CO and N_2.

Since the effect of the current-dependence of the exchange–correlation functional on the NMR shielding constant predictions remains unclear, further investigations that go beyond the local density approximation (LDA) (GGA

current-density functionals have been developed but no NMR shielding results have been presented yet[39]) and include heavier nuclei (especially transition metals) will be crucially important. In addition to providing insight into the physics of the current-density effects in different molecular environments it will also provide a better understanding of the *limiting* performance of approximate DFT methods which do not have any current-density dependence. The use of orbitals and eigenvalues in the NMR shielding equations that can be regarded as good approximations to the *exact* Kohn–Sham quantities—in the absence of a magnetic field—have provided an estimate of the limiting performance of DFT methods.[40]

In contrast to the above CDFT method that solves the Kohn–Sham equations in a *vector potential*, an alternative approach has been developed whereby local energy functionals depend on the *magnetic field* and the electron density. This approach, named magnetic field density functional theory (BDFT), has been applied to the prediction of some rare-gas and proton NMR shieldings with promising results.[41,42]

3.4. Basis sets and the gauge-origin problem

In any *ab initio* calculation, in the limit of a complete basis set all gauge-origin methods converge to the same result. In reality, since finite basis sets are utilised in the calculation the particular basis set/gauge-origin combination must be chosen carefully in order to obtain a balance between accuracy and computational cost. Compared to the *ab initio* methods which include dynamical electron-correlation effects, the basis set requirements for DFT methods are generally more modest since an explicit description of the coulomb hole is not required.[8] However, the necessity to accurately describe the magnetic-field perturbations means the NMR shielding calculations are ultimately very sensitive to the quality of the basis set and gauge-origin method employed. The effect of basis set size and the treatment of the gauge-origin problem on the NMR shielding constants (and chemical shifts) have been investigated in several studies by comparing the convergence properties between various DFT methods and Hartree–Fock theory.

The main disadvantage of popular basis sets in use today from an NMR perspective is that they are energy-optimised and therefore concentrate on optimising the basis functions associated with the inner-shell electrons since they account for the majority of the total energy. The calculated diamagnetic shielding term for a particular nucleus under investigation remains almost invariant to changes in its molecular electronic environment (this term is dominated by contributions from the inner-shell electrons). Therefore, from a basis set perspective, the accurate determination of the shielding constant/chemical shift requires large, flexible basis sets that are capable of describing the valence and virtual orbitals that affect the paramagnetic shielding term.

The most widely used basis sets in all-electron DFT-NMR calculations utilise contracted Gaussian-type orbitals (CGTOs) that describe the core atomic orbitals with a particular contraction scheme and include two (split-valence) or three (triple-zeta) valence functions for each valence atomic orbital. Slater-type orbitals (STOs) have also been utilised to a lesser extent. In heavy atom systems involving a large number of electrons, the computational effort can be reduced by representing the inner shells by effective core potentials (ECPs). As a result, only the valence electrons are treated in the all electron calculations. This approach can still provide satisfactory correlation with experiment but the magnitude of the absolute shieldings can be significantly different to experiment.[43] This discrepancy arises from the incorrect behaviour of the molecular orbitals derived from ECPs at distances close to the nucleus (i.e., their values are too small). As a result, the paramagnetic term, containing an r^{-3} dependence, is significantly underestimated. ECPs can also approximately account for relativistic effects (RECPs) (see Section 4.4). In addition, plane-wave basis sets have also been used in condensed matter calculations.[44]

Variation in basis-set quality can lead to very different NMR shielding results. In general, larger basis sets produce results of better quality (although there are exceptions[45]), as seen in a recent study where the NMR shielding calculations have been extrapolated to the large basis set limit for a series of basis sets within the framework of Hartree–Fock theory and DFT.[46] As general rule of thumb, accurate predictions of isotropic and anisotropic NMR shielding constants require a basis set of at least triple-zeta quality, with enough flexibility in the outer-core inner-valence regions.[8,47] In addition, they should contain at least one set of polarisation functions (for example, up to 3d basis functions are required for the central atom in first-row hydrides while for second-row hydrides it is necessary to include 4d and 5d basis functions.[48] The triple-zeta polarisation basis sets such as 6-311+ G(2d,p) (or the smaller 6-31G(d) basis commonly used in larger systems) have proved popular in DFT-NMR studies, although the larger and more flexible IGLO-III and IGLO-IV basis sets[49,50] are more reliable, though of course more expensive.

From a gauge-origin perspective, the accuracy of the NMR shielding calculations critically depends on the choice of gauge-origin (in conjunction with the basis set). For example, the placement of the gauge origin at a particular centre may be preferential in order to preserve molecular symmetry and thus the magnetic selection rules.[51] The vast majority of magnetic property calculations utilise the Gauge-Including Atomic Orbital (GIAO) method because it provides the optimum route to overcome the gauge-origin problem.[52–60] The GIAO method uses the following explicit field-dependent basis functions that represent the first-order solutions for the one-electron, one-centre, uniform magnetic field problem:

$$\chi_\mu(\boldsymbol{B}) = \exp[-(i/2c)(\boldsymbol{B} \times \boldsymbol{R}_\mu) \cdot \boldsymbol{r}]\chi_\mu(\boldsymbol{0}) \tag{34}$$

where $\boldsymbol{R}_\mu$ is the position vector of the basis function χ_μ and $\chi_\mu(\mathbf{0})$ denotes the usual field-independent basis functions. In contrast, other gauge methods such as the Individual Gauges for Localised Orbitals (IGLO)[61–63] and the Localised Orbital/Local Origin (LORG) gauge[64] expand the first-order perturbation of the wavefunctions in a set of localised *molecular* (rather than atomic) orbitals with individual gauge origins at the centroid of the orbitals. Several other gauges have also been used in conjunction with DFT-NMR studies. The Continuous Set of Gauge Transformations (CSGT) method[65–68] achieves gauge-invariance by accurately calculating the induced first-order electronic current density by performing a gauge transformation for each point in space. The method of Individual Gauges for Atoms in Molecules (IGAIM)[65] uses a separate nuclear centred gauge origin for each atom in a molecule.

At both the Hartree–Fock and DFT levels, the GIAO method has been observed to suffer less degradation in quality with decreasing basis set size compared to the other gauge-origin methods for a variety of different nuclei in a wide range of systems highlighted in the following studies (GIAO versus [Gauge method]): IGLO;[63,69–71] LORG;[47] CSGT;[60] IGAIM.[72,73]

The full potential of the GIAO-DFT-NMR approach therefore lies in its ability to describe larger chemically and biologically important systems where high-level wavefunction-based *ab initio* methods are prohibitively expensive. For example, some of the systems studied using DFT-NMR methods include macromolecules, chlorophylls, peptides, porphyrins, antibiotics, proteins, nucleic acids, and fullerenes.[7,74–81]

4. ASSESSMENT OF THE EXCHANGE–CORRELATION FUNCTIONALS

The large number of exchange–correlation functionals that have been developed reflects the fact that there is no systematic route for the improvement of the approximate exchange–correlation functional even though several properties (sum rules, scaling properties and asymptotic properties) of the exact exchange–correlation functional are known and can be satisfied.[82] Some are purely mathematical and largely parameter-free, based on the uniform electron gas description and some of the properties of the exact exchange–correlation functional. Others involve parameters optimised in a more semi-empirical approach. The existing approximate exchange–correlation functionals have been conveniently classified into five main categories that become increasingly more sophisticated as they build upon the properties of the previous category:[83]

1. *Local density approximation* (LDA)[33,34] based on the uniform electron gas. This approximation combines Slater exchange[84] and the Vosko–Wilk–Nusair correlation functional (usually expression 5).[85]

2. *Generalised gradient approximation* (GGA). The exchange–correlation energy E_{XC} now has an explicit dependence on the gradient of the density approximated by a local $F_{XC}(\rho, \nabla\rho)$ in the general form $E_{XC} = \int \rho^{4/3} g(s^2)\, dr$, where $g(s^2)$ is a function of the dimensionless reduced gradient density $s = |\nabla\rho|/\rho^{4/3}$.
3. *Meta-GGAs*. The exchange–correlation energy for this 'beyond GGA' functional, $E_{XC} = \int F_{XC}(\rho, \nabla\rho, \nabla^2\rho, \tau)$, now has an explicit dependence on the Laplacian of the density, $\nabla^2\rho$, or the kinetic energy density, $\tau = \sum_j (\nabla\varphi_j)^2$.
4. *Exact exchange and compatible correlation*. The GGA and beyond GGA functionals now include an explicit dependence on the occupied orbitals. The most popular functionals are the hybrid functionals that include a fraction of exact orbital (Hartree–Fock) exchange ξ

$$E_{XC} = E_{CONT} - \xi/4 \int\int \frac{|\rho^1(\boldsymbol{r}, \boldsymbol{r}')|^2}{|\boldsymbol{r} - \boldsymbol{r}'|}\, d\boldsymbol{r}\, d\boldsymbol{r}', \tag{35}$$

   where E_{CONT} is the continuum, GGA or beyond GGA, functional.
5. *Exact exchange and exact partial correlation*. Includes an explicit dependence on the unoccupied orbitals and represents a fully non-local functional.

At the present time, the author is only aware of exchange–correlation functionals in the categories 1, 2 and 4 that have been utilised in NMR shielding studies.

An up-to-date assessment of the performance of the various conventional exchange–correlation functionals currently in use today will follow. Trends in performance within each functional category (1, 2 and 4) as well as trends between the categories will be highlighted. It is only possible to draw firm conclusions about the performance of the various DFT methods where a reliable assessment has been carried out. In order to provide a meaningful comparison, only those DFT-NMR studies that eliminate inconsistencies arising from differences in the basis set, gauge-origin method, and geometries employed, are considered. In addition, the range of molecular environments included in the test set of molecules, the reference data used (experiment or *ab initio*), and whether chemical shift or absolute shielding values are calculated will also influence the quality of the assessment. For systems containing heavier nuclei, the scarcity of accurate absolute shielding scales and benchmark *ab initio* data, as well as the importance of relativistic effects can affect the assessment process. As a consequence, the heavier nuclei such as transition metals will be considered separately in Section 4.2.

4.1. First- and second-row nuclei

4.1.1. *Local density approximation (LDA)*

In molecules, LDA generally provides poor isotropic shieldings that are significantly too deshielded.[47,60,63,86–89] Indeed, Hartree–Fock theory has been observed to outperform LDA in a large NMR study involving a representative set of molecular environments.[86] However, this trend is reversed when the molecules under investigation contain significant electron-correlation effects.[47]

4.1.2. *Generalised gradient approximations (GGAs)*

The most common route for GGA (and beyond GGA) development is based on fitting to some set of experimental data, and satisfying a number of well known physical constants (i.e., known properties of the exact exchange–correlation functional). The success of DFT for molecules really began with the introduction of the density gradient dependent term (reduced density gradient) that introduces inhomogeneity (i.e., shell structure into the exchange potential). The first exchange functionals, B86[90] and P86[91] were derived from the homogeneous electron gas and designed to correct the deficient asymptotic behaviour of LDA. One of the most popular exchange functionals in use today is B88.[92] Only small differences are observed in the NMR shieldings of first-row nuclei between B88 and P86 (when used in conjunction with the P86 correlation functional). On average, PP86 tends to provide slightly more deshielded values than BP86.[63]

A variety of correlation functionals have been derived separately either from the uniform electron gas or from rare-gas calculations (as a result, the correlation functionals only include short range dynamical correlation effects). Popular correlation functionals include P86[93] empirically fitted to the correlation energy of the Ne atom, the LYP functional[94] based upon the correlation energy of the He atom determined from high level *ab initio* calculations, and the correlation functional PW91.[95] A parameter-free exchange–correlation functional PW91PW91[96] derived from properties of the slowly varying electron gas has also been developed. The most popular combinations of exchange (i.e., B88) and correlation functional that have been employed include BP86, BPW91, PW91PW91, BLYP, etc. For first-row nuclei, they provide a significant improvement over LDA shieldings, although their predictions still remain significantly too deshielded and they struggle to approach MP2 quality. The greatest deviations between these types of functionals occur for systems that exhibit significant correlation effects.[86,88,97] These general trends are also reflected in a large chemical shift study.[69]

Approaches that determine the *whole* exchange–correlation functional may reduce any potential inconsistencies that arise when the exchange and correlation parts are combined from different sources. Typically, such approaches are

semi-empirical in nature, based on the GGA functional form proposed by Becke:[98]

$$E_{XC}^{B97}(\text{GGA part}) = E_X^{\alpha\alpha} + E_X^{\beta\beta} + E_C^{\alpha\alpha} + E_C^{\beta\beta} + E_C^{\alpha\beta} \tag{36}$$

Each component involving exchange, parallel spin correlation and anti-parallel spin correlation is expressed in a power series involving the density and the reduced density gradient. The fitted linear coefficients are optimised such that thermochemical data (typically from the G2 set of molecules[99]) are reproduced as accurately as possible. One such functional, HCTH,[100] with a flexible functional form using 15 parameters was also fitted to accurate exchange–correlation potentials and nuclear gradient data (the expansion was truncated at fourth-order). In general, it was observed to provide a 50 and 30% improvement in the shielding constants over LDA and BLYP, respectively. Although the HCTH isotropic shieldings do approach MP2 quality they still remain significantly too deshielded.[86,101]

In an attempt to break away from these highly empirical approaches the PBE functional[102] was developed with parameters that are fundamental constants (except for those in the local spin density component). It has shown some promise for the determination of NMR shielding constants[103,104] improving upon BLYP but remaining inferior to HCTH and MP2.[105]

4.1.3. *Hybrid functionals*

The most widely used approximations in the chemical literature are hybrid functionals (or adiabatic connection method (ACM) functionals[106]) which include a fraction (usually between about 0.2 and 0.25) of exact orbital exchange. The most common approaches are semi-empirical ones based on Becke's original three parameter exchange–correlation functional (B3PW91)[107] whose form is represented by

$$E_{XC}^{B3PW91} = aE_X^{LSDA} + (1-a)E_X^{exact} + b\Delta E_X^{B88} + E_C^{LSDA} + c\Delta E_C^{PW91} \tag{37}$$

The weights of the components of exact orbital exchange, exchange, and correlation obtained by fitting to experimental data and which depend on the form chosen for E_C^{GGA}, are $a = 0.80$, $b = 0.72$ and $c = 0.81$. The most widely used hybrid functional of this general form is B3LYP[108] obtained from B3PW91 by replacing ΔE_C^{PW91} by $(E_C^{LYP} - E_C^{LSDA})$. Other such functionals employed in DFT-NMR studies include B3P86[108] which uses P86 correlation instead of PW91, and Becke's original one-parameter functional B1LYP.[109] These one- and three-parameter (ACM) type hybrid functionals predict NMR shielding constants that are generally significantly more deshielded than their GGA counterparts in first-row nuclei that exhibit negative (large paramagnetic contributions arising from the presence of significant correlation effects or low-lying excited states) isotropic shieldings. Less significant differences between

the hybrid and GGA functionals are observed for nuclei exhibiting positive isotropic shieldings. The relative performance of the hybrid and GGA functionals is therefore sensitive to the type of molecules included in the data set. Like their GGA counterparts, these hybrid functionals remain poor in comparison to MP2 (typically 2–3 times worse).[10,47,60,103,104,110] For ^{31}P chemical shifts, the hybrid and GGA functionals provide similar quality predictions (generally of MP2 quality) although they perform less well for the molecules PCl_3 and PN.[70] Large deviations in the calculated shieldings from experiment are also observed in the PN, P_2H_2 and SO_2 molecules.[32]

Approaches based on the GGA functional form (36) including an additional amount of exact orbital exchange also represent a popular approach for determining hybrid functionals. Becke's original 10 parameter functional B97[98] (the expansion was truncated at second-order) determined in a basis set free, non self-consistent manner (based on LDA densities) for the G2 set of molecules resulted in ~ 0.19 fraction of orbital exchange. B97 provides NMR shielding constants that are superior to BLYP but are inferior to HCTH, although it does outperform B3LYP.[86,101]

Re-optimisation of B97 using the extended G2 test set led to the B98 functional[111] (this functional should not be confused with the meta-GGA functional also called B98[112]). The 2c linear expansion coefficients[111] (with ~ 0.22 orbital exchange) were used in the shielding calculations.[113] Although no direct comparison is made between B97 and B98, for the limited range of molecules investigated, B98 provided a significant improvement over B3LYP (though no significant improvement for proton shieldings) with results approaching MP2 quality.

The original B97 functional was reparameterised in a self-consistent procedure (i.e., using densities optimised within the same functional at the TZ2P basis set level) with an expansion also truncated at second-order. The optimal value for the fraction of orbital exchange in this 10 parameter functional named B97-1[100] was 0.21. No direct comparison has been made between calculated B97 and B97-1 NMR shielding constants. Although it provides a $\sim 10\%$ reduction in the errors compared to B3LYP, they still remain unacceptably large (~ 50 ppm for the mean absolute errors).[114] A further self-consistent reparameterisation of B97-1 was undertaken fitting to thermochemical and accurate exchange–correlation potentials (see HCTH above) leading to the B97-2 functional.[114] The value for the fraction of orbital exchange in this 10 parameter functional was chosen to be 0.21 so that its performance could be directly compared to that of B97-1, and the influence of accurate multiplicative potential data on hybrid functional development could be assessed (see Section 6.2.1). The calculated shielding constants improved from B97-1 to B97-2 by $\sim 6\%$[114] but it certainly cannot compete with its GGA counterpart HCTH (mean absolute error ~ 30 ppm).[40,115]

The GGA functional PBE has been extended to the hybrid functional PBE0 (or PBE1PBE)[116] using a theoretically determined value of 0.25 orbital

exchange. For NMR shielding constants, PBE and PBE0 perform similarly using B3LYP/6-31G(d) optimised geometries,[103] whilst there is an improvement of ~40% moving from PBE to PBE0 using self-consistent optimised geometries, providing comparable quality with MP2. The performance of PBE0 for the challenging ozone molecule is poor, providing similar results as B3LYP.[116] Since geometrical effects are clearly significant, and bearing in mind the fact that reference experimental shieldings are used, perhaps a more meaningful assessment should utilise experimental geometries too, in addition to employing a wider range of molecular environments. However, these studies do seem to suggest that PBE0 does provide improvement over the conventional ACM3 methods.

The mPW91PW91 functional[117]—based on PW91PW91—is a one-parameter hybrid functional containing 0.25 exact orbital exchange (modified to improve its description of long-range interaction effects) that provides very similar shieldings to those of PBE0.[116] mPW91PW91 has also been observed to provide similar accuracy to the conventional ACM3 type functionals for the prediction of ^{19}F NMR shielding constants,[110] and has delivered some promising results for ^{13}C chemical shifts.[118–120]

4.2. Small and large shielding ranges: protons and heavy nuclei

Proton NMR provides a wealth of chemical and biological structural information. Crucially, accurate theoretical predictions would aid the assignment of unknown resonances in the experimental NMR spectra. The small chemical shift range of non H-bonded protons (typically 0–12 ppm) reflects the fact that electron correlation effects are generally not significant (typically ~0.2 ppm or less for organic systems), although there are exceptions, especially in carbenes, organic cations, aromatic systems, transition metal complexes, or in strong H-bonds.[47,103,121–123] However, it is still an open question as to whether or not conventional DFT methods can predict proton shieldings and chemical shifts with useful accuracy bearing in mind the fact that rovibrational and intermolecular effects may be comparable in magnitude with the small chemical shift ranges. For example, the use of proton shifts predictions to aid structural studies in proteins requires a predictive accuracy of 0.1–0.2 ppm.[121]

In general, for non-H-bonded protons, their shieldings are found to be relatively insensitive to basis set and geometry effects as well as the exchange–correlation functional employed.[72,124] For the absolute shieldings, the hybrid and GGA functionals provide proton shielding constant predictions that are generally similar in accuracy (with mean absolute errors typically ~0.3–0.4 ppm)[86,104] and which significantly outperform LDA (mean absolute errors typically ~0.6 ppm) but remain inferior to MP2 (mean absolute errors typically ~0.2 ppm). An extreme example where the predicted proton

shieldings are very sensitive to the DFT method employed (relecting the large electron-correlation effects present) is in the CH_2 molecule.[47]

Slightly reduced errors are observed for the chemical shift predictions compared to the absolute shielding ones quoted above for LDA and GGA functionals which may indicate the presence of error cancellation effects.[87] Several hybrid functional DFT studies[72,121,125] have shown promise in their ability to reproduce the condensed phase experimental chemical shift trends using linear scaling techniques. The largest errors occurred for conjugated π-systems and H-bonded species—due to larger electron-correlation effects and stronger interaction with solvent. Therefore, significant further improvements in proton NMR shielding predictions are only likely to occur if rovibrational corrections and solvent effects are included in the calculations (see Sections 7 and 8).

4.2.1. *Non-relativistic heavy atom shieldings*

The full potential of DFT for determining NMR shielding constants lies in its ability to provide accurate predictions for computationally demanding systems where the cost is prohibitive for high-level *ab initio* correlated methods. DFT represents the only viable alternative to wavefunction-based methods when electron-correlation effects are significant because Hartree–Fock and MP2 methods often become very unreliable. The inclusion of relativisitic effects becomes increasingly important for the NMR shieldings in heavier nuclei—these effects will be discussed later in Section 4.4.

Transition metals

The presence of large correlation effects and low-lying excited states in the first-row (3d) transition metal complexes are a result of the strong repulsive interactions between the compact 3d orbitals (having similar radial extents to the metal 3s and 3p orbitals) and the ligand orbitals. As a consequence, very wide shielding ranges (typically 10^3–10^4 ppm) and chemical shifts that are very sensitive to ligand type are associated with these nuclei. Thus, the prediction of the metal NMR shielding and chemical shifts in first-row transition metal complexes represents a severe challenge for DFT. For the second- (4d) and third-row (5d) transition metal complexes these effects become less severe due to reduced metal–ligand interactions.

The scarcity of reliable absolute shielding scales and gas phase data for these nuclei means that calculated chemical shifts are compared to solution or solid state experimental data. Thus, meaningful comparison with experiment may be hampered by the presence of intermolecular crystal/solvent effects. However, in the case of the metal shieldings/chemical shifts such effects have been shown to be small.[126–128]

The $[Co(CN)_6]^{3-}$ complex has proven to be an important and widely used benchmark for DFT-NMR methods because a reliable estimate of the absolute shielding (relative to the bare nucleus) of ^{59}Co is available (−5400 ppm).[129]

Before the performance of DFT is assessed for this species it is worthwhile mentioning that for such highly charged complexes, the convergence properties of the energy calculations can be poor. This can be overcome by the inclusion of positive point charges to act as counterions, thus ensuring only negative occupied orbital energies are obtained. However, only the bare complexes are considered in the majority of NMR shielding calculations. The GGA functional predictions of the ^{59}Co shielding in this complex provide little or no improvement over LDA and are dramatically too shielded relative to experiment (on average by $\sim$30–40%).[105,130] In stark contrast, the hybrid functionals (typically containing about 20% fraction of exact orbital exchange) dramatically outperform the GGAs providing errors with experiment of only a few percent.[71,105,114,131] For the cobalt complexes in general, the hybrid functionals have also been successful in reproducing the experimental ^{59}Co principal shielding tensor elements, the large chemical shift ranges in a variety of complexes (up to $\sim$13 000 ppm), as well as the Co–C bond length shielding derivatives.[71,128,131]

Similar dramatic improvements over GGAs are observed in the hybrid functional chemical shift trends for the ^{55}Mn, ^{57}Fe and ^{103}Rh nuclei in a range of complexes.[105,132–134] However, ^{51}V, ^{55}Mn, ^{53}Cr studies[135,136] have shown that GGA functionals can provide reasonably good chemical shift predictions and the performance of the hybrid functionals become similar to, or even slightly worse than, the GGA functionals.[105,136] For the ^{95}Mo chemical shifts the GGAs provide good agreement with experiment and can actually outperform the hybrid functionals.[137,138] Like their GGA counterparts in Co, Fe and Rh complexes, there are also situations when hybrid functionals fail to reproduce the experimental metal chemical shift range. For example, only about 5% of the experimental ^{183}W chemical shift range ($\sim$8000 ppm) in a series of tungsten complexes was recovered using the B3LYP functional.[139]

The unpredictability in performance amongst the various exchange–correlation functionals for metal chemical shifts in transition metal complexes has not yet been satisfactorily explained, let alone resolved. As a consequence, careful calibration of the available DFT methods must be carried out before each transition metal chemical shift study. The underlying mechanisms that produce the dramatic differences between the GGA and hybrid functional ^{59}Fe shielding in ferrocene due to the influence of exact orbital exchange have been investigated in detail.[134] The influence of exact orbital exchange on the calculated shielding constants will be discussed in more detail in Section 5.

Transition metal ligands

The NMR shielding and chemical shift predictions of the ligand atoms in transition metal complexes remains an active area of research. Although other ligand types have been investigated (e.g. ^{1}H and ^{31}P [137,140]), it is the simple mononuclear transition metal complexes containing oxo and carbonyl ligands that have proved the most popular testing ground for DFT-NMR studies.

As well as highlighting the promising performance of the DFT-NMR methods, several of these studies have also provided valuable insight into the factors responsible for the observed ligand shielding trends.

For the oxo compounds Hartree–Fock and MP2 provide a very poor description of the ligand shieldings being in error by more than an order of magnitude.[51] This has been rationalised in terms of the large electron-correlation effects and low-lying excited states present in these compounds. The application of more advanced wavefunction-based methods to these systems would be computationally too demanding and so DFT represents the only viable alternative. For a convenient comparison with experiment, the aqueous ^{17}O chemical shifts[141] have been converted into absolute shieldings.[51] Several studies have highlighted the fact that, in general, both the hybrid and GGA functionals predict values that are too deshielded, with the GGA shieldings lying closer to experiment.[51,105,127,135] The largest deviations with experiment were observed in the 3d transition metal complexes. This has been rationalised in terms of the present exchange–correlation functionals being unable to accurately describe the more compact 3d shell.[135]

For the carbonyl transition metal complexes, the ^{13}C and ^{17}O isotropic shieldings determined from hybrid and non-hybrid functionals are too deshielded relative to experiment. In general, non-hybrid functionals produce the superior quality ligand shieldings.[105,142,143] The hybrid functionals tend to exhibit larger shielding anisotropies that are in worse agreement with experiment.[105,143] Other DFT-NMR carbonyl ligand studies have proved successful in their attempts to reproduce experimental data and provide insights into the effect of ligand–metal complexation in several species. Bridging carbonyl ligand shieldings have been successfully reproduced by GGA functionals.[144,145] The observed decrease in the calculated ^{13}C chemical shifts along the 3d (Cr, Mn, Fe), 4d (Mo, Tc, Ru), and 5d (Hf, Ta, W, Re, Os) rows in a series of isoelectronic metal hexacarbonyls[146] have been rationalised in terms of the oxidation state, and π- and σ-bonding contributions to the paramagnetic shieldings. The ^{13}C and ^{17}O DFT(BPW91)-NMR study in iron porphyrins[147] has provided insight into the CO binding effects.

Other heavy nuclei

DFT-NMR studies focussing on non-transition metal heavy nuclei are still relatively rare in the literature even though a wealth of experimental data is available and even in some cases experimental absolute shielding scales exist. The selenium nuclei is a good case in point, although care must be taken in comparing non-relativistic predictions with the relativistically corrected absolute shielding scale—converting to chemical shifts will reduce this uniform discrepancy though.[148] The prediction of ^{77}Se shielding constants in small molecules has proven very challenging for DFT since substantial electron correlation effects are present. Conventional DFT isotropic and anisotropic shielding errors remain unacceptably large for many of these systems.[97,148–152]

The promising performance of DFT methods for the prediction of ^{119}Sn NMR shielding constants was highlighted in several early studies.[12,153] More recently, a hybrid functional DFT study has reproduced the observed chemical shift trends in a series of organometallic tin cyanide compounds.[154] In addition, the similar performance of LDA, GGA and hybrid functionals were observed to overestimate the experimental ^{119}Sn chemical shifts in a series of tetra-organo tin compounds.[155] A large study on a series of tetracoordinated tin compounds indicated that the B3PW91 functional provided excellent results both in the absolute and relative sense for the majority of compounds studied.[156]

Relativistic effects have been shown to have a significant effect on the absolute shielding scale of ^{125}Te. However, the *relative* chemical shift trends in a series of tellurium compounds have been reproduced using a GGA functional but some significant differences with experiment still remain.[157]

4.3. *Ad hoc* methods for improving the DFT shielding predictions

With the exception of transition metal nuclei, the conventional exchange–correlation functionals discussed above have generally failed to compete with correlated *ab initio* methods for the prediction of NMR shielding constants. Whilst the GGA functionals provide significant improvements over LDA, their isotropic shieldings still remain significantly too deshielded, suggesting that the gradient corrections may be unable to adequately compensate for the major deficiency of the uniform electron gas distribution.[69] It is clear that existing approximate *energy* optimised exchange–correlation functionals are not yet optimal for describing the paramagnetic shielding terms that critically depend upon an accurate description of both the occupied *and* virtual orbitals (the diamagnetic shielding terms remain largely invariant to functional type). If the full potential of DFT is to be exploited in the determination of NMR shielding constants then the errors must be reduced considerably. Several *ad hoc* procedures within the framework of uncoupled DFT-NMR have been developed and their theoretical justification comes from the fact they can lead to significant improvements in the calculated NMR shielding constants.

4.3.1. *Sum-over-states density functional perturbation theory*

One such approach that has been widely used for the improved description of NMR shielding constants is the sum-over-states density functional perturbation theory (SOS-DFPT) method[97] which utilises a level shift correction to the eigenvalue differences obtained within the uncoupled Kohn–Sham shielding equations. The eigenvalue difference terms $\varepsilon_b - \varepsilon_j$ in the denominator of the paramagnetic shielding expression (27) are replaced by the term

$(\varepsilon_b - \varepsilon_j + \Delta E^{XC}_{j\to b})$. Using the simple LDA, the Local 1 correction (Loc.1) is defined as

$$\Delta E^{XC}_{j \longrightarrow b}(\text{Loc.1}) = -\int \rho_j(\boldsymbol{r})\, \frac{\delta \varepsilon^{LDA}_{XC}(\boldsymbol{r})}{\delta \rho^{\uparrow}(\boldsymbol{r})} \rho_b(\boldsymbol{r})\, d\boldsymbol{r}$$
$$= \tfrac{1}{2}(3/4\pi)^{1/3} \int \rho(\boldsymbol{r})^{(-2/3)} \rho_j(\boldsymbol{r}) \rho_b(\boldsymbol{r})\, d\boldsymbol{r} \qquad (38)$$

where $\rho_j(\boldsymbol{r})$ and $\rho_b(\boldsymbol{r})$ are the occupied and virtual orbital densities, respectively. The alternative Local 2 correction (Loc.2) is defined as

$$\Delta E^{XC}_{j \longrightarrow b}(\text{Loc.2}) = -\int \rho_j(\boldsymbol{r})\, \frac{\delta \nu^{\uparrow LDA}_{XC}(\boldsymbol{r})}{\delta \rho^{\uparrow}(\boldsymbol{r})} \rho_b(\boldsymbol{r})\, d\boldsymbol{r}$$
$$= \tfrac{2}{3}(3/4\pi)^{1/3} \int \rho(\boldsymbol{r})^{(-2/3)} \rho_j(\boldsymbol{r}) \rho_b(\boldsymbol{r})\, d\boldsymbol{r} \qquad (39)$$

where $\rho_j(\boldsymbol{r})$ and $\rho_b(\boldsymbol{r})$ are the occupied and virtual orbital densities, respectively. The Loc.2 approximation is larger than Loc.1 by a factor of 4/3. They are designed to correct for the deficient eigenvalue difference terms through the change in the exchange–correlation interaction when an electron is excited from an occupied to virtual molecular orbital. Although the method has been shown to lack gauge invariance, for practical basis sets this effect is small.[158,159]

A detailed and systematic investigation of the performance of Loc.1 versus Loc.2 has been carried out for the determination of ^{13}C, ^{15}N and ^{17}O NMR shielding constants[88,89] and chemical shifts.[69] The SOS-DFPT method has been used in conjunction with several functionals on a wide range of nuclei, in a variety of bonding environments. Significant improvements in the predicted NMR shielding constants and chemical shifts are observed. On average, the SOS-DFPT correction accounts for about a 20–30% improvement in shielding constants for first-, second- and third-row nuclei.[86,149] However, inclusion of the SOS-DFPT correction (Loc.1) provided no overall improvement in ^{1}H DFT predictions.[86] For the metal absolute shieldings and chemical shifts in transition metal complexes, in several cases the conventional continuum functional predictions are already significantly too shielded relative to experiment (i.e., for ^{57}Fe, ^{59}Co), therefore inclusion of the SOS-DFPT correction simply increases the discrepancy with experiment. On average, an $\sim 20\%$ degradation in performance is typically observed for these systems.[105] Finally, the corrections to the DFT-NMR values from the SOS-DFPT approach vanish for periodic systems, where the eigenstates are always extended.[44]

A Loc.3 approximation derived within the rigorous framework of time-dependent density-functional theory (TDDFT) has recently been applied in conjunction with several exchange–correlation functionals.[88,89] In essence, the

electric field linear response expression in TDDFT for magnetic perturbations is utilised. The Loc.3 approximation (where K_{jb} is a coupling matrix term)

$$\Delta E_{j \longrightarrow b}^{\mathrm{XC}}(\mathrm{Loc.3}) = 2K_{jb} + \int \rho_j(\boldsymbol{r}) \left(\frac{\delta v_{\mathrm{XC}}^{\uparrow \mathrm{LDA}}(\boldsymbol{r})}{\delta \rho^{\uparrow}(\boldsymbol{r})} + \frac{\delta v_{\mathrm{XC}}^{\uparrow \mathrm{LDA}}(\boldsymbol{r})}{\delta \rho^{\downarrow}(\boldsymbol{r})} \; \rho_{\alpha}(\boldsymbol{r}) \right) \rho_b(\boldsymbol{r}) \, \mathrm{d}\boldsymbol{r} \quad (40)$$

is derived by applying the electric field SOS expression to magnetic fields within the two-level model and Tamm–Dancoff approximation (TDA). For the determination of isotropic NMR shieldings it performs at least as well as the Loc.1 and Loc.2 approximations of SOS-DFPT.

4.3.2. *The WAH method*

The WAH method has been shown to provide significant improvements over conventional functionals for first-, second- and third-row (excluding transition metals) NMR shielding constant predictions.[47,101,149] The uncoupled shielding expression (27) was evaluated with orbitals and eigenvalues from a non-multiplicative operator, using modified functionals involving 0.04 fraction of orbital exchange in conjunction with B97-1, WAH(0.04), or 0.05 fraction of orbital exchange with B3LYP, WAH(0.05). Although, the optimal amount of exact orbital exchange is small, the similar performance of both functionals indicates the stability of the procedure. The scheme assumes that the correlation parts of the hybrid functionals are satisfactory but that the nature of the virtual orbitals critically depends upon the exchange part. From a rigorous viewpoint the approach is inconsistent because it leads to a loss of gauge-invariance because a non-multiplicative operator should not be used in conjunction with the uncoupled shielding expression.[70]

4.4. Scalar and spin–orbit relativistic effects

In recent years there has been increased interest in the role of relativistic effects on NMR shielding constants in heavy atom systems. *Ab initio*, fully relativistic (four-component) formulations[160] are computationally very demanding, and are only slowly beginning to emerge. However, approximate relativistic methods within the framework of DFT have been shown to offer promising NMR results both in terms of accuracy and computational cost. The high velocities associated with the core electrons in heavy nuclei contribute significant relativistic effects to the heavy atom (or neighbouring light atom) NMR shielding parameters. The magnitude of the relativistic effects increases down the periodic table, and by the sixth period (i.e., third-row transition metals, Pb, etc.) inclusion of these effects in the calculations becomes mandatory.[7] Relativistic effects can influence NMR shieldings in one of two ways: either indirectly, by affecting molecular structures (i.e., through a

contraction in the bond length); or directly, by affecting the electronic structure at a fixed geometry. These effects do not necessarily enforce each other.[135,161] In this review, only direct relativistic effects will be discussed. In general, relativistic effects contract the inner-core s- and p-orbitals producing larger diamagnetic shielding terms (these will tend to cancel out in relative chemical shift calculations). For the valence orbitals, the s- and p-orbitals become more contracted and as a consequence the d- and f-orbitals are more efficiently screened from the nucleus, and thus expand. As a result, the changes in the molecular orbital energies and the r^{-3} expectation values arising from relativistic effects can have a significant impact on the NMR shieldings. The lack of accurate absolute shielding scales for heavy atom systems means that chemical shifts rather than absolute shieldings are more commonly used which tend to attenuate the relativistic effects (i.e., chemical shifts arise from the valence and not the core electron properties).[162]

4.4.1. *Scalar relativistic effects*

The first attempts to include scalar (not including spin–orbit) relativistic effects in DFT-NMR shielding constant calculations involved the use of relativistic effective core potentials (RECPs).[127] The main disadvantage of RECPs arises from the fact that the resulting valence orbitals display the wrong asymptotic nodal behaviour near the nucleus. It has been shown that the NMR shieldings are mainly determined by the core tails of the valence orbitals and not by the core orbitals themselves.[5] Thus, the use of RECPs on heavy atoms is restricted to the prediction of ligand rather than the heavy atom NMR shieldings. The importance of including scalar relativistic effects for the neighbouring light atom (ligand) NMR shieldings is highlighted in non-relativistic ^{31}P studies on the Cr, Mo and W transition metal complexes, where agreement between experiment and theory worsens down the periodic table due to lack of relativistic corrections.[137,163] Scalar relativistic have been investigated for several types of ligand atom shieldings. For the ^{17}O in transition metal oxo complexes,[51,127] large scalar relativistic effects were observed in the 5d complexes that led to a lowering in the paramagnetic shielding terms resulting from the increased energy denominators.[51] The ^{13}C shieldings in a variety of organometallic and inorganic transition metal complexes have also been investigated.[142]

In the fully relativistic (four-component) DFT formulation, the relativistic effects are included in the non-relativistic Kohn–Sham equations (based on the *relativistic orbitals*) via the mass-velocity (h^{MV}), Darwin (h^{DAR}), and one- and two-electron spin–orbit (h_1^{SO} and h_2^{SO}, respectively) perturbative operators.[8] A popular and less computationally demanding route that also provides promising accuracy in the description of the relativistic effects utilises the Breit–Pauli approximation whereby a quasi-relativistic (QR) (two-component) DFT-NMR method includes the h^{MV} and h^{DAR} operators only (collectively known as the Pauli–Hamiltonian). They represent *scalar* relativistic corrections

to the kinetic and nuclear-attraction energies, respectively. The spin–orbit operators describe the coupling between electron spin and the orbital angular momentum of the electrons. Spin–orbit effects on the NMR shielding constants will be discussed in Section 4.4.2.

In certain situations the Pauli–Hamiltonian becomes unstable leading to large negative energies.[5,135] This problem can be eliminated using the frozen-core approximation[164] that provides valence electrons that are orthogonalised against the frozen core orbitals (obtained from four-component atomic Dirac–Fock calculations). This ensures the correct tails of the valence orbitals close to the nucleus. QR two-component relativistic effects on the DFT-NMR ^{17}O shieldings in transition metal oxo complexes and the metal chemical shifts in transition metal carbonyls have been investigated.[135] For the metal chemical shifts and ligand shieldings the inclusion of relativistic effects was found to be essential in the 5d complexes. For the 4d and 3d complexes the effects are seen to be smaller and less regular. Relativistic stabilisation of the occupied orbitals (or destabilisation of the virtual orbitals) increased the eigenvalue differences leading to a reduction in the paramagnetic contributions.

A promising two-component variational relativistic method based on the 'zero-order regular approximation' (ZORA) provides a better description of relativistic effects near the nuclei. Its main advantage over the QR approach is in its variational stability and its ability to perform all-electron calculations. It has been applied to NMR shielding constants with promising results.[165] ZORA (all-electron) versus QR (frozen core) DFT-NMR calculations for the metal nuclei in a series of transition metal oxides MO^{4n-} (M = Cr, Mn, Fe, Mo, Tc, Ru, W, Re, Os) and carbonyl complexes $M(CO)_6$ (M = Cr, Mo, W) have been compared.[166] Although significant differences in the ZORA and QR absolute shieldings occurred (up to 300 ppm in the 5d metals), the calculated chemical shifts were found to be much closer in agreement provided the valence basis set used is sufficiently flexible in the core region. Comparison to experiment shows that the errors of the most precise ZORA chemical shifts are ca. 10% (in the order of a few 100 ppm) for both the light and heavy transition metals. The ZORA and QR approaches produced ^{195}Pt chemical shift values that were within 10–20% of each other[167] also indicating that the frozen core approximation is a valid one. Calculated frozen-core ^{207}Pb and ^{183}W shieldings[168] have indicated that the ZORA–Hamiltonian outperformed the Pauli–Hamiltonian for both nuclei. The spin–orbit term was found to be small in ^{183}W but dominated the trends in ^{207}Pb. ZORA-DFT-NMR calculations have also reproduced the experimental ^{95}Mo and associated ligand chemical shift tensor data. The large chemical shift anisotropy was found to be dominated by the HOMO–LUMO excitations.[169]

DFT-NMR ligand shielding studies on the actinide (U, Np, Pu) compounds have now appeared.[170] In general, the ZORA and QR (Pauli–Hamiltonian) approaches are observed to provide similar quality values that are in good agreement with experiment (although some shortcomings with experiment are

observed in some of the calculated ^{19}F chemical shifts), but the RECP method was unable to cope. A more detailed analysis reveals that the QR approach is more accurate for the ^{1}H NMR in UF_6–$n(OCH_3)(n)$ compounds whereas ZORA is more accurate in other cases. This finding contradicts earlier studies that *always* showed ZORA to be superior.[171]

4.4.2. *Spin–orbit effects*

Electronic spin–orbit interactions can have a dramatic effect on NMR shielding constants when heavy nuclei are present.[172,173] Most studies on the role of spin–orbit effects on NMR shieldings have focused upon ligand atoms directly bonded to the heavy atom nuclei. The ^{1}H nucleus is found to be more sensitive to spin–orbit effects than other heavier ligand atoms[161] and as a consequence has received more attentional from theoretical DFT-NMR studies. Spin–orbit effects up to 12 ppm for the ^{1}H shielding in the HI molecule have been observed—comparable in magnitude to the full proton chemical shift range.[174] An RECP DFT-NMR study has also highlighted the strong influence of spin–orbit coupling on the ^{1}H ligand in several mercury compounds.[161] The inclusion of spin–orbit effects in a QR/frozen-core approximation DFT-NMR study have improved the ^{1}H chemical shift predictions in hydrogen halides.[175] Large spin–orbit effects (~ 7 ppm) in the ^{1}H ligand NMR chemical shift has been observed in the actinide compound $UF_5(OCH_3)$ where the proton is not directly attached to the heavy atom have also been observed. Only small effects are observed for the other ligand nuclei.[171] Inclusion of spin–orbit effects have also been investigated in DFT-NMR studies for heavier ligand nuclei such as ^{13}C [161,175] and ^{31}P.[176] The spin–orbit couplings are seen to provide a significant effect on the rovibrational corrections, temperature dependence, and secondary isotope shifts in the ^{13}C DFT(SOS-DFPT)-NMR shieldings in CX_2 (X = O, S, Se, Te).[177]

In diamagnetic systems (where all electrons are paired) a spin density at a particular nucleus can be generated (the spin–orbit coupling and external magnetic field effectively mix triplet states into the singlet ground state). The NMR shielding at this nucleus can then be affected when the resulting spin polarisation interacts with the nuclear magnetic moment via the Fermi-contact term.[175] The rules governing the propagation of these effects through the molecule are closely analogous to the well-established mechanisms for indirect Fermi-contact nuclear spin–spin coupling.[175,178] For example, the magnitude of the spin–orbit coupling (and hence the Fermi-contact term) is inversely proportional to the size of the occupied-virtual eigenvalue differences and the amount of spin–density transfer critically depends on the nature of the bonding mechanisms involved (i.e., increased s-orbital character on the central heavy atom leads to increased Fermi-contact terms). A very effective Fermi-contact mechanism is observed in a DFT-NMR study on PI_4^+ where large spin–orbit contributions from the four heavy iodine substituents are transmitted to the ^{31}P nucleus resulting in a large change in chemical shift of (-520 ppm).[176]

In several DFT studies the predicted scalar relativistic ^{1}H NMR shifts in hydrogen halides and ^{13}C in methyl halides[175,179] and transition metal carbonyl complexes[175] improved with experiment when spin–orbit coupling and the Fermi-contact term were included. The inclusion of spin–orbit effects in ZORA-DFT-NMR studies on heavy atom nuclei highlighted the importance of the Fermi-contact term on the ^{207}Pb, and ^{183}W chemical shift trends. The Fermi-contact term was found to be important in the lead series but less important in the tungsten series of compounds investigated.[168]

5. THE ROLE OF EXACT ORBITAL EXCHANGE

A proper understanding of the role of exact orbital (Hartree–Fock) exchange in hybrid functionals is crucial to future development of improved functionals containing no exact Hartree–Fock exchange.[9] For the calculation of NMR shielding constants, the role of exact orbital exchange still remains controversial. In Hartree–Fock theory, for a molecule containing N-electrons the occupied and virtual MOs feel the effect of $N-1$ and N electrons, respectively. In pure DFT (where no fraction of orbital exchange is included in the functional) the occupied and virtual MOs feel the influence of $N-1$ electrons. As a consequence, the occupied-virtual eigenvalue differences are generally overestimated in HF theory and underestimated in DFT. The inclusion of a fraction of orbital exchange (typically about 20%) in the hybrid functionals can lead to a marked increase in the eigenvalue differences. Compared to LDA and GGAs, inclusion of orbital exchange in hybrid functionals produces significant stabilisation of the occupied orbitals and a slight destabilisation of the unoccupied orbitals leading to larger eigenvalue differences that are in much better agreement with experimental excitation energies.

5.1. HOMO–LUMO gaps and coupling terms

Although GGA functionals predict shieldings that are generally too deshielded, the fact that orbital exchange increases the gaps between the occupied and virtual Kohn–Sham orbitals does not necessarily lead to improved results when hybrid functional shieldings are determined in the conventional coupled formalism. In addition, hybrid functionals containing increased amounts of orbital exchange (i.e., BHLYP incorporates 50% orbital exchange) have been shown to provide shielding predictions that are inferior to functionals containing 20% orbital exchange.[51] A recent study has systematically investigated the influence of orbital exchange on NMR shielding constants in molecules containing first- and second-row atoms using a series of functionals (based on B97-1) containing varying fractions of orbital exchange ($\xi = 0.0, 0.1, 0.2, \ldots, 1.0$).[180] On average, the shieldings from the conventional coupled

approach became progressively less accurate as ξ increased from 0.0 to 1.0, overall becoming uniformly more deshielded. When $\xi = 0.0$ optimal shieldings were obtained when no orbital exchange was present and the functional is a continuum functional displaying isotropic shieldings that were uniformly too deshielded. This supports the observation that continuum functionals can be more successful than hybrid functionals for the determination of shielding constants involving first- and second-row atoms.

Although the HOMO–LUMO eigenvalue differences varied dramatically with ξ (and significantly overestimated the reference values), the variation in the shieldings with ξ, were comparatively small. This highlights the importance of the coupling terms in the conventional coupled formalism. In the presence of orbital exchange the functional of the Kohn–Sham operator in Eq. (11) becomes non-multiplicative due to the operator $P_{rr'}$, and the magnetic hessian matrix (22) is non-diagonal. The resulting coupled-perturbed shielding equation (26) is solved. In addition to the derivatives of the one-electron Hamiltonian, the calculation of the NMR shielding tensor also requires the derivative of the density matrix with respect to the magnetic field. This is obtained via solution of the coupled-perturbed equations.[60] There is no exchange–correlation contribution to this equation because standard functionals depend only on ρ and its derivatives and not on the magnetic field explicitly (they only have an explicit dependence on the magnetic field via the basis functions). However, in the framework of current-DFT, the current-dependent part of the exchange–correlation functional will introduce coupling terms in the magnetic Hessian.[181] The significant overestimation of the ^{17}O paramagnetic shielding terms in a series of transition metal oxo complexes have also been rationalised in terms of the presence of the coupling terms (neglect of coupling led to an equally large underestimate).[51] Thus, for first- and second-row nuclei, the inclusion of orbital exchange in the functional would seem to be undesirable when the shieldings are determined in the conventional coupled formalism. The coupling was also found to increase the ^{57}Fe paramagnetic shielding in ferrocene (the coupling was found to be proportional to ξ and inversely proportional to the eigenvalue energy difference).[134] In contrast to the first- and second-row nuclei, the coupling terms are desirable for the metal shieldings in transition metal complexes.

As well as an analysis of the eigenvalue differences in the denominator of the paramagnetic shielding term, the numerator matrix element terms $(b|l^{\alpha}|j)$ and $(j|l_{\mathrm{K}}^{\beta} r_{\mathrm{A}}^{-3}|b)$ have also provided further insight into the effects of exact orbital exchange on the metal shieldings in transition metal systems. From an analysis of the dominant d–d excitations in the ^{57}Fe shieldings,[134] the effect of including a fraction of orbital exchange results in more diffuse virtual orbitals compared to the continuum functionals leading to an increase in the numerator matrix elements of the paramagnetic shielding terms. This effect and the introduction of coupling due to orbital exchange were found to dominate over the resulting changes to the eigenvalue differences. The net effect was an increase in the

paramagnetic shieldings. Similar conclusions can be drawn from a study on ^{59}Co metal shieldings.[105] The poor performance of the continuum functionals was rationalised in terms of their underestimation of the numerator matrix elements rather than any significant deficiencies in their description of the eigenvalue differences. The relative increase in the magnitude of the eigenvalue differences following inclusion of a fraction of orbital exchange was found to be less than the corresponding increase in the numerator matrix elements. The net effect is a significant increase in the paramagnetic shielding terms for hybrid functionals compared to continuum functionals.

6. THE ROLE OF MULTIPLICATIVE EXCHANGE–CORRELATION POTENTIALS

It is clear that existing approximate *energy* optimised exchange–correlation functionals are not yet optimal for property calculations, especially for second-order response properties such as NMR shielding constants that critically depend upon an accurate description of both the occupied *and* virtual orbitals. Therefore, a promising route towards more accurate shielding constants will be to develop more accurate exchange–correlation *potentials* since the quality of the orbitals and eigenvalues critically depend upon υ_{XC} rather than the integrated quantity E_{XC} in the functional. The most theoretically appealing approach would involve solving the Kohn–Sham equations in terms of a purely multiplicative υ_{XC} (i.e., defined at each point in space). Such a local multiplicative potential, free of self-interaction, and displaying the correct asymptotic behaviour would be highly desirable for the description of the orbital energies.[182]

Although not yet widely used in DFT-NMR studies, accurate multiplicative exchange–correlation potentials represent a theoretically appealing approach not only because they lead to simple uncoupled expressions for the NMR shielding tensors but also because they can provide insight into the nature of the exact exchange–correlation potential, and the form of the exact functional.[181] Several alternative ways have been developed to generate accurate multiplicative potentials. However, only those approaches that have been employed in DFT-NMR shielding studies will be considered here. The first involves the Optimised Effective Potentials (OEP) approach[183,184] that minimises the energy with respect to the potential (rather than the orbitals). This has been implemented in order to investigate the effect of the SIC on the calculated NMR shielding constants. An alternative route involves the Zhao, Morrison and Parr (ZMP) method based on a constrained-search formulation of DFT.[185] The resulting multiplicative exchange–correlation potentials obtained from the reference densities have been used to generate Kohn–Sham orbitals and eigenvalues used in the uncoupled shielding equations (MKS method[40]), and in semi-empirical functional development (HCTH, etc.).

In recent years, improvements in the long-range asymptotic behaviour of v_{XC} rather than the continuum part of E_{XC} have been developed. Several of these 'model potentials' with an asymptotic correction have been applied to NMR shielding constants.

6.1. Self-interaction free potentials

One of the properties of the exact exchange–correlation functional is that it must be self-interaction free.[186] Although self-interaction can be most easily identified in one electron systems, where the exchange–correlation energy must exactly cancel the Coulomb self-interaction energy, it applies to all N-electron systems. The OEP method has been implemented self-consistently using the Krieger-Li-Iafrate approximation (KLI-OEP) in order to investigate the effect of the Perdew–Zunger SIC on the calculated NMR shielding constants.[87,187] The SIC-LDA(VWN) and SIC-GGA(PBE) methods were found to be similar in performance, providing significant improvements in the observed shieldings for first- and second-row nuclei (although a significant improvement in the proton shieldings using SIC-GGA(PBE) was observed for proton shieldings). The improvements were rationalised in terms of an improved description for the Kohn–Sham orbitals (less delocalised) and the eigenvalues (increased occupied-virtual eigenvalue differences). Changes in the HOMO–LUMO gap provided the major source of improvement. The largest SICs were found in systems with more compact electron densities (i.e., those containing short multiple bonds). Removal of self-interaction was anticipated to reduce the excessive covalency described by conventional functionals. This may be particularly beneficial in the heavier elements such as transition metals.

6.2. Near-exact potentials

6.2.1. *ZMP potentials in functional development*

Conventional functionals only constrain integrated quantities such as E_{XC} to be accurate but do not constrain the exchange–correlation potential (i.e., its functional derivative) to be accurate at all points in space. Critically, the Kohn–Sham orbitals and eigenvalues used in the shielding expressions are therefore not constrained to be accurate. In order to alleviate this problem, GGA (HCTH) and hybrid (B97-2) semi-empirical functionals have been fitted to accurate (BD and MP2) ZMP exchange–correlation potentials (in addition to thermochemical data). The HCTH functional has shown promise for NMR shielding constant predictions but significant errors still remain. These deficiencies were rationalised in terms of the inability of the exchange–correlation potential of the fitted functional to correctly reproduce the accurate

ZMP potential. Only minimal improvements in the shieldings were obtained over HCTH when the thermochemical and nuclear-gradient data from the fitting procedure were eliminated and its parameters were refined by demanding its potential was maximally parallel to the ZMP potential,[115] i.e., shieldings comparable to MKS(BD) or MKS(MP2).[40] This failing clearly demonstrated that an accurate potential could not be reproduced because the HCTH functional form was not sufficiently flexible to simultaneously reproduce the ZMP potentials in all regions of space *important* for NMR properties. When regions of space close to the nuclei were emphasised by the weighting function in the fitting procedure, contributions to the paramagnetic shielding tensor from low-lying excitations improved, while those from higher excitations degraded. The converse was true when regions far from the nuclei were emphasised.

The conventional GGA functionals (HCTH, PBE, etc.) have been shown to give HOMO–LUMO eigenvalue differences that are smaller than those from the accurate ZMP procedure. By explicitly forcing GGA HOMO–LUMO eigenvalue differences to equal those from the ZMP approach, significant improvements in the NMR shielding constants can be obtained.[188] In light of these observations, Keal and Tozer have attempted to determine new XC functionals with improved potentials. Their best functional provides NMR shieldings close to those of MKS(BD)[189] (see below).

6.2.2. *The multiplicative Kohn–Sham method*

In view of the limitations of the functionals form discussed above, the multiplicative exchange–correlation potentials obtained from the reference densities via the ZMP approach have been used directly to generate Kohn–Sham orbitals and eigenvalues used in the uncoupled shielding equations. The method was denoted multiplicative Kohn–Sham (MKS)[40] followed in parenthesis by the method used to determine the reference density. The accuracy of the MKS shielding constants can be summarised as MKS(BD) $\geq$ MKS(B97-1) $>$ MKS(MP2) $>$ MKS(HCTH) $>$ MKS(HF), reflecting the accuracy of the reference electron densities. Given that the BD density is the most accurate of those considered in this study, the MKS(BD) orbitals and eigenvalues can be regarded as a good approximation to the exact Kohn–Sham quantities in the absence of a magnetic field, providing some indication of the accuracy that can be achieved from explicit functionals of just the electron density without inclusion of the current density (it is worth noting that the same ZMP approach has been used to generate exchange vector potentials from densities and current densities[181]). The best MKS NMR shieldings were found to be typically 2–3 times more accurate than conventional DFT approaches.

A series of exchange–correlation functionals based on B97-1 with fractions of orbital exchange $(0.0, 0.1, 0.2, \ldots, 1.0)$ were used to generate reference densities within the MKS scheme.[180] With increasing ξ the MKS shieldings became progressively more shielded for all systems and the optimal fraction of

orbital exchange occurred for $\xi = 0.25$. In line with the shieldings, optimal HOMO–LUMO eigenvalue differences were obtained near $\xi = 0.30$ supporting the view that the quality of the HOMO–LUMO gaps are critical in uncoupled DFT-NMR shielding calculations. For the conventional coupled calculations optimal HOMO–LUMO gaps were obtained with $\xi = 0.04$. This goes some way to explaining the success of the WAH method[47,101,149] (see Section 4.3.2) for determining accurate shieldings for first-, second- and third-row atoms.

6.3. Asymptotically-corrected potentials

Conventional exchange–correlation functionals exhibit the wrong asymptotic behaviour both in regions close to and far away from the nucleus. Improvements in the short-range functional form represent important regions for the diamagnetic shielding and relativistic effects. However, in recent years, the main focus has been directed towards improving the long-range asymptotic behaviour of υ_{XC} rather than the continuum part of E_{XC}.

The long-range asymptotic behaviour of the exchange–correlation potential must be[190]

$$\upsilon_{XC}^{GGA}(\boldsymbol{r}) \longrightarrow -1/r + I + \varepsilon_{HOMO}. \tag{41}$$

With increasing distance from the molecule the exchange–correlation potentials of conventional continuum functionals (LDA, GGAs) break down.[188,191] Their potentials vanish asymptotically, rather than approximately averaging over the integer discontinuity. Several 'model potentials' with an asymptotic correction AC-LDA[192,193] and HCTH(AC)[194] have been applied to NMR shielding constants.[86,88,89] The results were found to be generally relatively insensitive to an asymptotic correction because contributions involving high-lying virtual orbitals are relatively unimportant (although larger effects were witnessed for $CH_3C^{15}N$, $^{15}N_2$ and $^{17}OF_4$ [89]). This is consistent with the presence of the r^{-3} term in the numerator matrix elements and the fact that these excitations involve relatively large eigenvalue differences in the denominator. For this reason, the influence of exchange–correlation functionals on the paramagnetic shielding is critically dependent on the low-lying occupied-virtual excitations, of which the HOMO–LUMO contribution is likely to be significant, given that it involves relatively compact orbitals and the smallest eigenvalue difference.

The fact that the potentials of conventional continuum functionals vanish asymptotically, rather than approximately averaging over the integer discontinuity is consistent with their underestimated HOMO–LUMO eigenvalue differences[195,196] and overestimated paramagnetic shielding terms. HOMO–LUMO eigenvalue differences are important when electrons are added or subtracted from a system. For the exact exchange–correlation potential

(which yields the exact density) the discontinuity Δ_{XC} at integer number of electrons can be related to the HOMO–LUMO eigenvalue difference by

$$\varepsilon_{LUMO} - \varepsilon_{HOMO} = I - A - \Delta_{XC} \tag{42}$$

where I and A are the ionisation potential and electron affinity, respectively.[188] Using HOMO–LUMO eigenvalue differences obtained from accurate electron densities via the ZMP approach, and experimental values of I and A, an approach for correcting the GGA HOMO–LUMO eigenvalue differences has been based on an analysis of the HOMO eigenvalues and the magnitude of the integer discontinuity. ε^{GGA}_{LUMO} is replaced with $-(I + A) - \varepsilon^{GGA}_{HOMO}$ for the systems where reliable experimental values of I and A are available. The accuracy of the HOMO–LUMO differences (and the NMR shielding constants) obtained from this correction are critically dependent on how well the HOMO eigenvalue averages over the discontinuity.[188]

7. NMR SHIELDING SURFACES: ROVIBRATIONAL AND ISOTOPE EFFECTS

Calculated NMR shielding constants determined within the Born–Oppenheimer approximation (i.e., at a fixed molecular geometry) are independent of rovibrational effects and isotopic substitution. However, significant differences may occur between the shielding tensors calculated at the equilibrium geometry and one averaged over nuclear motions.[197] In order to provide more meaningful comparison with the gas-phase experimental NMR data these effects can be important and must be included in the calculations.[198] In recent years, high-level *ab initio* methods are now increasingly employed to determine the rovibrational corrections, isotope effects, and the temperature dependence of the NMR shielding tensors.[8,199] The level of sophistication of the *ab initio* methods is such that their accuracy in determining absolute shielding scales for example, is now competitive with the experimental predictions. The effects of rovibrational averaging over the shielding surface on the temperature dependence and isotope-shifts in DFT-NMR shielding tensor calculations will be discussed.

The shielding constant in a particular rovibronic state is determined by averaging the shielding constant (which varies as a function of the nuclear coordinates) over the calculated rovibrational wave function. Accurate predictions critically depend on the quality of the theoretical method used to determine the shielding constants at a particular bond length and also on the quality of the potential curves generated.[200] Differences between benchmark *ab initio* and the DFT first and second derivatives of the shielding constant, σ, with respect to a given general displacement, ξ, given by $(\partial\sigma/\partial\xi)_e$ and $(\partial^2\sigma/\partial\xi^2)_e$, respectively, can provide an indication of the accuracy of the DFT

rovibrational corrections to the shielding (inclusion of the quadratic term has been shown to be important for isotopic effects when the shielding is described as a function of the bond coordinate.[201] Calculating a multi-dimensional shielding surface that depends on small variations in the equilibrium molecular geometry in the vicinity of the nucleus of interest would be very time consuming. As a consequence, DFT methods have so far tended to focus on predicting rovibrational corrections in relatively small molecules. The SOS-DFPT method determined the first and second derivatives of the shieldings for HF, F_2, N_2, CO, that are in good agreement with the CCSD(T) values.[200] The quality of theoretically calculated shielding surfaces have also been gauged against experimental isotopic shift data in transition metal complexes. Compared to first-row atoms, the much larger shielding derivatives calculated in the DFT-B3LYP-NMR study[131] predicted the first-order vibrational shielding derivative $\partial\sigma/\partial r_{CoC}$ in $[Co(CN)_6]^{3-}$ to be about $-5000\,\text{ppm}\,\text{Å}^{-1}$ giving the correct magnitude and sign as the experimental value of $-7500\,\text{ppm}\,\text{Å}^{-1}$ (based on the temperature dependence of ^{59}Co chemical shift and isotopic shift experiments). In addition, very large geometry effects on the ^{57}Fe DFT-NMR chemical shifts have also been reported.[202]

DFT (BLYP and BPW91) first and second derivatives, isotope shifts and temperature dependencies of the ^{77}Se and ^{13}C shielding constants were found to be in very good agreement (^{13}C to a lesser extent) with corresponding multi-configurational *ab initio* predictions and experiment.[152] In order to gain the correct description of the isotope shifts, the first-order isotope effect (due to changes in the bond not directly attached to the nucleus under investigation) is often considered unimportant. However, their inclusion together with the second-order isotope contributions was found to be crucially important in this system. Isotope shift predictions using the SOS-DFPT method for ^{13}C and ^{17}O shieldings in CO were found to agree well with experiment but the deuterium induced isotope shift on the ^{19}F shielding in HF was observed to significantly overestimate experiment.[200]

Several DFT studies have investigated rovibrational and isotope effects, as well as the temperature dependence on proton NMR shieldings. For the very small rovibrational corrections in proton shieldings, theoretical methods may indeed have surpassed experimental techniques (i.e., CCSD(T) benchmark for shielding surfaces of small molecules[203]). Inclusion of the geometrical and zero-point vibrational corrections (ZPVCs) in the B3LYP-NMR hydroxyl proton chemical shift calculations in ethanol are found to be in very good agreement with the gas phase experimental data.[124] These effects have also been investigated in a range of ^{1}H DFT-NMR studies on H-bonded systems.[204–206] The effect of vibrational averaging in the one-dimensional proton reaction coordinate on the proton and heavy atom shielding constants in the $Br\cdots H\cdots NH_3$ complex have been investigated using DFT (B3LYP) and *ab initio* methods.[207] Significant changes in the NMR shielding constants of the proton compared to heavy nuclei indicated that the proton's electronic environment is

more easily perturbed than for the heavy nuclei. The largest electron correlation effects were observed in the region around the potential minimum.

Theoretical temperature-dependent NMR shielding constants have been obtained from a Boltzmann average of the rovibrational state-dependent shielding constants.[208,209] Although not state specific, the temperature-dependent conformational averaging of the ^{1}H NMR resonances in vinylcyclopropane (combining DFT (B3LYP) and MP2 methods with Boltzmann statistics) have successfully reproduced the observed experimental temperature dependence.[210] Boltzmann weighted (MM3) DFT-NMR (SOS-DFPT) calculations have also been able to reproduce the ^{13}C chemical shifts in flexible molecules thus aiding the determination of their relative configurations.[211]

8. INTERMOLECULAR EFFECTS

Accurate experimental gas-phase NMR data extrapolated to zero pressure provides the most satisfactory comparison with the calculated absolute shielding constants in isolated molecules. In reality, experimental gas-phase data is often not available (especially for heavier nuclei such as transition metals). In the condensed (solvent, crystal/solid) phase, intermolecular effects can significantly perturb the NMR shielding constants (one of the best indicators of intermolecular interactions is the observed gas-to-liquid shift for example—where the magnitude of the effect tends to increase with the chemical-shift range of the nucleus). The magnitude of these medium effects on the NMR shieldings are known to be the same order of magnitude as electron-correlation and rovibrational effects, and therefore cannot be neglected if accurate comparisons with the liquid-phase measurements are needed.[212] In this section, DFT studies that have probed the intermolecular effects on the calculated shielding constants will be discussed for electrostatic (i.e., solvent, crystal, H-bonding), dispersion, and magnetic (i.e., ring currents) interactions. Since the experimental NMR shielding tensor components can act as sensitive probes of intermolecular interactions, their accurate calculation using DFT methods can provide important additional electronic structure information. Although the vast majority of *ab initio* studies use static interacting systems to model the intermolecular effects on NMR shielding predictions, in recent years, dynamic effects have also now been successfully included.[213,214] In the following sections, DFT-NMR studies that utilise static and dynamic approaches to model the intermolecular effects will be discussed.

8.1. H-bonding, solvent, and crystal effects

Two distinct theoretical approaches have been used to model the intermolecular effects in solvents and crystals on the NMR shielding constants: (i) the

specific type approach incorporates actual interactions such as specific H-bonding interactions, or include the actual nearest neighbour species (atom(s) or molecule(s)); (ii) the *non-specific* approach describes the intermolecular interactions in an average way by employing for example a dielectric medium or point charge model to simulate solvent and crystal effects. The main drawback of this approach is the fact that specific, close range interactions such as H-bonding will obviously not be described adequately.

8.1.1. *Specific interactions*

Inclusion of electron correlation is crucial to elucidate the molecular properties of the intramolecular hydrogen bonding systems.[215] One of the most important and active areas of theoretical NMR research involves the accurate representation of H-bonding effects.[216] Crucially, the DFT approach represents the only viable method for accurate NMR computation in larger, chemically and biologically important systems. For example, DFT-NMR studies have been used successfully to gain important information on H-bond donor–acceptor distances in interresidue DNA nucleic acids,[217] as well as on the relationship between proton chemical shifts and H-bond strengths.[218] Experimental solid state NMR techniques can provide crucial information on whether or not a hydrogen bond is present in a particular system since it acts as a sensitive probe of the shielding tensor of the H nucleus as well as the donor–acceptor nuclei involved in the H-bond. DFT-NMR isotropic and anisotropic shielding constants have been determined to evaluate the H-bonding properties of $CH\cdots O$ interactions based upon NMR spectra.[219] The electrostatic/covalent character of the H-bond remains controversial. For example, DFT and high level *ab initio* NMR studies have confirmed the covalent character of the hydrogen bonds in the clusters formed between F^- and $(HF)(n)$.[220]

The role of solvent effects on proton NMR shieldings remains an important area of theoretical research in a wide range of systems.[221,222] The use of continuum and discrete solvation models to simulate the solvent effects on the DFT(B3LYP)-NMR shieldings in hydrogen bonds have been investigated.[223] The solvent effects on the DFT-NMR proton chemical shifts in liquid water has proven an active area of research both in terms of accurately reproducing the experimentally observed gas-to-liquid chemical shifts, as well as understanding the physics behind these shifts.[213] In order to avoid the size limitations of conventional finite cluster methods, an *ab initio* DFT-NMR approach (using LDA) has been developed to calculate condensed phase shielding constants using an infinite, periodic system.[44,224] It has been used in conjunction with *ab initio* DFT Car–Parrinello molecular dynamics simulations to investigate the NMR chemical shifts of ice and liquid water as well as providing an insight into how sensitive the NMR properties are to geometric and electric field effects.[213] In test calculations, at fixed geometries, the DFT-NMR proton chemical shift predictions were found to be relatively insensitive to functional type (LDA and PW91). It was suggested that the DFT molecular

dynamic description of the H-bond geometries rather than the LDA chemical shift predictions might be responsible for discrepancies with experiment. The sensitivity of the proton chemical shifts of water under normal and super-critical conditions have also been shown to be very sensitive to the H-bond network in a similar DFT study.[225]

The most popular approach for modelling specific interactions involves computations that include neighbouring atoms. The limitation of this approach when only nearest neighbour atoms or molecules are included can be seen for example from the poor correlation obtained between DFT and experimentally observed ^{19}F chemical shifts in a series of solid alkali metal fluorides $[M_6F]^{5+}$.[226] The shieldings involving highly electronegative atoms seem to be sensitive not only to their nearest neighbours but also to their next nearest neighbours too. In such cluster type calculations the inclusion of neighbouring molecules can lead to significant basis-set superposition errors (BSSE).[8] These effects are generally not investigated in the majority of theoretical studies that investigate specific intermolecular interaction effects on NMR shielding constants. The counterpoise correction (CP) has been successfully applied in NMR studies in small systems.[227] It represents a correction equal to the difference between the shieldings obtained from the molecule in the presence of the basis functions of the other interacting unit (without its electrons or nuclei) and those from the complete 'supermolecule' unit. In some cases, the inclusion of BSSE effects have proved inappropriate in DFT-NMR studies in larger systems.[228]

An *ab initio* DFT method for calculating NMR shielding constants that include all the intermolecular interactions in solid periodic systems (crystals, surfaces, or polymers) and non-periodic systems (amorphous materials, liquids, or solids with defects) has been developed for the first time (MPL method).[44,229] Using the LDA functional in conjunction with pseudopotentials and a plane wave basis set, H-atom shieldings for the ionic LiH crystal and the H-bonded crystal HF were found to be excellent agreement with experiment (the H atoms are not effected by the use of these pseudopotentials). Other NMR applications of the MPL method have included investigations on insulators,[230] to aid characterisation of particular crystalline phases in carbon nitride compounds,[231] and on how the ^{13}C surface atom shieldings are affected by the presence of the localised electronic surface states[232] (the ^{13}C values were in fact found to vary linearly with the density of surface states). The MPL method has also been extended to include atomic orbital basis sets for comparative isolated molecular shielding calculations.[224]

8.1.2. *Non-specific interactions*

A popular approach that describes the long-range, non-specific *bulk* solvent effects on the NMR shielding parameters in the theoretical calculations utilises the dielectric continuum model. The solvation effects are taken into account within the framework of the self-consistent reaction field (SCRF) method

where the solute molecule polarises the solvent (described in terms of a uniform dielectric constant), which in turn, induces an electric field response (the 'reaction field') which then interacts with the solute. The various SCRF approaches vary in how they describe the cavity and the reaction field. The Polarisable Continuum Model (PCM) defines the cavity as a series of interlocking atomic spheres and has been utilised in several DFT-NMR applications.[233] The polarisation effects of the solvent on the calculated DFT-NMR shieldings have been taken into account in two alternative ways using the PCM method. The *indirect* approach optimises the geometry of the solute molecule in the solvent cavity and then calculates the chemical shift values at the optimised geometry. For different dielectric solvent strengths calculated B3LYP-NMR ^{1}H chemical shifts were found to correlate reasonably well with the experiment ones.[234] Alternatively, the solute shielding calculations are performed at a fixed geometry (usually gas-phase optimised) in the presence of the solvent field itself, as in a recent B3LYP-PCM study.[235] It is probably more advisable to follow the second approach, although optimisation of the structures in the presence of the solvent model as well would represent a fully consistent approach. Although the PCM model is incapable of describing the specific close-range interactions that may occur in solution, the experimental gas-to-liquid chemical shifts have been successfully estimated when used in conjunction with DFT(B3LYP)-NMR methods.[236] In addition, analysis of H-bond $n \rightarrow \pi^*$ excitations provided useful insight into the role of polarisation effects on the paramagnetic shielding term.

In molecules or crystals, a simple low cost approach to modelling electrostatic intermolecular effects is through the use of atom centered point charges. Obviously, the accuracy of this approach is critically dependent on how well the point charge distribution mimics the true electrostatic potential of the real interacting system. Although simplistic in nature, the point charge models derived from *ab initio* electrostatic potentials have been shown to be competitive with the nearest-neighbour cluster type methods. For example, crystalline intermolecular effects on the DFT (B3LYP, BLYP) ^{19}F and ^{15}N chemical shifts modelled with a point charge distribution and cluster methods were found to be in good agreement.[237,238] However, the use of charge-field approximations in conjunction with DFT (B3LYP)-NMR studies proved less satisfactory in accounting for the experimentally observed ^{19}F shieldings in larger systems.[228] The embedded cluster model (i.e., the geometry optimised bare cluster, suitably terminated, is embedded in either an array of point charges or nearest-neighbour atoms) has been used in conjunction with DFT-NMR methods. For example, the lattice effects on the ^{9}Si NMR chemical shifts of silane and hydroxyl groups in silica have been investigated.[239]

Solvent water effects on transition metal NMR chemical shifts have also been modelled using point charge distributions. ^{51}V DFT (B3LYP)-NMR chemical shift calculations were performed on the calculated equilibrium geometries and 'snapshot' configurations of a vanadate complex solvated with

12 water molecules (using O and H atom centred point charges obtained from a B3LYP population analysis of water) was obtained from molecular dynamics simulations using the DFT (BLYP) based Car–Parrinello scheme. The combined solvent and thermal averaging effects provided relatively small changes in the ^{51}V chemical shifts.[214] This point charge approach and an earlier study that used two actual water molecules to model specific solvation effects[240] produced similar changes in the calculated chemical shifts.

Finally, the effect of a static electric field on molecular magnetic properties (NMR shielding polarisabilities)[241] can provide valuable insight into the role of solvent and intramolecular effects on the NMR shielding constants. The author is unaware of any DFT-NMR calculations of shielding polarisabilities at present.

8.2. Intermolecular dispersion

The accurate description of van der Waals type interactions (corresponding to the long-range region of the NMR shielding surface) represents a difficult and important challenge. In order to describe the intermolecular dispersion effects arising from the long-range, non-local, attractive forces acting between the separated atoms/molecules, wavefunction-based *ab initio* methods employ a high level treatment of electron-correlation theory and large basis sets. In larger systems, DFT methods therefore represent the only viable approach to describe these important electron-correlation effects.

The influence of weak dispersion effects on NMR shielding constants has been investigated predominantly by high level *ab initio* wavefunction-based methods that have determined intermolecular NMR shielding surfaces in small van der Waals systems, such as He–He, Ne–Ne and Xe–X [X = CO_2, N_2, and CO] for example.[7,242–244] Ne–Ne intermolecular NMR shielding surfaces have been calculated using a range of density functionals (VWN, BPW91, BLYP and B3LYP) and their performance compared with the benchmark CCSD(T) surface.[7] At present, it still remains unclear whether or not the weak electron-correlation effects arising from intermolecular dispersion interactions in van der Waals type systems have any significant effect on the calculated DFT shielding constants. This, coupled with the fact that DFT methods tend to be fairly unreliable in their prediction of experimental intermolecular dispersion energies[10] indicates that the structural predictions rather than the NMR shielding calculations may be the limiting factor for DFT-NMR studies on these weakly bound systems.[7]

In order to describe intermolecular dispersion effects, the DFT method employed must contain some form of non-local ($1/r_{12}$) dependence with the correct long-range behaviour. It remains an open question as to whether or not hybrid or GGA functionals will perform better in these systems since, at large distances, where dispersion dominates, the interaction energy arising from

exchange effects vanishes since it depends only on the *overlapping* charge distributions.

8.3. Magnetic interactions

Molecules containing π-bonds can generate significant long range, through-space magnetic shielding or deshielding effects on nuclei that are positioned in their proximity. From a theoretical viewpoint, these through-space magnetic effects have been investigated by calculating the shieldings in a reference molecular probe placed in the vicinity of the functional group containing the π-bond(s) or from nucleus-independent chemical shift (NICS) calculations. For the latter, a three-dimensional magnetic shielding surface in the atoms and molecules can be generated[245] (normally the NMR shielding tensor is calculated at the *position of a nucleus* with a non-zero magnetic moment). A theoretical analysis of the origin of the through-space proton NMR deshieldings by selected organic functional groups has been carried out using the molecular probe and NICS approaches in conjunction with the PW91 functional.[246] An important indicator of aromaticity/antiaromaticity in cyclic organic compounds containing π-bonds is the presence of abnormal proton chemical shifts arising from the magnetic contributions generated by the ring-currents associated with mobile delocalised electrons. DFT-NICS methods (where the GIAO-B3LYP-NICS combination represents the most widely used approach) has been employed to investigate the shielding surfaces and centre-of-ring shieldings in a wide range of these important organic compounds in order to characterise their aromatic/antiaromatic character (see Ref. [247] and references therein for some representative examples). Overall, the DFT-NICS method provides results that are in agreement with experiment, although some discrepancies have been observed. The characterisation of the aromaticity in fullerenes and fullerene derivatives, as well as smaller fullerene systems and their heteroanalogues have been measured with encapsulated ^{3}He probe atoms and/or DFT-NICS.[248,249] In the absence of a suitable NMR active substituent, SOS-DFPT-NICS has been used to characterise aromaticity in inorganic rings by partitioning the total NICS into constituent NICS(σ) and NICS(π) contributions.[250]

9. RECENT DEVELOPMENTS IN *AB INITIO* NMR METHODS

Developments in high-level *ab initio* wavefunction-based methods provide crucially important benchmark calibrations for DFT-NMR methods in the absence of accurate experimental data. They also enable absolute shielding scales to be determined with an accuracy that is often higher than that

of experiment. In this section, some of the important methodological developments that have occurred in wavefunction-based *ab initio* calculations of NMR shielding constants will be discussed.

Analytic second derivatives in benchmark high-order many-body perturbation theory (MBPT)[251] and coupled-cluster (CC) theory have been developed and used in the determination of NMR shielding constants. For the CC-NMR methods, several approximate treatments of the triple excitations (CCSD(T), CCSDT-n ($n = 1$–3) and CC3) have been presented for the nuclei in H_2O, CO and N_2O.[252] Implementation of the analytic second derivatives has also been extended to the full CC singles, doubles, and triples model (CCSDT) providing the highest level benchmark shielding constants for the nuclei in BH, HF, CO, N_2, N_2O, and O_3.[253]

Unfortunately, due to their high computational costs, these high-level methodologies are only suitable for very small molecules. The MP2-GIAO approach represents the only viable wavefunction-based correlated method for calculating NMR shielding constants in larger systems. Crucially, for first- and second-row nuclei, it generally outperforms most conventional DFT functionals (although catastrophic failures in systems that contain large correlation effects or low-lying excited states have been observed i.e., in O_3 or transition metal complexes). Improved scaling in the computational cost for the computed GIAO-MP2 shieldings have been achieved using local correction methods (GIAO-LMP2). The differences in the calculated values between the two methods are small leading to the possibility of MP2 quality shielding predictions on larger systems.[254] MP2-GIAO quality shieldings have been achieved within the two-level ONIOM2(MP2-GIAO:HF-GIAO) scheme providing a substantial reduction in the computational costs.[255] The molecule is subdivided into two layers, MP2 theory is used in the inner layer that contains the most important part of the molecule, and the second layer is represented by the less sophisticated HF-GIAO treatment. Of course, several layers could be employed, with the outer-layers being represented by cheaper approaches in larger molecules. For example, the MNDO approximation has been used to determine shielding parameters for H, C, N, and O nuclei[256] and could be incorporated into the ONIOM scheme. The presence of high-symmetry in systems has been exploited in order to demonstrate the possibility of obtaining reliable NMR shielding constants predictions in large molecules involving more than 600 basis functions using direct MP2 methods.[257] Unfortunately, large chemically and biologically important systems tend to lack symmetry. In Section 6.2 the promising performance of mixed DFT/wavefunction-based methods for the prediction of NMR shielding constants was highlighted. An alternative approach involves variational-perturbation within the framework of DFT (the energy functional is expanded up to second-order in the perturbation). The calculated isotropic ^1H and ^{13}C NMR shieldings in a small range of compounds using the BLYP functional are found to be in reasonable agreement with

experiment.[258] Other variational-perturbation methods employing moderate size basis sets have also been used for the calculation of NMR shielding constants.[259]

Several *ab initio* relativistic NMR shielding studies have appeared in recent years. For example, full four-component relativistic random phase approximation calculations provide benchmark NMR shielding tensors in hydrogen halides.[260] The routine inclusion of the one-electron spin–orbit correction in calculations of hydrogen shieldings for hydrogens bonded to heavy atoms is recommended. In addition, for the heavy nucleus shieldings an additional mass-velocity correction should also be included. A comparison between Dirac–Fock calculations and quasi-relativistic methods for the prediction of NMR shielding constants of protons and heavy nuclei in XH_2 (X = O, S, Se, and Te) has also been undertaken.[261] The Dirac–Fock method is observed to be valid for the heavy elements up to Te. Further comparisons between the performance of *ab initio* relativistic four- and two-component methods highlights the superior performance of the former over the latter method.[262] The reliability of relativistic mass-velocity corrected perturbation Hamiltonians for the prediction ^{1}H NMR shieldings in a series of hydrogen halides has been assessed.[263]

Shielding surfaces, rovibrational effects, temperature dependence, and isotope effects on the NMR shieldings in a variety of systems have been investigated. Although there is excellent agreement between the calculated MCSCF shielding surfaces of water in two independent studies, there is a significant difference between the calculated equilibrium value of the shielding σ_e for ^{17}O.[264,265] Another MCSCF shielding surface study on acetylene indicates that calculated isotope effects within 10% of experimental can be obtained.[266] The influence of nuclear fluctuations on the calculated NMR shieldings of benzene and ethylene within the framework of a Feynman path integral-*ab initio* approach has been presented.[267] Zero-point vibrational effects on the computed Hartree–Fock ^{1}H NMR shieldings in a wide range of systems indicates that even without explicit inclusion of correlation effects significant errors in the chemical shifts (by more than 1 ppm in certain cases) is observed.[268] Vibrational averaging effects on the NMR shielding constants (calculated at the MP2 level) have been investigated in a model hydrogen-bonded complex $CN\cdots H\cdots NCH$.[269] The effect of an external electric field (via changes in the optimised structures—the electric field was turned off in the MP2-NMR shielding calculations) was investigated for complexes stabilised by N–H–N hydrogen bonds. It was suggested that the proton-shared or ion-pair N–H–N hydrogen bonds were unlikely to form in neutral complexes.

Intermolecular effects have been investigated in several *ab initio* NMR studies. The usefulness of shielding constant calculations to aid the detection and characterisation of H-bonds is highlighted in a growing number of theoretical studies. Progress in *ab initio* NMR studies of the hydrogen bond

have been reviewed[216] and the importance of electron correlation in strong H-bonds have been investigated.[122] Calculations at the MP2 level indicate that electron correlation has a strong effect on the ^{1}H isotropic and anisotropic chemical shifts of the hydrogen bonds and must be included in order to obtain accurate results. MP2 level studies on the ^{1}H NMR chemical shifts in a variety of H-bonds have also shown that a correlation exists between the increasing hydrogen bond strength and the increasing proton chemical shifts.[270] Benchmark (MP4 and CCSD) shielding constants in the water dimer have been reported and the effects from hydrogen bond formation have been quantified.[271] Electron correlation (MP2 level) and basis set effects on the ^{17}O and ^{1}H NMR shieldings in small water clusters $H_2O(n)$ ($n = 2$–6) have been investigated.[272] Whilst BSSE effects on the isotropic and anisotropic shieldings of the H-bonded protons could be safely neglected, this was found not to be the case for the oxygen atom involved in the H-bond. These small water cluster models were found to be an unreliable model for the prediction of NMR shieldings in water's liquid state even when SCRFs were included.[273] The influence of electrostatic and dispersion interactions on the NMR parameters in acetylene complexes ($C_2H_2 \cdots H+$ and $C_2H_2 \cdots He$) using high-level *ab initio* methods have also indicated that BSSE effects are negligible for the ^{1}H shieldings but cannot be ignored for the ^{13}C shieldings.[274]

The solvent effects (modelled using continuum electrostatic approximations) on the computed high level *ab initio* NMR properties of azole, H_2Se, acetylene, H_2S and HCN can be substantial,[212,275–277] and in general cannot be ignored if meaningful comparisons with solution state NMR is required. The effect of external electric and magnetic effects on the calculated NMR shielding constants have been investigated in several studies. Shielding polarisabilities arising from a static electric field on the NMR shielding constants have been calculated in several small molecules at the MPn ($n = 2$–3), and CC (L-CCD, CCSD(T)) levels of theory.[241,278] The effect of circularly polarised light on the NMR properties of CS_2 have also been reported.[279]

10. SUMMARY

Kohn–Sham DFT is the most widely used method in computational quantum chemistry offering the possibility of high accuracy at low computational cost. Present exchange–correlation functionals are not yet optimal for the prediction of NMR shielding constants that critically depend upon an accurate description of both the occupied *and* virtual orbitals. They have generally failed to compete with correlated *ab initio* methods for the prediction of NMR shielding constants. If the full potential of DFT is to be exploited in the determination of this important property then the errors must be reduced considerably.

The development of exchange–correlation functionals with improved exchange–correlation potentials represents one promising route because the

quality of the orbitals and eigenvalues critically depend upon the exchange–correlation potential in the functionals. Since the effect of the current-dependence of the exchange–correlation functional on the NMR shielding constant predictions remains unclear, further investigations that go beyond the LDA are needed. In addition, none of the conventional exchange–correlation functionals is self-interaction free even though this has been shown to represent a significant source of error in the shielding calculations. Research in these important areas that investigate systems containing heavier nuclei (especially transition metals) will be crucially important.

The role of exact orbital exchange on the calculated DFT-NMR shielding constants still remains controversial. Improved functionals without exact orbital exchange are theoretically desirable and recent studies have highlighted the fact that continuum functionals can be more successful than hybrid functionals for the determination of shielding constants involving first- and second-row atoms. However, at the present time it is still not possible to predict *a priori* how well a particular functional will perform for the metal shieldings in transition metal systems. Although progress has been made in trying to provide a proper understanding of the role of exact orbital exchange in these important systems, new insights are crucial for the future development of improved continuum functionals.

Improving DFT routes for the inclusion of relativistic effects in heavy atom systems where the computational costs are prohibitively large for wavefunction-based *ab initio* methods remains an important and active area of research. In recent years, the introduction of the ZORA–Hamiltonian within the framework of density functional NMR shielding calculations is showing considerable promise. Rovibrational and intermolecular effects are also important factors that must be taken into account in order to provide a more meaningful comparison with experiment. The success of density functional approaches for the inclusion of these important effects in the NMR shielding calculations is encouraging.

Acknowledgements

During the period of writing this review the author gratefully acknowledges the Edinburgh University Computing Service for the generous provision of time on their systems. The author also thanks Dr David Tozer for support and helpful discussions.

REFERENCES

1. F. Bloch and I. I. Rabi, *Rev. Mod. Phys*., 1945, **17**, 237.
2. E. M. Purcell, H. C. Torrey and R. V. Pound, *Phys. Rev*., 1946, **69**, 37.

3. M. Kaupp, V. G. Malkin and O. L. Malkina, *Encyclopedia of Computational Chemistry*, P.v.R. Schleyer, editor-in-chief, Wiley, New York, 1998, 1857.
4. N. F. Ramsey, *Phys. Rev.*, 1950, **78**, 699.
5. G. Schreckenbach and T. Ziegler, *Theor. Chem. Acc.*, 1998, **99**, 71.
6. C.-H. Hu and D. P. Chong, *Encyclopedia of Computational Chemistry*, P.v.R. Schleyer, editor-in-chief, Wiley, New York, 1998, 664.
7. M. Buhl, M. Kaupp, O. L. Malkina and V. G. Malkin, *J. Comput. Chem.*, 1999, **20**, 91.
8. T. Helgaker, M. Jaszunski and K. Ruud, *Chem. Rev.*, 1999, **99**, 293.
9. C. J. Jameson and A. C. de Dios, *Specialist Periodical Reports on NMR*, Vol. 31, G. A. Webb, ed., Royal Society of Chemistry, London, 2002.
10. W. Koch and M. C. Holthausen, *A Chemist's Guide to Density Functional Theory*, Wiley-VCH, Weinheim, 2001. Chapter 11.
11. J. Gauss and J. F. Stanton, *Adv. Chem. Phys.*, 2002, **123**, 355.
12. A. C. de Dios, *Magn. Reson. Chem.*, 1996, **34**, 773.
13. W. H. Flygare and R. C. Benson, *Mol. Phys.*, 1971, **20**, 225.
14. W. H. Flygare, *Chem. Rev.*, 1974, **74**, 653.
15. N. F. Ramsey, *Molecular Beams*, Clarendon Press, Oxford, 1956.
16. D. K. Hindermann and C. D. Cornwell, *J. Chem. Phys.*, 1968, **48**, 4148.
17. A. K. Jameson and C. J. Jameson, *Chem. Phys. Lett.*, 1987, **134**, 461.
18. C. J. Jameson and A. K. Jameson, *Chem. Phys. Lett.*, 1988, **149**, 300.
19. W. T. Raynes, R. McVay and S. J. Wright, *J. Chem. Soc., Faraday Trans. 2*, 1989, **85**, 759.
20. C. J. Jameson, A. C. de Dios and A. K. Jameson, *Chem. Phys. Lett.*, 1990, **167**, 575.
21. K. Jackowski, M. Jaszunski, W. Makulski and J. Vaara, *J. Magn. Reson.*, 1998, **135**, 444.
22. M. Gee, R. E. Wasylishen and A. Laaksonen, *J. Phys. Chem.*, 1999, **103**, 10 805.
23. K. J. Jackowski, *J. Mol. Struct.*, 2001, **563**, 159.
24. W. Makulski and K. Jackowski, *Chem. Phys. Lett.*, 2001, **341**, 369.
25. A. Laaksonen and R. E. Wasylishen, *J. Am. Chem. Soc.*, 1995, **117**, 392.
26. C. J. Jameson, *Encyclopedia of NMR*, Vol. 2, D. M. Grant and R. K. Harris (Eds.-in-Chief), J. Wiley & Sons, Chichester, 1996, 1273.
27. C. J. Jameson and A. K. Jameson, *Chem. Phys. Lett.*, 1987, **135**, 254.
28. K. K. Baldridge and J. S. Siegel, *J. Phys. Chem. A*, 1999, **103**, 4038.
29. T. Heine, A. Goursot, G. Seifert and J. Weber, *J. Phys. Chem. A*, 2001, **105**, 620.
30. D. A. Forsyth and A. B. Sebag, *J. Am. Chem. Soc.*, 1997, **119**, 9483.
31. W. B. Smith, *Magn. Reson. Chem.*, 1999, **37**, 107.
32. I. Alkorta and J. Elguero, *Struct. Chem.*, 1998, **9**, 187.
33. P. Hohenberg and W. Kohn, *Phys. Rev. A*, 1964, **136**, 864.
34. W. Kohn and L. J. Sham, *Phys. Rev. A*, 1965, **140**, 1133.
35. A. K. Rajagopal and J. C. Callaway, *Phys. Rev. B*, 1973, **7**, 1912.
36. G. Vignale and M. Rasolt, *Phys. Rev. Lett.*, 1987, **59**, 2360.
37. G. Vignale and M. Rasolt, *Phys. Rev. B*, 1988, **37**, 10 685.
38. A. M. Lee, N. C. Handy and S. M. Colwell, *J. Chem. Phys.*, 1995, **103**, 10 095.
39. A. D. Becke, *Can. J. Chem.*, 1996, **74**, 995.
40. P. J. Wilson and D. J. Tozer, *Chem. Phys. Lett.*, 2001, **337**, 341.
41. F. R. Salsbury and R. A. Harris, *J. Chem. Phys.*, 1997, **107**, 7350.
42. F. R. Salsbury and R. A. Harris, *Chem. Phys. Lett.*, 1997, **279**, 247.
43. A. Bagno and M. Bonchio, *Eur. J. Inorg. Chem.*, 2002, **6**, 1475.
44. F. Mauri, B. G. Pfrommer and S. G. Louie, *Phys. Rev. Lett.*, 1996, **77**, 5300.
45. G. A. Webb, P. B. Karadakov and J. A. England, *B. Pol. Acad. Sci.-Chem.*, 2000, **48**, 101.
46. T. Kupka, M. Kolaski, G. Pasterna and K. Ruud, *J. Mol. Struct. (Theochem.)*, 1999, **467**, 63.
47. T. Helgaker, P. J. Wilson, R. D. Amos and N. C. Handy, *J. Chem. Phys.*, 2000, **113**, 1.
48. P. Laszlo *NMR of Newly Accessible Nuclei*, Vol. 1, Academic Press, New York, 1983, 84.
49. S. Huzinaga, *Approximate Atomic Functions*, University of Alberta, Edmonton, 1971.

50. W. Kutzelnigg, U. Fleischer and M. Schlindler, *NMR-Basic Principles and Progress*, Vol. 23, Springer, Heidelberg, 1990.
51. M. Kaupp, O. L. Malkina and V. G. Malkin, *J. Chem. Phys.*, 1997, **106**, 9201.
52. F. London, *J. Phys. Radium*, 1937, **8**, 397.
53. H. F. Hameka, *Mol. Phys.*, 1958, **1**, 203.
54. H. F. Hameka, *Mol. Phys.*, 1959, **2**, 64.
55. R. Ditchfield, *Mol. Phys.*, 1974, **27**, 789.
56. K. W. Wolinski, J. F. Hinton and P. Pulay, *J. Am. Chem. Soc.*, 1990, **112**, 8251.
57. G. Schreckenback and T. Ziegler, *J. Phys. Chem.*, 1995, **99**, 606.
58. A. M. Lee, N. C. Handy and S. M. Colwell, *J. Chem. Phys.*, 1995, **103**, 10 095.
59. G. Rauhut, S. Puyear, K. Wolinski and P. Pulay, *J. Phys. Chem.*, 1996, **100**, 6310.
60. J. R. Cheeseman, G. W. Trucks, T. A. Keith and M. J. Frisch, *J. Chem. Phys.*, 1996, **104**, 5497.
61. K. Kutzelnigg, *Isr. J. Chem.*, 1980, **19**, 193.
62. M. Schindlerand and W. Kutzelnigg, *J. Chem. Phys.*, 1982, **76**, 1919.
63. V. G. Malkin, O. L. Malkina and D. R. Salahub, *Chem. Phys. Lett.*, 1993, **204**, 80.
64. A. E. Hansen and T. D. Bouman, *J. Chem. Phys.*, 1985, **82**, 5035.
65. T. A. Keith and R. F. W. Bader, *Chem. Phys. Lett.*, 1992, **194**, 1.
66. T. A. Keith and R. F. W. Bader, *J. Chem. Phys.*, 1993, **99**, 3669.
67. R. F. W. Bader and T. A. Keith, *J. Chem. Phys.*, 1993, **99**, 3683.
68. T. A. Keith and R. F. W. Bader, *Chem. Phys. Lett.*, 1993, **210**, 223.
69. L. Olsson and D. Cremer, *J. Chem. Phys.*, 1996, **105**, 8995.
70. C. van Wullen, *Phys. Chem. Chem. Phys.*, 2000, **2**, 2137.
71. J. C. C. Chan and S. C. F. Au-Yeung, *J. Mol. Struct. (Theochem.)*, 1997, **393**, 93.
72. P. R. Rablen, S. A. Pearlman and J. Finkbiner, *J. Phys. Chem. A*, 1999, **103**, 7357.
73. K. B. Wiberg, J. D. Hammer, K. W. Zilm and J. R. Cheeseman, *J. Org. Chem.*, 1999, **64**, 6394.
74. D. S. Wishart and D. A. Case, *Nuclear Magnetic Resonance of Biological Macromolecules, Methods in Enzymology*, Vol. 338, Part A, 2001, 3–34.
75. J. C. Facelli, *J. Phys. Chem. B*, 1998, **102**, 2111.
76. M. D. Segall, *J. Phys. Condens. Matter*, 2002, **14**, 2957.
77. D. Sitkoff and D. A. Case, *J. Am. Chem. Soc.*, 1997, **119**, 12 262.
78. R. Salzmann, M. T. McMahon, N. Godbout, L. K. Sander, M. Wojdelski and E. Oldfield, *J. Am. Chem. Soc.*, 1999, **121**, 3818.
79. N. Godbout, L. K. Sanders, R. Salzmann, R. H. Havlin, M. Wojdelski and E. Oldfield, *J. Am. Chem. Soc.*, 1999, **121**, 3829.
80. J. E. Rich, M. N. Manalo and A. C. de Dios, *J. Phys. Chem. A*, 2000, **104**, 5837.
81. X. P. Xu and S. C. F. Au-Yeung, *J. Phys. Chem. B*, 2000, **104**, 5641.
82. M. Levy and J. P. Perdew, *Int. J. Quantum Chem.*, 1994, **49**, 539.
83. J. P. Perdew and K. Schmidt, *Density Functional Theory and its Applications to Materials*, V. E. Van Doren, K. Van Alseoy and P. Geerlings (eds), American Institute of Physics, 2001.
84. J. C. Slater, *Quantum Theory of Molecules and Solids In: "The Self-Consistent Field for Molecules and Solids"*, Vol. 4, McGraw-Hill, New York, 1947.
85. S. H. Vosko, L. Wilk and M. Nusair, *Can. J. Phys.*, 1980, **58**, 1200.
86. P. J. Wilson, R. D. Amos and N. C. Handy, *Mol. Phys.*, 1999, **97**, 757.
87. S. Patchkovskii, J. Autschbach and T. Ziegler, *J. Chem. Phys.*, 2001, **115**, 26.
88. E. Fadda, M. E. Casida and D. R. Salahub, *Int. J. Quantum Chem.*, 2003, **91**, 67.
89. E. Fadda, M. E. Casida and D. R. Salahub, submitted to *J. Chem. Phys.*
90. A. D. Becke, *J. Chem. Phys.*, 1986, **84**, 4524.
91. J. P. Perdew and Y. Wang, *Phys. Rev. B*, 1986, **33**, 8800.
92. A. D. Becke, *Phys. Rev. A*, 1988, **38**, 3098.
93. J. P. Perdew and W. Yue, *Phys. Rev. B*, 1986, **33**, 8822; *erratum*, 1986, **34**, 7406.
94. C. Lee, W. Yang and R. G. Parr, *Phys. Rev. B*, 1988, **37**, 785.

95. J. P. Perdew and Y. Wang, *Phys. Rev. B*, 1992, **45**, 13 244.
96. J. P. Perdew, *Electronic Structures of Solids '91*, P. Ziesche and H. Eschrig, eds., Akademie Verlag, Berlin, 1991, 11.
97. V. G. Malkin, O. L. Malkina, M. E. Casida and D. R. Salahub, *J. Am. Chem. Soc.*, 1994, **116**, 5898.
98. A. D. Becke, *J. Chem. Phys.*, 1997, **107**, 8554.
99. K. Raghavachari, P. C. Redfern and J. A. Pople, *J. Chem. Phys.*, 1997, **106**, 1063.
100. F. A. Hamprecht, A. J. Cohen, D. J. Tozer and N. C. Handy, *J. Chem. Phys.*, 1998, **109**, 6264.
101. P. J. Wilson, R. D. Amos and N. C. Handy, *Chem. Phys. Lett.*, 1999, **312**, 475.
102. J. P. Perdew, K. Burke and M. Ernzerhof, *Phys. Rev. Lett.*, 1996, **77**, 3865; *erratum*, 1997, **78**, 1396.
103. C. Adamo and V. Barone, *Chem. Phys. Lett.*, 1998, **298**, 113.
104. C. Adamo, M. Cossi and V. Barone, *J. Mol. Struct. (Theochem.)*, 1999, **493**, 145.
105. P. J. Wilson, R. D. Amos and N. C. Handy, *Phys. Chem. Chem. Phys.*, 2000, **2**, 187.
106. D. C. Langreth and J. P. Perdew, *Phys. Rev. B*, 1977, **15**, 2884.
107. A. D. Becke, *J. Chem. Phys.*, 1993, **98**, 5648.
108. P. J. Stephens, F. Devlin, C. F. Chabalowski and M. J. Frisch, *J. Phys. Chem.*, 1994, **98**, 11 623.
109. A. D. Becke, *J. Chem. Phys.*, 1996, **104**, 1040.
110. J. C. C. Chan and H. Eckert, *J. Mol. Struct. (Theochem.)*, 2001, **535**, 1.
111. H. L. Schmider and A. D. Becke, *J. Chem. Phys.*, 1998, **108**, 9624.
112. A. D. Becke, *J. Chem. Phys.*, 1998, **109**, 2092.
113. M. Bienati, C. Adamo and V. Barone, *Chem. Phys. Lett.*, 1999, **311**, 69.
114. P. J. Wilson, T. J. Bradley and D. J. Tozer, *J. Chem. Phys.*, 2001, **115**, 9233.
115. G. Menconi, P. J. Wilson and D. J. Tozer, *J. Chem. Phys.*, 2001, **114**, 3958.
116. C. Adamo and V. Barone, *J. Chem. Phys.*, 1999, **110**, 6158.
117. C. Adamo and V. Barone, *J. Chem. Phys.*, 1998, **108**, 664.
118. D. Vikic-Topic and L. Pejov, *Croatica Chemica Acta*, 2001, **74**, 277.
119. D. Vikic-Topic and L. Pejov, *J. Chem. Inf. Comp. Sci.*, 2001, **41**, 1478.
120. K. B. Wiberg, *J. Comput. Chem.*, 1999, **20**, 1299.
121. B. Wang, U. Fleischer, J. F. Hinton and P. Pulay, *J. Comput. Chem.*, 2001, **22**, 1887.
122. D. H. Barich, J. B. Nicholas and J. F. Haw, *J. Phys. Chem. A*, 2001, **105**, 4708.
123. A. Karlsson, A. Broo and P. Ahlberg, *Can. J. Chem.-Revue Canadienne de Chimie*, 1999, **77**, 628.
124. P. Borowski, T. Janowski and K. Wolinski, *Mol. Phys.*, 2000, **98**, 1331.
125. B. Wang, J. F. Hinton and P. Pulay, *J. Comput. Chem.*, 2002, **23**, 492.
126. D. R. Eaton, R. J. Buist and B. G. Sayer, *Can. J. Chem.*, 1987, **65**, 1332.
127. M. Kaupp, V. G. Malkin, O. L. Malkina and D. R. Salahub, *J. Am. Chem. Soc.*, 1995, **117**, 1851.
128. P. Zhou, S. C. F. Au-Yeung and X. P. Xu, *J. Am. Chem. Soc.*, 1999, **121**, 1030.
129. R. Bramley, M. Brorson, A. M. Sargeson and C. E. Schaffer, *J. Am. Chem. Soc.*, 1985, **107**, 2780.
130. J. C. C. Chan, S. C. F. Au-Yeung, P. J. Wilson and G. A. Webb, *J. Mol. Struct. (Theochem.)*, 1996, **365**, 125.
131. N. Godbout and E. Oldfield, *J. Am. Chem. Soc.*, 1997, **119**, 8065.
132. M. Buhl, *Theor. Chem. Acc.*, 2002, **107**, 336.
133. M. Buhl, *Chem. Phys. Lett.*, 1997, **267**, 251.
134. G. Schreckenbach, *J. Chem. Phys.*, 1999, **110**, 11 936.
135. G. Schreckenbach and T. Ziegler, *Int. J. Quantum Chem.*, 1997, **61**, 899.
136. M. Buhl and F. A. Hamprecht, *J. Comput. Chem.*, 1998, **19**, 113.
137. Y. Ruiz-Morales and T. Ziegler, *J. Phys. Chem.*, 1998, **102**, 3970.
138. M. Buhl, *Chem. Eur. J.*, 1999, **5**, 3514.

139. A. Bagno and M. Bonchio, *Chem. Phys. Lett*., 2000, **317**, 123.
140. Y. Ruiz-Morales, G. Schreckenbach and T. Ziegler, *Organometallics*, 1996, **15**, 3920.
141. B. N. Figgis, R. G. Kidd and R. S. Nyholm, *Proc. R. Soc. London, Ser. A*, 1962, **269**, 469.
142. M. Kaupp, V. G. Malkin, O. L. Malkina and D. R. Salahub, *Chem. Phys. Lett*., 1995, **235**, 382.
143. Y. Ruiz-Morales, G. Schreckenbach and T. Ziegler, *J. Phys. Chem*., 1996, **100**, 3359.
144. M. Kaupp, *Chem. Ber*., 1996, **129**, 527.
145. R. Salzmann, M. Kaupp, M. T. McMahon and E. Oldfield, *J. Am. Chem. Soc*., 1998, **120**, 4771.
146. A. W. Ehlers, Y. Ruiz-Morales, E. J. Baerends and T. Ziegler, *Inorg. Chem*., 1997, **36**, 5031.
147. M. T. McMahon, A. C. de Dios, N. Godbout, R. Salzmann, D. D. Laws, H. B. Le, R. H. Havlin and E. Oldfield, *J. Am. Chem. Soc*., 1998, **120**, 4784.
148. G. Schreckenbach, Y. Ruiz-Morales and T. Ziegler, *J. Chem. Phys*., 1996, **104**, 8605.
149. P. J. Wilson, *Mol. Phys*., 2001, **99**, 363.
150. W. Nakanishi and S. Hayashi, *J. Phys. Chem*., 1999, **103**, 6074.
151. G. Grossmann, M. J. Potrzebowski, U. Fleischer, K. Kruger, O. L. Malkina and W. Ciesielski, *Solid State Nucl. Magn. Reson*., 1998, **13**, 71.
152. J. Lounila, J. Vaara, Y. Hiltunen, A. Pulkkinen, J. Jokisaari, M. AlaKorpela and K. Ruud, *J. Chem. Phys*., 1997, **107**, 1350.
153. R. Habrovsky, B. Wrackmeyer, O. L. Malkina and V. G. Malkin, *Chemicke Listy*, 1997, **91**, 731.
154. P. Avalle, R. K. Harris and R. D. Fischer, *Phys. Chem. Chem. Phys*., 2002, **4**, 3558.
155. P. Avalle, R. K. Harris, P. B. Karadakov and Philip J. Wilson, *Phys. Chem. Chem. Phys*., 2002, **24**, 5925.
156. R. Vivas-Reyes, F. De Proft, M. Biesemans, R. Willem and P. Geerlings, *J. Phys. Chem. A*, 2002, **106**, 2753.
157. Y. Ruiz-Morales, G. Schreckenbach and T. Ziegler, *J. Phys. Chem*., 1997, **101**, 4121.
158. V. G. Malkin, O. L. Malkina and D. R. Salahub, *J. Chem. Phys*., 1996, **104**, 1163.
159. C. van Wullen, *J. Chem. Phys*., 1996, **104**, 1165.
160. P. Pyykko, *Chem. Phys*., 1983, **74**, 1.
161. M. Kaupp and O. L. Malkina, *J. Chem. Phys*., 1998, **108**, 3648.
162. M. Buhl, G. Hopp, W. von Philipsborn, M.-H. Prosenc, U. Rief and H.-H. Brintzinger, *Organometallics*, 1996, **15**, 778.
163. M. Kaupp, *Chem. Ber*., 1996, **129**, 535.
164. G. Schreckenbach and T. Ziegler, *Int. J. Quantum Chem*., 1996, **60**, 753.
165. S. K. Wolff, T. Ziegler, E. van Lenthe and E. J. Baerends, *J. Chem. Phys*., 1999, **110**, 7689.
166. R. Bouten, E. J. Baerends, E. van Lenthe, L. Visscher, G. Schreckenbach and T. Ziegler, *J. Phys. Chem. A*, 2000, **104**, 5600.
167. T. M. Gilbert and T. Ziegler, *J. Phys. Chem. A*, 1999, **103**, 7535.
168. A. Rodriguez-Fortea, P. Alemany and T. Ziegler, *J. Phys. Chem*., 1999, **103**, 8288.
169. D. L. Bryce and R. E. Wasylishen, *Phys. Chem. Chem. Phys*., 2002, **4**, 3591.
170. G. Schreckenbach, P. J. Hay and R. L. Martin, *J. Comput. Chem*., 1999, **20**, 70.
171. G. Schreckenbach, S. K. Wolff and T. Ziegler, *J. Phys. Chem. A*, 2000, **104**, 8244.
172. B. Minaev, J. Vaara, K. Ruud, O. Vahtras and H. Agren, *Chem. Phys. Lett*., 1998, **295**, 455.
173. J. Vaara, O. L. Malkina, H. Stoll, V. G. Malkin and M. Kaupp, *J. Chem. Phys*., 2001, **114**, 61.
174. J. Vaara, K. Ruud and O. J. Vahtras, *J. Chem. Phys*., 1999, **111**, 2900.
175. S. K. Wolff and T. Ziegler, *J. Chem. Phys*., 1998, **109**, 895.
176. M. Kaupp, C. Aubauer, G. Engelhardt, T. M. Klapötke and O. L. Malkina, *J. Chem. Phys*., 1999, **110**, 3897.
177. P. Lantto, J. Vaara, A. M. Kantola, V. V. Telkki, B. Schimmelpfennig, K. Ruud and J. Jokisaari, *J. Am. Chem. Soc*., 2002, **124**, 2762.
178. M. Kaupp, O. L. Malkina, V. G. Malkin and P. Pyykko, *Chem.-Eur. J*., 1998, **4**, 118.
179. V. G. Malkin, O. L. Malkina and D. R. Salahub, *Chem. Phys. Lett*., 1996, **261**, 335.
180. P. J. Wilson and D. J. Tozer, *J. Chem. Phys*., 2002, **116**, 10 139.

181. A. M. Lee and N. C. Handy, *Phys. Rev. A*, 1999, **59**, 209.
182. J. Garza, J. A. Nichols and D. A. Dixon, *J. Chem. Phys.*, 2000, **113**, 6029.
183. R. T. Sharp and G. K. Horton, *Phys. Rev.*, 1953, **30**, 317.
184. M. R. Norman and D. D. Koelling, *Phys. Rev. B*, 1984, **30**, 5530.
185. Q. Zhao, R. C. Morrison and R. G. Parr, *Phys. Rev. A*, 1994, **50**, 2138.
186. V. Polo, E. Kraka and D. Cremer, *Mol. Phys.*, 2002, **100**, 1771.
187. S. Patchkovskii and T. Ziegler, *J. Phys. Chem. A*, 2002, **106**, 1088.
188. M. J. Allen and D. J. Tozer, *Mol. Phys.*, 2002, **100**, 433.
189. T. W. Keal and D. J. Tozer, submitted to *J. Chem. Phys.*
190. J. P. Perdew, R. G. Parr, M. Levy and J. L. Balduz, *Phys. Rev. Lett.*, 1982, **49**, 1691.
191. D. J. Tozer, *Phys. Rev. A*, 1997, **56**, 2726.
192. M. E. Casida, K. C. Casida and D. R. Salahub, *Int. J. Quantum Chem.*, 1998, **70**, 933.
193. M. E. Casida and D. R. Salahub, *J. Chem. Phys.*, 2000, **113**, 8918.
194. D. J. Tozer and N. C. Handy, *J. Chem. Phys.*, 1998, **109**, 10 180.
195. U. Salzner, J. B. Lagowski, P. G. Pickup and R. A. Poirier, *J. Comput. Chem.*, 1997, **18**, 1943.
196. D. J. Tozer and N. C. Handy, *J. Chem. Phys.*, 1998, **108**, 2545.
197. C. J. Jameson, *J. Chem. Phys.*, 1980, **73**, 6013.
198. C. J. Jameson and A. C. deDios, *Nuclear Magnetic Shieldings and Molecular Structure NATO ASI Series C*, Vol. 386, J. Tossell, ed., Kluwer, Dordrecht, 1993.
199. C. J. Jameson, *Annu. Rev. Phys. Chem.*, 1996, **47**, 135.
200. B. Cromp, T. Carrington, D. R. Salahub, O. L. Malkina and V. G. Malkin, *J. Chem. Phys.*, 1999, **110**, 7153.
201. D. Sundholm and J. Gauss, *Mol. Phys.*, 1997, **92**, 1007.
202. M. Buhl, F. T. Mauschick, F. Terstegen and B. Wrackmeyer, *Angewandte Chemie-International Edition*, 2002, **41**, 2312.
203. D. Sundholm, J. Gauss and A. Schafer, *J. Chem. Phys.*, 1996, **105**, 11 051.
204. M. Garcia-Viloca, R. Gelabert, A. Gonzalez-Lafont, M. Moreno and J. M. Lluch, *J. Am. Chem. Soc.*, 1998, **120**, 10 203.
205. S. Bolvig and P. E. Hansen, *Curr. Org. Chem.*, 1997, **4**, 1350.
206. S. Bolvig and P. E. Hansen, *Curr. Org. Chem.*, 2000, **4**, 19.
207. A. M. Aicken, A. D. Buckingham and Y. Tantirungrotechai, *Mol. Phys.*, 1999, **97**, 167.
208. I. Paidarova, J. Komasa and J. Oddershede, *Mol. Phys.*, 1991, **72**, 559.
209. S. P. A. Sauer, V. Pirko, I. Paidarová and J. Oddershede, *Chem. Phys.*, 1994, **184**, 1.
210. C. W. Swalina, E. P. O'Brien and G. Moyna, *Magn. Reson. Chem.*, 2002, **40**, 195.
211. M. Stahl, U. Schopfer, G. Frenking and R. W. Hoffmann, *Mol. Phys.*, 1997, **92**, 569.
212. K. V. Mikkelsen, K. Ruud and T. Helgaker, *J. Comput. Chem.*, 1999, **20**, 1281.
213. G. Pfrommer, F. Mauri and S. G. Louie, *J. Am. Chem. Soc.*, 2000, **122**, 123.
214. M. Buhl and M. Parrinello, *Chem. Eur. J.*, 2001, **7**, 4487.
215. Y. Kwon, *J. Mol. Struct. (Theochem.)*, 2000, **532**, 227.
216. J. E. Del Bene and M. J. T. Jordan, *J. Mol. Struct. (Theochem.)*, 2001, **573**, 11.
217. M. Barfield, A. J. Dingley, J. Feigon and S. Grzesiek, *J. Am. Chem. Soc.*, 2001, **123**, 4014.
218. G. A. Kumar and M. A. McAllister, *J. Org. Chem.*, 1998, **63**, 6968.
219. S. Scheiner, Y. Gu and T. Kar, *J. Mol. Struct. (Theochem.)*, 2000, **500**, 441.
220. I. G. Shenderovich, S. N. Smirnov, G. S. Denisov, V. A. Gindin, N. S. Golubev, A. Dunger, R. Reibke, S. Kirpekar, O. L. Malkina, H. H. Limbach, *Berichte der Bunsen-Gesellschaft-Phys. Chem. Chem. Phys.*, 1998, **102**, 422.
221. V. Barone, O. Crescenzi and R. Improta, *Quant. Struct.-Act. Relat.*, 2002, **21**, 105.
222. J. B. Nicholas, *Topics Catal.*, 1999, **9**, 181.
223. B. Mennucci, J. M. Martinez and J. Tomasi, *J. Phys. Chem. A*, 2001, **105**, 7287.
224. T. Gregor, F. Mauri and R. Car, *J. Chem. Phys.*, 1999, **111**, 1815.
225. D. Sebastiani and M. Parrinello, *CHEMPHYSCHEM*, 2002, **3**, 675.
226. S. H. Cai, Z. Chen, X. Xu and H. L. Wan, *Chem. Phys. Lett.*, 1999, **302**, 73.

227. A. C. de Dios and E. Oldfield, *Chem. Phys. Lett*., 1993, **205**, 108.
228. A. DerHovanessian, P. R. Rablen and A. Jain, *J. Phys. Chem. A*, 2000, **104**, 6056.
229. S. G. Louie, *Phys. Rev. Lett*., 1997, **79**, 2340.
230. C. J. Pickard and F. Mauri, *Phys. Rev. B*, 2001, **63**, 24 5101.
231. Y. G. Yoon, B. G. Pfrommer, F. Mauri and S. G. Louie, *Phys. Rev. Lett*., 1998, **80**, 3388.
232. F. Mauri, B. G. Pfrommer and S. G. Louie, *Phys. Rev. B*, 1999, **60**, 2941.
233. J. Tomasi, R. Cammi and B. Mennucci, *Int. J. Quantum Chem*., 1999, **75**, 783.
234. M. Garcia-Viloca, A. Gonzalez-Lafont and J. M. Lluch, *Org. Lett*., 2001, **3**, 589.
235. R. Fazaeli, M. Monajjemi, F. Ataherian and K. Zare, *J. Mol. Struct. (Theochem.)*, 2002, **581**, 51.
236. B. Mennucci, *J. Am. Chem. Soc*., 2002, **124**, 1506.
237. D. Solis, M. B. Ferraro and J. C. Facelli, *J. Mol. Struct*., 2002, **602**, 159.
238. M. B. Ferraro, V. Repetto and J. C. Facelli, *Solid State Nucl. Magn. Reson*., 1998, **10**, 185.
239. J. Casanovasa, F. Illasb and G. Pacchionic, *Chem. Phys. Lett*., 2000, **326**, 523.
240. M. Bühl, *J. Comput. Chem*., 1999, **20**, 1254.
241. A. Rizzo and J. Gauss, *J. Chem. Phys*., 2002, **116**, 869.
242. C. J. Jameson and A. C. de Dios, *J. Chem. Phys*., 1992, **97**, 417.
243. C. J. Jameson and A. C. deDios, *J. Chem. Phys*., 1997, **107**, 4253.
244. C. van Wullen and W. Kutzelnigg, *J. Chem. Phys*., 1996, **104**, 2330.
245. P.v.R. Schleyer, C. Maerker, A. Dransfeld, H. Jiao and N.J.R.v.E. Hommes, *J. Am. Chem. Soc*., 1996, **118**, 6317.
246. N. H. Martin, J. D. Brown, K. H. Nance, H. F. Schaefer, P. V. Schleyer, Z. X. Wang and H. L. Woodcock, *Org. Lett*., 2001, **3**, 3823.
247. I. Alkorta, I. Rozas and J. Elguero, *Tetrahedron*, 2001, **57**, 6043.
248. M. Buhl, *Zeit. Anorg. Allg. Chem*., 2000, **626**, 332.
249. Z. F. Chen, H. J. Jiao, M. Buhl, A. Hirsch and W. Thiel, *Theor. Chem. Acc*., 2001, **106**, 352.
250. P.v.R. Schleyer, J. Haijun, N.J.R.v.E. Hommes, V. G. Malkin and O. L. Malkina, *J. Am. Chem. Soc*., 1997, **119**, 12 669.
251. J. F. Stanton and J. Gauss, *Int. Rev. Phys. Chem*., 2000, **19**, 61.
252. J. Gauss and J. F. Stanton, *Phys. Chem. Chem. Phys*., 2000, **2**, 2047.
253. J. Gauss, *J. Chem. Phys*., 2002, **116**, 4773.
254. J. Gauss and H.-J. Werner, *Phys. Chem. Chem. Phys*., 2000, **2**, 2083.
255. P. B. Karadakov and K. Morokuma, *Chem. Phys. Lett*., 2000, **317**, 589.
256. S. Patchkovskii and W. Thiel, *J. Comput. Chem*., 1999, **20**, 1220.
257. M. Kollwitz, M. Haser and J. Gauss, *J. Chem. Phys*., 1998, **108**, 8295.
258. A. Putrino, D. Sebastiani and M. Parrinello, *J. Chem. Phys*., 2000, **113**, 7102.
259. V. B. Mushkin and R. M. Aminova, *J. Mol. Struct. (Theochem.)*, 2001, **572**, 185.
260. L. Visscher, T. Enevoldsen, T. Saue, H. J. A. Jensen and J. Oddershede, *J. Comput. Chem*., 1999, **20**, 1262.
261. M. Hada, R. Fukuda and H. Nakatsuji, *Chem. Phys. Lett*., 2000, **321**, 452.
262. H. M. Quiney, H. Skaane and I. P. Grant, *Adv. Quantum Chem. Quantum Syst. Chem. Phys*., 1999, **32**, 1.
263. T. Baba and H. Fukui, *Mol. Phys*., 2002, **100**, 623.
264. R. D. Wigglesworth, W. T. Raynes, S. P. A. Sauer and J. Oddershede, *Mol. Phys*., 1999, **96**, 1595.
265. J. Vaara, J. Lounila, K. Ruud and T. Helgaker, *J. Chem. Phys*., 1998, **109**, 8388.
266. R. D. Wigglesworth, W. T. Raynes, S. Kirpekar, J. Oddershede and S. P. A. Sauer, *J. Chem. Phys*., 2000, **112**, 736.
267. M. C. Bohm, J. Schulte and R. Ramirez, *Int. J. Quantum Chem*., 2002, **86**, 280.
268. K. Ruud, P. O. Astrand and P. R. Taylor, *J. Am. Chem. Soc*., 2001, **123**, 4826.
269. M. J. T. Jordan, J. S. S. Toh and J. E. Del Bene, *Chem. Phys. Lett*., 2001, **346**, 288.
270. J. E. Del Bene, S. A. Perera and R. J. Bartlett, *J. Phys. Chem. A*, 1999, **103**, 8121.
271. M. Pecul, J. Lewandowski and J. Sadlej, *Chem. Phys. Lett*., 2001, **333**, 139.
272. P. B. Karadakov, *J. Mol. Struct*., 2002, **602**, 293.

273. D. B. Chesnut, *J. Phys. Chem. A*, 2002, **106**, 6876.
274. M. Pecul and J. Sadlej, *Chem. Phys.*, 1999, **248**, 27.
275. M. Jaszunski, K. V. Mikkelsen, A. Rizzo and M. Witanowski, *J. Phys. Chem. A*, 2000, **104**, 1466.
276. M. Pecul and J. Sadlej, *Chem. Phys.*, 1998, **234**, 111.
277. P. O. Astrand, K. V. Mikkelsen, P. Jorgensen, K. Ruud and T. Helgaker, *J. Chem. Phys.*, 1998, **108**, 2528.
278. S. M. Cybulski and D. M. Bishop, *Mol. Phys.*, 1998, **93**, 739.
279. M. Jaszunski and A. Rizzo, *Mol. Phys.*, 1999, **96**, 855.

NMR Studies of *lac* Operator and *lac* Repressor

GÉRARD LANCELOT* and FRANÇOISE PAQUET

Centre de Biophysique Moléculaire, Rue Charles Sadron, 45071 Orléans Cedex 2, France

In memory of Professor Claude Hélène

For many years, and even now, the lac operon of Escherichia coli has been a model for gene regulation. The lac repressor is a tetrameric protein that binds strongly the lac operator and the affinity of which is modulated by an inducer molecule. The lac repressor–lac operator complex was the first nucleic

*Corresponding author. Fax: +33-(0)2-38-631517; E-mail: lancelot@cnrs-orleans.fr

ANNUAL REPORTS ON NMR SPECTROSCOPY
VOLUME 49 ISSN 0066-4103

acid–protein complex studied with success by NMR. The NMR studies began in 1973 and gave publications until now. ^{1}H, ^{13}C, ^{15}N, ^{19}F, ^{31}P NMR and photo-CIDNP studies increased progressively the level of understanding of the system during these decades. At first, it appeared to be possible to duplicate the basic lac repressor–lac operator interaction by using a smaller protein: the lac repressor N-terminal fragment. In 1987, the Kaptein's group reported the first model of interaction where the motif helix-turn-helix plays a central role in the recognition process of the large groove of the operator by the protein. Later, heteronuclear NMR studies refined the NMR solution structure of both free protein and complexed protein. ^{13}C and ^{15}N relaxation rate measurements showed dynamic processes in both nucleic acid and protein moieties during the complexation. By studying a larger headpiece (1-62) Kaptein's group showed the fundamental role played by the hinge helix, which interacts, in the minor groove of the DNA. The protection factor of a dimeric lac repressor headpiece mutant, which has a high affinity for DNA, was measured and used to qualify the folding of this protein during the complexation. The role played by the asymmetry of the lac operator was studied and explained. NMR studies allowed proposing a scheme to explain the loss in affinity of the lac repressor for its operator when binding to an inducer molecule. Comparison of these data with crystal structures showed that, until now, the more detailed view of the lac repressor–lac operator interaction comes from NMR studies. The NMR solution structures and the dynamic processes revealed by relaxation are in agreement with all the genetic and biochemical data.

1. INTRODUCTION

For many years, and even now, the *lac* operon of *Escherichia coli* has been a model for gene regulation. Few proteins have had such a strong impact in molecular biology. For decades, a prodigious amount of genetic and biochemical information on *lac* repressor has awaited structural interpretation.[1,2] The *lac* repressor (*lac*I) negatively regulates *lac* mRNA synthesis by binding with high affinity to its target lactose operator site and thereby precludes transcription by DNA polymerase.[1,3–8] The repressor contains 360 amino acids[9] that associate into a dimer of dimers of 154 520 Da molecular mass.[10–12] This protein recognizes and binds strongly to the *lac* operator section of DNA, a unique 21-bp partially palindromic sequence, about 10 million times more strongly than the rest of the *E. coli* chromosome.[13] The binding of a small inducer such as allolactose or isopropyl-β-D-1-thiogalactoside (IPTG) to the core domain (60–360) results in disruption of specific DNA binding.[3,4] In the jargon of allostery[14] the free *Lac* I or *lac*I core-inducer complex represents the T-state (tense state) whereas the *lac*I-operator complex represents the R-state (relaxed state).

Although the results of a number of genetic studies suggested possible regions of contact between the *lac* repressor and the *lac* operator,[15–24] and although the crystallographic structure was obtained at 2.6 Å resolution,[25] the

exact nature of the binding interaction on a molecular level was not revealed by these data. Multidimensional proton and heteronuclear NMR (^{13}C, ^{15}N, ^{19}F and ^{31}P) on ^{13}C, ^{15}N, ^{17}O and ^{19}F labeled proteins and DNA samples, provided detailed information on the structural and dynamics aspects of these recognition processes.

Tables 1 and 2 report the history of the NMR studies and of the level of understanding of the *lac* repressor–*lac* operator interaction. It is quite interesting to note that the technical evolution of the high resolution NMR is closely related to the prodigious wealth of structural information available on this biological system. During the last decade, the continuing improvement in NMR technologies, combined with the facilities for preparing proteins and oligonucleotides in chemical or biochemical ways, paved the way for structural studies. The *lac* repressor system was ideal for studying DNA–protein interactions by NMR. Firstly, it is appeared to be possible to duplicate the basic *lac* operator–*lac* repressor protein interaction by using a smaller protein: the *lac* operator headpiece N-terminal domain fragment. The relatively small size of the *lac* repressor headpiece and its ready availability allowed the study of its structure and interactions with DNA operator by using NMR techniques. Later a symmetrical 22 base pair oligonucleotide was used (Fig. 1). Headpieces of various lengths (HP 1-51, HP 1-56, HP 1-59, and HP1-62) and an engineered dimer of the HP62–V52C mutant were prepared and studied. The N-terminal DNA-binding domain has been studied extensively by NMR spectroscopy, an approach required by the inability to discern electron density for the free N-terminal domain in the crystal form.[26–34] Today, the crystal structures of the *lac* repressor core bound to IPTG,[28] the intact *lac* repressor,[27] the intact *lac* repressor complexes with IPTG,[27] a 21 base pair symmetric operator[27] and the natural O1 operator,[35] and the NMR refined headpiece of the *lac* repressor free[31] and complexed[29] have been determined. Structural data (crystal structure or NMR solution structure) on the *lac*I family of repressor such as fructose repressor or *pur* repressor[36,37] are also available. These structures have provided a framework for understanding a wealth of biochemical and genetic information[2,38,39] (Table 3).

2. NMR STUDIES DEVOTED TO *lac* REPRESSOR FREE OR *lac* OPERATOR FREE

2.1. The first NMR studies of the *lac* repressor

Figure 1 presents the amino acid sequence of the N-terminal part of the *lac* repressor and the sequence of the natural O1 *lac* operator. Although many investigations have been carried out on the functional properties of the *lac* repressor of *E. coli* using biochemical or genetic methods,[11,40] the size of this protein (4×360 residues) prevented one from doing classical ^{1}H NMR studies

Table 1. Comparative history of NMR solution structure of headpiece *lac* repressor and of proteins

1768–1830	Fourier transform Jean Batiste Fourier	
1945	First NMR experiment Block Purcell	
1955	Theoretical foundations of NOE[222]	
1957	First report of a 1D proton NMR spectrum on a protein: ribonuclease 40 MHz[223]	
1965	Discrete Fourier transform[224]	
1966	Fourier transform applied to NMR[225]	
1973		First 1D NMR report on *lac* repressor[226]
1977	First report of 2D NMR spectrum on proteins. 2D ^{1}H J-resolved spectrum 10 mM, D_2O, 60 °C, 360 MHz[227]	
1978		First 1D NMR report on headpiece[48]
1979	First report of 2D correlated spectroscopy on proteins. SECSY 10 mM, D_2O, 70 °C, 360 MHz[228]	
1979	First report of the sequential assignment on proteins. 1D spectra[229]	
1980	First report of NOESY spectra on proteins 20 mM, D_2O, 18 °C, 360 MHz[230]	
1983	First report of phase-sensitive 2D NMR spectrum on protein. Measurement of $J(^{1}H–^{1}H)$ coupling constants COSY 16 mM, H_2O, 45 °C, 500 MHz[231]	
1983	First NMR solution structure deposited in the PDB[232,233]	
1985		First ^{1}H NMR solution structure of HP[26,34,62,88,234]
1987	Use of ^{15}N labeled proteins[235]	
1989–1992	Measurement of ^{15}N relaxation rates to map the internal dynamics of proteins[133–135]	First ^{15}N NMR studies on HP[144]
1996–2000		^{15}N and ^{13}C NMR studies on HP[63,152] and *lac* operator[93,131]
1999		Hinge helix formation on 1-62 HP ^{13}C, ^{15}N[78,152]

Table 2. History of structural NMR study reports concerning the *lac* repressor–*lac* operator complex

1973[226]	Whole repressor	First report of NMR studies on *lac* repressor Binding of an inducer and of an anti-inducer
1978[48]	Mixing of HP51 and of HP59	First report of NMR studies on HP Differential mobility of HP
1980[149]	*lac* repressor–DNA	First report of *lac* repressor–DNA (poly[d(AT)]) complex CIDNP
1981[52–54,236–238]	1-HP	First assignment of ^{1}H resonances (aromatic protons)
1981[87]	14 bp operator	First report of NMR studies on operator imino protons
1983[101,105]	HP–*lac* operator	First NMR report of a specifical binding of HP51 upon the *lac* operator
1983[57,58]	HP56	First NMR report of the secondary structure of HP51
1985[26,34,62,88,234]	HP51	First ^{1}H NMR solution structure of HP51
1987[32]	HP51–*lac* operator	First model of DNA–headpiece complex
1987[95]	*lac* operator	Assignment of ^{31}P resonances
1989[151]	HP–*lac* operator	First NMR-based molecular dynamics simulation of the complex
1992[144]	HP51	First ^{15}N NMR studies report
1994[90]	HP51–*lac* operator	First comparison of NMR solution structures of the *lac* operator free and complexed to the 1-51 HP
1996[63,79]	^{15}N,^{13}C labeled HP56	^{15}N and ^{13}C NMR studies report on HP and on HP–*lac* operator complex
1996[31]	HP56–14 bp *lac* operator	Refined structure of the 1-56 HP–*lac* operator
1996[93]	^{13}C labeled *lac* operator	Internal dynamics of *lac* operator Relaxation exchange process
1997[132]	^{15}N labeled HP56	Backbone and side-chains dynamics ^{15}N NMR studies
1999[78,152]	HP62–22 bp *lac* operator	Hinge helix formation and DNA bending in various *lac* repressor operator complexes
2000[131]	HP51–^{13}C,^{15}N labeled-11 bp operator	NMR relaxation studies showing conformational changes in *lac* operator between the specific and the nonspecific complex

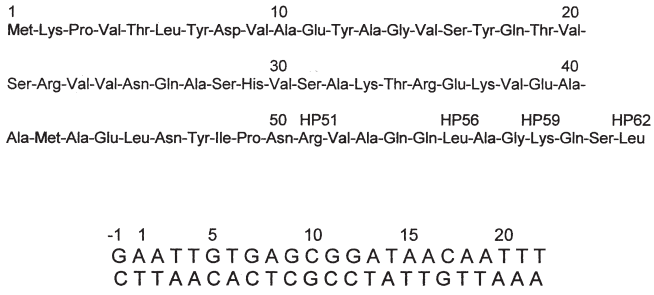

Fig. 1. Amino acid sequence of the N-terminal part of the *lac* repressor (top) and sequence of the natural O1 *lac* operator (down). The enzymes clostripain, chymotrypsin and trypsin cleave the *lac* repressor after the residues Arg51, Leu56, Lys59, respectively. It can be pointed out that the two binding parts of the natural O1 operator are not symmetric. They are referred to the left (base pairs 1–10) and right (base pairs 11–20) operator. The symmetrical left (20 base pairs) and right (22 base pairs) operator were constructed by linking the 5′d(G_1-$\cdots$-C_{10}) part to its complementary 5′d(G_{10}-$\cdots$-C_{-1}) part and the 3′d(A_{22}-$\cdots$-C_{11}) part to its complementary 3′d(G_{11}-$\cdots$-T_{22}) part, respectively.

on available spectrometers. The only few attempts to elucidate the structure of this protein were performed in ^{19}F on a protein derivative containing only (3-^{19}F) tyrosine residues instead of normal tyrosines,[41–47] and in ^{1}H on a mixture of deuterated amino acids and (2,6-^{2}H) tyrosine.[46] In this case all the ring proton resonances, except the tyrosine 3,5 proton resonances have disappeared from the spectrum. This result suggested a special mobility of the tyrosine residues (four tyrosines belonged to the N terminal part of the protein) as compared with the other aromatic residues (tryptophanes, histidines, and phenylalanines) distributed on the core of the protein. One fundamental advance in the dynamical and structural investigations of the *lac* repressor was obtained in 1978[48] and 1979.[49] The ^{1}H NMR spectra of the native protein run at 360 MHz show few relatively narrow resonances representing only a part of the 21 aromatic amino acids. Moreover, a few of these resonances exhibited strong pH-dependence which were assigned to the HC2 and HC5 resonances of the histidine and were both present in the N-terminal part of the protein. In order to get further evidence of flexible regions within the *lac* repressor, a tryptic digestion was performed and the resulting monomeric headpieces (1-51 and 1-59) were separated from the tetrameric core. The comparison of the ^{1}H NMR spectra of the headpiece with those of the native protein presented evidence in favor of an identical and defined tertiary structure for both N-terminal parts of the *lac* repressor and its headpiece (Fig. 2). Moreover, the tetrameric core showed only broad resonances. It was suggested that this amino-terminal domain was linked to a rigid repressor core by a hinge region qualified of "surprising high flexibility".[48]

^{19}F NMR spectra showed that the N-terminal domain is able to discriminate between the *lac* operator and the nonspecific DNA sequence.[42] It was suggested

Table 3. History of the understanding of the structural aspect of the *lac* repressor–*lac* operator system

Date	Origin of the data	Nature of the data	Originality
1961[239]	Molecular biology	Gene regulation model	*E. coli* lactose operon: a first model for gene regulation
		Identification of the *lac* operator	
1961[240]	Molecular biology	Inducer molecule: IPTG	
1963[241]	Molecular biology	Unified view of conformational transitions in multimeric proteins	Affinity of the repressor for the operator could be regulated by allosteric effectors
1964[242]	Molecular biology	Natural inducer: allolactose	
1966[9]	Molecular biology	Protein sequence	Composition: 360 residues
1973[243]	Molecular biology	The tetramer can be cleaved by limited protease digestion	The N-terminal part (60 residues) binds specifically to the *lac* operator
1975[244]	Molecular biology	The *lac* operator O1 has two auxiliary operators O2 and O3	
1976,[11] 1978[12]	Molecular biology		The *lac* repressor is a tetramer
1987[32]	NMR	Model of complex between the 1-51 HP and a 14 bp *lac* operator fragment	First structural model report of the complex
			Helix-turn-helix motif
1993[30]	NMR	Refinement of the structure of a 1-56 HP–14 bp operator	Good resolution of the structure
1996[27]	Crystallography	Structure of the whole *lac* repressor with a 22 bp *lac* operator	The first structure at low-resolution (4.8 Å) of the *lac* repressor complex suggests a hinge helix formation
1999[78,152]	NMR	Hinge helix formation and DNA bending in various *lac* repressor–operator complexes	The interactions protein–protein in the complex induce the hinge helix formation
2000[25]	Crystallography	Structure of the *lac* repressor binding to a 22 bp *lac* operator	Good resolution (2.6 Å) results in agreement with the NMR data
2002[190]	NMR	Hydrogen exchange	Model of associative pathway of the *lac* operator by HP61

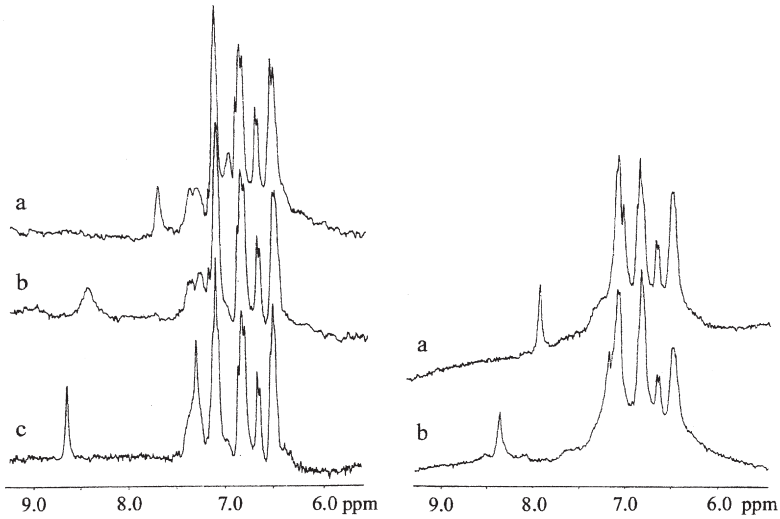

Fig. 2. The comparison of the aromatic part of the NMR spectra of the *lac* repressor and of its headpiece suggests strongly that the N-terminal part of the protein is linked to the rigid core by a region of high flexibility. Left: Aromatic region of the ^{1}H NMR spectra of the *lac* repressor headpiece in 0.4 M NaCl at pH: (a) 9.12, (b) 6.05, and 4.60 (c). Right: Aromatic region of the ^{1}H NMR spectra of the *lac* repressor in 0.4 M NaCl at pH: (a) 6.87, (b) 5.99. The variation in chemical shift with the pH allowed one to assign an aromatic histidine resonance. (Figure arranged according to Buck *et al.*[48] with permission.)

that two N-terminal fragments are bound to one operator in the specific complex.[42] Later, it was shown that the *lac* repressor bound differently the right and the left part of the operator.[45]

2.2. NMR structural studies of the free *lac* repressor headpiece

In 1977, Geisler and Weber[50] isolated the N-terminal part of the *lac* repressor necessary for DNA binding. From 1980, the *lac* repressor headpiece and its nucleic acid complexes were extensively investigated by NMR.[51] Individual assignments for the histidines and the four tyrosines[44,52–56] and of peripheral methyl groups in aliphatic residues[53] were identified by one-dimensional conventional methods. Applications of two-dimensional ^{1}H NMR spectroscopy (COSY, SECSY, NOESY) allowed the assignment of almost all the resonance lines of the 1-51 headpiece[57,58] in 0.4 M KCl using the sequential assignment method described by Wüthrich[59] and Kaptein.[60] Three α helices were located from NOE data and from amide proton exchange studies.[61] Later, the assignment of several ^{1}H resonance lines were completed[31,34,62,63] and stereospecific assignments were obtained for ten β-methylene proton pairs and

for five valine residues γ-methyl groups. Then, the free 1-56 headpiece *lac* repressor structure was refined.[31,64] The structure[31] was derived from 1546 restraints giving an average of 27.6 restraints per residue. These constraints comprise 389 intraresidual, 402 sequential, 385 medium range and 325 long-range distance restraints and also 30 Φ and 15 χ^1 dihedral angle restraints. The structure determination was performed by the method of direct refinement against NOE peak volumes, using the program DINOSAUR.[65–67] The solution structure was well determined for the region constituting residues 3–49 and the r.m.s. deviation from the average structure was 0.43 ± 0.08 Å for the backbone and 0.95 ± 0.08 Å for all heavy atoms of the residues 3–49. This region was constituted of three α helices called helix I, helix II and helix III (6–13, 17–24 and 32–45) and two loops joining these helices. The helix-turn-helix motif of the *lac* repressor headpiece shows significant structural similarity with other helix-turn-helix proteins: λ repressor,[68] 434 repressor,[69] *trp* repressor,[70–72] *pur* repressor,[37] *tet* repressor,[73] λ *cro* protein,[74] and 434 *cro* protein.[75,76] The N- and C-terminal ends of the protein appeared completely disordered, whereas the loop between helices II and III was slightly disordered in agreement with the low protection factor exchange factor measured later.[77] This lack of closeness explained the low electronic density measured in crystallography which precluded to obtain the structure of the N-terminal part of the free *lac* repressor.[27] NMR studies performed on a longer free *lac* repressor headpiece (1-62) showed that the C-terminal region 50–62 is also completely disordered.[78] Such a lack of structure for the C-terminal domain has also been found on the free *fructose* repressor.[36] On the contrary, when the *lac* repressor headpiece was complexed to the 22 base pair long *lac* operator (complex 2 proteins for one operator), protein–protein interactions led to the formation of a hinge helix for the residues 50–58[78] (see Section 4.2.4).

2.3. NMR structural studies of the *lac* operator

The *lac* operator DNA contains two sequence repeats related by a pseudo-dyad axis (Fig. 1). Several biophysical studies on the *lac* operator–*lac* repressor system that has employed symmetrized operator to simplify analysis could not assess the importance of the deviation from symmetry of the natural sequence. Using ^{19}F NMR and 5-fluoro-deoxyuridine-substituted O1 DNA, Rastinejad *et al.*[45] observed distinct spectral differences for binding of the two independent N-terminal domains to the two-half-site sequence. The asymmetry appears to be related to the 13A/T base pair.[45] ^{1}H and ^{15}N NMR studies on complexes between the 1-56 headpiece and the left compared to the right *lac* operator half-site showed that different residues of the protein are affected by binding different half-sites of the operator.[79] These data were in agreement with methylation and DNAse protection studies,[80–82] effects of sequence variation on binding[83–85] and analyses of repressor–operator complexes[19,32,86] which

report that the *lac* repressor binds differently the two parts of the operator and that the N-terminal part binds more strongly the left part of the O1 operator than the right part.

The hydrogen-bonded imino and amino protons resonance of a 14 base pair *lac* operator fragment were studied by NMR[87] and sequentially assigned.[88] The nonexchangeable proton resonances were sequentially assigned on a 7 base pair[89] and on a 9 base pair operator fragment[90] and its solution structure determined from a restricted number of inter-proton distances and torsional angles derived from NOESY and COSY experiments.[90] A method based on molecular mechanics in internal coordinates space using the JUMNA algorithm[91] was used. This program included a standard process[92] involving the determination of interatomic distances by iteratively refining molecular conformations in order to reproduce the NOE intensities at different mixing times. The resulting structure belonged to the B family but showed large structural variations with respect to the standard B conformation. The average twist of 37.6° was larger than for a standard B-DNA, the large winding angles being found at the central base pairs. Conversely, the rise was larger at the extremities leading to an average value of 3.66 Å. The helical axis showed a slight inclination and the total angle bending was 10°, oriented approximately toward the minor groove.[90] Measurement of ^{13}C relaxation rates on a $^{13}C1'$ selectively labeled 11 base pair *lac* operator fragment showed that slow exchange processes occurred in the *lac* operator free. This peculiarity was interpreted in terms of fast conformational exchange states which translate the predisposition of this sequence to bind the *lac* operator headpiece by adapting its conformation to those of the protein in order to form a specific complex[93] (see Section 4.2.1). In another group, the ^{31}P resonances of a symmetrical *lac* operator fragment as well three mutants were assigned[94–96] (see Section 3.3).

3. NMR STRUCTURAL STUDIES OF THE *lac* REPRESSOR HEADPIECE–*lac* OPERATOR COMPLEX

3.1. The headpiece of the *lac* repressor binds specifically the *lac* operator

Several data suggested the fundamental role played by the N-terminal part in the complexation of the *lac* operator with the *lac* repressor: (1) the functional repressor parts of the tetrameric *lac* repressor are organized as dimers;[42,97] (2) low-angle X-ray data revealed a pairwise distribution of the four N-terminal domains over the *lac* repressor molecule;[98] (3) the headpieces were located far (67 ± 10 Å) from the center of mass of the core;[99] (4) circular dichroism measurements confirmed that the *lac* repressor can bind simultaneously two DNA fragments containing the *lac* operator;[100] (5) ^1H NMR studies on imino protons proved that two headpiece molecules can be bound by DNA fragments of 51 and 62 base pairs containing the *lac* operator;[101] (6) methylation

experiments demonstrated that the contact sites of the protein with the *lac* operator are concentrated in its N-terminal domain[80] in agreement with conclusions from studies of mutated *lac*I gene products.[24] Moreover, Ogata and Gilbert[102] showed that the headpiece binds the left part of the asymmetric *lac* operator (Fig. 1) with higher affinity than the right part. From these data, a lot of experiments were devoted to the specific or nonspecific interactions of the *lac* repressor headpiece with the *lac* operator.[103,104] Scheek *et al.*[105] studied a chemically synthesized 14 base pair DNA fragment comprising half the *lac* operator because there are strong reasons to believe that half of the *lac* operator is the smallest functional unit able to form a specific complex with headpiece. Titration of the 14 base pair *lac* operator fragment with the 1-51 headpiece showed several chemical shift variations of the imino protons of DNA and of the aromatic resonances of the four tyrosines (7, 12, 17, and 47) and an important downfield shift of the C2H and C4H resonances of the histidine 29. Comparison of these data with those obtained by titrated slightly larger headpiece molecules (1-56) with a 36 base pair DNA fragment containing the complete *lac* operator sequence[42] or short headpiece with a DNA restriction fragment containing two copies of the complete *lac* operator in tandem[101] showed that the *lac* repressor short headpiece binds the 14 base pair *lac* operator fragment in the same way as it binds to the corresponding half of the complete *lac* operator. In a 0.05 M phosphate, 0.5 mM DSS and 0.02% (w/v) NaN_3, pH 7.05 in D_2O at 25 °C, analysis of the titration curves showed the existence of two complexes corresponding to the specific and nonspecific binding. Although a rigorous analysis of the data was not possible because the presence of the two types of binding at this ionic strength, a value of 2×10^{-5} M was estimated as an upper limit for the dissociation constant of the specific complex.[105] For comparison the dissociation constant of the specific binding of the full tetrameric repressor with the *lac* operator was measured 10^{-13} M.[106,107] It is difficult to estimate the dissociation constant of the *lac* repressor monomer since the monomeric specie does not exist in solution and since its association is entropy driven.[108] Nevertheless, assuming that the enthalpy is divided by two for a monomer because two monomers are fixed on one operator in the tetramer and that the association constant decrease with the ionic strength,[109] the dissociation constant of a *lac* repressor monomer could be assumed to 10^{-7} M. This value is smaller than the measured one on the 1-56 headpiece (10^{-6} M) by one order of magnitude.[80] One explanation was given by showing the central role played by the residues 50–58 (in a 1-62 headpiece) helix which bind to the minor groove of the *lac* operator[33] and which is involved in stabilizing protein–protein interactions. Based on the crystallographic structure of an artificial symmetrical left *lac* operator–*lac* repressor complex, Falcon *et al.*[110] designed a mutation at Val52 which is expected to contribute favorably to the stability of the complex by formation of a disulfide bond Cys52-Cys52′. They showed that the oxidized form binds DNA with an approximately sixfold higher affinity than the wild-type *lac*

repressor. Guided by this increased of affinity, Kalodimos *et al.*[77] constructed, by linking two monomeric mutants of the headpiece 1-62 where the residue Val52 was replaced by a cysteine, a dimeric species obtained by S–S bridge formation between the two cysteines. The binding properties of this HP62–V52C mutant have been exploited in various ways. This protein has been converted in two forms, reduced (monomeric form) and oxidized form (dimeric form). The HP62–V52C dimeric form binds to wild type *lac* repressor with the same affinity that the *lac* repressor intact ($K_d = 3 \times 10^{-11}$ M) whereas the addition of reducing agent decreases the binding by four orders of magnitude ($K_d = 2 \times 10^{-7}$ M).[77] The dramatic enhancement of binding strength demonstrates that DNA-binding domains can be rationally designated to restore the affinity of the natural repressor[77] (see Sections 4.4 and 4.5).

3.2. Structure of the specific *lac* repressor headpiece–*lac* operator complex

The *lac* operator complexed with the *lac* repressor headpiece was one of the first nucleic acid–protein structure obtained by NMR studies.[32] Scheek *et al.* showed that the complex formed by the 14 base pair operator fragment d(GGAATTGTGAGCGG).d(CCGCTCACAATTCC) and the headpiece 1-56 was in fast exchange with the constituents on the NMR time-scale.[105] This property greatly simplified the assignments because the resonances can be followed by titration.[101,105,111] The NOESY map of this complex was obtained in D_2O, 0.2 M KCl, 10 mM phosphate, 27 °C, pH 7 and analyzed (Fig. 3). The high ionic strength used prevented the formation of high content of unspecific complexes and allowed the analysis of the specific one. The total analysis of the map was complicated by the overlapping of both nucleic acid and protein resonance lines and by the variation of their chemical shift in the complex. Nevertheless, the lack of overlap in the region aromatic–H1′ allowed the total sequential assignment of the aromatic and H1′ resonances as well as some of the other sugar resonances. Using these assignments, it was possible to detect the cross peak due to the NOE between the protons of protein and DNA.[32,112] Several NOEs implying Tyr7 and Tyr17 as well as His29 with different aromatic or sugar protons of the nucleic bases were observed (Fig. 3). The NMR data showed that *lac* repressor helix makes contacts in the major groove of *lac* operator as has been suggested before by other groups for this[32,113] and other repressors.[114,115] On the base of the observed NOEs, the helices were positioned in the major groove (Fig. 4). On the one hand, this model was in agreement with the helix-turn-helix super structure of the protein, the second helix interacting with the protein as already observed on the crystal structure of the catabolite activator protein (CAP),[116] of the *trp* repressor[117] and of the *cro* repressor from bacteriophage λ[118] and *cI*.[119] On the other hand, the recognition helix was directed in an opposite sense to that proposed by the model of Matthews[115] and the predictions of Rein[120] and Ebright.[121] Later, other

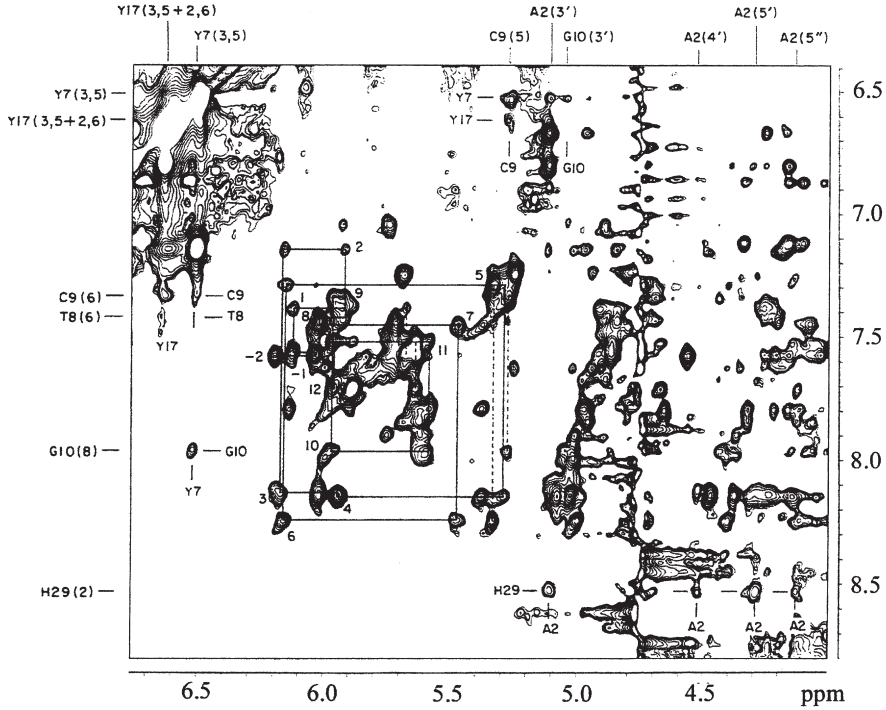

Fig. 3. Part of the 500 MHz NOESY spectrum of the complex of *lac* repressor headpiece 1-56 with a 14 base pair *lac* operator fragment. Five millimolar protein, 5 mM DNA, 0.2 M KCl, 10 mM phosphate, pH 7, 27 °C. This map represents the sum of two NOESY maps recorded at 100 and 250 ms mixing times (according to Boelens *et al.*[32] with permission).

structural works confirmed this orientation (see Section 4.2.3). After this pioneering study, a lot of investigations were devoted to this complex. The quality of the structure of the complex has been steadily improving for the past decade (see Section 4).

3.3. ^{31}P NMR studies devoted to the *lac* operator–*lac* repressor headpiece

Phosphorus NMR can potentially provide information on protein–DNA phosphate backbone interactions because ^{31}P chemical shifts supply direct information on the conformation of the phosphate diester.[122–124] Local helical parameters such as twist and base pair roll appear to affect the ^{31}P chemical shift by stretching or contracting the sugar-phosphate backbone. Phosphates in a gauche$^-$ conformation about one of the P–O ester bonds have their ^{31}P resonances shifted to low frequency by 1.6 ppm as compared with a phosphate involved in a *trans* conformation.[123,125] The ^{31}P NMR spectra of unmodified

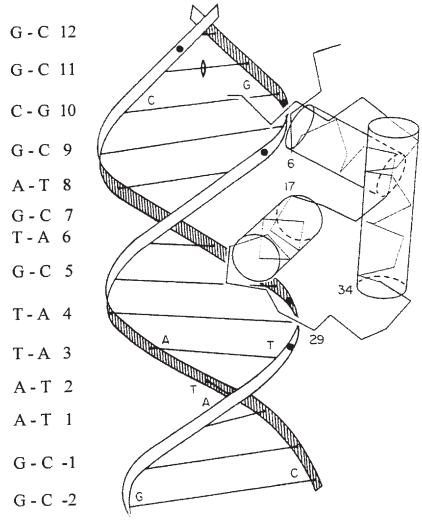

Fig. 4. Model of the *lac* repressor headpiece–*lac* operator complex. The relative position of the helix II with respect to DNA was adjusted in order to best satisfy the experimental NOEs (according to Boelens *et al.*[32] with permission).

oligonucleotides generally spread out on 3–4 ppm only. Moreover, the chemical anisotropy relaxation process of ^{31}P prevents the increase of resolution with the increase of magnetic field strength. Consequently, the assignment of the 48 phosphorus resonances *lac* operator is almost impossible to make and assignment of the *lac* operator was undertaken on a wild type symmetrical *lac* operator. In this case the 14 base pair *lac* operator segment needs the assignment of 13 resonances, which still represents a difficult task. By synthesizing a mono (^{17}O) phosphoryl-labeled oligonucleotide with only one phosphate labeled along a strand, the corresponding ^{31}P resonance is easily assigned. This is because the quadrupolar ^{17}O nucleus broadens the ^{31}P signal.[95] Using two-dimensional NMR techniques[95,96,126,127] and site-specific ^{17}O labeling[95] of the phosphoryl group, the phosphorus resonances of a wild type symmetrical and three symmetrical mutants were assigned.[94] The wild-type symmetrical operator d(T**A**TGAGCGCTCAT**A**)$_2$ called O1 and three mutants called O2: d(TGTG**T**GCGC**A**CACA)$_2$, O3: d(T**C**TGAGCGCTCA**G**A)$_2$ and O4: d(TGTGAGCGCTCACA)$_2$ were synthesized. The ^{31}P spectra of these oligonucleotides free in solution were complexed with a wild-type 1-56 headpiece or a mutant Y7I and were compared. On the basis of the different observed chemical shift variations, it was proposed that specific operator–protein complexes retain the inherent phosphate ester conformational flexibility of the operator itself, whereas the phosphate esters are conformationally restricted in the weak-binding operator–protein complexes.

In order to test the influence of the symmetry of these operators as compared to that of the wild type, four symmetrical operators of 22 base pairs long of sequence:

O1: d(GAATTGTGAGCGCTCACAATTC)$_2$,
O2: d(GAATT**A**TGAGCGCTCA**G**AATTC)$_2$,
O3: d(GAATTGTG**T**GCGC**A**CACAATTC)$_2$,
O4: d(GAATTGT**C**AGCGCTCA**G**AATTC)$_2$

were synthesized. These sequence alterations result in an 8–10-fold increase in repressor binding affinity over the natural operator sequence.[128] The alkaline phosphatase assay was used for the determination of dissociation constants. At an ionic strength of 0.35 M the dissociation constants with a 1-56 headpiece were computed 5.4×10^{-8}, 7.0×10^{-8}, 2.6×10^{-7}, 6.4×10^{-8} M for the symmetrical wild-type O1, and the mutants O2, O3 and O4, respectively. For the nonspecific binding, the symmetrical 22 base pair oligonucleotide d(CCCAGC AACCTAGGTTGCTGGG)$_2$ was used and a K_D value of 1.1×10^{-6} M was calculated.[129] In all these computations it was assumed that no interaction occurs between the binding sites. The temperature and salt dependence on the dissociation constants support the conclusion that the headpiece contains the major DNA recognition portion of the protein. The analysis of ^{31}P spectra of these oligonucleotides free or bound to wild-type 1-56 headpiece or to a Y7I mutant are in agreement with the conclusion of Karslake *et al.*[130] The authors conclude that the retention of backbone torsional freedom in tight complexes is entropically favorable and provides a mechanism for protein discrimination of different operator binding sites.

3.4. ^{13}C and ^{15}N NMR studies devoted to internal dynamics of the *lac* repressor headpiece–*lac* operator complex formation

The internal dynamics of oligonucleotides is of considerable importance in understanding the mechanism of recognition of specific DNA sequences by proteins such as repressor. NMR relaxation experiments can, as a rule, provide a detailed description of nucleic acid or protein dynamics. This is often accomplished using T_1, $T_{1\rho}$ and NOE experiments, which are related to the spectral density functions describing such motions at different frequencies. For each nucleus, these data depend on the magnitude and of the rate of the relative motions of all its surrounding nuclei. The use of ^{13}C or ^{15}N NMR relaxation parameters for dynamic analysis is attractive because the C–H or the N–H distance is nearly constant. Thus, the interpretation of the relaxation parameters is reduced to the analysis of the ^{13}C–H or ^{15}N–H vectors orientation in function of time. In order to increase the low natural abundance of the isotope, selectively or uniformly ^{13}C or ^{15}N molecules are required. Measurement of the ^{13}C relaxation parameters on the *lac* operator free[93] or

complexed by the *lac* repressor headpiece[131] and of the ^{15}N relaxation parameters on the *lac* repressor headpiece free or complexed by the *lac* operator[132] were obtained following a well-established NMR technique.[133–135]

A half of the *lac* operator (11 base pairs) of sequence (the numeration is in agreement with those of Fig. 1) d(A_1 A_2 T_3 T_4 G_5 T_6 G_7 A_8 G_9 C_{10} G_{11}).d(C_{11} G_{10} C_9 T_8 C_7 A_6 C_5 A_4 A_3 T_2 T_1) was selectively ^{13}C-labeled on C1′, and the corresponding H1′ and ^{13}C resonances assigned on the free[136] and complexed oligonucleotide.[137] ^{13}C relaxation rates were measured[93,131] and analyzed as already reported for oligonucleotides.[138–142] Variation of the relaxation rates were found along the sequence and relaxation process of the C1′ was described as governed by the motion of the sugar relative to the base and in terms of bending of the whole duplex. The fit of $R(C_z)$, $R(C_{x,y})$ and $R(H_z \rightarrow C_z)$ using the Lipari–Szabo relations gave evidence of supplementary relaxation process. The variation of $R(C_{x,y})$ between 10 and 22 s^{-1} along the sequence was interpreted as exchange relaxation process with a time-scale of about 160 μs. Such slow motions of large amplitude involved G_7A_8 and the $A_1A_2T_3T_4$ sequences. It should be pointed out that these residues were found in close contacts with the *lac* repressor headpiece in the complex[32] and more peculiarly with the recognition helix and with the loop linking the helices II and III (Fig. 5).

^{13}C relaxation measurements were also performed on the complex formed by this $^{13}C1'$ selectively labeled 11-base pair *lac* operator fragment and the 1-51 *lac* repressor headpiece (1 : 1) 0.8 mM in D_2O, 3 mM KCl, 10 mM phosphate, pH 6.8. It was found that the $R(C_{x,y})$ relaxation rate varied strongly along the sequence (28.6–67.8 s^{-1}). Analysis of these data by the Lipari–Szabo relation showed an excess of the experimental value of $R(C_{x,y})$ by comparison with the computed one when the other relaxation rates $R(C_z)$ and $R(C_z \rightarrow H_z)$ were well fitted. Moreover, an increase of $R(C_{x,y})$ was observed by decreasing the

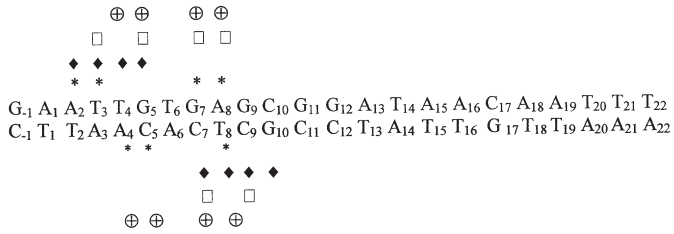

Fig. 5. Summary of the data involving differences between structure and dynamics of the *lac* operator upon complexation with the *lac* repressor headpiece. * Note strong chemical exchange processes when complexed with HP51.[131] □ Note the important chemical shift observed upon complexation.[143] ◆ Note the observed NOEs between the *lac* operator and the *lac* repressor headpiece HP62[152] or HP51.[90] ⊕ Note the structural changes observed after modeling the operator in the complex 9 base pair-*lac* operator–HP51.[90] Strong deviations of the values of the roll, twist and slide for the residues G11 and C11 in the center of DNA were observed when a 22 bp symmetrical operator was complexed to HP62. These deviations result of the observed bending of 45° in the DNA helical axis upon DNA binding of *lac* repressor.[152]

spin-lock power, demonstrating the presence of an exchange relaxation process. This exchange process affected particularly nucleotides belonging to region in close contact with the protein in the complex. There is no doubt that in the experimental conditions used (low ionic strength) unspecific and specific complexes coexist in solution. This correspond to favorable experimental conditions to underscore possible structural change upon the complexation and the exchange relaxation process was described in terms of structural changes between the specific and the unspecific complex. As a matter of fact, the residues A2, T3, G7, and A8, which have fairly efficient chemical exchange processes, participate within the direct contact points between the operator and the protein[90,143] and this process has also been demonstrated for the free operator.[131] It can be pointed out that relaxation rate data were interpreted in terms of dynamics structural changes and are not in disagreement with the average structures of the *lac* operator which was found to be almost invariant upon complexation.[90] Relaxation rates data reflect dynamical changes upon binding of the *lac* repressor headpiece but do not mean that the average surrounding of the involved nucleotides is drastically modified. The slow exchange processes reported in *lac* operator free could translate the predisposition of this sequence to adapt itself to *lac* operator headpiece to form specific complexes.

^{15}N uniformly labeled 1-51[144] and 1-56[79,132] *lac* repressor headpiece were biochemically prepared and the corresponding ^{15}N resonances assigned. The ^{15}N relaxation rates indicated that a rigid backbone was found for the residues in the three α helices and for the turn of the helix-turn-helix motif. The loop between the helices II and III shows increased mobility. The detected side-chains are very mobile. When the headpiece was complexed with a half of *lac* operator (11 base pairs, see above for the numbering) several changes in mobility take place. The most remarkable change was found for the loop region between the helices II and III where the residue histidine 29 within the loop interacts with the thymine 3 of the half operator. Then, upon complexation, this mobile loop adapts itself to the DNA and becomes more rigid.[132] Moreover, most of the DNA-contacting side-chains become more rigid. These results suggest that the mobility of the regions within the *lac* repressor headpiece is important for complexation. Such a conclusion has also been found for the *lac* operator.[131] These data will be discussed in Section 4.2.

3.5. Photo-CIDNP investigations of *lac* repressor

Chemically induced dynamic nuclear polarization (CIDNP) originates from magnetic interactions in pairs of free radicals and is observed in their reaction products.[145,146] A solution containing a protein (or any substrate) and a dye in low concentration (10^{-4} M) is irradiated by an argon ion laser in the probe of a spectrometer. By example in presence of flavin, the polarization of tyrosines

arises from a reversible hydrogen atom transfer from its hydroxylic group OH to the photoexcited triplet state of the flavin. CIDNP is generated from a spin-selective recombination of the radical pair. Due to the strong gyromagnetic ratio of the electron compared to those of the proton, a strong enhancement of the resonance of the tyrosine is observed. Similarly to the NOE, the sign of the polarization transferred by cross-relaxation changes with the value of $\omega\tau_c$. Alternately "light" and "dark" FIDs are recorded, and subtraction yields the photo-CIDNP difference spectrum. Mechanism involved in CIDNP for aromatic residues tyrosine, histidine and tryptophane has been described.[145] Photo-CIDNP reactions need dye and aromatic residues to be in proximity to achieve polarization transfer. Consequently, it is possible to distinguish aromatic side-chains exposed to solvent from that which are buried and thus protected against the attack of the dye. Photo-CIDNP experiments have been used with several proteins such as BPTI,[147] hen egg white lysozyme, RNase A and S, ribonuclease[145] and *lac* repressor.[148,149]

The interaction of the *lac* repressor headpiece (1-51) with synthetic oligo(d(AT)) was studied by photo-CIDNP.[149] In the HP51 free, three of the four tyrosine residues 7, 17, and 47 as well as histidine 29 were found polarized indicating that they were fully accessible to the photoexcited dye. *lac* Repressor headpiece (1-59) and intact *lac* repressor have also been studied by photo-CIDNP free and complexed to a 14 base pair *lac* operator.[148] At neutral pH His29, Tyr12, Tyr17 and Met1 were found to be polarized. His29 polarization was weaker and broader than in HP51. The photo-CIDNP of the *lac* repressor was quite similar showing that the same residues were accessible to the flavin (and not the Trp of the core) and that His29 was more accessible to dye in the intact *lac* repressor than in the HP59. Binding of HP59 upon the 14 base pair *lac* operator strongly suppressed the photo-CIDNP effect of Tyr7 and Tyr17 and abolished the His29 polarization.[148] The photo-CIDNP spectrum of *lac* repressor did not change in the presence of the inducer IPTG or of the anti-inducer ONPF.

4. NMR SOLUTION STRUCTURE OF THE *lac* REPRESSOR HEADPIECE–*lac* OPERATOR COMPLEX

4.1. The 1-56 headpiece

4.1.1. *Interaction of the helix-turn-helix motif in the major groove of the operator*

NOESY spectra run at 500 MHz of the 1:1 complex between the *lac* repressor headpiece and an half of the *lac* operator d(GGAATTGTGAGCGG).d (CCGCTCACAATTCC) (corresponding to the sequence −2–12 in Fig. 1) have been recorded at 100 and 250 ms mixing time.[32] Several NOEs between the

aromatic protons of the tyrosines 7 and 17, the histidine 29 and the protons of the bases of A2, A3, T8, C9 and C10 have been assigned and reported.[32] On the basis of these NOEs, of the headpiece free structure[26,34] and of a standard B-DNA structure, a model of interaction has been proposed. In this model, the second helix of the motif helix-turn-helix (called the recognition helix) makes contacts in the major groove of the operator as already suggested for other repressors. Interestingly, the recognition helix orientation was opposite to that in the 434-operator complex[114] and in the *cro*-OR3 model[115] and to that predicted on the basis of these complexes.[120,121] This was in agreement with all of the genetic and biochemical evidence known at the time.[113] More detailed structures of the *lac* operator–*lac* repressor headpiece were published later (see Sections 4.1.4 and 4.2).

4.1.2. *Structural changes observed on the operator during the complexation*

The solution structure of both 9 base pairs *lac* operator free $d(A_2T_3T_4G_5T_6G_7A_8G_9C_{10})$. $d(G_{10}C_9T_8C_7A_6C_5A_4A_3T_2)$ (with the numeration of Fig. 1) and complexed by a 1-51 headpiece were resolved by 2D ^{1}H NMR spectroscopy.[90] Fig. 5 presents the most important structural and dynamical changes observed during the complexation. 2D NOESY map of the complex showed 22 NOEs between the two partners involving the Thr5, Leu6, Tyr7, Ser16, Tyr17 and the His29 with different aromatic and sugar protons of A2, T3, T4, G7, T8, C9, and G10 in agreement with the data of Scheek[32] and Lamerichs.[150] These NOEs are indicative that the 1-51 headpiece forms a specific complex with the 12 base pair complex and that the observed conformational changes reported affected the specific complex. The free and complexed operator adopted both a right-handed B helical conformation, but a more detailed analysis of the conformational parameters shows some striking differences. It was found that the free and complexed operator has a very different behavior along the sequence. In the complexed operator, major and minor grooves open up from the 5′ to the 3′ end. The major groove is slightly smaller than the standard B-DNA, while the minor groove is wider. In the free operator structure, the major groove is narrower at the 3′ end and the minor groove width fluctuates along the sequence. For the isolated operator, bending occurs towards the major groove; the width of the minor groove is smaller than in B-DNA while the major groove opens up. For the complexed operator, bending towards the major groove closes up the major groove and widens the minor groove. The more drastic difference occurs in the groove deeps. The free operator major groove is extremely shallow compared to the standard B-DNA. Conversely, the complexed operator major groove is deeper than in DNA, the 5′ end being deeper than the 3′ end. The complexed operator structure exhibits striking fluctuations of the rise which are very large (up to 5 Å) at both ends of the nucleotide and becomes as small as 2.7 Å at step A6/C7 and A4/C5, the bending occurs at step C5/A6. These structural characteristics support the chemical shift changes of the *lac* operator resonances upon complexation.[143]

These changes occur at base pairs $(TA)_4$, $(GC)_5$, $(GC)_7$, and $(AT)_8$ which correspond to the regions where significant differences were observed between the isolated and complexed operator structures, specially in the twists and the rises and in the groove depths and widths.[90] A large low frequency shift is observed for the imino proton of the $(TA)_6$, where the bending occurs. These data are in agreement with the fast conformational equilibrium found between the specific and nonspecific complex reported by measuring the $^{13}C1'$ relaxation rates[131] where the most striking exchange process was observed on the same residues (see Section 3.4).

4.1.3. *Toward a greater affinity of lac repressor headpiece to lac operator*

Several improvements to the structure of the first *lac* operator–*lac* repressor headpiece model were presented. In 1989, Lamerichs[143] studied a complex between the *lac* repressor headpiece 1-56 and a fully symmetric tight-binding 22 base pair *lac* operator by 2D ^1H NMR. With a molecular weight of approximately 26,000, this complex was the largest system studied in detail by NMR at that time and rests among the largest ones to date. Many NOE cross-peaks between the headpiece and DNA were identified, and changes in proton chemical shifts were analyzed. The NMR data showed that two headpieces are symmetrically fixed on the operator. The orientation of the recognition helix in the major groove of DNA is opposite to that found for *cro* and *lambda* repressors.[118,119] One year later, an NMR study at 600 MHz of a 1-56 headpiece complexed to a 11 base pair *lac* operator fragment was published by the same group.[150] The smaller size of this complex allowed the detection of a lot of new intraprotein and inter DNA–protein NOEs. The observed NOE between the amide protons of Gln18 and H5C of C7 confirm the specific contact proposed from genetic experiments between these residues. The X-ray structures of the *E. coli lac* repressor and its complex with the inducer IPTG and operator DNA[27] and of the *lac* repressor core complexed with IPTG[27] suggested the central role played by the hinge between the headpiece and the core. This hinge helix which binds in the minor groove DNA was also found in the crystal structure of the *pur* repressor complexed to its operator.[37] Unfortunately, the low resolution of the co-crystal structure of the *lac* repressor–*lac* operator complex (4.8 Å) did not allow a precise description of this region. In 1996 a more sophisticated (^1H, ^{15}N) NOESY-HSQC study at 750 MHz on a 22 base pair *lac* operator–1-56 *lac* repressor headpiece complex produced some light on the central role played by the so-called hinge helix (residues 50–58). The 3D NOESY-HSQC spectra showed that the C-terminal domain of the 1-62 headpiece *lac* repressor is not structured in the free HP but that the 50–58 residues forms an α helix in the HP complexed to the 22 base pair operator. This hinge helix was shown to be bound to the minor groove of the DNA. However, no indication of this helix formation was found in the 1-62 HP bound to an 11 base pair operator. These results suggested that the hinge helices are stabilized mainly by protein–protein interactions in the HP62–22

base pair complex and that binding of the headpiece is co-operative. Moreover, on the NMR timescale, the HP62–22 base pair complex is in a slow chemical exchange while the HP62–14 base pair complex is in fast exchange in agreement with a co-operative binding on the 22 base pair *lac* operator. The NOEs identified between the H1′ and NH2 guanine protons on the central GC base pair and Leu56 δCH3 of the hinge helix showed binding of the hinge helix to the minor groove of the DNA. Consequently, it is clear that the hinge helices are formed only when the protein is in the repressed state, in agreement with the structure of the X-ray *lac* repressor bound to the natural operator O1 structure.[35]

4.1.4. *Structure of the complex of lac repressor headpiece and an half-operator determined by NMR and restrained molecular dynamics*

A great number of structural studies based on molecular mechanics, docking and restrained molecular dynamics in presence[30,151,152] or in absence of water and counterions have been devoted to the determination of the structure of the complex between the *lac* repressor headpiece and the *lac* operator. All these studies imply a half of (or a part of) the operator:

5′	d–(G	G	A	A	T	T	G	T	G	A	G	C	G	G)
3′	d–(C	C	T	T	A	A	C	A	C	T	C	G	C	G)
		−2	−1	1	2	3	4	5	6	7	8	9	10	11	12

and the headpieces 1-51, 1-56 or 1-62. As already described in Section 3, and in order to facilitate the discussion, structural elements of the N-terminal of the *lac* repressor are remembered. This domain contains four α helices (6–13, 17–24, 32–45 and 50–56), the first two of which are part of a helix-turn-helix motif that is a common feature of several DNA-binding proteins.[153–158] It was shown that the fourth helix which links the N-terminal domain to the core—the so-called hinge helix—is formed only in presence of DNA.[33]

The first molecular dynamics study of the complex *lac* repressor headpiece–*lac* operator in the presence of water molecules and counterions[151] used a 14 base pair operator and the 1-56 headpiece. In total 193 distances were derived from NOESY measurements, 169 of which were within the headpiece and 24 between operator and headpiece. The operator structure was restrained by 36 hydrogen bonds between base pairs and in order to avoid distortion during the MD in vacuum, the positions of its backbone atoms P, O5′, C5′, C4′, C3′ and O3′ were restrained. The initial structure was obtained by docking the free headpiece structure on the free *lac* operator structure obtained from restrained molecular dynamics in vacuum. This complex structure was placed in a box with 3950 molecules of water in order to get a density of 1.05 g cm^{-3}. Thirty-four Na^+ and 10 Cl^- ions were added in order to bring the salt concentration to approximately the same value (0.2–0.3 M) as used during the NMR measurements of the complex.[32,159] The results of a 125 ps trajectory of this system containing 12,889 atoms gave a complex structure which satisfied

essentially all experimental distance information derived from the 2D experiments. Nevertheless, although the global position of the protein was correctly predicted, the enormous size of the configurational space was not searched completely. Moreover, the small number of available NOEs at this time led to MD simulations which were not sufficiently reliable to predict interactions at the atomic level. For example, it was found that the interaction between the headpiece and the operator was based on many direct- and water-mediated hydrogen bonds and nonpolar groups and, to a lesser extent, through water-mediated hydrogen bonds. They did not find stable direct hydrogen bonds between donor and acceptor groups of the base and the amino acid side-chains. Four years later, another restrained molecular dynamics study using more NMR restraints found also water-bridged contacts to phosphates from residues but get evidence of direct hydrogen bonds between amino acid side-chains and nucleic acid bases.[30] Another example lies in the fact that this structure was enable to explain the genetic data concerning Gln18[160] while the data of the second MD[30] found the predicted contact between Gln18 and C7 as observed in NOESY[150] but not introduced as experimental restraint in the first MD.[151] This last restrained Molecular Dynamics used 508 distances derived from NOESY experiments, 260 of which within the headpiece, 212 within the operator and 36 between operator and headpiece. After refinement of the both partners molecules in vacuum by MD, the refined 1-51 headpiece complexed to a 11 base pair operator and a total of 3384 water molecules, 28 Na^+, 10 Cl^- ions were placed in an rectangular box of $36.6 \times 54.3 \times 58$ Å. The total system contained 11,065 atoms. The calculations were performed using GROMOS and after several equilibrium periods, heating at 1000 K and then cooled down to 300 K, an 85 ps trajectory was obtained and used to analyze the structure. Although the simulation was too short for full thermodynamics averaging, the energy data suggest that the trajectory represented an equilibrium set of protein–DNA configurations. The operator was observed to be slightly bent around the headpiece and the major groove compressed somewhat around helix II of the headpiece.[30] Such a change of the operator conformation during the complexation was in agreement with data reported on the basis of restrained molecular mechanics[161] and ^{13}C relaxation rate measurements on *lac* operator[93,131] (Fig. 5). Two strong direct H-bonds between protein side-chains of helix II and DNA bases were observed: one contact was formed between $O_{\varepsilon 1}$ of the amide group of Gln18 and the N_4H2 amino group of C7, the other between the NH2 groups of Arg22 and O_6 of G5. Interestingly, such hydrogen bond formation has been predicted by NMR studies on complexes between side-chains of amino acids and bases of nucleic acids.[108] Except for an H-bond between $N_{\varepsilon 2}$ of Gln18 and O_4 of T8, which was observed in 14% of the configurations, the other H-bonding contacts were formed to phosphate groups. Three residues of the helix II $O_{\gamma 1}H$ (Thr19)-O_1P (T4) and -O_2P (T4), $O_{\gamma}H$ (Ser21)-O_2P (T8), $N_{\delta 2}$ (Asn25)-O_1P (T8) are involved as well as His29 ($N_{\delta 1}$)-O_2P (T3) in the loop following helix II. Stable hydrogen bonds were

formed between the DNA backbone and groups near the beginning of helix I (NH (Leu6)-O_2P (C9)) and in the C-terminal region ($O_\eta H$ (Tyr47)-O_1P (C9) and NH (Asn50)-O_1P (C9)). Some intraprotein hydrogen bonds (the hydroxylic group of Thr19 with the peptide amide groups of Thr19 and Gln18, the side-chains of Arg22 with Gln18 and Gln26) were proposed to add extra specificity and binding strengths by orienting residues Ser16, Thr19 and Arg22 and both glutamines which are involved in direct or water-bridged contacts to the operator. Several apolar contacts involve the residues of the helix I (Leu6), of the helix II (Tyr17, Gln18, Ser21) of the loop between the helices II and III (Asn25, Gln26, His29), of the helix III (Asn50, Arg51) and the base (C5, C6) or the sugar (C2′, C3′) or the backbone (C4′, C5′) of the nucleotides C9, T8, C7, T3, A2, C9 and G10, respectively were observed.

Many water-bridged contacts were observed between the headpiece and the operator (Fig. 6). Most of them involved phosphate groups: NH (Ser16)-O1P (T4), $O_\gamma H$ (Ser16)-O5′ (G5), NH (Gln26)-O_2P (C7), CO (His29)-O1P (T4), $O_{\gamma 1}H_{\gamma 1}$ (Thr34)-O1P (T4), $N_{\eta 1}H_1$ (Arg51)-O1P (G10). Some water-bridged contacts were also found within the protein: Ser21-Asn25, His29-Thr34 and Ser31-Thr34. The precision of this structure, based on the average r.m.s.d. on backbone atoms between pair of structures, was around 1.3 Å. These data

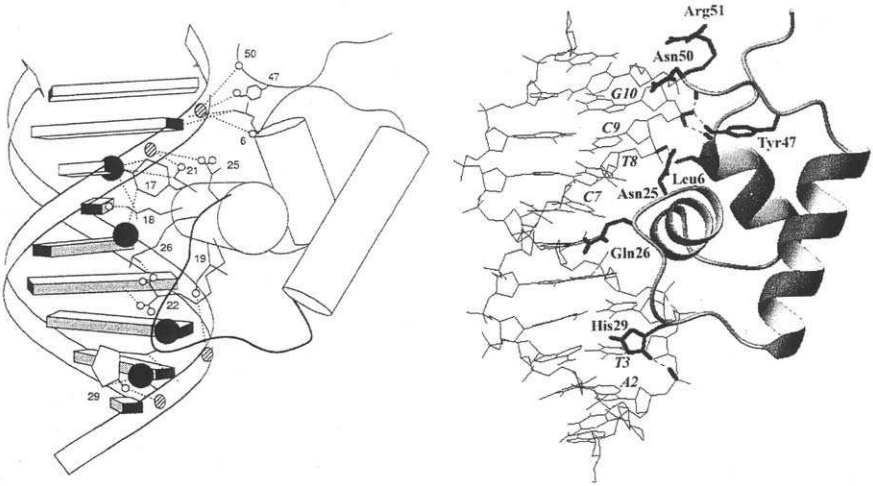

Fig. 6. Schematic view of headpiece–DNA interactions showing hydrogen bonds and apolar contacts between the headpiece and the operator. Right: an internal hydrogen bond between Arg22 and Gln26 plus the apolar contact between the thymine methyl groups and Leu6 are shown. Methyl groups are indicated by black balls, phosphate groups by striped circles and protons in H-bonds by small circles (according to Chuprina *et al.*[30] with permission). Left: General view of the complex, and intermolecular interactions between the helixes I and III or the loops with DNA. Hydrogen bonds are indicated in dotted lines and atoms participating in the apolar contact are in bold. The figure was composed according to the PDB code 1LCC.

allowed some discussions and conclusions on the atomic patterns involved in the specific recognition of the *lac* operator by the *lac* repressor headpiece. The comparison of these data with those from other techniques is presented below.

4.2. The 1-62 headpiece

The 56–62 residues of the *lac* repressor N-terminal part play a key role in the mechanism by which *lac* repressor discerns its specific target DNA. Binding a *lac*I mutant series in which the C-terminus of the hinge region was altered to the wild-type O1 or the symmetric operator showed important differences in binding affinity and in allosteric response.[162]

4.2.1. *The NMR spectra of labeled $^{13}C/^{15}N$ headpiece recorded at 750 MHz*

The NMR solution structure of the *lac* repressor binding domain (headpiece 1-62) complexed by a 22 base pair symmetrical operator was published by Spronk *et al.*[152] The experimental restraints were based on a NMR study[33] implying the 1-62 headpiece binding to a 22 base pair symmetrical operator showing the formation of a hinge helix. Analysis of the structure revealed specific interactions, which were not found in previous investigated complexes involving *lac* repressor 1-51 or 1-56 headpiece.

The solution structure of the complex between 1-62 *lac* repressor headpiece and a palindromic 22 base pair 5′d$(GAATTGTGAGCGCTCACAATTC)_2$ was obtained by using data given by heteronuclear NMR studies recorded at 750 MHz. HP62 assignments were obtained with a $^{15}N/^{13}C$ protein[163] and DNA assignments from 2D NOE and simultaneous ^{13}C–^{15}N double-half filter NOE experiments. Protein–DNA interactions were assigned from 2D time-shared ^{13}C–^{15}N double-half filter, 2D NOE and 3D NOESY-HSQC experiments. Protein–protein interactions were identified in a 3D-^{13}C-filtered-NOESY-HSQC[164] on a mixture 50% unlabeled/50% $^{15}N/^{13}C$ labeled HP62 complexed to the 22 base pair operator. The NMR spectra showed numerous NOEs between the hinge helices and the central part of the operator. The structure calculations were performed with XPLOR 3.851. An initial ensemble of 250 structures was generated. After refinement, 46 structures were selected, docked onto the 22 base pair *lac* operator and annealed. The 14 best structures were selected for restricted MD simulations in water using the CHARMM22 force field.[165] Analysis of the protein–protein and protein–DNA interactions was performed on the last 3 ps of the trajectory (whole trajectory of 24 ps) of 11 selected final structures.

4.2.2. *Use of isotope-filter for observation of NOE between protein and nucleic acid*

Nucleic acid and protein 1D spectra showed numerous resonances which can be assigned by using conventional ^1H NOESY spectra if the molecules are not

too large: 100–140 residues for a protein and 20–30 base pairs for an unself-complementary oligodeoxynucleotide are generally the superior limit in size. When a protein is complexed to a nucleic acid, numerous overlappings occur between connectivities in the 2D NOESY spectra and the conventional sequential assignment can no longer be used for the protein. Generally the sequential assignment of the complexed nucleic acid is easier than the protein one because the H6/8-H1′ region, crucial for the assignment of aromatic resonances, is not—or almost not if numerous aromatic residues are present in the protein—overlapped by the intraprotein connectivities. Then, some protein–nucleic contacts can be observed and Kaptein's group used this property to get the first known contacts between the headpiece 1-56 and a half of operator. Nevertheless, this procedure is limited and some contact not always sure.

Another way is to use uniformly labeled $^{13}C/^{15}N$ protein or nucleic acid. Using of isotope filter has greatly improved the confidence of the data. In the most general sense, an isotope filter discriminates between coherences that involve proton spins and an heteronuclear (X) spin, and those that do not involve the spin X. Half-filters[166,167] or and X(ω_1, ω_2) double half-filter[168] allow to distinguish between intra- and intermolecular NOEs of molecular complexes in which one of the components has been uniformly labeled. The desired simplified spectra are obtained by inserting ^{15}N or ^{13}C half-filters consisting of a (-τ/2-π(^{1}H) π(^{15}N or ^{13}C)-τ/2-π(^{15}N or ^{13}C)) pulse sequence, either before the evolution period (ω_1 half-filter) or immediately before the detection (ω_2 half-filter) of the conventional 2D ^{1}H NMR experiments. Efficiency of the half-filter relies on the fact that $^{1}J(^{1}H, ^{15}N)$ or $^{1}J(^{1}H, ^{13}C)$ coupling constant values vary only by a few percent between the different residues of the polypeptide chain and that the values of the other coupling constants are quite different. Addition of a supplementary π(^{13}C or ^{15}N) pulse (or a variant of this process) changes the sign of the antiphase component but led invariable the sign of the component relative to the^{13}C- or ^{15}N-unattached proton. Depending on the introduction of a supplementary π(^{13}C or ^{15}N) pulse, two subspectra can be recorded $^{1}J(^{1}H, ^{15}N)$.[166] The first subspectrum contains cross-peaks between ^{13}C- or ^{15}N-attached protons in one direction and any proton in the second direction. The sum of the two subspectra contains all the connectivities, which would be recorded with an unlabeled molecule and the difference of the two subspectra. The double half-filter uses a half-filter X(ω_1) in conjunction with another half-filter X(ω_2), allowing one to discriminate between X-attached or -unattached protons in both directions X.[168] Improved and modified versions of the X-half filter have been proposed.[169–172] The efficiency of these sequences have been improved by using adiabatic pulses,[63] time-shared (^{13}C, ^{15}N) half-filter[63] or z filter implemented by pulse field gradient.[173]

Using of (^{13}C, ^{15}N) double half-filter NOE allows one to obtain: (1) the intra-DNA ($^{12}C/^{14}N$, $^{12}C/^{14}N$) spectra which allow the sequential assignment of complexed DNA resonances; (2) the intraprotein (^{13}C, ^{13}C), (^{15}N, ^{15}N) and (^{13}C, ^{15}N) spectra which allow the sequential assignment of the complexed

protein resonances; the interprotein–DNA (^{13}C, $^{12}C/^{14}N$) and (^{15}N, $^{12}C/^{14}N$) spectra which allow to observe the NOE connectivities between the two partners. These techniques have been applied to solve various problems such as: (1) finding intermolecular contacts in the complex of ^{13}C-labeled DNA-binding domain of P22 *c*2 repressor with DNA[169] and in the complex of $^{13}C/^{15}N$-labeled *lac* repressor headpiece with the *lac* operator,[30,152] (2) finding evidence of protein–protein contact between the hinge helices of $^{13}C/^{15}N$-labeled *lac* repressor headpiece bound to DNA,[152] (3) observing of intra- or intermonomer NOEs in various situations such as the dimeric gene V protein[169] and the *arc* repressor,[169] (4) distinguishing between duplex or hairpin forms of dimers.[174]

4.2.3. *The helix-turn-helix motif*

The determination of the crystal structure of four DNA binding proteins, i.e. the CAP by McKay and Steitz,[116] the *trp* repressor by Schevitz *et al.*,[117] the *cro* repressor from the bacteriophage *lambda*[118] and the *lambda* repressor[119] showed a common structural feature of the interacting proteins. These data led to the proposal that the motif called helix-turn-helix with the second helix interacting in the major groove[22,153] was responsible for the specific recognition of the *lac* repressor by the *lac* operator. Detailed models were proposed by Matthews *et al.*[115] and by Weber *et al.*[175] on the basis of an analogy with *cro*-OR3 and CAP–DNA complexes, respectively.

The spatial structure of the free headpiece has been derived from NMR data and showed a small globular domain with a hydrophobic core formed by three helixes in which is found the helix-turn-helix motif.[26,34] NMR data showed that the second helix is bound to the major groove of DNA but the orientation of the *lac* operator with respect to the binding protein is inverted from the orientation found in the other complexes.[114,115] This orientation has been corroborated by genetic data.[15,21] Other genetic data suggest that this orientation occurs for operator complexes of other bacterial repressor proteins.[176]

The residues of the first helix of HP62 that contact the *lac* operator are Thr5, Leu6 and Tyr7. The most prominent feature is the very stable H-bond formed between the backbone amide group (NH) of Leu6 and a nonesterified oxygen O_2P of the phosphate group of C9.[30] The position of the side-chain of Leu6 is well-defined (12 NOEs to the DNA) in contrast with the conformation found in the half-site complex. The side-chain of Leu6 presents nonpolar interactions to the bases of T8 and C9 and to the backbone of G10. A water-mediated contact occurred between the hydroxylic group of Thr5 and the phosphate of G10.

The second helix is called the recognition because it has numerous contacts with DNA. Tyr17 interacted with the bases of T6, G7 and T8. Gln18 interacted with C7 and A6 through both hydrogen bonds ($O_{\varepsilon 1}$(Gln18)-N4H (C7), $O_{\varepsilon 1}$(Gln18)-N_6H (A6)) and hydrophobic contacts (C_δ(Gln18)-C_5 (C7)). These results are in close agreement with the genetic experimental data[16,21] which conclude that the specific binding of Tyr17 and Gln18 is directed towards the base pairs 7 and 6. Three other residues (Ser21, Arg22, and Asn25) were found

important for the interaction with DNA. The hydroxyl group of Ser21 formed an hydrogen bond with O_2P of T8 and a part of the time formed a water-bridged hydrogen bond to the carbonyl C=O of Asn25. The amino group of Asn25 was directed to G6 by forming an hydrogen bond to the oxygen O_1P of the phosphate of T8 as suggested by the high frequency shift observed for the NH2 resonance of Asn25 in the HP62–*lac* operator complex. No conclusion can be drawn in the complex with HP62 for Arg22 in HP62 because the structural disorder of its side-chain. Genetic[21] and structural data[30] indicate that Arg22 is important for the interaction of the headpiece with DNA. This residue could be interacted with several different base pairs of the *lac* operator in a dynamic process causing a broadening of its resonance lines by chemical exchange process. It could be pointed out that a hydrogen bond between the NH2 of the guanidinium group of Arg22 and O6 of the base of G5 was reported with HP56.[30]

The loop following the recognition helix is, as shown by several NMR studies,[33,132,143] involved in the interaction with the DNA. These interactions involve the residues His29, Val30 and Ser31. His29 directly contacts the nucleotides A2 and T3 through apolar (C_β with $C_{2'}$ (T3), $C_{\varepsilon 1}$ with $C_{2'}$ (A2), $C_{\varepsilon 1}$ with C_5CH3 (T3)) and hydrogen bonding ($N_{\delta 1}H$ with O_2P (T3)) interactions. These interactions are in agreement with the genetic data that show low mutation sensitivity for residues 26–28, whereas residues 29–31 are sensitive to mutations.[24] It is important to point out that ^{15}N dynamic NMR studies[132] show that this loop is characterized by some flexibility in the free state. This flexibility provides some adaptability to the helixes II and III and to the loop itself for binding the target DNA.

In the third helix, which is important for the stability of the headpiece, only Thr34 showed interactions with DNA. Just beyond this helix important and stable hydrogen bond are formed between DNA and the Tyr47 side-chain. These interactions are in agreement with the observation of the hydroxylic group of Tyr47 which implies a slow chemical exchange of this proton with water and its NOE with H3′ of C9. Tyr47 which is implied in the interactions with DNA which has also a stabilizing role on the structure of the protein as shown by its NOE with Val24 of the second helix.[34] The double role played by Tyr47 was reflected by its intolerance to mutations and its highly conserved nature in the *lac*I family of repressors.[24,177,178]

4.2.4. *The hinge helix and protein–protein interactions*

Several years after the first model of the headpiece–*lac* operator structure derived for NMR data, it was shown[78] that a fourth helix called hinge helix was present in the HP62–22 base pair *lac* operator complex and unfolded in absence of DNA in agreement with the crystallographic structure of the homologous *pur* repressor complexed with its operator.[37] Later, this motif was also found in the *lac* repressor–*lac* operator complex.[27] A heteronuclear NMR study on the 1-62 HP showed that in the free HP62 the C-terminal region 50–62

is disordered in solution but that the residues 50–58 form a hinge helix when the HP62 is bound to a full 22 base pair symmetric *lac* operator.[33] The interactions of HP62 with the minor groove were all formed by the residues of the hinge helix. It was shown that the Asn50, at the beginning of the hinge helix, anchored the helix to DNA backbone by hydrogen bonds involving its backbone amide and side-chain NH2 groups. Ala53 and Leu56 were both involved in protein–DNA and protein–protein interactions. Leu56 intercalated in the central base pair step of the operator and was largely responsible for the distortions of the DNA structure.[152] Gln54 was involved in hydrogen bonding with its side-chain NH2 group to DNA backbone at T8, in agreement with the decreased mobility of this side-chain upon bonding.[132]

In order to discriminate between intra and inter NOE protein, a 3D-filtered-NOESY-HSQC[164] was used on a sample containing 50% ^{15}N–^{13}C labeled/50% unlabeled HP62 in complex with *lac* operator. Height NOEs were observed between the residues Val52–Val52′, Val52–Gln55′, Val52–Leu56′ and Ala53–Leu56′. The protein–protein interactions found in the HP62–22 base pair *lac* operator were in agreement with the fact that the induction of the *lac* repressor causes changes at the hinge region and consequently disrupts the helix-stabilizing interactions. These data are in agreement with the genetic data which show that all of the residues in the hinge helix are highly sensitive to amino acid replacements[24,179] and with the location of the conserved residues (Asn50, Ala53, Gln54 and Leu56). Crosslinking by oxidation of the two hinges of a mutant where Val52 was replaced by cysteine (Fig. 7) yields a repressor that binds the *lac* operator with six times higher affinity than the wild-type repressor does. As a consequence this complex was not inductible, proving the importance of the residue Val52.[110]

4.3. Difference between the HP56– and the HP62–*lac* operator complex

The major difference between the HP56–DNA and HP62–DNA complexes is the presence of the hinge helix, which participates in supplementary interacting points with the DNA and stabilizes the molecular edifice by protein–protein contacts. This increases the affinity of the *lac* repressor for its operator.[162] Interactions of the hinge helix with the nucleotides C9, C10 and G10 in the minor groove cause a bend of the operator of about 45° and open the minor groove. As a consequence, the surface of the major groove is changed and the protein–DNA interactions of the second helix are modified. For example, the aromatic-ring-stacking of Tyr7 and Tyr17 in the HP56–DNA complex disappears in the HP62–DNA complex as indicated by the differences in chemical shifts of the Tyr17 ring protons. This can be explained by the fact that the change in the surface of the major groove causes a steric clash between Leu6, Tyr7 and DNA, precluding the stacking of Tyr17. Another difference is the absence of interactions between Gln26 and DNA in the HP62–DNA

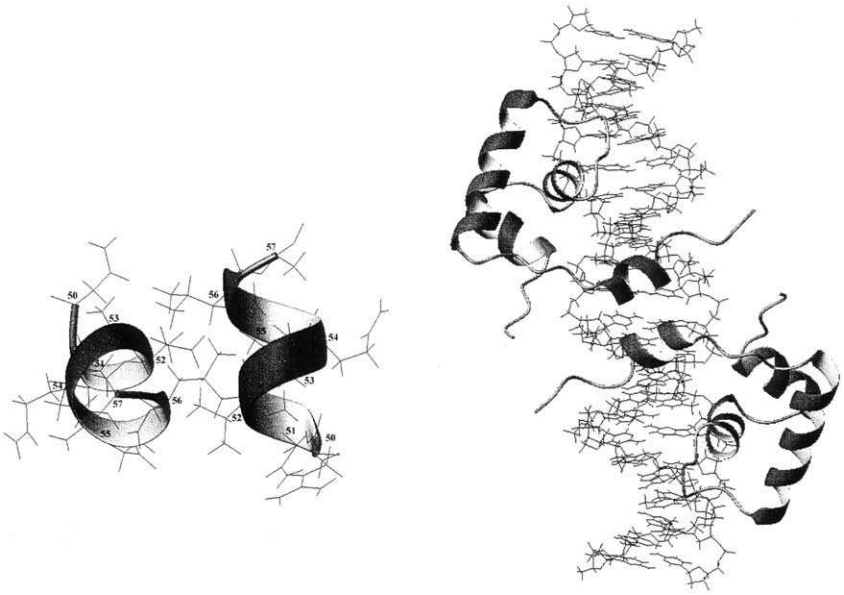

Fig. 7. Intermolecular interactions in the HP62–DNA complex. Right: General view of the complex. Left: Position of the hinge helixes in the minor groove of the operator. The figure was composed according to the PDB code 1CJT.

complex whereas the side-chain of this residue forms apolar contacts with the base of C7 and that its peptidic NH forms a water–hydrogen bond mediated with the phosphate of C7 in the HP56–DNA complex. The formation of a protein–protein interface between the two hinge helices induces tight binding of the operator[77,152] and plays a major role in the action of inducer molecules.

4.4. Hydrogen exchange in protein–DNA complexes: a probe for the protein–DNA association pathway

Proton resonances of protein amide groups cannot be observed if they are in fast exchange with water. Starting from this property, amide proton exchange is well established as a powerful technique in the study of protein stability, folding and dynamics.[77,152,180–186] Following the scheme of Hvidt and Nielsen,[187] the exchange rates were analyzed according to the following scheme:

$$\text{Closed (NH)} \underset{k_{cl}}{\overset{k_{op}}{\rightleftharpoons}} \text{Open (NH)} \xrightarrow[D_2O]{k_{int}} \text{Exchanged (ND)}$$

where open and closed conformations interconvert with mean exchange rates k_{op} and k_{cl}, respectively. Exchange can take place with a rate constant k_{int}

which can be easily calculated from reference rate constants for random structure.[188] Studies on the function of pH allow one to work on large-scale exchange rates since exchange is catalyzed by acids and bases.

The measured apparent exchange rate is $k_{obs} = k_{op}k_{int}/(k_{op}+k_{cl}+k_{int})$. Two limit cases are interesting to examine. In the first case, k_{cl} is much greater than k_{int} and the observed hydrogen exchange $k_{obs} = (k_{op}/k_{cl})k_{int} = k_{op}k_{int}$ were k_{op} is the constant for exchange competent. This is known as EX2 exchange and the results are often reported as the apparent free energy of opening or exchange $\Delta G = -RT\ln(k_{op})$. In the second case, called EX1 exchange, k_{int} is much greater than k_{cl} (typically above pH 8–9) and $k_{obs} = k_{op}k_{int}$ depends on sequence, pH and temperature can be easily calculated as demonstrated by Bai *et al.*[188] Thus, exchange rates measured in the two conditions (pH lower to 7 and pH in the range of 8–9) can be used to extract both the thermodynamic and kinetic data of the opening event. Sivaraman *et al.*[189] showed, by investigating NH exchange in native ubiquitine that values k_{op} and k_{cl} for the most slowly exchanging amide protons were equivalent to the rate constants for the unfolding and folding conditions.

Kalodimos *et al.*[190] demonstrated, by measuring exchange rates from ^{15}N HSQC spectra, that this methodology can be used to acquire thermodynamic and kinetic information on protein–DNA complexes at the residue level. The protection factor $P = k_{int}/k_{obs}$ is used to qualify the folding of a dimeric *lac* repressor headpiece mutant called HP62–V52C which has a high affinity for DNA.[77] Protection factors of the *lac* HP62–V45C in the free state were found to be low (average value $< 10^2$) at 17 °C and pD 4.5[190] whereas in a folded protein they are in the range of 10^4–10^8. This low stability of the molecule was corroborated by a low melting temperature. Upon binding a symmetrical L operator (right part of the operator O1 symmetrized), the protection factor was increased until 10^8. Interestingly, the protection was not limited to the binding site but throughout the entire molecule. This clearly means that binding of the headpiece to the operator reduces the conformational states from which exchange can occur.

In order to follow the dissociation of the protein–DNA complex with residue level specificity, the hydrogen exchange of the *lac* HP62–V52C bound to the symmetrical left operator was measured. The exchange rates of the different NH proton were classed in four distinct groups.[190] The hinge helix is the first group to open is ($0.20\,h^{-1}$), followed by Asn50 and the C-terminal residues of the third helix ($0.11\,h^{-1}$). Unfolding of this part of the protein is propagated to the rest of the molecule, resulting in dissociation with a rate of $0.02\,h^{-1}$.

In view of the asymmetry of the two binding sites of the natural *lac* operator, protection factors were measured and found to be the same for the protein subunits bound on the left and right sides of O1. The opening rates were found to be the same for both protein subunits but hinge helices open with a 10-fold higher rate, whereas the complex dissociates 20 times faster ($0.39\,h^{-1}$). Based on the opening rates for the individual sites, a model of progressive unfolding

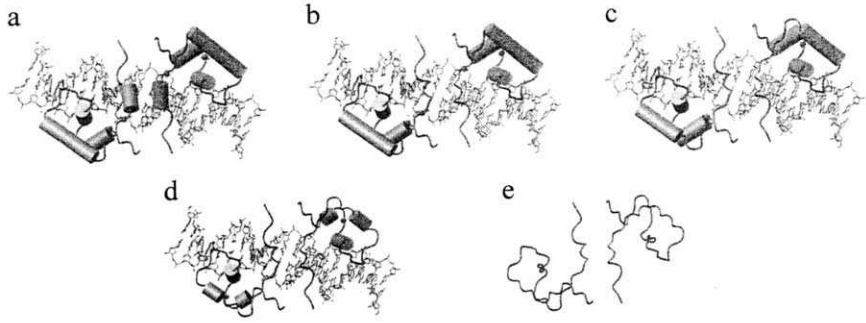

Fig. 8. Model of dissociation pathway of the *lac* repressor from the ideal left symmetrical *lac* operator (according to Kalodimos *et al*.[77] with permission).

of the individual units was proposed (Fig. 8). In this model, the first structural unit to unfold is the hinge helix, followed by the disruption the NH (Asn50)–PO4 hydrogen bond and the third helix. Then, the NH (Leu6)–PO4 hydrogen bond is disrupted leaving only the recognition helix linked to DNA by its numerous contacts. Finally, all of the protein is unbounded.

From the analyses of the protection rates of an important residue for the recognition helix Gln18 ($40\,s^{-1}$), of Leu6 ($20\,s^{-1}$), a residue at the beginning of the first helix, of Asn50 and of the hinge helix formation which is slower than Gln18 protection by a factor of 10, a protein–DNA association pathway was proposed.[190] In this scheme, ''flexibility of the DNA-binding domain of the *lac* repressor in the presence of noncognate operator sites allows it to slide along the DNA, facilitating target location. Once, the specific site is reached, the DNA sequence is first read in the major groove by recognition helix, followed by discrimination of the minor groove by the hinge region''[190] (Fig. 8).

4.5. Differences in binding mode of the left and right part of *lac* operator upon *lac* repressor

As already remarked (see Section 2.3), *lac* repressor binds the left part of the *lac* operator with higher affinity than the right part. Several studies have been devoted to explain the origin of this difference. For example, cross-links of *lac* operator specifically substituted with bromodeoxyuridine upon the *lac* repressor reflected the asymmetry of the interaction.[191]

It is interesting to compare the degree of affinity by which DNA binds upon a headpiece dimer. This has been accomplished by using the oxidized form of the HP62–V52C and the fact that the *lac* repressor protein interacts more

strongly with the left half-site of the operator than it does with the right half-site.[35,128] The highest affinity of the engineering dimer was measured for the left symmetrical operator (Fig. 1), followed by the wild type (twofold decrease) and the left symmetrical operator (10-fold decrease). The degree to which DNA bends upon repressor binding was found to follow the same trend: 33° for the left symmetric dimer, 24° for the wild type and 17° for the right symmetric dimer.[77] These biochemical results are very similar to the NMR results determined on the intact HP62. They strongly suggest that the dimeric HP62–V52C structure and the intact repressor behaves in the same way.[77]

NOE and chemical data observed on ^{15}N HSQC and ^{15}N NOESY-HSQC spectra of the free dimer HP62–V52C and its complex with the wild type operator show unambiguously that the C-terminal region of the dimer free is unstructured and that the hinge regions of both the left and right sites form an α helix when complexed to the operator.[77] Contacts and chemical shift variations observed in complexes with the left and right symmetrical operator show that differences in the sequence of the two sites influence the mode by which contacts are made with the headpiece. In particular, the results suggest strongly that the highly conserved residue Asn50, which is hydrogen bonded in the complex with the left part of the operator is not hydrogen bonded in the complex with the right part. This contact orients the hinge helix within the minor groove of the left part of the operator. The lack of this clamp destabilizes the linked conformation in the complex with the right part and is an element explaining the difference in affinity of the sites. Additional and independent experimental evidence of differential binding to the left and right side of the wild-type operator have been obtained by amide exchange experiments on the HP62–V52C complex. High protection factors have been observed for residues participating in hydrogen bonding. In particular, the NH signals of Leu6 and Ser31 were present in the spectrum 2 days and 12 h after, respectively, suggesting that the corresponding protein–DNA is present in both sites. Exchange rates of the Asn50 amide proton indicates that the backbone amide is protected only in the left site, in agreement with the NOE data of the protein-left and -right symmetrical operator and the deuterium exchange experiments. Quantification of exchange in the hinge region showed that the right hinge helix exchanges with a twofold higher rate than with those of the right site. NMR analysis indicates slow exchange (of order of $10\,s^{-1}$) of hinge region residues between the α helix and random coil form. This instability in the right half-site originates from the local contact of the protein in the minor groove and is most probably related to the absence of hydrogen bonds between the backbone of Asn52 and DNA.[77] Consequently, protein–DNA interactions in the minor groove modulate efficiency of the binding and can explain the affinity variations among the variant operator sites. In simple words, the *lac* repressor sequentially reads out the DNA sequence in the major and in the minor groove and fulfills to the well-known notion of sequence complementarily between the two partners.

4.6. Comparison with other structures of *lac* repressor

The crystal structure of the whole tetrameric *lac* repressor complexed to a symmetrized operator,[25,27] of the *lac* repressor core tetramer,[28] a dimer of a *lac* repressor varian[192] and a crystallographic analysis of *lac* repressor bound to its natural operator have been solved.[35] At present, the most detailed view of the repressor–operator interactions comes from NMR studies because of the limited resolution of the crystallographic structures. Nevertheless, the crystal structure of the complex[35] was obtained with the natural operator O1 whereas the NMR solution structure of the complex was obtained with a symmetrical operator. The twofold symmetry of the wild operator is broken by a variation in sequence between the two half-sites and by a central G.C base pair giving an odd number of base pairs (Fig. 1). Moreover, the symmetrical sequence binds the *lac* repressor with a higher affinity than the wild one. Consequently, it is interesting to compare the crystallographic data obtained from the wild operator at 4.0 Å resolution and the NMR structure. It is found[35] that the natural operator O1 sequence is bent in the same way as the symmetrical sequence due to the bending of the hinge helices of the repressor in the minor groove at the GCGG sequence of O1. Comparison of the structures of the natural and symmetrical bound operators shows similar overall structures. Only slight rearrangements of the headpiece were observed. Protein–protein and protein–DNA interactions between the hinge helices and the minor groove of the operator stabilized the bent conformation of the DNA in the same way in both structures (see Section 4.5).

The crystal structures of the lactose operon repressor and its complexes with symmetrical DNA and inducer IPTG led to a structural model of the interaction of IPTG. Figure 9 represents a view of the *lac* repressor–DNA complex monomer. Assembly of the tetramer is mediated by two separate regions: the monomer–monomer interface which is generated by contacts throughout the core domain primary sequence and a dimer–dimer interface formed by a short segment at the C terminus of the protein (340–360) that assemble via a leucine heptad repeat sequence into a 4-helical anti-parallel coiled-coil structure.[23,27,28,193–201] IPTG is found to be bound on the core formed by the two subdomains that are topologically similar, with a six-stranded parallel β sheet that is sandwiched between the four α helices.[27] The structural change between the induced and repressed states is propagated via the hinge helices of the headpieces. The change in the dimer interface within the NH2-terminal subdomain results in the displacement of the α carbon of the first residue of the core by 3.5 Å. According to this model, IPTG binding alters the orientation of the headpieces, which, in turn, displaces the hinge helices from the minor groove of the operator and drastically reduce the affinity of the *lac* repressor for the operator. This model is in agreement with the genetic data[202,203] and the disulfide bond between the two headpieces which disrupts the allosteric linkage.[204]

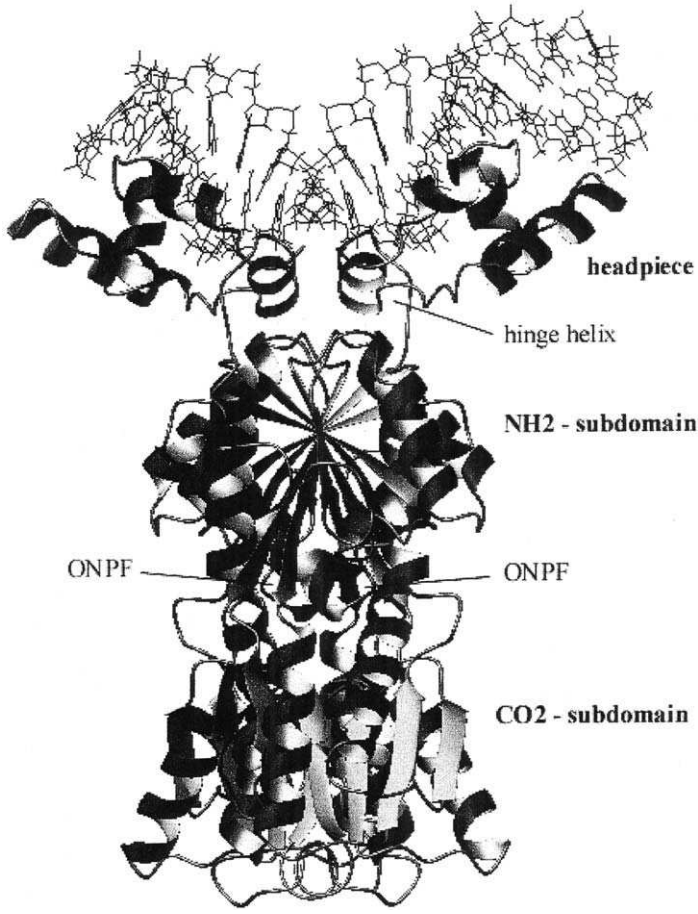

Fig. 9. View of the dimeric *lac* repressor–DNA complex monomer. Two arrows show the position of ONPF. Despite having opposite effects, ONPF and IPTG bind to the same site on the repressor.[25] This figure was composed according to the PDB code 1EFA.

The purine repressor belongs as does the *lac* repressor, to the 36 putative members of the *lac*I family. The free purine repressor (1-59) structure has been determined by NMR[205] and the purine repressor dimer structure complexed to its operator has been solved by X-ray crystallography.[37] The structures of the complex with DNA obtained by the two methods are very similar as in the case of the *lac* repressor headpiece.[206] Superposition of these structures on the C_α atoms[152] yields an average pairwise r.m.s.d. of 0.72 Å for the *pur* repressor (residues 4–32 and 32–35) and 0.94 Å for *lac* repressor (residues 6–25 and 34–57). Free or complexed *lac* repressor headpiece and *pur* repressor exhibit a very similar helix-turn-helix motif as well as a stabilizing third helix. The crystal

structure of the purine show, in the case of the headpiece *lac* repressor, specific contacts of the second helix with the major groove of its operator and of the hinge helix with the minor groove.[37]

The fructose repressor is organized in two functional domains, as are the other members of the *lac*I family. Its N-terminal domain is formed of 60 residues and is responsible for the binding of its operator and its core displays inducer-binding properties.[207,208] ^{1}H and ^{15}N NMR studies[36] show that the fructose repressor headpiece exhibits, as does the *lac* repressor headpiece, a helix-turn-helix motif stabilized by a third helix with a C-terminal domain unstructured in the free state.

5. CONCLUSION

The great number of studies devoted to the NMR solution structures and crystal structures of the *lac* repressor–*lac* operator complexes, show clearly the complementarily of these methods. NMR is able to bring structural and dynamic information on molecules or complexes of moderate size, whereas crystallography can give structural information on molecules of higher size. The *lac* repressor–*lac* operator system is a typical case where both small structural units (1-62 headpiece) and multimeric proteins are necessary to the allosteric function. Reinforcing the credibility of NMR protein structures, well established by Wüthrichs group,[209–211] the most detailed view of the *lac* repressor–*lac* operator interaction comes, at present, from NMR studies. This is the result of the ability of NMR data to produce structures of molecules showing dynamics. However, the size of the *lac* repressor tetramer (4×360 residues) is, today, too great to be structure-resolved by NMR. Recently, several crystallography structures have revealed that the binding of the hinge helix in the small groove mediates the transmission of the allosteric signals that show the DNA-binding activity. Although the IPTG inducer binds to a pocket at the junction of the N subdomain and to the C subdomain of the core (62–333), comparison of the free or bound HP62 NMR solution structures, allow one to propose a scheme explaining the loss of affinity of the *lac* repressor for its operator when binding to the inducer. This model is in agreement with the genetic data and with the crystal structure of the repressor bound to the inducer (4 or 4.8 Å resolution).

The high resolution of this protein–DNA complex allows one to highlight its topography and the different types of interactions involving the different functional groups of the two partners. A great number of apolar interactions involving C_5 or C_6 of cytosines, C_5CH_3 of thymines, C_2 of guanines, the carbons $C_{1'}$, $C_{2'}$, $C_{3'}$, $C_{4'}$ or $C_{5'}$ of the sugars and the carbons of the side-chains stabilize this complex. A lot of hydrogen bonds, direct or water-mediated, are also found. For example direct hydrogen bonds are found between the two interacting molecules (NH_2–OH, NH_2–PO_4, NH_2–$CONH_2$). All these types of

hydrogen bond formation had already been expected and demonstrated by NMR studies on amino acid–nucleotide complexes.[108,212–219] They can be considered as modular bases of the recognition process. No intercalation of aromatic amino acids between the nucleic acid bases was observed, in agreement with the rotation diffusion measurements.[220] Surprising, no ionic interactions involving charged groups of the two partners such as NH_3^+ of lysines or the guanidinium group of the arginines with phosphates were observed. All these features highlight the importance of the complementarity of structure of the two partners in the specific recognition processes. ^{15}N and ^{13}C relaxation rate measurements point out the internal dynamics of the protein and of the operator and underline the importance of the adaptability of the structure of the two partners in order to optimize the affinity of a protein for a nucleic acid sequence.

6. PDB ACCESSION CODES OF STRUCTURES DEPOSITED WITH THE PROTEIN DATA BANK

Several NMR solution structures and crystallographic structures are available on the PDB under the accession codes:

1CJG (NMR)	NMR structure of *lac* repressor HP62–DNA complex[152]
1EFA (X-ray diffraction)	*lac* operator bound to a 20 bp symmetric operator and ONPF[25]
1JYE (X-ray diffraction)	Structure of a dimeric *lac* repressor with C-terminal deletion and **K84L** substitution[192]
1JWL (X-ray diffraction)	*lac* repressor bound to the natural operator and ONPF[35]
1JYF (X-ray diffraction)	Structure of the dimeric *lac* repressor with an 11-residue C-terminal deletion[192]
1K9H (NMR)	NMR structure of DNA TGTGAGCGCTCACA[221]
1K9L (NMR)	Solution structure of DNA TATGAGCGCTCATA[221]
1LBI (X-ray diffraction)	*lac* repressor[27]
1LCC and **1LCD** (NMR)	Structure of the complex of *lac* repressor headpiece and an 11 base pair half-operator corresponding to the left half of the wild type *lac* operator[30]
1LQC (NMR)	*lac* repressor headpiece structure[31]
1TLF (X-ray diffraction)	Crystal structure of *lac* repressor core tetramer and its implications for DNA looping[28]

REFERENCES

1. B. Müller-Hill, *The lac Operon: A Short History of a Genetic Paradigm*, W. de Gruyter (ed), Berlin, New York, 1996, 1.
2. C. E. Bell and M. Lewis, *Curr. Opin. Struct. Biol.*, 2001, **11**, 19.
3. K. S. Matthews and J. C. Nichols, *Prog. Nucleic Acid Res. Mol. Biol.*, 1998, **58**, 127.
4. J. H. Miller and W. S. Reznikoff,The Operon, 2nd edn, Cold Spring Harbor, NY, 1980, 1.
5. U. Deuschle, R. Gentz and H. Bujard, *Proc. Natl. Acad. Sci. USA*, 1986, **83**, 4134.
6. S. B. Straney and D. M. Crothers, *Cell*, 1987, **51**, 699.
7. J. Lee and A. Goldfarb, *Cell*, 1991, **66**, 793.
8. P. J. Schlax, M. W. Capp and Record, M. T., Jr., *J. Mol. Biol.*, 1995, **245**, 331.
9. W. Gilbert and B. Müller-Hill, *Proc. Natl. Acad. Sci. USA*, 1966, **56**, 1891.
10. K. Beyreuther, K. Adler, N. Geisler and A. Klemm, *Proc. Natl. Acad. Sci. USA*, 1973, **70**, 3576.
11. S. Bourgeois and M. Pfahl, *Adv. Prot. Chem.*, 1976, **30**, 1.
12. P. J. Farabaugh, *Nature*, 1978, **274**, 765.
13. O. G. Berg, R. B. Winter and P. H. von Hippel, *Trends Biochem. Sci.*, 1982, **7**, 52.
14. J. Monod, J. Wyman and J. P. Changeux, *J. Mol. Biol.*, 1965, **12**, 88.
15. N. Lehming, J. Sartorius, S. Oehler, B. von Wilcken-Bergmann and B. Müller-Hill, *Proc. Natl. Acad. Sci. USA*, 1988, **85**, 7947.
16. J. Sartorius, N. Lehming, B. Kisters-Woike, B. von Wilcken-Bergmann and B. Müller-Hill, *J. Mol. Biol.*, 1991, **218**, 313.
17. D. V. Goeddel, D. G. Yansura and M. H. Caruthers, *Proc. Natl. Acad. Sci. USA*, 1978, **75**, 3578.
18. A. M. Khoury, H. S. Nick and P. Lu, *J. Mol. Biol.*, 1991, **219**, 623.
19. N. Lehming, J. Sartorius, M. Niemoller, G. Genenger, B. v Wilcken-Bergmann and B. Müller-Hill, *EMBO J.*, 1987, **6**, 3145.
20. J. H. Miller and W. S. Reznikoff, *The Operon*, Cold Spring Harbor, NY, 1978, 1.
21. J. Sartorius, N. Lehming, B. Kisters, B. von Wilcken-Bergmann and B. Müller-Hill, *EMBO J.*, 1989, **8**, 1265.
22. Y. Takeda, D. H. Ohlendorf, W. F. Anderson and B. W. Matthews, *Science*, 1983, **221**, 1020.
23. H. C. Pace, M. A. Kercher, P. Lu, P. Markiewicz, J. H. Miller, G. Chang and M. Lewis, *Trends Biochem. Sci.*, 1997, **22**, 334.
24. P. Markiewicz, L. G. Kleina, C. Cruz, S. Ehret and J. H. Miller, *J. Mol. Biol.*, 1994, **240**, 421.
25. C. E. Bell and M. Lewis, *Nat. Struct. Biol.*, 2000, **7**, 209.
26. E. R. Zuiderweg, R. M. Scheek, R. Boelens, W. F. van Gunsteren and R. Kaptein, *Biochimie*, 1985, **67**, 707.
27. M. Lewis, G. Chang, N. C. Horton, M. A. Kercher, H. C. Pace, M. A. Schumacher, R. G. Brennan and P. Lu, *Science*, 1996, **271**, 1247.
28. A. M. Friedman, T. O. Fischmann and T. A. Steitz, *Science*, 1995, **268**, 1721.
29. R. Kaptein, M. Slijper and R. Boelens, *Toxicol. Lett.*, 1995, **82–83**, 591.
30. V. P. Chuprina, J. A. Rullmann, R. M. Lamerichs, J. H. van Boom, R. Boelens and R. Kaptein, *J. Mol. Biol.*, 1993, **234**, 446.
31. M. Slijper, A. M. Bonvin, R. Boelens and R. Kaptein, *J. Mol. Biol.*, 1996, **259**, 761.
32. R. Boelens, R. M. Scheek, J. H. van Boom and R. Kaptein, *J. Mol. Biol.*, 1987, **193**, 213.
33. C. A. Spronk, M. Slijper, J. H. van Boom, R. Kaptein and R. Boelens, *Nat. Struct. Biol.*, 1996, **3**, 916.
34. R. Kaptein, E. R. Zuiderweg, R. M. Scheek, R. Boelens and W. F. van Gunsteren, *J. Mol. Biol.*, 1985, **182**, 179.
35. C. E. Bell and M. Lewis, *J. Mol. Biol.*, 2001, **312**, 921.
36. F. Penin, C. Geourjon, R. Montserret, A. Bockmann, A. Lesage, Y. S. Yang, C. Bonod-Bidaud, J. C. Cortay, D. Negre, A. J. Cozzone, G. Deleage, *J. Mol. Biol.*, 1997, **270**, 496.
37. M. A. Schumacher, K. Y. Choi, H. Zalkin and R. G. Brennan, *Science*, 1994, **266**, 763.
38. K. S. Matthews, C. M. Falcon and L. Swint-Kruse, *Nat. Struct. Biol.*, 2000, **7**, 184.

39. R. T. Sauer, *Structure*, 1996, **4**, 219.
40. B. Müller-Hill, *Prog. Biophys. Mol. Biol.*, 1975, **30**, 227.
41. K. Arndt, H. Nick, F. Boschelli, P. Lu and J. Sadler, *J. Mol. Biol.*, 1982, **161**, 439.
42. H. Nick, K. Arndt, F. Boschelli, M. A. Jarema, M. Lillis, J. Sadler, M. Caruthers and P. Lu, *Proc. Natl. Acad. Sci. USA*, 1982, **79**, 218.
43. H. Nick, K. Arndt, F. Boschelli, M. A. Jarema, M. Lillis, H. Sommer, P. Lu and J. Sadler, *J. Mol. Biol.*, 1982, **161**, 417.
44. M. A. Jarema, P. Lu and J. H. Miller, *Proc. Natl. Acad. Sci. USA*, 1981, **78**, 2707.
45. F. Rastinejad, P. Artz and P. Lu, *J. Mol. Biol.*, 1993, **233**, 389.
46. P. Lu, M. Jarema, K. Mosser and W. E. Daniel, *Proc. Natl. Acad. Sci. USA*, 1976, **73**, 3471.
47. M. A. Jarema, K. T. Arndt, M. Savage, P. Lu and J. H. Miller, *J. Biol. Chem.*, 1981, **256**, 6544.
48. F. Buck, H. Ruterjans and K. Beyreuther, *FEBS Lett.*, 1978, **96**, 335.
49. N. Wade-Jardetzky, R. P. Bray, W. W. Conover, O. Jardetzky, N. Geisler and K. Weber, *J. Mol. Biol.*, 1979, **128**, 259.
50. N. Geisler and K. Weber, *Biochemistry*, 1977, **16**, 938.
51. M. Hogan, D. Wemmer, R. P. Bray, N. Wade-Jardetzky and O. Jardetzky, *FEBS Lett.*, 1981, **124**, 202.
52. D. Wemmer, A. A. Ribeiro, R. P. Bray, N. G. Wade-Jardetzky and O. Jardetzky, *Biochemistry*, 1981, **20**, 829.
53. A. A. Ribeiro, D. Wemmer, R. P. Bray, N. G. Wade-Jardetzky and O. Jardetzky, *Biochemistry*, 1981, **20**, 823.
54. A. A. Ribeiro, D. Wemmer, R. P. Bray, N. G. Wade-Jardetzky and O. Jardetzky, *Biochemistry*, 1981, **20**, 818.
55. K. Wüthrich, G. Wider, G. Wagner and W. Braun, *J. Mol. Biol.*, 1982, **155**, 311.
56. K. T. Arndt, F. Boschelli, P. Lu and J. H. Miller, *Biochemistry*, 1981, **20**, 6109.
57. E. R. Zuiderweg, R. Kaptein and K. Wüthrich, *Proc. Natl. Acad. Sci. USA*, 1983, **80**, 5837.
58. E. R. Zuiderweg, R. Kaptein and K. Wüthrich, *Eur. J. Biochem.*, 1983, **137**, 279.
59. K. Wüthrich, *NMR of Proteins and Nucleic Acids*, Wiley-Interscience, New York, 1986, 203.
60. R. Kaptein, R. Boelens, R. M. Scheek and W. F. van Gunsteren, *Biochemistry*, 1988, **27**, 5389.
61. E. R. Zuiderweg, M. Billeter, R. Boelens, R. M. Scheek, K. Wüthrich and R. Kaptein, *FEBS Lett.*, 1984, **174**, 243.
62. E. R. Zuiderweg, R. M. Scheek and R. Kaptein, *Biopolymers*, 1985, **24**, 2257.
63. M. Slijper, R. Kaptein and R. Boelens, *J. Magn. Reson. B*, 1996, **111**, 199.
64. J. de Vlieg, R. M. Scheek, W. F. van Gunsteren, H. J. Berendsen, R. Kaptein and J. Thomason, *Proteins*, 1988, **3**, 209.
65. A. M. Bonvin, R. Boelens and R. Kaptein, *J. Biomol. NMR*, 1991, **1**, 305.
66. A. M. Bonvin, R. Boelens and R. Kaptein, *Biopolymers*, 1994, **34**, 39.
67. A. M. Bonvin, H. Vis, J. N. Breg, M. J. Burgering, R. Boelens and R. Kaptein, *J. Mol. Biol.*, 1994, **236**, 328.
68. L. J. Beamer and C. O. Pabo, *J. Mol. Biol.*, 1992, **227**, 177.
69. A. K. Aggarwal, D. W. Rodgers, M. Drottar, M. Ptashne and S. C. Harrison, *Science*, 1988, **242**, 899.
70. Z. Otwinowski, R. W. Schevitz, R. G. Zhang, C. L. Lawson, A. Joachimiak, R. Q. Marmorstein, B. F. Luisi and P. B. Sigler, *Nature*, 1988, **335**, 321.
71. C. L. Lawson and J. Carey, *Nature*, 1993, **366**, 178.
72. D. Zhao, C. H. Arrowsmith, X. Jia and O. Jardetzky, *J. Mol. Biol.*, 1993, **229**, 735.
73. W. Hinrichs, C. Kisker, M. Duvel, A. Muller, K. Tovar, W. Hillen and W. Saenger, *Science*, 1994, **264**, 418.
74. R. G. Brennan, S. L. Roderick, Y. Takeda and B. W. Matthews, *Proc. Natl. Acad. Sci. USA*, 1990, **87**, 8165.
75. A. Mondragon and S. C. Harrison, *J. Mol. Biol.*, 1991, **219**, 321.
76. A. Mondragon, C. Wolberger and S. C. Harrison, *J. Mol. Biol.*, 1989, **205**, 179.

77. C. G. Kalodimos, G. E. Folkers, R. Boelens and R. Kaptein, *Proc. Natl. Acad. Sci. USA*, 2001, **98**, 6039.
78. C. A. Spronk, G. E. Folkers, A. M. Noordman, R. Wechselberger, N. van den Brink, R. Boelens and R. Kaptein, *EMBO J.*, 1999, **18**, 6472.
79. P. G. Artz, K. G. Valentine, S. J. Opella and P. Lu, *J. Mol. Recognit.*, 1996, **9**, 13.
80. R. T. Ogata and W. Gilbert, *J. Mol. Biol.*, 1979, **132**, 709.
81. A. Schmitz and D. J. Galas, *Nucleic Acids Res.*, 1979, **6**, 111.
82. M. M. Becker and J. C. Wang, *Nature*, 1984, **309**, 682.
83. W. Gilbert, F. Gralla, J. Majors and A. Maxam, *Symposium on Protein–Ligand Interactions*, H. Sund and G. Blauer, eds., de Gruyter, Berlin, 1975, 193.
84. M. H. Caruthers, S. L. Beaucage, J. W. Efcavitch, E. F. Fisher, R. A. Goldman, P. L. deHaseth, W. Mandecki, M. D. Matteucci, M. S. Rosendahl, Y. Stabinsky, *Cold Spring Harbor Symp. Quant. Biol.*, 1983, **47**, 411.
85. J. L. Betz, H. M. Sasmor, F. Buck, M. Y. Insley and M. H. Caruthers, *Gene*, 1986, **50**, 123.
86. X. Zhang and P. A. Gottlieb, *Nucleic Acids Res.*, 1995, **23**, 1502.
87. E. R. Zuiderweg, R. M. Scheek, G. Veeneman, J. H. van Boom, R. Kaptein, H. Ruterjans and K. Beyreuther, *Nucleic Acids Res.*, 1981, **9**, 6553.
88. R. Boelens, R. Scheek, K. Dijksta and R. Kaptein, *J. Magn. Reson.*, 1985, **62**, 378.
89. R. M. Scheek, R. Boelens, N. Russo, J. H. van Boom and R. Kaptein, *Biochemistry*, 1984, **23**, 1371.
90. E. Gincel, G. Lancelot, J. C. Maurizot, N. T. Thuong and F. Vovelle, *Biochimie*, 1994, **76**, 141.
91. R. Lavery, *DNA Bending and Curvature*, W. K. Olson, R. H. Sarma, M. H. Sarma and M. Sundralingam (eds), Adenine Press, New York, 1988, 191.
92. G. Lancelot, J. L. Guesnet and F. Vovelle, *Biochemistry*, 1989, **28**, 7871.
93. F. Paquet, F. Gaudin and G. Lancelot, *J. Biomol. NMR*, 1996, **8**, 252.
94. D. G. Gorenstein, S. A. Schroeder, J. M. Fu, J. T. Metz, V. Roongta and C. R. Jones, *Biochemistry*, 1988, **27**, 7223.
95. S. A. Schroeder, J. M. Fu, C. R. Jones and D. G. Gorenstein, *Biochemistry*, 1987, **26**, 3812.
96. J. M. Fu, S. A. Schroeder, C. R. Jones, R. Santini and D. G. Gorenstein, *J. Magn. Reson.*, 1988, **77**, 577.
97. J. Kania and D. T. Brown, *Proc. Natl. Acad. Sci. USA*, 1976, **73**, 3529.
98. I. Pilz, K. Goral, O. Kratky, R. P. Bray, N. G. Wade-Jardetzky and O. Jardetzky, *Biochemistry*, 1980, **19**, 4087.
99. M. Charlier, J. C. Maurizot and G. Zaccai, *Nature*, 1980, **286**, 423.
100. F. Culard and J. C. Maurizot, *Nucleic Acids Res.*, 1981, **9**, 5175.
101. F. Buck, K. D. Hahn, W. Zemann, H. Ruterjans, J. R. Sadler, K. Beyreuther, R. Kaptein, R. Scheek and W. E. Hull, *Eur. J. Biochem.*, 1983, **132**, 321.
102. R. Ogata and W. Gilbert, *Proc. Natl. Acad. Sci. USA*, 1977, **74**, 4973.
103. R. Boelens, R. M. Lamerichs, J. A. Rullmann, J. H. van Boom and R. Kaptein, *Protein Seq. Data Anal.*, 1988, **1**, 487.
104. R. Kaptein, R. Boelens, V. P. Chuprina, J. A. Rullmann and M. Slijper, *Methods Enzymol.*, 1995, **261**, 513.
105. R. M. Scheek, E. R. Zuiderweg, K. J. Klappe, J. H. van Boom, R. Kaptein, H. Ruterjans and K. Beyreuther, *Biochemistry*, 1983, **22**, 228.
106. A. D. Riggs, H. Suzuki and S. Bourgeois, *J. Mol. Biol.*, 1970, **48**, 67.
107. A. D. Riggs, S. Bourgeois and M. Cohn, *J. Mol. Biol.*, 1970, **53**, 401.
108. C. Hélène and G. Lancelot, *Prog. Biophys. Mol. Biol.*, 1982, **39**, 1.
109. M. T., Jr., deHaseth, P. L. Record and T. M. Lohman, *Biochemistry*, 1977, **16**, 4791.
110. C. M. Falcon, L. Swint-Kruse and K. S. Matthews, *J. Biol. Chem.*, 1997, **272**, 26,818.
111. F. Buck, K. D. Hahn, W. Brill, H. Ruterjans, B. K. Chernov, K. G. Skryabin, M. P. Kirpichnikov and A. A. Bayev, *J. Biomol. Struct. Dyn.*, 1986, **3**, 899.

112. R. Kaptein, R. M. Lamerichs, R. Boelens and J. A. Rullmann, *Biochem. Pharmacol.*, 1990, **40**, 89.
113. M. D. Barkley and S. Bourgeois, *The Operon*, 2nd edn, J. H. Miller and W. S. Reznikoff, eds., Cold Spring Harbor, NY, 1978, 177.
114. J. E. Anderson, M. Ptashne and S. C. Harrison, *Nature*, 1985, **316**, 596.
115. B. W. Matthews, D. H. Ohlendorf, W. F. Anderson and Y. Takeda, *Proc. Natl. Acad. Sci. USA*, 1982, **79**, 1428.
116. D. B. McKay and T. A. Steitz, *Nature*, 1981, **290**, 744.
117. R. W. Schevitz, Z. Otwinowski, A. Joachimiak, C. L. Lawson and P. B. Sigler, *Nature*, 1985, **317**, 782.
118. W. F. Anderson, D. H. Ohlendorf, Y. Takeda and B. W. Matthews, *Nature*, 1981, **290**, 754.
119. C. O. Pabo and M. Lewis, *Nature*, 1982, **298**, 443.
120. R. Rein, T. Kieber-Emmons, K. Haydock, R. Garduno-Juarez and M. Shibata, *J. Biomol. Struct. Dyn.*, 1983, **1**, 1051.
121. R. H. Ebright, *Proc. Natl. Acad. Sci. USA*, 1986, **83**, 303.
122. C. Karslake, S. Schroeder, P. L. Wang and D. G. Gorenstein, *Biochemistry*, 1990, **29**, 6578.
123. V. A. Roongta, C. R. Jones and D. G. Gorenstein, *Biochemistry*, 1990, **29**, 5245.
124. S. A. Schroeder, V. Roongta, J. M. Fu, C. R. Jones and D. G. Gorenstein, *Biochemistry*, 1989, **28**, 8292.
125. D. G. Gorenstein, *Phosphorus-31 NMR: Principles and Applications*, D. G. Gorenstein (ed), Harcourt Brace Jovanovich, Orlando, 1984, 253.
126. D. Marion and G. Lancelot, *Biochem. Biophys. Res. Commun.*, 1984, **124**, 774.
127. V. Sklenar, H. Miyashiro, G. Zon, H. T. Miles and A. Bax, *FEBS Lett.*, 1986, **208**, 94.
128. J. R. Sadler, H. Sasmor and J. L. Betz, *Proc. Natl. Acad. Sci. USA*, 1983, **80**, 6785.
129. M. V. Botuyan, D. A. Keire, C. Kroen and D. G. Gorenstein, *Biochemistry*, 1993, **32**, 6863.
130. C. Karslake, M. V. Botuyan and D. G. Gorenstein, *Biochemistry*, 1992, **31**, 1849.
131. F. Paquet, J. C. Maurizot and G. Lancelot, *Magn. Reson. Chem.*, 2000, **38**, 946.
132. M. Slijper, R. Boelens, A. L. Davis, R. N. Konings, G. A. van der Marel, J. H. van Boom and R. Kaptein, *Biochemistry*, 1997, **36**, 249.
133. L. E. Kay, D. A. Torchia and A. Bax, *Biochemistry*, 1989, **28**, 8972.
134. J. W. Peng and G. Wagner, *Biochemistry*, 1992, **31**, 8571.
135. J. W. Peng and G. Wagner, *J. Magn. Reson.*, 1992, **98**, 308.
136. G. Lancelot, L. Chanteloup, J. M. Beau and N. T. Thuong, *J. Am. Chem. Soc.*, 1993, **115**, 1599.
137. G. Lancelot, J. C. Maurizot, M. Chassignol, N. T. Thuong, L. Chanteloup and J. M. Beau, *Magn. Reson. Chem.*, 1994, **32**, 605.
138. G. Lipari and Z. Szabo, *J. Am. Chem. Soc.*, 1982, **104**, 4546.
139. G. Lipari and Z. Szabo, *J. Am. Chem. Soc.*, 1982, **104**, 4559.
140. G. M. Clore, P. C. Driscoll, P. T. Wingfield and A. M. Gronenborn, *Biochemistry*, 1990, **29**, 7387.
141. G. M. Clore, Z. Szabo, A. Bax, L. E. Kay, P. C. Driscoll and A. M. Gronenborn, *J. Am. Chem. Soc.*, 1990, **112**, 4989.
142. F. Gaudin, F. Paquet, L. Chanteloup, J. M. Beau, T. T. Nguyen and G. Lancelot, *J. Biomol. NMR*, 1995, **5**, 49.
143. R. M. Lamerichs, R. Boelens, G. A. van der Marel, J. H. van Boom, R. Kaptein, F. Buck, B. Fera and H. Ruterjans, *Biochemistry*, 1989, **28**, 2985.
144. G. Lancelot, A. Gervais and J. C. Maurizot, *J. Biomol. Struct. Dyn.*, 1992, **9**, 921.
145. R. Kaptein, *Chemically Induced Magnetic Polarization*, L. T. Muus, P. W. Atkins, K. A. McLauchlan and J. B. Pedersen (eds), Reidel, R., Dordrecht, Holland, 1977, 1.
146. R. Kaptein, K. Dijkstra and K. Nicolay, *Nature*, 1978, **274**, 293.
147. R. Kaptein, *Structural Information from Photo-CIDNP in Proteins*, B. Pullman, ed., Reidel, R, Dordrecht, Holland, 1978, 211.
148. S. Stob, R. M. Scheek, R. Boelens and R. Kaptein, *FEBS Lett.*, 1988, **239**, 99.

149. F. Buck, H. Ruterjans, R. Kaptein and K. Beyreuther, *Proc. Natl. Acad. Sci. USA*, 1980, **77**, 5145.
150. R. M. Lamerichs, R. Boelens, G. A. Van der Marel, J. H. Van Boom and R. Kaptein, *Eur. J. Biochem.*, 1990, **194**, 629.
151. J. de Vlieg, H. J. Berendsen and W. F. van Gunsteren, *Proteins*, 1989, **6**, 104.
152. C. A. Spronk, A. M. Bonvin, P. K. Radha, G. Melacini, R. Boelens and R. Kaptein, *Struct. Fold Des.*, 1999, **7**, 1483.
153. C. O. Pabo and R. T. Sauer, *Annu. Rev. Biochem.*, 1984, **53**, 293.
154. C. O. Pabo and R. T. Sauer, *Annu. Rev. Biochem.*, 1992, **61**, 1053.
155. S. C. Harrison and A. K. Aggarwal, *Annu. Rev. Biochem.*, 1990, **59**, 933.
156. T. A. Steitz, *Q. Rev. Biophys.*, 1990, **23**, 205.
157. S. C. Harrison, *Nature*, 1991, **353**, 715.
158. R. G. Brennan, *Curr. Opin. Struct. Biol.*, 1992, **2**, 100.
159. R. Boelens, R. M. Scheek, R. M. N. J. Lamerichs, J. de Vlieg, J. H. van Boom and R. Kaptein, *A Two-dimensional NMR Study of the Complex of lac Repressor Headpiece with a 14 Base Pair lac Operator Fragment*, W. Guschlbauer and W. Saenger, eds., Plenum, New York, 1987, 191.
160. R. H. Ebright, *J. Biomol. Struct. Dyn.*, 1985, **3**, 281.
161. E. C. van Geerestein-Ujah, M. Slijper, R. Boelens and R. Kaptein, *J. Biomol. NMR*, 1995, **6**, 67.
162. C. M. Falcon and K. S. Matthews, *Biochemistry*, 2000, **39**, 11,074.
163. M. Slijper, *PhD Thesis: NMR-studies of Protein–DNA Interaction in the lac Operon*, Utrecht University, Utrecht, The Netherlands, 1996, 1.
164. C. Zwahlen, P. Legault, S. J. F. Vincent, J. Greenblatt, R. Konrat and L. E. Kay, *J. Am. Chem. Soc.*, 1997, **119**, 6711.
165. J. A. D. MacKerell and M. Karplus, *FASEB J.*, 1992, **6**, A143.
166. G. Otting, H. Widmer, G. Wagner and K. Wüthrich, *J. Magn. Reson.*, 1986, **66**, 187.
167. A. L. Breeze, *Prog. Nucl. Magn. Reson. Spectrosc.*, 2000, **36**, 323.
168. G. Otting, H. Senn, G. Wagner and K. Wüthrich, *J. Magn. Reson.*, 1986, **70**, 500.
169. G. Otting and K. Wüthrich, *J. Magn. Reson.*, 1989, **85**, 586.
170. M. J. Burgering, R. Boelens, M. Caffrey, J. N. Breg and R. Kaptein, *FEBS Lett.*, 1993, **330**, 105.
171. M. J. Burgering, R. Boelens and R. Kaptein, *J. Biomol. NMR*, 1993, **3**, 709.
172. P. J. M. Folkers, R. H. A. Folmer, R. N. H. Konings and K. Hallenga, *J. Am. Chem. Soc.*, 1993, **115**, 3798.
173. K. Ogura, H. Terasawa and F. Inagaki, *J. Biomol. NMR*, 1996, **8**, 492.
174. F. Aboul-ela, E. P. Nikonowicz and A. Pardi, *FEBS Lett.*, 1994, **347**, 261.
175. I. T. Weber, D. B. McKay and T. A. Steitz, *Nucleic Acids Res.*, 1982, **10**, 5085.
176. N. Lehming, J. Sartorius, B. Kisters-Woike, B. von Wilcken-Bergmann and B. Muller-Hill, *EMBO J.*, 1990, **9**, 615.
177. M. J. Weickert and S. Adhya, *J. Biol. Chem.*, 1992, **267**, 15,869.
178. C. C. Nguyen and Saier, M. H., Jr., *FEBS Lett.*, 1995, **377**, 98.
179. L. G. Kleina and J. H. Miller, *J. Mol. Biol.*, 1990, **212**, 295.
180. S. W. Englander, *Annu. Rev. Biophys. Biomol. Struct.*, 2000, **29**, 213.
181. S. W. Englander and M. M. Krishna, *Nat. Struct. Biol.*, 2001, **8**, 741.
182. Y. Xu, L. Mayne and S. W. Englander, *Nat. Struct. Biol.*, 1998, **5**, 774.
183. A. K. Chamberlain, T. M. Handel and S. Marqusee, *Nat. Struct. Biol.*, 1996, **3**, 782.
184. T. Kiefhaber and R. L. Baldwin, *Proc. Natl. Acad. Sci. USA*, 1995, **92**, 2657.
185. M. J. Parker, C. E. Dempsey, L. L. Hosszu, J. P. Waltho and A. R. Clarke, *Nat. Struct. Biol.*, 1998, **5**, 194.
186. R. Zahn, S. Perrett, G. Stenberg and A. R. Fersht, *Science*, 1996, **271**, 642.
187. A. Hvidt and S. O. Nielsen, *Adv. Protein Chem.*, 1966, **21**, 287.
188. Y. Bai, J. S. Milne, L. Mayne and S. W. Englander, *Proteins*, 1993, **17**, 75.
189. T. Sivaraman, C. B. Arrington and A. D. Robertson, *Nat. Struct. Biol.*, 2001, **8**, 331.

190. C. G. Kalodimos, R. Boelens and R. Kaptein, *Nat. Struct. Biol.*, 2002, **9**, 193.
191. T. D. Allen, K. L. Wick and K. S. Matthews, *J. Biol. Chem.*, 1991, **266**, 6113.
192. C. E. Bell, J. Barry, K. S. Matthews and M. Lewis, *J. Mol. Biol.*, 2001, **313**, 99.
193. A. E. Chakerian and K. S. Matthews, *J. Biol. Chem.*, 1991, **266**, 22,206.
194. A. E. Chakerian, V. M. Tesmer, S. P. Manly, J. K. Brackett, M. J. Lynch, J. T. Hoh and K. S. Matthews, *J. Biol. Chem.*, 1991, **266**, 1371.
195. S. Alberti, S. Oehler, B. von Wilcken-Bergmann, H. Kramer and B. Müller-Hill, *New Biol.*, 1991, **3**, 57.
196. S. Alberti, S. Oehler, B. von Wilcken-Bergmann and B. Müller-Hill, *EMBO J.*, 1993, **12**, 3227.
197. J. Chen and K. S. Matthews, *J. Biol. Chem.*, 1992, **267**, 13,843.
198. J. Suckow, P. Markiewicz, L. G. Kleina, J. Miller, B. Kisters-Woike and B. Müller-Hill, *J. Mol. Biol.*, 1996, **261**, 509.
199. A. Schmitz, U. Schmeissner and J. H. Miller, *J. Biol. Chem.*, 1976, **251**, 3359.
200. T. J. Daly and K. S. Matthews, *Biochemistry*, 1986, **25**, 5474.
201. W. I. Chang, J. S. Olson and K. S. Matthews, *J. Biol. Chem.*, 1993, **268**, 17,613.
202. J. C. Nichols and K. S. Matthews, *J. Biol. Chem.*, 1997, **272**, 18,550.
203. J. C. Nichols, N. K. Vyas, F. A. Quiocho and K. S. Matthews, *J. Biol. Chem.*, 1993, **268**, 17,602.
204. L. P. Gerk, O. Leven and B. Müller-Hill, *J. Mol. Biol.*, 2000, **299**, 805.
205. A. Nagadoi, M. Souichi, S. Morikawa, H. Nakamura, M. Enari, K. Kobayashi, H. Yamamoto, G. Sampei, K. Mizobuchi, M. A. Schumacher, R. G. Brennan, Y. Nishimura, *Structure*, 1995, **3**, 1217.
206. M. A. Schumacher, J. R. Macdonald, J. Bjorkman, S. L. Mowbray and R. G. Brennan, *J. Biol. Chem.*, 1993, **268**, 12,282.
207. J. C. Cortay, D. Negre, M. Scarabel, T. M. Ramseier, N. B. Vartak, J. Reizer, M. H. Saier, Jr. and A. J. Cozzone, *J. Biol. Chem.*, 1994, **269**, 14,885.
208. M. Scarabel, F. Penin, C. Bonod-Bidaud, D. Negre, A. J. Cozzone and J. C. Cortay, *Gene*, 1995, **153**, 9.
209. A. D. Kline, W. Braun and K. Wüthrich, *J. Mol. Biol.*, 1986, **189**, 377.
210. A. D. Kline and K. Wüthrich, *J. Mol. Biol.*, 1985, **183**, 503.
211. K. Wüthrich, *NMR in Structural Biology: A Collection of Papers*, K. Wüthrich, ed., World Scientic Publishing, Singapore, New Jersey, London, Hong Kong, 1995, 343.
212. G. Lancelot, *J. Am. Chem. Soc.*, 1977, **99**, 7037.
213. G. Lancelot, *Biophys. J.*, 1977, **17**, 243.
214. G. Lancelot, *Biochimie*, 1977, **59**, 587.
215. G. Lancelot and C. Hélène, *Proc. Natl. Acad. Sci. USA*, 1977, **74**, 4872.
216. G. Lancelot and C. Hélène, *Nucleic Acids Res.*, 1979, **6**, 1063.
217. G. Lancelot, R. Mayer and C. Hélène, *Biochim. Biophys. Acta*, 1979, **564**, 181.
218. G. Lancelot, R. Mayer and C. Hélène, *J. Am. Chem. Soc.*, 1979, **101**, 1569.
219. G. Lancelot and R. Mayer, *FEBS Lett.*, 1981, **130**, 7.
220. D. Porschke, N. Geisler and W. Hillen, *Nucleic Acids Res.*, 1982, **10**, 3791.
221. K. Kaluarachchi, D. G. Gorenstein and B. A. Luxon, *J. Biomol. Struct. Dyn. Conversation*, 2000, **11**, 123.
222. I. Solomon, *Phys. Rev.*, 1955, **99**, 559.
223. M. Saunders, A. Wishnia and J. G. Kirkwood, *J. Am. Chem. Soc.*, 1957, **79**, 3289.
224. J. W. Cooley and J. W. Tukey, *Math. Comput.*, 1965, **19**, 297.
225. R. R. Ernst and W. A. Anderson, *Rev. Sci. Instrum.*, 1966, **37**, 93.
226. H. R. Matthews, H. W. Thielmann, K. S. Matthews and O. Jardetzky, *Ann. N.Y. Acad. Sci.*, 1973, **222**, 226.
227. K. Nagayama, K. Wüthrich, P. Bachmann and R. R. Ernst, *Biochem. Biophys. Res. Commun.*, 1977, **78**, 99.
228. K. Nagayama, K. Wüthrich and R. R. Ernst, *Biochem. Biophys. Res. Commun.*, 1979, **90**, 305.

229. A. Dubs, G. Wagner and K. Wüthrich, *Biochim. Biophys. Acta*, 1979, **577**, 177.
230. A. Kumar, R. R. Ernst and K. Wüthrich, *Biochem. Biophys. Res. Commun.*, 1980, **95**, 1.
231. D. Marion and K. Wüthrich, *Biochem. Biophys. Res. Commun.*, 1983, **113**, 967.
232. P. Strop, G. Wider and K. Wüthrich, *J. Mol. Biol.*, 1983, **166**, 641.
233. P. Strop and K. Wüthrich, *J. Mol. Biol.*, 1983, **166**, 631.
234. R. Boelens, P. Gros, R. M. Scheek, J. A. Verpoorte and R. Kaptein, *J. Biomol. Struct. Dyn.*, 1985, **3**, 269.
235. R. H. Griffey and A. G. Redfield, *Q. Rev. Biophys.*, 1987, **19**, 51.
236. A. A. Ribeiro, D. Wemmer, R. P. Bray and O. Jardetzky, *Biochemistry*, 1981, **20**, 3346.
237. A. A. Ribeiro, D. Wemmer, R. P. Bray and O. Jardetzky, *Biochem. Biophys. Res. Commun.*, 1981, **99**, 668.
238. D. Wemmer, H. Shvo, A. A. Ribeiro, R. P. Bray and O. Jardetzky, *Biochemistry*, 1981, **20**, 3351.
239. F. Jacob and J. Monod, *J. Mol. Biol.*, 1961, **3**, 318.
240. F. Jacob and J. Monod, *Cold Spring Harbor Symp. Quant. Biol.*, 1961, **26**, 193.
241. J. Monod, J. P. Changeux and F. Jacob, *J. Mol. Biol.*, 1963, **6**, 306.
242. B. Müller-Hill, K. Rickenberg and J. Wallenfels, *J. Mol. Biol.*, 1964, **10**, 303.
243. T. Platt, J. G. Files and K. Weber, *J. Biol. Chem.*, 1973, **248**, 110.
244. W. Gilbert, *Protein–Ligand Interactions*, H. Sund and G. Blauer, eds., de Gruyter, Berlin, 1975, 193.

This Page Intentionally Left Blank

Intramolecular Interactions of Polyethers and Polysulfides, Investigated by NMR, *Ab Initio* Molecular Orbital Calculations, and Rotational Isomeric State Scheme: An Advanced Analysis of NMR Data

YUJI SASANUMA*

Department of Materials Technology, Faculty of Engineering, Chiba University, 1-33 Yayoi-cho, Inage-ku, Chiba 263-8522, Japan

*Tel./fax: +81-43-290-3394; E-mail: sasanuma@tc.chiba-u.ac.jp

ANNUAL REPORTS ON NMR SPECTROSCOPY
VOLUME 49 ISSN 0066-4103

*Intramolecular interactions of representative polyethers and polysulfides such as poly(methylene oxide) (PMO), poly(ethylene oxide) (PEO), poly (propylene oxide) (PPO), poly(methylene sulfide) (PMS), poly(ethylene sulfide) (PES), and poly(propylene sulfide) (PPS) have been investigated by NMR, ab initio molecular orbital (MO) calculations, and statistical mechanics of chain molecules, viz., the so-called rotational isomeric state (RIS) scheme. A conformational analysis of isotactic PPO was carried out from vicinal ^{1}H–^{1}H coupling constants observed from its monomeric model compound, 1,2-dimethoxypropane, and the gauche preference of the OC–C*O bond was found to due to intramolecular (C–H)···O hydrogen bonds formed in the $g^{\pm}g^{\mp}$ conformations for the C–O/C–C* bond pair. Carbon-13 NMR chemical shifts of six PPO dimers having different regio- and stereosequences were assigned and simulated by RIS calculations based on γ- and δ-effects of substituents. As a consequence, the hydrogen bonds were proved to exist in the PPO dimers as well. Conformational analyses of PMS, PES, and PPS were carried out from vicinal ^{1}H–^{1}H and ^{13}C–^{1}H coupling constants to determine their conformational energies defined on the RIS approximation. In parallel, conformational characteristics of PMO and PEO were investigated, and the origin and nature of intramolecular interactions of the polyethers and polysulfides were successfully elucidated as follows: (1) gauche stabilizations of C–X bonds (X = O and S) of PMO and PMS, due to lone pair (n_X) → antibonding orbital (σ^{*}_{C-X}) hyperconjugations and intramolecular dipole–dipole interactions; (2) a competitive equilibrium between the intramolecular (C–H)···O hydrogen bond and the so-called attractive gauche effect of PEO; (3) gauche preferences of C–S bonds of PES and PPS, mainly due to $n_S \rightarrow \sigma^{*}_{C-C}$ and $n_S \rightarrow \sigma^{*}_{C-H}$ delocalizations; (4) trans preferences of C–C bonds of PES and PPS, due to steric S···S repulsions in the gauche conformations; (5) induced dipole–dipole interactions in $g^{\pm}tg^{\mp}$ states of PES. The NMR experiments combined with ab initio MO calculations and the RIS scheme have been demonstrated to be a powerful methodology for conformational analysis of polymers.*

1. INTRODUCTION

Conformational analyses of polymers have often been carried out from experimental observations of configuration-dependent properties such as characteristic ratio and dipole moment ratio.[1] Then, the polymer is required to be kept in the unperturbed state (the Θ state),[2] where the excluded volume effect essentially disappears and hence the chain configuration may depend only on short-range intramolecular interactions between atoms and groups separated by up to five chemical bonds. The Θ point, at which the second virial coefficient falls close to null, has been found for each polymer by viscosity and/or light scattering measurements.[3] In early studies, conformational energies, E_ξ's (ξ: intramolecular interaction and the corresponding statistical weight), of polyethylene[4] and polypropylene[5] were determined by analyses based on the rotational isomeric state (RIS) scheme[1,6] for characteristic ratios and molecular mechanics calculations.

Polymers including heterogeneous atoms such as oxygen, sulfur, and nitrogen have a dipole moment, which depends on the spatial configuration of the polymer.[7] For polymers possessing a mirror plane, a twofold axis of symmetry, and/or a center of symmetry between adjoining repeating units in the all-trans conformation, the dipole moments are not affected by the excluded volume effect.[8,9] Poly(ethylene oxide) (PEO, $[CH_2CH_2O]_x$) and poly(ethylene sulfide) (PES, $[CH_2CH_2S]_x$) satisfy these conditions; therefore, their dipole moments are always free from the excluded volume effect. Conformational energies of polyethers and polysulfides have been estimated by RIS analyses of chain dimensions and dipole moments with the aid of molecular mechanics calculations. Then, some peculiar phenomena were found: a strong gauche stability in the C–O bond of poly(methylene oxide) (PMO, $[CH_2O]_x$)[1,10,11] and moderate gauche preferences in C–C bonds of PEO[1,11–13] and poly(propylene oxide) (PPO, $[CH_2C^*H(CH_3)O]_x$).[14–16] Here, the asterisk denotes the asymmetrical carbon. The former corresponds to the anomeric effect found for carbohydrates, and the latter to the attractive gauche effect of the X–C–C–Y bond sequences (X and Y: electronegative elements such as oxygen and halogens).[17,18] Gauche stabilities in C–X bonds of poly(methylene sulfide) (PMS, $[CH_2S]_x$),[19,20] PES,[21] and poly(propylene sulfide) (PPS, $[CH_2C^*H(CH_3)S]_x$)[22] and trans preferences of the C–C bonds of PES[21] and PPS[22] can also be mentioned. In polymer science, however, these phenomena have been left unsolved for over two decades.

In the RIS scheme,[1,6] the chain dimension and dipole moment are functions of bond lengths, bond angles, and dihedral angles as well as conformational energies. In contrast with these spatial configurations, NMR vicinal coupling constants directly yield bond conformations, p_η's ($\eta =$ e.g., t, g^+, and g^-), of individual constituent bonds.[23] Because of the restricted molecular mobility of polymers, however, the NMR signals are occasionally so broadened that we can hardly derive detailed information on the chain conformation therefrom.

In the NMR experiments, therefore, small model compounds having the same skeletal bonds are often substituted for the polymer itself. This alternative may be justified because the conformation of a polymer in the Θ state depends on only short-range intramolecular interactions;[1] that is, both polymer and model compounds are assumed to have the same conformational energies. The RIS scheme[1,6] allows us to derive conformational energies from the bond conformations and calculate various configuration-dependent properties of the polymer.

Indeed the NMR method may give accurate conformational energies but does not directly elucidate the origin and nature of intramolecular interactions. *Ab initio* molecular orbital (MO) calculations, which provide a variety of physicochemical quantities, e.g., self-consistent field (SCF) energy, zero-point energy, thermal energy, electron density, and dipole moment, have been recently accepted as reliable tools to investigate the electronic structure of molecules.[24] Therefore, the *ab initio* MO calculations are expected to compensate for the insufficiency of the NMR experiments. Our methodology for conformational analysis of polymers is, in principle, based on the following procedures. (1) Monomeric and/or oligomeric model compounds, which have the same bond sequence as the polymer of interest, are prepared and subjected to NMR measurements to yield NMR parameters, such as chemical shifts and vicinal coupling constants (^3J's) across the interesting bonds. The ^3J values between spins in the trans (^3J_T) and gauche (^3J_G) positions, being treated as constants in Gutowsky-style expressions[23] for observed ^3J's, are experimentally determined from a cyclic compound having the same bond sequence as the model compound. From the NMR data thus obtained, the experimental bond conformations are evaluated. (2) *Ab initio* MO calculations are carried out for the model compound(s) to obtain the conformer free energies, geometrical parameters, and electronic properties. The bond conformations are theoretically estimated from the conformer free energies, and compared with the corresponding observations. If the validity of the MO calculations is confirmed, the conformational energies (E_ξ's) representing intramolecular interactions are calculated from the conformer free energies according to the RIS scheme. (3) The experimental E_ξ values are also determined by an RIS simulation for the experimental bond conformations and, if available, the chain dimension and dipole moment of the unperturbed polymer. (4) The MO parameters such as electron densities, geometrical parameters, and dipole moments are analyzed to reveal the origin and nature of the intramolecular interactions.

In this series of studies, we first carried out conformational analysis of isotactic PPO according to the above procedure and found a gauche preference of the C–C* bond, due to intramolecular (C–H)$\cdots$O hydrogen bonds formed in the $g^{\pm}g^{\mp}$ conformations for the C–O/C–C bond pair.[25–27] To confirm the existence of the (C–H)$\cdots$O interactions in PPO, we prepared its dimeric model compounds having different regio- and stereosequences. Carbon-13 NMR

chemical shifts of the PPO dimers were assigned and simulated by RIS calculations based on shielding and deshielding effects of substituents. As a consequence, conformational energies close to those of isotactic PPO were obtained, and hydrogen bonds were shown to be formed in the PPO dimers as well.[28] A weak (C–H)$\cdots$O attraction was also found in poly(tetramethylene oxide) and its model compounds.[27,29] According to the procedures described above, conformational analyses of polysulfides, i.e., PMS,[30] PES,[31] and PPS[32] were carried out. In parallel, we investigated conformational characteristics of the corresponding polyethers, i.e., PMO[30] and PEO,[31] and successfully elucidated the origin and nature of intramolecular interactions formed in these polymers as follows: (1) gauche stabilizations of C–X bonds (X = O and S) of PMO and PMS, due to lone pair (n_X) $\rightarrow$ antibonding orbital σ^*_{C-X} hyperconjugations and intramolecular dipole–dipole interactions; (2) a competitive equilibrium between intramolecular (C–H)$\cdots$O hydrogen bond and intermolecular interactions with solvents as well as the attractive gauche effect of PEO; (3) gauche preferences of C–S bonds of PES and PPS, due to $n_S \rightarrow \sigma^*_{C-C}$ interactions, etc.; (4) trans preferences of C–C bonds of PES and PPS, due to steric S$\cdots$S repulsion in the gauche conformation; (5) induced dipole–dipole interactions in $g^{\pm}tg^{\mp}$ states of PES. In this report, the individual studies are described in detail.

2. METHODS

2.1. NMR measurements

Proton (^{13}C) NMR spectra were mainly measured at 500 MHz (125.65 MHz) on a JEOL JNM-LA500 spectrometer equipped with a variable temperature controller. During the measurements, the probe temperature was maintained within $\pm 0.01\,^{\circ}$C fluctuations. In the measurements, free induction decays were accumulated 8–64 (hundreds to ten thousands) times. The $\pi/2$ pulse width, data acquisition time, and recycle decay were typically 5.6 (4.8) μs, 13.1 (10.4) s, and 3.7 (2.5) s, respectively. The solvents were, e.g., cyclohexane-d_6, benzene-d_6, chloroform-d_1, methanol-d_4, and dimethyl sulfoxide-d_6 (DMSO-d_6), the internal standard was tetramethylsilane, and the solute concentration was 5 vol%. Here, the values in the parentheses represent ^{13}C NMR parameters. The gated decoupling technique was used in the ^{13}C NMR measurements.

For vaporized samples, instrumental conditions were, in principle, the same as those for liquid samples. The samples were prepared as follows. About 2 μl of compound was injected into a standard 3-mm o.d. tube, which was sealed at a height of ca. 4 cm from the bottom. Placed in a 5-mm o.d. tube was the 3-mm tube, of which top and bottom were fixed with Teflon plugs. Between the inner and outer tubes, DMSO-d_6 was filled up to the Teflon plug for ^{2}H field-frequency lock. The outer tube was also sealed.

The vapor pressure of samples was estimated as follows. Enthalpy of vaporization (ΔH_{vap}) was calculated from Trouton's rule: $\Delta H_{vap}/T_{bp} \simeq 85\,J\,mol^{-1}\,K^{-1}$, where T_{bp} is the boiling point of the compound at 1 atm.[33] The substitution of the ΔH_{vap} value into the Clausius–Clapeyron equation gave the vapor pressure.[33] Therefore, the inner pressure of the sample tube was approximately estimated as the sum of vapor and atmospheric pressures.

2.2. *Ab initio* molecular orbital (MO) calculations

Ab initio MO calculations were carried out with the GAUSSIAN-92 program[34] on a Cray C916 supercomputer or a cluster of IBM RS/6000 computers in the Advanced Industrial Science and Technology (AIST), Tsukuba, or the GAUSSIAN-98[35] on a Compaq XP1000 workstation in Chiba University. Geometrical parameters were fully optimized, and the zero-point energies, thermal energies, and entropies were also calculated at various theoretical levels, e.g., by the Hartree–Fock (HF) method using the 6-31G(d) basis set (abbreviated as HF/6-31G(d)). Then, a scale factor of 0.9135 was used to correct the overestimated thermodynamic quantities.[24,36] With the geometries thus determined, single-point calculations were carried out by e.g., the second-order Møller–Plesset (MP2) correlation theory[37] using the 6-311+G(3df, 2p) basis set (MP2/6-311+G(3df, 2p)//HF/6-31G(d)), atomic charges and dipole moments were computed by the Merz–Singh–Kollman method,[38,39] and the natural bond orbital (NBO) analysis[40] was concomitantly performed if necessary. Conformational free energies of the individual conformers were evaluated from the SCF energy and thermodynamic quantities. The free energies, atomic charges, and dipole moments were also calculated by the density functional method of e.g., Becke's three-parameter functional[41] using the Lee–Yang–Parr correlation functional[42] (B3LYP), the 6-311+G(3df, 2p) basis set, and geometrical parameters optimized at the B3LYP/6-31G(d) level (B3LYP/6-311+G(3df, 2p)//B3LYP/6-31G(d)). Then, the scale factor was 0.9804.[24,36] For 1,2-dimethoxypropane (DMP, $CH_3OCH_2C^*H(CH_3)OCH_3$), solvent effects on the SCF energy and thermochemical quantities were estimated by the self-consistent reaction field (SCRF) method.[43]

3. ISOTACTIC POLY(PROPYLENE OXIDE) (PPO)

As stated in Section 1, the C–C bond in the O–C–C–O sequence of ethers often exhibits a gauche preference (the attractive gauche effect).[17,18] The simplest polymer including this bond sequence may be PEO. Conformational energies of PEO were determined so as to attain the best agreement between calculated and observed unperturbed dimensions and dipole moments.[11–13] The gauche state of the C–C bond was indicated to be more stable by 0.4–0.5 kcal mol^{-1}

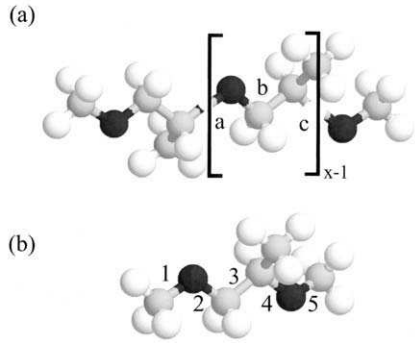

Fig. 1. (a) Isotactic poly((*R*)-propylene oxide)dimethyl ether; and (b) its monomeric model compound (*R*)-1,2-dimethoxypropane (DMP) in their all-trans conformations. As indicated, the skeletal bonds are termed. *x* is the degree of polymerization.

than the trans state. In NMR studies on 1,2-dimethoxyethane (DME, $CH_3OCH_2CH_2OCH_3$), a monomeric model compound of PEO, it was reported that the conformational energy (E_σ), depending largely on the medium, varies from -0.4 (in the gas phase) to $-1.2\,\mathrm{kcal\,mol^{-1}}$ (in water).[44,45]

The attractive gauche effect was also found for PPO.[14–16] Because of the asymmetric methine carbon atom, PPO has two stereochemical arrangements, i.e., (*R*)- and (*S*)-optical isomers. In this report, (*R*)-isomers are treated as models for isotactic PPO and its model compounds (Fig. 1). However, arguments stated here are also valid for the (*S*)-forms. It should be noted that two gauche states, g^+ and g^-, of the O–C, C–C*, and C*–O bonds of the repeating unit are nonequivalent; therefore, a number of energy parameters are required to represent the conformation of PPO. Here, dihedral angles are defined by convention in polymer science;[1] the potential minima are assumed to be located around 0 (t), 120 (g^+), and -120° (g^-).

3.1. ^{1}H NMR vicinal coupling constants

Bond conformations of the C–C* bond of DMP were determined from vicinal coupling constants between protons A and C ($^3J_{AC}$) and B and C ($^3J_{BC}$) (see Fig. 2). The observed $^3J_{AC}$ and $^3J_{BC}$ values are related to the bond conformations by

$$^3J_{AC} = {}^3J_T^{HH} p_t^{CC^*} + {}^3J_G^{HH} p_{g^+}^{CC^*} + {}^3J_G^{HH} p_{g^-}^{CC^*} \quad (1)$$

and

$$^3J_{BC} = {}^3J_G^{HH} p_t^{CC^*} + {}^3J_T^{HH} p_{g^+}^{CC^*} + {}^3J_G^{HH} p_{g^-}^{CC^*} \quad (2)$$

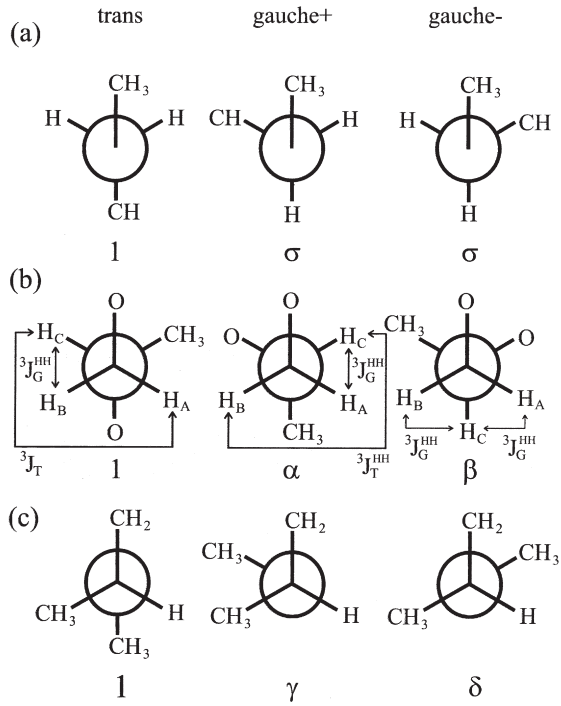

Fig. 2. Newman projections of: (a) O–C; (b) C–C*; and (c) C*–O bonds of DMP, illustrating vicinal coupling constants around the C–C* bond. First-order intramolecular interactions of DMP and PPO are represented by the corresponding statistical weights (Greek letters).

where $^3J_T^{HH}$ and $^3J_G^{HH}$ are, respectively, vicinal coupling constants between protons in trans and gauche positions, and $p_\eta^{CC^*}$ is the fraction of conformation η ($\eta = t$, g^+, or g^-), i.e., bond conformation. From the definition, it follows that

$$p_t^{CC^*} + p_{g^+}^{CC^*} + p_{g^-}^{CC^*} = 1 \tag{3}$$

Shown in Fig. 3, parts a and b, are examples of the methine and methylene part of the 500 MHz ^{1}H NMR spectra of DMP-d_6 ($CD_3OCH_2CH(CH_3)OCD_3$). Since the methoxy signals of DMP partly overlap with those of the methine and methylene parts, the partially deuterated compound was prepared and subjected to the NMR measurements. The spin system is regarded as $ABCX_3$. According to a previous NMR study on partially deuterated isotactic PPO, $[CH_2CD(CH_3)O]_x$,[14] the low frequency portion of the spectra can be assigned to the methylene A proton and the high frequency region to the methylene B and methine C protons. For all the media used, quality spectra were obtained, and the LAOCOON III simulations[46] satisfactorily reproduced the experimental observations. The $^3J_T^{HH}$ and $^3J_G^{HH}$ values were determined

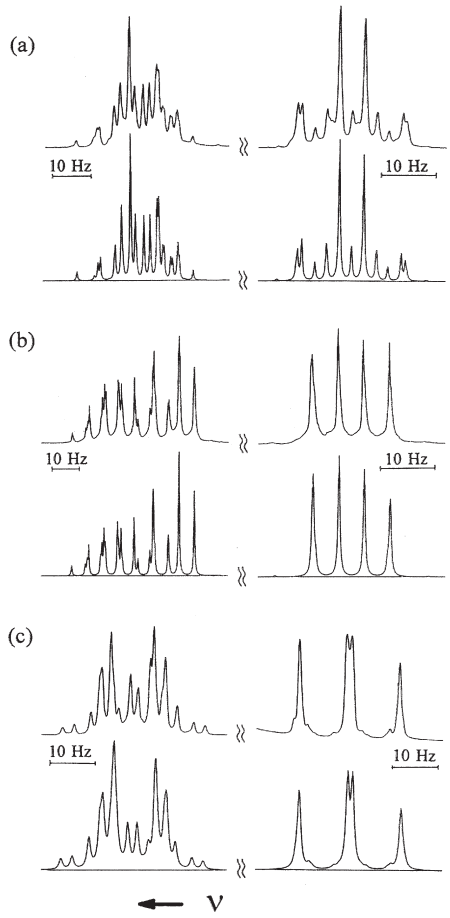

Fig. 3. Examples of the methine and methylene part of observed (above) and calculated (below) ^{1}H NMR spectra. (a) $CD_3OCH_2CH(CH_3)OCD_3$ (DMP-d_6) in the gas phase at 180 °C, (b) DMP-d_6 in benzene-d_6 at 43 °C, and (c) *cis*-DMDO in DMSO-d_6 at 80 °C. The spectra a and b were recorded at 500 MHz and the spectrum c at 270 MHz. (Reproduced with permission from *J. Phys. Chem.*, 1994, **98**, 13486. Copyright 1994 Am. Chem. Soc.)

from a cyclic compound, *cis*-2,6-dimethyl-1,4-dioxane (*cis*-DMDO), which has the O–CH_2–$CH(CH_3)$–O bond sequence as shown in Fig. 4. Both methyl groups of *cis*-DMDO stay in the equatorial position to avoid the $CH_3 \cdots CH_3$ repulsion. Fig. 3c shows a 270 MHz ^{1}H NMR spectrum of *cis*-DMDO dissolved in DMSO-d_6. This spectrum was simulated as an $ABCM_3$ system, and satisfactorily reproduced as shown. The chemical shifts were found to vary slightly with temperature, but the coupling constants were essentially invariant over the temperature range. These facts indicate the rigidity of the *cis*-DMDO

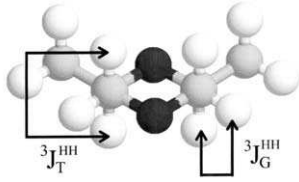

Fig. 4. *cis*-DMDO with definitions of vicinal coupling constants between protons in trans ($^3J_T^{HH}$) and gauche ($^3J_G^{HH}$) positions.

Table 1. Bond conformations of C–C* bond of DMP

Medium	Dielectric constant of medium	Temperature (°C)	$p_t^{CC^*}$	$p_{g^+}^{CC^*}$	$p_{g^-}^{CC^*}$
^1H *NMR*					
Gas	1.00	145	0.38	0.41	0.21
Cyclohexane	2.02	26	0.41	0.41	0.18
Benzene	2.28	26	0.34	0.44	0.22
Dimethyl sulfoxide	45.0	25	0.26	0.43	0.31
Ab initio *MO calculations*					
Gas	1.00	145	0.37	0.46	0.17

ring. The $^3J_T^{HH}$ and $^3J_G^{HH}$ values were determined as follows: $^3J_T^{HH} = 9.80 \pm 0.04$ Hz and $^3J_G^{HH} = 2.54 \pm 0.04$ Hz (cyclohexane-d_{12}); $^3J_T^{HH} = 9.87 \pm 0.05$ Hz and $^3J_G^{HH} = 2.54 \pm 0.05$ Hz (benzene-d_6); $^3J_T^{HH} = 10.25 \pm 0.08$ Hz and $^3J_G^{HH} = 2.52 \pm 0.05$ Hz (DMSO-d_6). From $^3J_{AC} = 5.24 \pm 0.02$ Hz and $^3J_{BC} = 5.47 \pm 0.01$ Hz of DMP in the gas phase at 180 °C, we have that $p_t^{CC^*} = 0.37$, $p_{g^+}^{CC^*} = 0.40$, and $p_{g^-}^{CC^*} = 0.22$. Then, the $^3J_T^{HH}$ and $^3J_G^{HH}$ values obtained from the cyclohexane-d_{12} solution were used. In Table 1, the bond conformations for individual media are listed. The bond conformations were evaluated in the order $g^+ > t > g^-$, except for the DMSO solution. The results show explicit solvent dependence; both gauche states are more stabilized as dielectric constant of medium increases. The DMP molecule becomes more polar with increasing polarity of solvent.

3.2. *Ab initio* MO calculations

Ab initio MO calculations were carried out for DMP using the GAUSSIAN-92 program.[34] For all the possible conformers, the Gibbs free energies were calculated at the MP2/6-31+G*//HF/6-31G* level. Solvent effects on the conformer free energies were estimated by the SCRF calculations.[43]

In Table 2, the conformer free energies ΔG_k's (k: conformer number) obtained from the MO calculations, are summarized. In Table 1, the bond

Table 2. Free energies (ΔG_k) of DMP, evaluated by *ab initio* MO calculations

k	Conformation[a]	Statistical weight[b]	ΔG_k[c] (kcal mol^{-1})
1	t t t	1	0.00
2	t t g^+	γ	3.20
3	t t g^-	δ	0.43
4	t g^+ t	α	0.62
5	t g^+ g^+	$\alpha\gamma$	3.80
6	t g^+ g^-	$\alpha\delta\omega_1$	−0.20
7	t g^- t	β	1.57
8	t g^- g^+	$\beta\gamma\omega_2$	2.18
9	t g^- g^-	$\beta\delta$	1.38
10	g^+ g^+ t	$\sigma\alpha$	2.30
11	g^+ g^+ g^+	$\sigma\alpha\gamma\chi$	4.02
12	g^+ g^+ g^-	$\sigma\alpha\delta\omega_1$	1.34
13	g^+ g^- t	$\sigma\beta\omega_2$	0.99
14	g^+ g^- g^-	$\sigma\beta\delta\omega_2$	1.51
15	g^- t t	σ	1.25
16	g^- t g^+	$\sigma\gamma$	4.46
17	g^- t g^-	$\sigma\delta$	1.87
18	g^- g^+ t	$\sigma\alpha\omega_1$	0.80
19	g^- g^+ g^+	$\sigma\alpha\gamma\omega_1$	4.28

[a]For example, the conformer tg^+g^- represents that bonds 2, 3, and 4 adopt t, g^+, and g^- conformations, respectively.

[b]The statistical weights are illustrated in Figs. 2 and 5.

[c]At the MP2/6-31+G*//HF/6-31G* level. Relative to the ΔG_k value of the all-trans conformation. At 25 °C and 1 atm.

conformations, evaluated from the ΔG_k values according to the Boltzmann distribution, are compared with those from the NMR experiments. From the table, the conformational stability of the order $g^+ > t > g^-$ is seen to be successfully reproduced by the MO calculations.

According to the RIS scheme including up to third-order intramolecular interactions,[47,48] statistical weight matrices of DMP may be given as

$$\mathbf{U}_2 = \begin{array}{c} \\ t \\ g^+ \\ g^- \end{array} \begin{array}{c} \begin{array}{ccc} t & g^+ & g^- \end{array} \\ \begin{pmatrix} 1 & \sigma & \sigma \\ 0 & 0 & 0 \\ 0 & 0 & 0 \end{pmatrix} \end{array} \tag{4}$$

$$\mathbf{U}_3 = \begin{array}{c} \\ t \\ g^+ \\ g^- \end{array} \begin{array}{c} \begin{array}{ccccccccc} t & g^+ & g^- & t & g^+ & g^- & t & g^+ & g^- \end{array} \\ \begin{pmatrix} 1 & \alpha & \beta & 0 & 0 & 0 & 0 & 0 & 0 \\ 0 & 0 & 0 & 0 & \alpha & \beta\omega_2 & 0 & 0 & 0 \\ 0 & 0 & 0 & 0 & 0 & 0 & 1 & \alpha\omega_1 & 0 \end{pmatrix} \end{array} \tag{5}$$

and

$$\mathbf{U}_4 = \begin{array}{c} \\ \mathrm{tt} \\ \mathrm{tg^+} \\ \mathrm{tg^-} \\ \mathrm{g^+t} \\ \mathrm{g^+g^+} \\ \mathrm{g^+g^-} \\ \mathrm{g^-t} \\ \mathrm{g^-g^+} \\ \mathrm{g^-g^-} \end{array} \begin{array}{c} \begin{array}{ccccccccc} \mathrm{t} & \mathrm{g^+} & \mathrm{g^-} & \mathrm{t} & \mathrm{g^+} & \mathrm{g^-} & \mathrm{t} & \mathrm{g^+} & \mathrm{g^-} \end{array} \\ \begin{pmatrix} 1 & \gamma & \delta & 0 & 0 & 0 & 0 & 0 & 0 \\ 0 & 0 & 0 & 1 & \gamma & \delta\omega_1 & 0 & 0 & 0 \\ 0 & 0 & 0 & 0 & 0 & 0 & 1 & \gamma\omega_2 & \delta \\ 1 & \gamma & \delta & 0 & 0 & 0 & 0 & 0 & 0 \\ 0 & 0 & 0 & 1 & \gamma\chi & \delta\omega_1 & 0 & 0 & 0 \\ 0 & 0 & 0 & 0 & 0 & 0 & 1 & 0 & \delta \\ 1 & \gamma & \delta & 0 & 0 & 0 & 0 & 0 & 0 \\ 0 & 0 & 0 & 1 & \gamma & 0 & 0 & 0 & 0 \\ 0 & 0 & 0 & 0 & 0 & 0 & 1 & \gamma\omega_2 & \delta \end{pmatrix} \end{array} \tag{6}$$

Here, the rows and columns of these matrices are indexed to rotational states for the preceding and current bonds. In the $\mathbf{U}_4$ matrix, for example, the fourth row is indexed by g^+t and the third column by g^-; the (4, 3) element represents the statistical weight (δ) for bond 4 when bonds 2, 3, and 4 adopt the g^+, t, and g^- conformations, respectively. The first-, second-, and third-order interactions are defined between atoms (atomic groups) separated by three, four, and five bonds, respectively. The first-order α, β, γ, δ, σ interactions are defined in Fig. 2, and the second-order ω_1 and ω_2 and third-order χ interactions are illustrated in Fig. 5. The intramolecular interactions are denoted by the corresponding statistical weights, which are related to the conformational energies through the Boltzmann factor; for example, $\alpha = \exp(-E_\alpha/RT)$. The statistical weight matrices were formulated by reference to a previous study[16] as well as by inspection of the molecular model and the *ab initio* MO calculations.

In the RIS scheme,[1,6] a conformer free energy ΔG_k is represented as a function of conformational energies. For example, the $g^+g^+g^+$ conformation of DMP has a weight of $\sigma\alpha\gamma\chi$; thus, its ΔG_k value may be approximated by $E_\sigma+E_\alpha+E_\gamma+E\chi$. The E_ξ values ($\xi = \alpha, \beta, \gamma, \delta, \sigma, \omega_1, \omega_2$, and χ) were determined by minimizing the standard deviation between ΔG_k's and sums of E_ξ's of the individual conformers. The temperature T was set to 298.15 K. The conformational energies thus determined are shown in Table 3. All the first-order interaction energies, E_α, E_β, E_γ, E_δ, and E_σ, were obtained as positives, whereas the second-order (E_{ω_1} and E_{ω_2}) and third-order (E_χ) interaction energies as negatives. These results indicate that the second- and third-order interactions are attractive. Fig. 5 shows the tg^+g^-, tg^-g^+, and $g^+g^+g^+$ conformers having the ω_1, ω_2, and χ interactions, respectively. Here, for example, the conformer tg^+g^- represents that bonds 2, 3, and 4 take t, g^+, and g^- states, respectively. The O···H distance in the tg^+g^-, tg^-g^+, and $g^+g^+g^+$ conformations were evaluated by the MO calculations to be 2.506, 2.590 and 2.495, and 2.631 Å, respectively, thus being smaller than the sum (2.70 Å) of van der Waals radii of oxygen and hydrogen atoms.[49] When bond 3 takes the

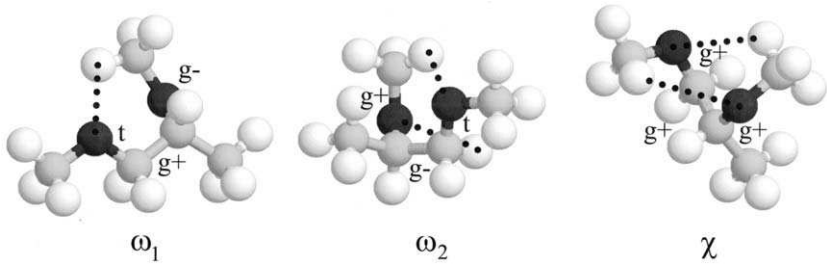

Fig. 5. Second-order (ω_1 and ω_2) and third-order (χ) intramolecular interactions defined for DMP and PPO: ω_1, in the tg^+g^- conformation of (*R*)-DMP; ω_2, in tg^-g^+; χ, $g^+g^+g^+$. The dotted lines represent the (C–H)$\cdots$O close contacts (intramolecular hydrogen bonds).

Table 3. Conformational energies[a] of DMP and isotactic PPO

	Gas phase		Cyclohexane		Benzene	
	MO[b]	NMR[c]	MO[b]	NMR[c]	MO[b]	NMR[c]
First-order interaction						
E_α	0.71	0.77 ± 0.04	0.53	0.71 ± 0.00	0.50	0.54 ± 0.03
E_β	1.30	1.2 ± 0.1	1.17	1.1 ± 0.0	1.15	0.83 ± 0.04
E_γ	3.06		2.98		2.97	
E_δ	0.35		0.24		0.22	
E_σ	1.52		1.42		1.41	
Second-order interaction						
E_{ω_1}	−1.24		−1.06		−1.04	
E_{ω_2}	−1.88		−1.77		−1.75	
Third-order interaction						
E_χ	−1.27		−0.95		−0.91	

[a]For the interactions, see Figs. 2 and 5.

[b]Determined from *ab initio* MO calculations on DMP at the MP2/6-31+G*//HF/6-31G* level including the SCRF calculations.

[c]By an RIS analysis of experimental observations of ^{1}H NMR vicinal coupling constants observed from DMP in the gas phase, cyclohexane, or benzene.

g^- conformation, a hydrogen atom of the pendant methyl group comes into contact with its nearest oxygen atom. Thus, the E_{ω_2} value is close to the double of E_{ω_1}. The $g^+g^+g^+$ conformer is seen to have two O$\cdots$H close contacts; however, one of them does not satisfy the above criterion (the O$\cdots$H distance is 2.880 Å). The E_χ value is comparable to E_{ω_1}. From the above discussion, it seems reasonable to conclude that the ω_1, ω_2, and χ interactions correspond to intramolecular hydrogen bonds (hereafter referred to as the (C–H)$\cdots$O interaction). Such weak hydrogen bonds have been found in molecular crystals and supermolecules.[50,51] However, this study has shown that the nonbonded

(C–H)$\cdots$O attractions strongly influence the conformational preferences of molecules in rapid motion, such as DMP and PPO.

3.3. Rotational isomeric state (RIS) analysis of bond conformations

As seen from Table 1, the conformation of the C–C* bond is subject to solvent effects. Accordingly, the E_α and E_β values were adjusted with other conformational energies fixed at those obtained from the SCRF calculations. In the RIS scheme, the bond conformation $p_\eta^{CC^*}$ is given by

$$p_\eta^{CC^*} = \frac{\mathbf{J}^*[\mathbf{U}_2\mathbf{U}_3'(\eta)\mathbf{U}_4]\mathbf{J}}{\mathbf{J}^*\left[\prod_{i=2}^{4}\ \mathbf{U}_i\right]\mathbf{J}} \tag{7}$$

where $\mathbf{J}^* = [100]$, and $\mathbf{J}$ is the 9×1 column matrix of which elements are unity. The $\mathbf{U}_3'(\eta)$ matrix is obtained by filling the columns of $\mathbf{U}_3$ other than those corresponding to the η state with zero. Thus, the bond conformations around the C–C* bond of DMP are expressed as a function of statistical weights:

$$\frac{p_{g^+}^{CC^*}}{p_t^{CC^*}} = \frac{1 + \sigma + \sigma\omega_1 + \gamma(1 + \sigma\chi + \sigma\omega_1) + \delta\omega_1(1 + \sigma)}{(1 + \sigma)(1 + \gamma + \delta)}\ \alpha \tag{8}$$

$$\frac{p_{g^-}^{CC^*}}{p_t^{CC^*}} = \frac{1 + \sigma\omega_2 + \gamma\omega_2 + \delta(1 + \sigma\omega_2)}{(1 + \sigma)(1 + \gamma + \delta)}\ \beta \tag{9}$$

Equation (3) also holds here. Substituting the experimental $p_t^{CC^*}$, $p_{g^+}^{CC^*}$, and $p_{g^-}^{CC^*}$ values and theoretical E_γ, E_δ, E_σ, E_{ω_1}, E_{ω_2}, and E_χ values into Eqs. (8) and (9), we determined the E_α and E_β values. The results for the gas phase and cyclohexane and benzene solutions are listed in Table 3. From the table, it can be seen that the MO calculations yield good data, in particular, for the gas phase.

3.4. Configuration-dependent properties

The characteristic ratio ($\langle r^2\rangle_0/nl^2$) and dipole moment ratio ($\langle\mu^2\rangle/nm^2$) of isotactic PPO in the Θ state were calculated with the conformational energies determined as above, where r is the end-to-end distance, n is the number of skeletal bonds, l is the bond length, μ is the dipole moment, m is the bond dipole moment, the angular brackets represent the ensemble average, and the subscript 0 stands for the unperturbed state. Geometrical parameters used are as follows:[16] bond lengths, $l_{C\text{–}C^*} = 1.53$ Å and $l_{C\text{–}O} = 1.43$ Å; bond angles, $\angle COC = \angle CCO = 111.5^\circ$; dihedral angles, $\phi_t^a = 0^\circ$, $\phi_{g^\pm}^a = \pm 100^\circ$, $\phi_t^b = 0^\circ$,

$\phi^{b}_{g\pm} = \pm 120^\circ$, $\phi^{c}_{t} = -20^\circ$, $\phi^{c}_{g^+} = 120^\circ$, and $\phi^{c}_{g^-} = -100^\circ$, where the superscripts represent the bond symbols (Fig. 1). The bond dipole moments, m_{C-O} (m_{C^*-O}) and m_{C-C^*}, were assumed to be 1.17 and 0.00 D, respectively.[27]

Visual inspection of the molecular model led to statistical weight matrices for bonds a, b, and c of the repeating unit of isotactic PPO as follows:

$$\mathbf{U}_a = \begin{array}{c} \\ tt \\ tg^+ \\ tg^- \\ g^+t \\ g^+g^+ \\ g^+g^- \\ g^-t \\ g^-g^+ \\ g^-g^- \end{array} \begin{array}{c} \begin{array}{ccccccccc} t & g^+ & g^- & t & g^+ & g^- & t & g^+ & g^- \end{array} \\ \begin{pmatrix} 1 & \sigma & 0 & 0 & 0 & 0 & 0 & 0 & 0 \\ 0 & 0 & 0 & 1 & 0 & 0 & 0 & 0 & 0 \\ 0 & 0 & 0 & 0 & 0 & 0 & 1 & 0 & \sigma \\ 1 & \sigma & 0 & 0 & 0 & 0 & 0 & 0 & 0 \\ 0 & 0 & 0 & 1 & 0 & 0 & 0 & 0 & 0 \\ 0 & 0 & 0 & 0 & 0 & 0 & 1 & 0 & \sigma \\ 1 & \sigma & 0 & 0 & 0 & 0 & 0 & 0 & 0 \\ 0 & 0 & 0 & 1 & 0 & 0 & 0 & 0 & 0 \\ 0 & 0 & 0 & 0 & 0 & 0 & 1 & 0 & \sigma \end{pmatrix} \end{array} \tag{10}$$

$$\mathbf{U}_b = \begin{array}{c} \\ tt \\ tg^+ \\ tg^- \\ g^+t \\ g^+g^+ \\ g^+g^- \\ g^-t \\ g^-g^+ \\ g^-g^- \end{array} \begin{array}{c} \begin{array}{ccccccccc} t & g^+ & g^- & t & g^+ & g^- & t & g^+ & g^- \end{array} \\ \begin{pmatrix} 1 & \alpha & \beta & 0 & 0 & 0 & 0 & 0 & 0 \\ 0 & 0 & 0 & 0 & \alpha & \beta\omega_2 & 0 & 0 & 0 \\ 0 & 0 & 0 & 0 & 0 & 0 & 1 & 0 & 0 \\ 1 & \alpha & \beta & 0 & 0 & 0 & 0 & 0 & 0 \\ 0 & 0 & 0 & 0 & \alpha & 0 & 0 & 0 & 0 \\ 0 & 0 & 0 & 0 & 0 & 0 & 1 & 0 & 0 \\ 1 & \alpha & \beta & 0 & 0 & 0 & 0 & 0 & 0 \\ 0 & 0 & 0 & 0 & \alpha & 0 & 0 & 0 & 0 \\ 0 & 0 & 0 & 0 & 0 & 0 & 1 & \alpha\omega_1 & 0 \end{pmatrix} \end{array} \tag{11}$$

and

$$\mathbf{U}_c = \mathbf{U}_4 \tag{12}$$

From Eq. (A.2) (see Appendix A), the $\langle r^2\rangle_0/nl^2$ and $\langle \mu^2\rangle/nm^2$ values of isotactic PPO of x (degree of polymerization) = 100 were calculated to be 5.91 (6.01) and 0.43 (0.43), respectively, where the values in the parentheses are the corresponding experimental data. The experimental $\langle r^2\rangle_0/nl^2$ value was estimated from viscosity measurements under the Θ condition (isooctane at 50 °C),[52] and the dipole moment was observed from the benzene solution at 25 °C.[53] The $\langle r^2\rangle_0/nl^2$ and $\langle \mu^2\rangle/nm^2$ values were calculated from the conformational energy sets for the cyclohexane and benzene solutions, respectively. The good agreement between theory and experiment was attained; the conformational energies determined from the NMR experiments and *ab initio* MO calculations on DMP successfully reproduced the chain dimension and dipole moment of isotactic PPO. The analysis of the MO calculations revealed

the presence of the intramolecular hydrogen bonds illustrated in Fig. 5. By analogy with the "pentane effect",[1] which gives rise to severe steric repulsion between methylene (methyl) groups in *n*-alkanes, it was believed that the ω_1 and ω_2 interactions of PPO should be repulsive. Further evidence of the (C–H)$\cdots$O attractions is given in the next section.

4. CARBON-13 NMR CHEMICAL SHIFTS OF DIMERIC MODEL COMPOUNDS OF PPO

Poly(propylene oxide) is prepared by ring-opening polymerization of propylene oxide (PO).[54] If both C–O bonds of the monomer are cleaved, three kinds of linkages, head-to-tail (H–T), head-to-head (H–H), and tail-to-tail (T–T), are formed between the monomeric units, where H stands for the methine end and T for the methylene end. Propylene oxide, having a chiral methine carbon, exists in either of two optical forms, *R* and *S*. Therefore, the ^{13}C NMR spectra observed from atactic PPO are complicated.[55,56]

To assign ^{13}C NMR signals of polymers to the regio- and stereosequences, effects of substituents on chemical shifts have often been utilized.[57,58] In particular, the γ-substituent, which is separated from the observed carbon atom by three bonds, tends to shield the observed nucleus; the magnitude of the shielding effect depends on the distance between the two atoms, thus being sensitive to the conformation of the intervening bond.[57–59] By this method, the ^{13}C NMR chemical shifts of a variety of polymers have been related to their microstructures.[57,58]

This section describes an attempt to determine conformational energies of six dimeric model compounds (Fig. 6) of PPO from their ^{13}C NMR chemical shifts by a combined use of the RIS scheme and substituent effects. The dimers may be the simplest compounds having different regiosequences (H–T, H–H, and T–T) and stereosequences (*RR*, *RS*, *SR*, and *SS*). Hereafter the compounds (and molecules) with the H–T, H–H, and T–T linkages are, respectively, simply referred to as H–T, H–H, and T–T. For each linkage, four optical isomers *RR*, *RS*, *SR*, and *SS*, exist. However, the *RR* and *SS* isomers, and the *RS* and *SR* isomers are indistinguishable by NMR. Here, the four isomers are represented by only two, *RR* and *RS*.

4.1. Theoretical basis

According to the empirical additivity relationship,[59,60] the chemical shift δ_{i_C} of carbon i_C is given by

$$\delta_{i_C} = \sum_{n_{j,\alpha}} \Delta\delta_{\alpha,j} + \sum_{n_{j,\beta}} \Delta\delta_{\beta,j} + \sum_{\eta} \sum_{n_{j,\gamma}} p_\eta \Delta\delta^{\eta}_{\gamma,j} + \sum_{\eta\eta'} \sum_{n_{j,\delta}} p_{\eta\eta'} \Delta\delta^{\eta\eta'}_{\delta,j} + S \quad (13)$$

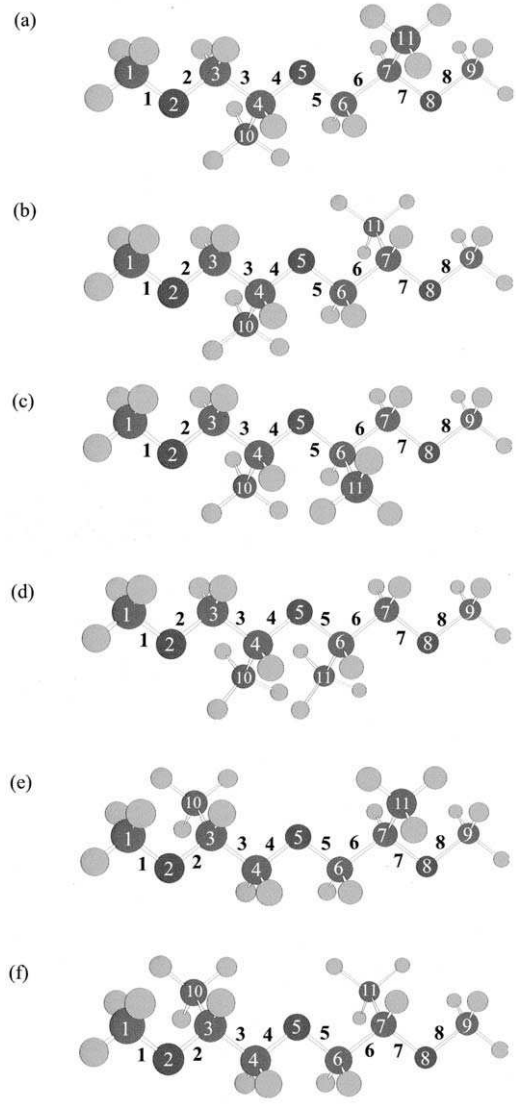

Fig. 6. Schematic representation of dimeric model compounds of PPO: (a) H–T (*RR*); (b) H–T (*RS*); (c) H–H (*RR*); (d) H–H (*RS*); (e) T–T (*RR*); and (f) T–T (*RS*) in their all-trans conformations. As indicated, the atoms and bonds are numbered. (Reproduced with permission from *J. Phys. Chem. A*, 2001, **105**, 3277. Copyright 2001 Am. Chem. Soc.)

where $n_{j,\alpha}$, $n_{j,\beta}$, $n_{j,\gamma}$, and $n_{j,\delta}$ are numbers of nonhydrogen atoms j at the α, β, γ, and δ positions (separated by one, two, three, and four bonds from the observed carbon i_C, respectively), $\Delta\delta_{\alpha,j}$ and $\Delta\delta_{\beta,j}$ are the chemical shift increments due to the atoms at the α and β positions, and $\Delta\delta^{\eta}_{\gamma,j}$, and $\Delta\delta^{\eta\eta'}_{\delta,j}$ are

those due to the γ and δ atoms with the intervening bond(s) being in the η (= t, g^+, or g^-) and $\eta\eta'$ (= tt, tg^+, ... or g^-g^-) conformations, respectively. Thus, the terms related to the γ- and δ-effects include the conformational probabilities, p_η and $p_{\eta\eta'}$, respectively. The α- and β-substituents induce downfield shifts (i.e., $\Delta\delta_{\alpha,j} > 0$ and $\Delta\delta_{\beta,j} > 0$), while the γ-substituent yields an upfield shift ($\Delta\delta^{\eta}_{\gamma,j} < 0$). The sign of $\Delta\delta^{\eta\eta'}_{\delta,j}$ is changeable with structure and conformation. The steric factor S is determined by the extent of branching at the carbon i_C and its adjacent carbons.

If the constant terms of Eq. (13) are unified, Eq. (13) may be rewritten as

$$\delta_{i_C} = \Delta\delta_{0,i_C} + \sum_{\eta} \sum_{n_{j,\gamma}} p_\eta \Delta\delta^{\eta}_{\gamma,j} + \sum_{\eta\eta'} \sum_{n_{j,\delta}} p_{\eta\eta'} \Delta\delta^{\eta\eta'}_{\delta,j} \tag{14}$$

where $\Delta\delta_{0,i_C}$ is the summation of the 1st, 2nd, and 5th terms of Eq. (13) with respect to the observed carbon atom i_C. The $\Delta\delta_{0,i_C}$ term, being independent of conformation, may be given from the molecule which has the same atoms at the α and β positions as the compound of interest and only hydrogen atoms at the γ positions. This molecule is designated as the *parent* compound. Parent compounds for the methine, methylene, pendant methyl, and terminal methoxy carbons of the six model compounds are 2-methoxy-1-propanol ($CH_3OCH(CH_3)CH_2OH$), 1-methoxy-2-propanol ($CH_3OCH_2CH(CH_3)OH$), 2-propanol ($CH_3CH(CH_3)OH$), and dimethyl ether (CH_3OCH_3), respectively. The individual carbon atoms have the same numbers and kinds of α and β atoms (*C*H, 2 α-C, 1 α-O, 1 β-C, and 1 β-O; *C*H_2, 1 α-C, 1 α-O, 2 β-C, and 1 β-O; *C*H_3, 1 α-C, 1 β-C, and 1 β-O; *C*H_3O, 1 α-O and 1 β-C), irrespective of linkage type and optical isomer. However, the β-substituent groups are not always common; e.g., for the methine carbons, ^{4}CH of H–T, 1 β-CH_2 and 1 β-O; ^{7}CH of H–T, 1 β-CH_3 and 1 β-O; ^{4}CH and ^{6}CH of H–H, 1 β-CH and 1 β-O, ^{3}CH and ^{7}CH of T–T, 1 β-CH_3 and 1 β-O. Here the superscripts correspond to the carbon numbers in Fig. 6. On this basis, it is preferable that the $\Delta\delta_{0,\zeta}$ (ζ = CH, CH_2, CH_3, or CH_3O) value should be defined according to the β-substituent group.

The γ-effect ($\Delta\delta^{t}_{\gamma,C}$) of carbon in the trans position, i.e., the γ-anti effect, is negligible small, while that ($\Delta\delta^{t}_{\gamma,O}$) of oxygen is comparatively large (−2–−3 ppm).[59,60] In ^{13}C NMR studies on alkanes and their oxygenated derivatives, the γ-gauche effects of carbon and oxygen ($\Delta\delta^{g^\pm}_{\gamma,C}$ and $\Delta\delta^{g^\pm}_{\gamma,O}$) have been found within ranges of −4–−6 and −6–−8 ppm, respectively.[55,57,58] The δ-effects, which are typically much smaller in magnitude ($\leq$ 0.5 ppm) than those of α-, β-, and γ-effects, have not been taken into account, except for the $g^\pm g^\mp$ conformations. In hydrocarbon polymers, the $g^\pm g^\mp$ conformations lead to a severe steric interaction called the pentane effect.[1] Thus, the δ-effect contribution ($\Delta\delta^{g^\pm g^\mp}_{\delta,C}$) to the chemical shift may be negligible in these cases. As shown in the previous section, however, the $g^\pm g^\mp$ conformations for the C–O/C–C* bond pairs of PPO and its model compounds are expected to be stabilized by the

intramolecular (C–H)$\cdots$O hydrogen bonds. The $\Delta\delta_{\delta,O}^{g^{\pm}g^{\mp}}$ values, estimated as 2–3 ppm,[59,60] have been included here, while the $\Delta\delta_{\delta,C}^{g^{\pm}g^{\mp}}$ effect may be negligible because of the pentane effect. Here, the δ-effects related to other conformations were assumed to be null.

According to the RIS scheme,[1,6] for example, the fraction $f_{g^+tg^-\ldots}$ of conformation $g^+tg^-\ldots$ can be calculated from statistical weight matrices $\mathbf{U}_i$'s according to

$$f_{g^+tg^-\ldots} = \frac{\mathbf{J}^*[\mathbf{U}'_2(g^+)\mathbf{U}'_3(g^+t)\mathbf{U}'_4(g^+tg^-)\ldots]\mathbf{J}}{\mathbf{J}^*\left[\prod_{i=2}^{n-1}\mathbf{U}_i\right]\mathbf{J}} \tag{15}$$

where **J*** and **J** are defined under Eq. (7), and n is the number of skeletal bonds. The $\mathbf{U}'_2(g^+)$ matrix can be obtained by filling the columns of the $\mathbf{U}_2$ matrix other than that corresponding to the g^+ state with zero, and the $\mathbf{U}'_3(g^+t)$ matrix by filling the elements of the $\mathbf{U}_3$ matrix other than that corresponding to the g^+t conformation with zero, etc. To facilitate the analysis, the six dimers have been assumed to have the same conformational energies. To distinguish the energy parameters from those established for isotactic PPO, statistical weights and interactions on the dimers are represented by the corresponding capital letters: A, B, Γ, Δ, Σ, Ω_1, Ω_2, and X.

The conformational probability p_η of the ith bond is given as the sum of fractions of conformers having the η state in the ith bond, and $p_{\eta\eta'}$ for the ith and $(i+1)$th bond pair as the sum of fractions of conformers having the $\eta\eta'$ conformation in the two bonds. The chemical shift δ_{i_C} may be calculated from $\Delta\delta_{0,\zeta}$'s, $\Delta\delta_{\gamma,O}^{t}$, $\Delta\delta_{\gamma,C}^{g^{\pm}}$, $\Delta\delta_{\gamma,O}^{g^{\pm}}$, $\Delta\delta_{\delta,O}^{g^{\pm}g^{\mp}}$, p_η's, and $p_{\eta\eta'}$'s.

4.2. Preparation, characterization, and purification of dimers

In the alcoholysis of PO, an acid catalyst yields a mixture of 2-alkoxy-1-propanol and 1-alkoxy-2-propanol in approximately equal amounts, while a base catalyst preferentially gives the latter compound.[61] The reactions provided all the six dimeric model compounds; PO was initially reacted with methanol to yield a mixture of 2-methoxy-1-propanol and 1-methoxy-2-propanol, and these products were further reacted with PO to produce the dimerized alcohols. Then, two combinations of the catalysts were used in the first and second steps: **1**, NaOH and H_2SO_4; **2**, H_2SO_4 and NaOH. The concentrations of the NaOH and H_2SO_4 catalysts were 0.3 and 1.3 mol%, respectively. The individual products were treated with sodium hydride and iodomethane to yield mixtures of the model compound (referred hereafter to as samples **1** and **2** in the order mentioned).

A combined use of supercritical fluid chromatography (SFC)[62] and mass spectrograph revealed the following facts: sample **1** contains a large amount of

both H–T and H–H with a small amount of T–T, while sample **2** includes a large amount of both T–T and H–T and a small amount of H–H. Therefore, samples **1** and **2** were mixed in equal quantities, dissolved in dichloromethane at 10 wt.%. To acquire sufficient amounts of the H–T, H–H, and T–T components for NMR measurements, fractionations by SFC were repeated ca. 250 times under the following conditions: CO_2 pressure of 90 kg cm^{-2}, column temperature of 60 °C, and injection of 8 μl.

4.3. ^{13}C NMR spectra and assignment

Figure 7 shows ^{13}C NMR ^{1}H broad-band decoupling spectra from benzene solutions of T–T, H–T, and H–H at 25 °C. The peaks at 17–18 ppm can be assigned to the pendant methyl carbons, and those around 56–59 ppm to terminal methoxy carbons. The signals around 74–78 ppm were assigned to methine and methylene carbons by reference to the DEPT spectra. In Fig. 8, the methine and methylene parts of DEPT(90) and DEPT(135) spectra of H–T in

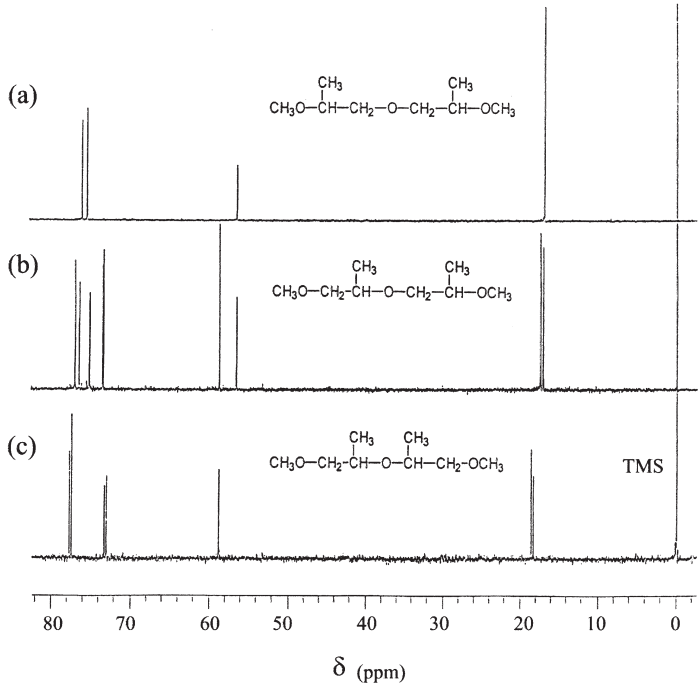

Fig. 7. ^{13}C NMR spectra observed from the benzene solutions at 25 °C by using ^{1}H broad-band decoupling: (a) T–T; (b) H–T; and (c) H–H. The internal standard was tetramethylsilane. (Reproduced with permission from *J. Phys. Chem. A*, 2001, **105**, 3277. Copyright 2001 Am. Chem. Soc.)

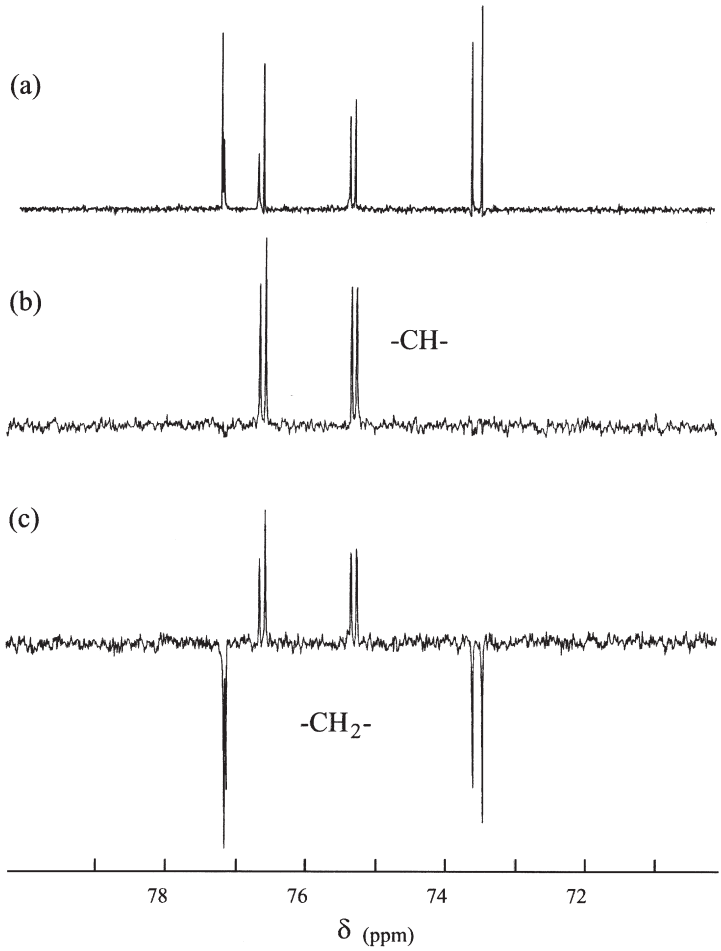

Fig. 8. Methine and methylene parts of ^{13}C NMR spectra of H–T in benzene at 25 °C: (a) ^{1}H broad-band decoupling; (b) DEPT(90); and (c) DEPT(135) spectra. The internal standard was tetramethylsilane. (Reproduced with permission from *J. Phys. Chem. A*, 2001, **105**, 3277. Copyright 2001 Am. Chem. Soc.)

benzene at 25 °C are compared with the corresponding ^{1}H broad-band decoupling spectrum. The methylene signals are removed by DEPT(90) and inverted by DEPT(135).[63] In H–T, only two methine and two methylene groups exist. However, four doublets are observed; one of the doublets arises from *RR* and the other from *RS*. The doublet spacing, corresponding to the chemical shift difference between *RR* and *RS*, ranges from 0.00 to 0.14 ppm for H–T. The number of peaks from H–H or T–T is smaller than that from H–T, because of the structural symmetry. The doublets from the H–H mixture show comparatively large spacings; CH and CH_2, 0.27 ppm; CH_3, 0.29 ppm; CH_3O,

0.02 ppm. For T–T, the doublet was observed only from the methylene carbons at 75.61 and 75.66 ppm. This is probably due to the two nearby chiral centers. Because of the structural similarity between H–T and H–H in atoms 1–5 and that between H–T and T–T in atoms 5–9, comparisons of the H–T spectrum with the T–T and H–H spectra enable us to assign the NMR peaks of H–T. The ^{13}C NMR chemical shifts of the parent compounds in benzene at 25 °C were also determined from ^{1}H broad-band decoupling and DEPT spectra.

4.4. Calculations of chemical shifts by RIS scheme

Statistical weight matrices for the six dimeric models were formulated from visual inspection of the molecular models and their symmetries (see Supporting Information of Ref. 28). The simulation based on Eq. (14) was carried out by the simplex method[64] to achieve the best agreement between calculated and observed chemical shifts (δ_{i_C}'s). The simulation was performed for average δ_{i_C} values of *RR* and *RS*. The variables were as follows: eight conformational energies, one γ-anti effect ($\Delta\delta^{t}_{\gamma,O}$), two γ-gauche effects ($\Delta\delta^{g^{\pm}}_{\gamma,C}$ and $\Delta\delta^{g^{\pm}}_{\gamma,O}$) and one δ-effect ($\Delta\delta^{g^{\pm}g^{\mp}}_{\delta,O}$) parameters, and three $\Delta\delta_{0,CH}$'s ($\Delta\delta_{0,CH}(1)$ including the effects of substituents, α-CH_2, α-CH_3, α-O, β-O, and β-CH_2; $\Delta\delta_{0,CH}(2)$, α-CH_2, α-CH_3, α-O, β-O, and β-CH_3O; $\Delta\delta_{0,CH}(3)$, α-CH_2, α-CH_3, α-O, β-O, and β-CH), three $\Delta\delta_{0,CH_2}$'s ($\Delta\delta_{0,CH_2}(1)$, α-O, α-CH, β-O, β-CH_3, β-CH_3O; $\Delta\delta_{0,CH_2}(2)$, α-O, α-CH, β-O, β-CH_3, β-CH; $\Delta\delta_{0,CH_2}(3)$, α-O, α-CH, β-O, β-CH_3, β-CH_2), one $\Delta\delta_{0,CH_3}$ ($\Delta\delta_{0,CH_3}(1)$, α-CH, β-CH_2, and β-O), and two $\Delta\delta_{0,CH_3O}$'s ($\Delta\delta_{0,CH_3O}(1)$, α-O and β-$CH_2$; $\Delta\delta_{0,CH_3O}(2)$, α-O and β-CH). As the initial values, the conformational energies E_α to E_χ of isotactic PPO (Table 3), recommended values of $\Delta\delta^{t}_{\gamma,O}$ (−3.0 ppm),[59] $\Delta\delta^{g^{\pm}}_{\gamma,C}$ (−5.0 ppm),[57,58] $\Delta\delta^{g^{\pm}}_{\gamma,O}$ (−7.0 ppm),[57,58] and $\Delta\delta^{g^{\pm}g^{\mp}}_{\delta,O}$ (2.0 ppm),[59,60] and chemical shifts of the parent compounds were employed.

In Table 4, the calculated δ_{i_C} values are compared with the corresponding experimental data. The overall root-mean-square error ($RMSE_{all}$) was minimized to 0.12 ppm, being comparable with or less than the magnitudes of the δ-effects for conformations other than $g^{\pm}g^{\mp}$.[59] These δ-effects have not been included in the calculations here. The conformational energies, E_A to E_X, differ slightly from E_α to E_χ (see Table 5).

From the E_A to E_X values, the t, g^+, and g^- fractions of the central C–C bond of DMP were, respectively, evaluated as 0.37 (0.34 ± 0.01), 0.47 (0.44 ± 0.01), and 0.16 (0.22 ± 0.01), where the values in the parentheses were determined from ^{1}H–^{1}H vicinal coupling constants for the benzene solution at 26 °C.[25] The γ- and δ-effect parameters were evaluated as follows: $\Delta\delta^{t}_{\gamma,O} = -2.6$ ppm (−2–−3 ppm),[59,60] $\Delta\delta^{g^{\pm}}_{\gamma,C} = -4.9$ ppm (−4–−6 ppm),[55,57,58] $\Delta\delta^{g^{\pm}}_{\gamma,O} = -7.9$ ppm (−6–−8 ppm),[55,57,58] and $\Delta\delta^{g^{\pm}g^{\mp}}_{\delta,O} = 2.1$ ppm (2–3 ppm).[59,60] All these parameters fall within the allowable ranges shown in parentheses.

Table 4. Observed and calculated chemical shifts of dimeric model compounds of PPO in benzene at 25 °C

	Carbon number[b] i_C	δ_{i_C}[a] (ppm)				
		Obsd		Calcd[c]		
		RR+*RS*	Average	*RR*	*RS*	Average
H–T	1	58.82	58.82	58.90	58.89	58.90
	3	77.11, 77.13	77.12	77.54	77.42	77.48
	4	75.27, 75.34	75.31	75.28	75.33	75.31
	6	73.50, 73.64	73.57	73.54	73.62	73.58
	7	76.55, 76.62	76.59	76.59	76.65	76.62
	9	56.65, 56.66	56.66	56.83	56.81	56.82
	10, 11[d]	17.17, 17.25	17.38	17.40	17.53	17.53
		17.52, 17.56		17.58	17.59	
$RMSE_{H-T}$[e]			0.16			
H–H	1	58.82, 58.84	58.83	58.83	58.74	58.79
	3	77.48, 77.75	77.62	77.55	77.29	77.42
	4	73.06, 73.33	73.20	73.21	73.13	73.17
	6	73.06, 73.33	73.20	73.21	73.13	73.17
	7	77.48, 77.75	77.62	77.55	77.29	77.42
	9	58.82, 58.84	58.83	58.83	58.74	58.79
	10	18.35, 18.64	18.50	18.24	18.50	18.37
	11	18.35, 18.64	18.50	18.24	18.50	18.37
$RMSE_{H-H}$[e]			0.12			
T–T	1	56.64	56.64	56.57	56.57	56.57
	3	76.27	76.27	76.24	76.27	76.26
	4	75.61, 75.66	75.64	75.61	75.64	75.63
	6	75.61, 75.66	75.64	75.61	75.64	75.63
	7	76.27	76.27	76.24	76.27	76.26
	9	56.64	56.64	56.57	56.57	56.57
	10	17.07	17.07	17.03	17.08	17.06
	11	17.07	17.07	17.03	17.08	17.06
$RMSE_{T-T}$[e]			0.04			
$RMSE_{all}$[f]			0.12			

[a]Relative to the chemical shift of tetramethylsilane.

[b]See Fig. 6.

[c]The optimized parameters are as follows: $\Delta\delta^{t}_{\gamma,O} = -2.6$ ppm, $\Delta\delta^{g^{\pm}}_{\gamma,C} = -4.9$ ppm, $\Delta\delta^{g^{\pm}}_{\gamma,O} = -7.9$ ppm, $\Delta\delta^{g^{\pm}g^{\mp}}_{\delta,O} = 2.1$ ppm, $\Delta\delta_{0,CH}(1) = 76.12$ ppm, $\Delta\delta_{0,CH}(2) = 77.33$ ppm, $\Delta\delta_{0,CH}(3) = 77.87$ ppm, $\Delta\delta_{0,CH_2}(1) = 79.87$ ppm, $\Delta\delta_{0,CH_2}(2) = 79.60$ ppm, $\Delta\delta_{0,CH_2}(3) = 77.73$ ppm, $\Delta\delta_{0,CH_3}(1) = 25.35$ ppm, $\Delta\delta_{0,CH_3O}(1) = 59.17$ ppm, and $\Delta\delta_{0,CH_3O}(2) = 61.09$ ppm. For these parameters, see text. The conformational energies obtained are listed in Table 5.

[d]The signals from carbons 10 and 11 of H–T were not distinguishable.

[e]The RMSE is defined as RMSE (ppm) $= [\sum_{i_C=1}^{I_C} (\delta^{av}_{i_C,calc} - \delta^{av}_{i_C,obsd})^2 / I_C]^{1/2}$, where I_C is the number of data.

[f]The RMSE for all the data. (Reproduced with permission from *J. Phys. Chem. A*, 2001, **105**, 3277. Copyright 2001 Am. Chem. Soc.)

Table 5. Conformational energies[a] of dimeric model compounds of PPO in benzene at 25 °C, determined from their ^{13}C NMR chemical shifts

First-order interaction	
E_A	0.36
E_B	1.00
E_Γ	2.86
E_Δ	0.44
E_Σ	1.40
Second-order interaction	
E_{Ω_1}	−0.88
E_{Ω_2}	−1.53
Third-order interaction	
E_X	−0.93

[a]The interactions are illustrated with the corresponding lower-case letters in Figs. 2 and 5.

In the previous section, conformational energies of isotactic PPO were determined from *ab initio* MO calculations and NMR vicinal coupling constants of DMP and the RIS analysis of the characteristic ratio and dipole moment ratio of isotactic PPO. The gauche stability of the C–C bond in the main chain was indicated to be due to the (C–H)···O hydrogen bonds. The six dimers treated here differ from each other in regio- and stereosequences. Nevertheless, a minor modification of the energy parameters of isotactic PPO gave reasonable agreement between the calculated and observed δ_{i_c}'s of all the dimers. These facts demonstrate the existence of the intramolecular (C–H)···O attractions in the six dimers and the validity of the RIS scheme for the chemical-shift calculations.

5. POLY(METHYLENE SULFIDE) (PMS) AND POLY(METHYLENE OXIDE) (PMO)

An alkoxy substituent at the C-2 site of pyranose ring prefers the axial (gauche) to the equatorial (trans) form (Fig. 9, X = O).[65] The gauche stabilization has been estimated as ca. $-0.9\,kcal\,mol^{-1}$ in free energy (ΔG).[66] This phenomenon, referred to as the anomeric effect, is a most familiar topic in stereochemistry[17,18] and considered to be caused by the followings: (1) dipole–dipole interaction between the C–O bonds of the pyranose ring and alkoxy substituent;[65] the gauche state with smaller resultant dipole moment is more stable. (2) Delocalization of lone pair electrons (n_O) of the oxygen atom by a hyperconjugation ($n_O \rightarrow \sigma^*_{C-O}$) with the antibonding orbital (σ^*_{C-O});[67] when the C–O bond adopts the gauche conformation, the lone pair is antiperiplanar to the acceptor C–O bond and hence the hyperconjugation is enhanced.[68]

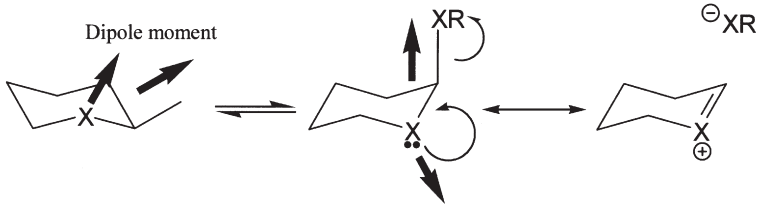

Fig. 9. The anomeric effect: lone pair (n_X) → antibonding orbital (σ^*_{C-X}) hyperconjugation and dipole–dipole interaction. The thick arrows and R stand for C–O bond dipole moments and an alkyl group, respectively. (Reproduced with permission from *Macromolecules*, 2001, **34**, 8321. Copyright 2001 Am. Chem. Soc.)

2-Alkylthiotetrahydrothiopyrans (Fig. 9, X = S) show a similar phenomenon;[69–71] the ΔG values are -0.42–$0.00\,\mathrm{kcal\,mol^{-1}}$, being smaller in magnitude than those of 2-alkoxyltetrahydropyrans (X = O). Thus, sulfur may be less effective in the gauche stability than oxygen.

The simplest polymeric chain having the O–C–O–C bond sequence may be PMO. The melting point ranges from 165 to 184 °C.[72,73] In the crystal, the PMO chain adopts a 29/16 helical structure,[74] in which all C–O bonds are in the gauche conformation. Because PMO is soluble in small number of organic solvents, the conformational analysis has been carried out for small model compounds, and the conformational energy E_σ representing the gauche stability in the C–O bond has been estimated as -1.4–$-1.5\,\mathrm{kcal\,mol^{-1}}$.[1,10,11]

In the crystal, PMS takes a 17/9 helical structure of all-gauche conformation.[75] This polymer is insoluble in almost all organic solvents and melts around 220–260 °C;[76,77] therefore, no quantity representing the Θ state has been reported. The S–C–S–C bond sequence has been implanted in other polymeric chains such as poly(1,3-dithiocane)[19] and poly(thiomethylene-1,4-*trans*-cyclohexylenemethylenethiomethylene)[20] to estimate the first-order interaction energy E_σ of the C–S bond as ca. $-1.2\,\mathrm{kcal\,mol^{-1}}$ from their dipole moment measurements.

In this study, we analyzed ^{13}C NMR vicinal C–H coupling constants observed from a dimeric model compound of PMS, bis(methylthio)methane, in the gas phase and solutions to evaluate the E_σ values, and carried out *ab initio* MO calculations for the oligomeric models to obtain the conformational free energies, geometrical parameters, dipole moments, atomic charges, and electron density distributions. The MO calculations were strictly compared with the corresponding experiments. In this section, the conformational characteristics and the anomeric effect of PMS are discussed in comparison with those of PMO.

Oligomeric model compounds of PMS and PMO are, respectively, designated as PMS-x and PMO-x (see Fig. 10), where x is the degree of polymerization, viz., the number of heterogeneous atoms X's (X = S or O) included: dimers, bis(methylthio)methane (PMS-2) and dimethoxymethane

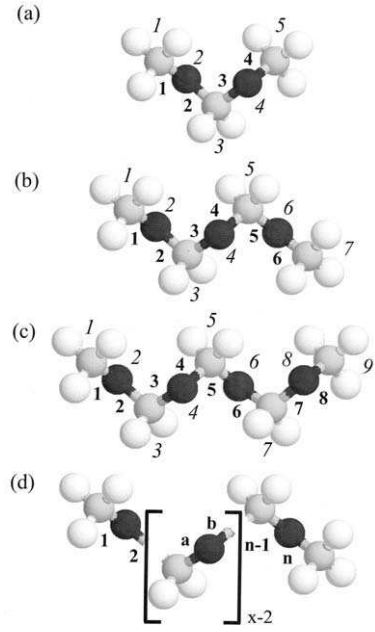

Fig. 10. Schematic representation of PMS, PMO, and their oligomeric model compounds: (a) dimers, bis(methylthio)methane (PMS-2) and dimethoxymethane (PMO-2); (b) trimers, bis[(methylthio)methyl]sulfide (PMS-3) and 1,3-dimethoxydimethylether (PMO-3); (c) tetramer, bis[(methylthio)methylthio]methane (PMS-4) and bis[(methoxy)methoxy]methane (PMO-4); (d) polymers, PMS and PMO. The bonds and atoms (atomic groups) are numbered as indicated, and x is the degree of polymerization. (Reproduced with permission from *Macromolecules*, 2001, **34**, 8321. Copyright 2001 Am. Chem. Soc.)

(PMO-2); trimers, bis[(methylthio)methyl]sulfide (PMS-3) and 1,3-dimethoxydimethylether (PMO-3); tetramers, bis[(methylthio)methylthio]methane (PMS-4) and bis[(methoxy) methoxy]methane (PMO-4).

5.1. ^{13}C NMR from model compounds

Shown in Fig. 11 are examples of ^{13}C NMR spectra observed from the labeled methyl carbon of PMS-2-^{13}C and methylene carbons of 2-methyl-1,3,5-trithiane (MTT). The ^{13}C NMR signal from PMS-2-^{13}C was split into four by direct couplings and further into three by vicinal couplings. For MTT, vicinal couplings of the methylene carbon with three protons (Fig. 12c) yield two triplets, which indicate that the MTT ring does not change conformation even at 70 °C.

The vicinal coupling constant $^3J_{CH}$ of PMS-2-^{13}C provides information regarding the conformation around the C–S bond. The observed $^3J_{CH}$ value

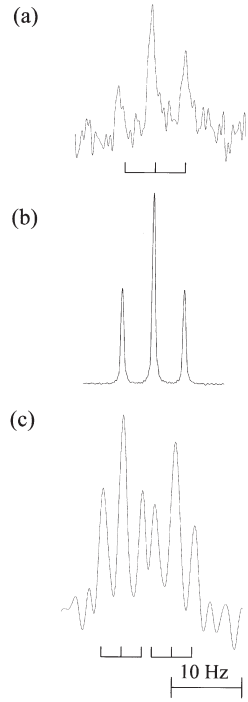

Fig. 11. ^{13}C NMR spectra observed from the labeled methyl carbon of PMS-2-^{13}C: (a) in the gas phase at 180 °C; and (b) in benzene at 70 °C; and (c) methylene carbons of MTT in benzene at 70 °C. (Reproduced with permission from *Macromolecules*, 2001, **34**, 8321. Copyright 2001 Am. Chem. Soc.)

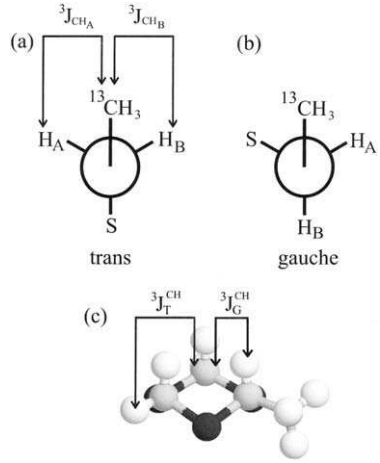

Fig. 12. Newman projections of: (a) trans; and (b) gauche conformations around the C–S bond of PMS-2, and (c) MTT with definitions of vicinal coupling constants between carbon and proton in the trans ($^3J_T^{CH}$) and gauche ($^3J_G^{CH}$) positions.

corresponds to the average of vicinal ^{13}C–$^{1}H_A$ and ^{13}C–$^{1}H_B$ coupling constants:

$$^{3}J_{CH} = \frac{^{3}J_{CH_A} + {}^{3}J_{CH_B}}{2} = \frac{2\,{}^{3}J_{G}^{CH}p_t + {}^{3}J_{T}^{CH}p_g + {}^{3}J_{G}^{CH}p_g}{2} \tag{16}$$

where $^{3}J_{T}^{CH}$ and $^{3}J_{G}^{CH}$ are, respectively, vicinal coupling constants between carbon and proton in trans and gauche positions, and p_t and p_g are trans and gauche fractions of the C–S bond. Therefore, it follows that

$$p_t + p_g = 1 \tag{17}$$

and

$$p_{g^+} = p_{g^-} = \frac{p_g}{2} \tag{18}$$

where p_{g^+} and p_{g^-} are gauche$^+$ and gauche$^-$ fractions. From these equations, we have

$$p_t = \frac{^{3}J_{T}^{CH} + {}^{3}J_{G}^{CH} - 2\,{}^{3}J_{CH}}{^{3}J_{T}^{CH} - {}^{3}J_{G}^{CH}} \tag{19}$$

Here, the $^{3}J_{T}^{CH}$ and $^{3}J_{G}^{CH}$ values were obtained from MTT dissolved in the corresponding solvent: $^{3}J_{T}^{CH} = 7.13 \pm 0.02$ Hz and $^{3}J_{G}^{CH} = 2.62 \pm 0.02$ Hz in benzene; $^{3}J_{T}^{CH} = 7.12 \pm 0.09$ Hz and $^{3}J_{G}^{CH} = 2.58 \pm 0.02$ Hz in chloroform; $^{3}J_{T}^{CH} = 7.27 \pm 0.05$ Hz and $^{3}J_{G}^{CH} = 2.54 \pm 0.02$ Hz in methanol; $^{3}J_{T}^{CH} = 6.92 \pm 0.07$ Hz and $^{3}J_{G}^{CH} = 2.71 \pm 0.04$ Hz in DMSO. Since MTT was insoluble in cyclohexane, the $^{3}J_{G}^{CH}$ and $^{3}J_{T}^{CH}$ values from the benzene solution were used for PMS-2-^{13}C in the gas phase and cyclohexane. Listed in Table 6 are the p_t and p_g values thus evaluated, together with the experimental $^{3}J_{CH}$ values.

Statistical weight matrices of PMS-2 and PMO-2 may be given simply as 3×3 matrices:

$$\mathbf{U}_2 = \begin{pmatrix} \sigma^{-1} & 1 & 1 \\ 0 & 0 & 0 \\ 0 & 0 & 0 \end{pmatrix} \tag{20}$$

$$\mathbf{U}_3 = \begin{pmatrix} \sigma^{-1} & 1 & 1 \\ \sigma^{-1} & 1 & 0 \\ \sigma^{-1} & 0 & 1 \end{pmatrix} \tag{21}$$

where σ is the statistical weight given from $\sigma = \exp(-E_\sigma/RT)$. Our MO calculations showed that the g^+g^- and g^-g^+ conformations of PMS-2 and PMO-2 are essentially absent because of severe steric repulsion between the

Table 6. Vicinal C–H coupling constants ($^3J_{CH}$'s), bond conformations (p_t's and p_g's), and gauche stability energies (E_σ's) for the C–S bond of PMS-2

Medium	Dielectric constant of medium	Temperature (°C)	$^3J_{CH}$ (Hz)	p_t	p_g	E_σ (kcal mol^{-1})
^{13}C NMR						
Gas[a]	1.00	180	4.52 ± 0.04	0.16 ± 0.02	0.84 ± 0.01	-1.43 ± 0.01
Cyclohexane	2.02	25	4.63	0.11	0.89	−1.21
Benzene	2.28	25	4.57	0.14	0.86	−1.05
Chloroform	4.81	25	4.51	0.15	0.85	−0.98
Methanol	32.6	25	4.55	0.15	0.85	−0.98
Dimethyl sulfoxide	45.0	25	4.49	0.15	0.85	−0.96
Ab initio *MO calculations*[b]						
Gas[a]	1.00	180		0.16	0.84	−1.38

[a]At 3.6 atm (estimated from the Clausius–Clapeyron equation, see Section 2.1).
[b]At the B3LYP/6-311+G(2d, p)//B3LYP/6-31G(d) level.

CH_3 terminals; therefore, the (2, 3) and (3, 2) elements of $\mathbf{U}_3$ are set to zero. From Eqs. (20) and (21), we have

$$p_t = \frac{2\sigma + 1}{2\sigma^2 + 4\sigma + 1} \tag{22}$$

$$p_g = \frac{2\sigma(\sigma + 1)}{2\sigma^2 + 4\sigma + 1} \tag{23}$$

From Eqs. (22) and (23), we evaluated the E_σ values (Table 6). The gauche stability in the C–S bond is reduced in polar solvents.

5.2. MO calculations on model compounds

Free energies of possible conformers of PMS-2, PMS-3, PMO-2, and PMO-3, obtained from MO calculations and represented as the difference from that of the most stable all-gauche state, are shown in Table 7. Therefore, in Eqs. (20), (21) and (24) (given below), a weight of unity is assigned to the gauche states.

Statistical weight matrices for the second and third C–S bonds of PMS-3 and PMO-3 are, respectively, given by Eqs. (20) and (21), and that for the fourth bond may be expressed as

$$\mathbf{U}_4 = \begin{pmatrix} \sigma^{-1} & 1 & 1 \\ \sigma^{-1} & 1 & \omega \\ \sigma^{-1} & \omega & 1 \end{pmatrix} \tag{24}$$

where ω is the Boltzmann factor for the second-order $X \cdots X$ (X = S or O) interaction occurring in the $g^{\pm}g^{\mp}$ conformations for the third and fourth C–X bond pairs. The $\mathbf{U}_5$ of the trimers is equivalent to $\mathbf{U}_3$.

For PMS-2 and PMO-2, the free energy difference between g^+g^+ and g^+t states may be adopted as the conformational energy E_σ: −1.54 (PMS-2) and $-2.15\,\text{kcal mol}^{-1}$ (PMO-2). According to the RIS scheme, the ΔG_k values of PMS-3 and PMO-3 are approximated as a function of E_σ and E_ω; for example, the ΔG_k value of the tg^+g^-t conformation may correspond to $-2E_\sigma + E_\omega$. The E_σ and E_ω values were determined by minimizing the following function:

$$S(\mathbf{E}) = \frac{1}{K} \sum_k \Delta_k^2(\mathbf{E}) \tag{25}$$

where

$$\Delta_k^2(\mathbf{E}) = \left(\sum_\xi L(\xi) E_\xi - \Delta G_k \right)^2 M_k \exp(-\Delta G_k / RT) \tag{26}$$

Table 7. Free energies (ΔG_k) of conformers of dimers, trimers, and tetramers of PMS and PMO, evaluated by *ab initio* MO calculations at the B3LYP/6-311+G(2d, p)//B3LYP/6-31G(d) level[a]

k	Conformation	M_k	Statistical weight(s)	ΔG_k (kcal mol^{-1})	
				PMS−x	PMO−x
Dimer ($x=2$)					
1	t t	1	σ^{-2}	5.12 (5.88)[b]	5.08
2	t g^+	4	σ^{-1}	1.54 (1.38)[b]	2.15
3	g^+ g^+	2	1	0.00 (0.00)[b]	0.00
Trimer ($x=3$)[c]					
1	t t t t	1	σ^{-4}	9.66	9.26
2	t t t g^+	4	σ^{-3}	_[d]	_[d]
3	t t g^+ t	4	σ^{-3}	_[d]	_[d]
4	t g^+ t g^+	4	σ^{-2}	2.76	3.35
5	t g^+ t g^-	4	σ^{-2}	2.94	3.80
6	t g^+ g^+ t	2	σ^{-2}	2.78	4.03
7	t g^+ g^+ g^+	4	σ^{-1}	1.50	2.08
8	t g^+ g^- t	2	$\sigma^{-2}\omega$	6.02	6.46
9	t g^+ g^- g^-	4	$\sigma^{-1}\omega$	3.28	3.46
10	g^+ t t g^+	2	σ^{-2}	2.85	3.96
11	g^+ t t g^-	2	σ^{-2}	3.16	4.60
12	g^+ t g^+ g^+	4	σ^{-1}	1.61	1.71
13	g^+ g^+ t g^-	4	σ^{-1}	1.69	1.57
14	g^+ g^+ g^+ g^+	2	1	0.00	0.00
15	g^+ g^+ g^- g^-	2	ω	3.07	2.08
Tetramer ($x=4$)					
1	t g^+ g^+ g^+ g^+	4	σ^{-1}	1.24	1.98
2	g^+ t g^+ g^+ g^+	4	σ^{-1}	_[d]	1.61
3	g^+ g^+ t g^+ g^+	4	σ^{-1}	1.61	1.66
4	g^+ g^+ g^+ g^+ g^+	2	1	0.00	0.00

[a]Relative to those of the all-gauche conformations. Calculated for the dimers, trimers, and tetramers at 298.15 K and 1 atm.

[b]For comparison with ^{13}C NMR experiment for gaseous PMS-2-^{13}C, the ΔG_k values for PMS-2 at 453 K and 3.6 atm are shown in the parentheses.

[c]According to the least-squares fittings, the E_σ and E_ω values were, respectively, determined as follows: −1.54 and 2.09 kcal mol^{-1} (PMS-3) and −1.72 and 1.98 kcal mol^{-1} (PMO-3).

[d]The local minimum of the potential was not found by the geometrical optimization. (Reproduced with permission from *Macromolecules*, 2001, **34**, 8321. Copyright 2001 Am. Chem. Soc.)

with K and M_k being the total number ($=\sum_k M_k$) of conformers and the multiplicity of conformation k. The function $L(\xi)$ gives the number of conformational energy E_ξ ($\xi=\sigma$ or ω) included in the conformation. The squared difference between ΔG_k and the sum of E_ξ's is multiplied by the Boltzmann factor $\exp(-\Delta G_k/RT)$ so as to weight low-energy conformations. The temperature T was set to 298.15 K. As a consequence of the optimization, the E_σ and E_ω values were, respectively, determined as follows: −1.54 and 2.09 kcal mol^{-1} (PMS-3) and −1.72 and 1.98 kcal mol^{-1} (PMO-3).

5.3. Comparison between theory and experiment

Our MO calculations gave the E_σ values of -2.15 and $-1.72\,\mathrm{kcal\,mol^{-1}}$ for gaseous PMO-2 and PMO-3, respectively. Abe *et al.*[78] evaluated an E_σ value of $-2.5 \pm 0.2\,\mathrm{kcal\,mol^{-1}}$ from ^{13}C NMR measurements for gaseous PMO-2. From dipole moment measurements for PMO-2 and PMO-3 in *n*-hexane at 25 °C, Uchida *et al.*[79] obtained the E_σ value as $-1.74\,\mathrm{kcal\,mol^{-1}}$. Our MO calculations well reproduced these experimental observations. Flory[1] estimated the E_σ and E_ω values as -1.5 and $1.8\,\mathrm{kcal\,mol^{-1}}$, respectively so as to reproduce the characteristic ratio of PMO as well as the data of Uchida *et al.*[79] Abe and Mark[11] offered an E_σ value of $-1.4\,\mathrm{kcal\,mol^{-1}}$ for unperturbed PMO. As stated above, the experimental E_σ values of PMO-*x*'s have been found within a wide range. One reason may be the solvent effect, and the other reason may be the chain-length dependence. Our calculations indicate that the gauche stability ($-2.15\,\mathrm{kcal\,mol^{-1}}$) of PMO-2 exceeds that ($-1.72\,\mathrm{kcal\,mol^{-1}}$) of PMO-3. For PMO-4, therefore, the free energies of the $tg^+g^+g^+g^+g^+$, $g^+tg^+g^+g^+g^+$, and $g^+g^+tg^+g^+g^+$ conformations were calculated. The E_σ value of PMO-4 depends on the bond position; bonds 2, 3, and 4 give E_σ's of -1.98, -1.61 and $-1.66\,\mathrm{kcal\,mol^{-1}}$, respectively. The outer bond seems to have a smaller E_σ than the inner bond. This tendency can be found for PMO-3; bonds 2 ($tg^+g^+g^+$) and 3 ($g^+tg^+g^+$ or $g^+g^+tg^-$) have E_σ's of -2.08 and -1.71 or $-1.57\,\mathrm{kcal\,mol^{-1}}$, respectively. Therefore, our MO calculations support Flory, Mark, and Abe's estimation[1,11] of $E_\sigma = -1.4$–$-1.5\,\mathrm{kcal\,mol^{-1}}$ for unperturbed PMO.

Our NMR analysis for gaseous PMS-2-^{13}C at 180° and 3.6 atm gave an E_σ value of $-1.43 \pm 0.01\,\mathrm{kcal\,mol^{-1}}$, which was closely reproduced by our MO calculation ($E_\sigma = -1.38\,\mathrm{kcal\,mol^{-1}}$). Thus, the MO calculations at the B3LYP/6-311+G(2d, p)//B3LYP/6-31G(d) level are fully quantitative for both PMS-*x*'s and PMO-*x*'s. The MO calculations gave an E_σ value ($-1.54\,\mathrm{kcal\,mol^{-1}}$) common to PMS-2 and PMS-3 but ΔG_k's of 1.24 and $1.61\,\mathrm{kcal\,mol^{-1}}$ for the $tg^+g^+g^+g^+g^+$ and $g^+g^+tg^+g^+g^+$ conformations of PMS-4, respectively; for PMS-*x*'s, no explicit chain-length dependence of E_σ can be found. Both experiments and calculations clearly show that PMS-*x*'s have weaker gauche preferences than PMO-*x*'s. The conformational energy E_σ was indirectly estimated as $-1.2\,\mathrm{kcal\,mol^{-1}}$ from dipole moments and their temperature coefficients of poly(1,3-dithiocane)[19] and poly(thiomethylene-1,4-*trans*-cyclohexylenemethylenethiomethylene)[20] in benzene. This estimate agrees well with our NMR data ($E_\sigma = -1.02$–$-1.11\,\mathrm{kcal\,mol^{-1}}$) for PMS-2-$^{13}C$ in benzene.

5.4. Electron densities, atomic charges, and anomeric effects

Illustrated in Fig. 13 are optimized geometries of all-trans, all-gauche, and g^+tg^+t conformations of PMS-3 and PMO-3, together with electron density

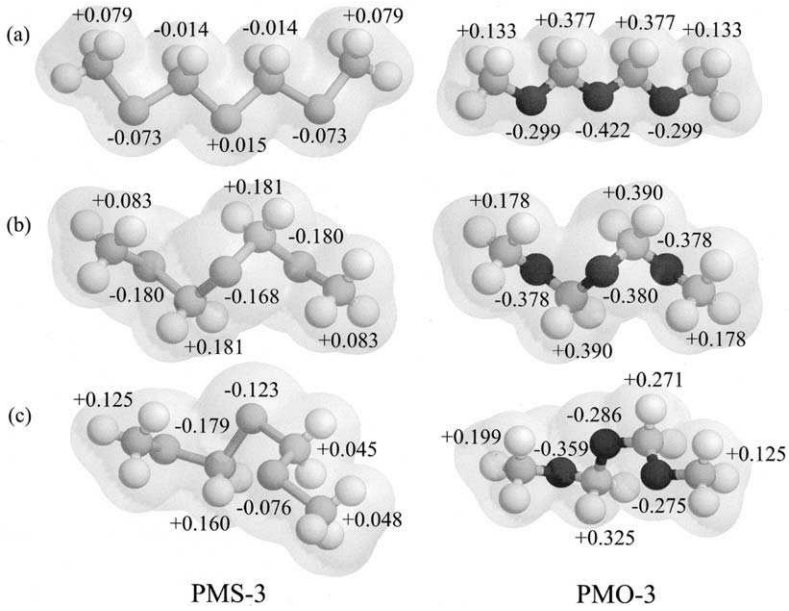

Fig. 13. Electron density distribution and atomic charges of: (a) all-trans; (b) all-gauche; and (c) g^+tg^+t conformations of PMS-3 and PMO-3. The atomic charges of hydrogens are summed into the bonded carbons. (Reproduced with permission from *Macromolecules*, 2001, **34**, 8321. Copyright 2001 Am. Chem. Soc.)

distributions and atomic (group) charges obtained by the Merz–Singh–Kollman method[38,39] at the B3LYP/6-311+G(2d, p) level. The all-trans conformer of PMS-3 is curved toward the methylene groups; bond angles ∠SCS's (108.35°) are larger than ∠CSC's (98.29 and 97.30°). On the other hand, the all-trans PMO-3 is curved toward the oxygen atoms; ∠OCO's (105.74°) are smaller than ∠COC's (112.40 and 113.03°). This may be due to the difference in van der Waals radius between sulfur and oxygen (1.80 Å for S and 1.52 Å for O).[49]

In all-trans PMO-3, all the oxygen atoms are negatively charged because oxygen has an electronegativity (3.5) larger than carbon (2.5).[80] In all-trans PMS-3, however, charge differences between S and CH_2 are slight, and the central S atom has a positive charge of +0.015. The electronegativity of sulfur is almost the same as that of carbon.[80] In addition, sulfur electrons may be so flexible as to reduce the S···S repulsion and unfavorable (parallel) dipole–dipole interaction.

In all-gauche PMS-3, all the sulfur atoms and methylene groups have negative and positive charges, respectively. The dipole moments formed along the bisector of ∠CSC angle cancel out each other and stabilize the all-gauche conformation. The all-gauche conformer has a larger S···S distance (3.13 Å) than the all-trans one (2.98 Å). These tendencies can also be found in the

all-gauche PMO-3. However, magnitudes of atomic charges of PMO-3 are about twice as large as those of PMS-3. The O···O distances of the all-gauche and all-trans PMO-3's are 2.35 and 2.23 Å, respectively.

The $n_O \rightarrow \sigma^*_{C-O}$ hyperconjugation has been justified by shorter O–C bonds in the gauche conformation. In the g^+tg^+t conformation of PMO-3, the O_2–C_3 (1.385 Å) and O_4–C_5 (1.384 Å) bonds in the gauche conformation are shorter than C_3–O_4 (1.427 Å) and C_5–O_6 (1.414 Å) in trans state (for the atom numbers, see Fig. 10). The similar tendency can also be seen for the g^+tg^+t conformer of PMS-3; the gauche S–C bonds are 1.819 and 1.825 Å long, and the trans bonds are 1.847 and 1.841 Å long. On average, the gauche bonds are shorter than the trans ones by 2.5% in PMO-3, but by only 1.2% in PMS-3. The gauche stability of polythioacetal has been indicated to stem from: (1) the favorable (antiparallel) dipole–dipole interaction; and (2) $n_S \rightarrow \sigma^*_{C-S}$ hyperconjugation occurring in the gauche conformation; and (3) the S···S repulsion; and (4) unfavorable (parallel) dipole–dipole interaction in the trans conformation.

6. POLY(ETHYLENE SULFIDE) (PES) AND POLY(ETHYLENE OXIDE) (PEO)

Poly(ethylene oxide) is soluble in a number of solvents, e.g., ordinary organic solvents, water, and aqueous solutions of inorganic salts and innocuous to organism.[81] As found for crown ethers, the O–C–C–O bond sequence acts as an effective electron donor. These peculiar physicochemical properties are due to the lone pair and electronegativity of oxygen.

Oxygen and sulfur belong to the group VIB in the periodic table. These atoms have analogous valence-shell configurations: O, $2s^22p^4$; S, $3s^23p^4$. However, PES exhibits physical and chemical properties different from those of PEO. For example, PES is soluble in a few solvents at temperatures above 140 °C. The melting point of PEO is, at the highest, 68 °C, whereas that of PES is as high as 216 °C.[82]

In the crystalline state, PES and PEO adopt different conformations. In the X–C–C–X (X = S or O) bond sequence, PES[83] and its monomeric model compound, 1,2-bis(methylthio)ethane (BMTE, $CH_3SCH_2CH_2SCH_3$, Fig. 14),[84] take g^+tg^- conformation, whereas PEO can adopt either tgt or ttt conformation.[85,86] However, the ttt form of PEO has been found only in stretched samples, thus being less stable than tgt. Indeed, crystallized DME adopts tgt conformation.[87]

The conformation of PEO has been extensively investigated. From experimental characteristic ratio and dipole moment ratio of PEO, Mark and Flory determined the conformational energies, E_σ and E_ρ, for the gauche states of the C–C and C–O bonds as -0.43 ± 0.07 and 0.90 ± 0.07 kcal mol^{-1}, respectively.[1,12,13] The second-order interaction energy E_ω was estimated to be

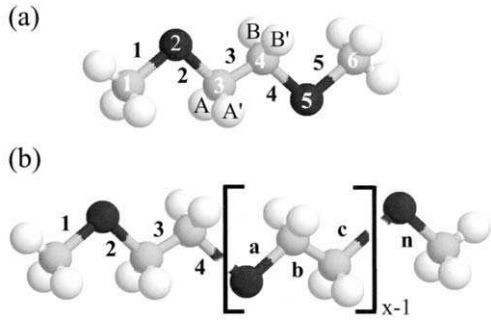

Fig. 14. Schematic representation of: (a) monomeric model compounds, BMTE and DME; and (b) polymers, PES and PEO. The bonds are numbered and the atoms are designated as indicated, and x is the degree of polymerization. (Reproduced with permission from *Macromolecules*, 2002, **35**, 3748. Copyright 2002 Am. Chem. Soc.)

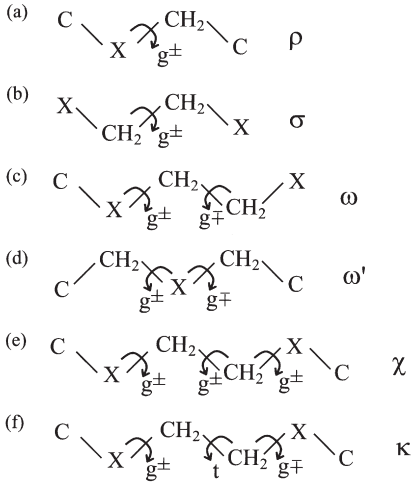

Fig. 15. Intramolecular interactions of PES and PEO. ρ and σ are the first-order interactions around the C–X and C–C bonds (X = S or O), respectively. ω and ω' are the second-order interactions occurring in the $g^{\pm}g^{\mp}$ conformations for the X–C/C–C and C–X/X–C bond pairs, respectively. χ and κ are the third-order interactions formed in the $g^{\pm}g^{\pm}g^{\pm}$ and $g^{\pm}tg^{\mp}$ conformations of the X–C–C–X bond sequence, respectively. (Reproduced with permission from *Macromolecules*, 2002, **35**, 3748. Copyright 2002 *Am. Chem. Soc.*)

$0.35 \pm 0.20\,\text{kcal mol}^{-1}$ (see Fig. 15c). The intramolecular interaction is similar to the ω_1 and ω_2 ones of PPO, thus being also referred here to as the (C–H)$\cdots$O interaction. Abe and Mark offered a minor modification of the energy parameters: $E_\sigma = -0.5$, $E_\rho = 0.9$, and $E_\omega = 0.4\,\text{kcal mol}^{-1}$.[11] These data mean that the attractive gauche effect of PEO is due to the first-order σ interaction; that is, the C–C bond itself has a gauche preference. As shown in previous

section, PPO forms intramolecular hydrogen bonds. *Ab initio* MO calculations on DME have estimated the E_σ and E_ω values to be 0.1–0.5 and −1.2–−1.4 kcal mol^{-1}, respectively.[88,89] The attractive (C–H)···O interaction is suggested to be formed in DME and stabilize the gauche state of the C–C bond. The MO calculations reasonably reproduced experimental conformer fractions of gaseous DME.[90,91] For PEO, however, all experimental facts on the gauche effect are not consistent with each other and cannot be elucidated only by the (C–H)···O attraction. For example, not tg^+g^- but tgt conformation is formed in crystallized PEO and DME.[85,87] The tgt conformation seems to be more stable than ttt, because the ttt form appears only in stretched samples.[86]

To investigate the nature of the (C–H)···O interactions, we carried out MO calculations for a series of dimethoxy ethers CH_3O–$(CH_2)_y$–OCH_3 ($y = 4$–8),[29] which correspond to higher homologues of DME and obtained the conformational free energies, equilibrium geometries, and partial charges. As a consequence, we found the following facts: (1) the (C–H)···O interaction energy (E_ω) depends on the number of methylene units between the two oxygen atoms. For example, the MO calculations at the MP2/6-31+G*//HF/6-31G* level yielded a negative E_ω value (−0.43 kcal mol^{-1}) only for 1,4-dimethoxybutane ($y = 4$) and positive values (0.24–0.66 kcal mol^{-1}) for the longer ethers ($5 \leq y \leq 8$). For the ethers of $5 \leq y \leq 8$, the E_ω values are almost equivalent to those (0.3–0.6 kcal mol^{-1}) estimated from molecular mechanics calculations. (2) The (C–H)···O interaction has an electrostatic character; the sign and magnitude of E_ω correlate to partial charges on the oxygen atom and methylene group.

In an early study,[21] conformational energies of PES were calculated by semiempirical potential energy functions; the E_σ and E_ρ values were estimated as 0.4 and −0.1 kcal mol^{-1}, respectively. The second-order interaction energies, E_ω and $E_{\omega'}$, arising in the $g^\pm g^\mp$ conformations for the S–C/C–C and C–S/S–C bond pairs (see Fig. 15), were calculated to be 1.1 and 0.4 kcal mol^{-1}, respectively. Riande and Guzmán[7,92] estimated the E_σ value indirectly from experimental dipole moments of an alternating copolymer of pentamethylene sulfide and ethylene sulfide as well as 1,2-bis(butylthio)ethane dissolved in benzene. The E_σ value was reported to be in a range of 0.4–0.7 kcal mol^{-1}.

In this study, the first- and second-order interaction energies for the S–C–C–S bond sequence were evaluated from ^{1}H and ^{13}C NMR vicinal coupling constants observed from BMTE dissolved in solutions. *Ab initio* MO calculations were carried out for BMTE and DME at the MP2/6-311+G(3df, 2p)//HF/6-31G(d) and B3LYP/6-311+G(3df, 2p)//HF/6-31G(d) levels. Conformational energies of PES and PEO in the gas phase and solutions were determined from the MO calculations and NMR data. From the energy parameters thus established, the $\langle r^2\rangle_0/nl^2$ and $\langle \mu^2\rangle/nm^2$ values were calculated and compared with the experiments.

6.1. ^{1}H NMR from model compounds of PES

Shown in Fig. 16 are satellite spectra observed from BMTE dissolved in C_6D_6 at 15 °C. As illustrated in Fig. 16a, naturally abundant ^{13}C atoms yield two groups of satellite peaks, which are separated from each other by the direct C–H coupling constant $^1J_{CH}$ and symmetrical with respect to the methylene peak. In Fig. 16b, the low frequency group is enlarged.

Newman projections for the trans and gauche states around the C–C bond of BMTE are shown in Fig. 17a. In the RIS approximation, the observed vicinal ^{1}H–^{1}H coupling constants, $^3J_{HH}$ and $^3J'_{HH}$, can be expressed as[44,45]

$$^3J_{HH} = {}^3J_{AB} = {}^3J_{A'B'} = {}^3J_G^{HH} p_t^{CC} + \frac{{}^3J_T'^{HH} + {}^3J_G''^{HH}}{2} p_g^{CC} \tag{27}$$

and

$$^3J'_{HH} = {}^3J_{AB'} = {}^3J_{A'B} = {}^3J_T^{HH} p_t^{CC} + {}^3J_G'^{HH} p_g^{CC} \tag{28}$$

where A, A′, B, and B′ represent the protons (Fig. 17), $^3J_T^{HH}$, $^3J_T'^{HH}$, $^3J_G^{HH}$, $^3J_G'^{HH}$, and $^3J_G''^{HH}$ are defined in Fig. 17a, and p_t^{CC} and p_g^{CC} are trans and gauche fractions of the C–C bond, respectively. Therefore, we have

$$p_t^{CC} + p_g^{CC} = 1 \tag{29}$$

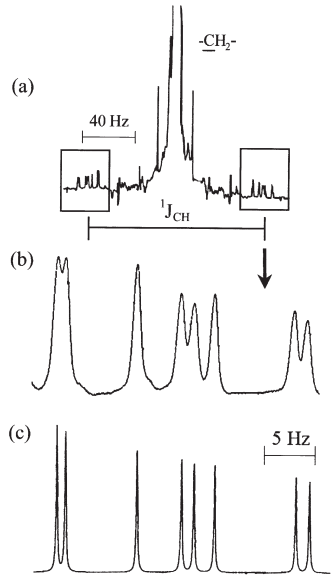

Fig. 16. ^{1}H NMR spectra of BMTE in C_6D_6 at 15 °C: (a) methylene peak portion; and (b) observed; and (c) simulated satellite peaks. (Reproduced with permission from *Macromolecules*, 2002, **35**, 3748. Copyright 2002 Am. Chem. Soc.)

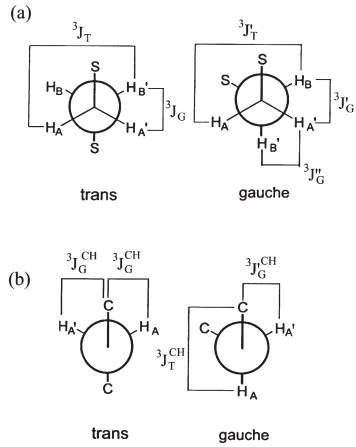

Fig. 17. Newman projections for: (a) C–C; and (b) C–S bonds of BMTE with definitions of vicinal coupling constants.

As shown in Fig. 16, the simulation based on AA′BB′X spin system satisfactorily reproduced the observed spectrum. For other spectra as well, the simulation gave good agreement with experiment.

To solve Eqs. (27)–(29), the vicinal coupling constants, ${}^3J_{\mathrm{T}}^{\mathrm{HH}}$, ${}^3J_{\mathrm{T}}'^{\mathrm{HH}}$, ${}^3J_{\mathrm{G}}^{\mathrm{HH}}$, ${}^3J_{\mathrm{G}}'^{\mathrm{HH}}$, and ${}^3J_{\mathrm{G}}''^{\mathrm{HH}}$, are required. We attempted to derive these coupling constants from a cyclic compound, 2-(1,1-dimethylethyl)-1,4-dithiane (DMEDT), which has the same S–CH_2–CH_2–S bond sequence as BMTE. The bulky *tert*-butyl substituent prevents the DMEDT ring from changing the conformation. Fig. 18a shows methine and methylene part of a ^{1}H NMR spectrum observed from DMEDT in $CDCl_3$ at 35 °C. In the region, signals of seven protons A–G (Fig. 19) overlap with one another. Using a commercially available computer program, gNMR,[93] we repeated simulations for the observed spectrum by reference to its homo- and heteronuclear COSY spectra,[94] but did not reach satisfactory agreement with experiment. Accordingly, we prepared DMEDT-d_4 and measured its ^{1}H NMR spectrum. Shown in Fig. 18c is a spectrum observed from DMEDT-d_4 in $CDCl_3$ at 35 °C. The spectrum includes signals from only three protons A–C. The simulation using gNMR for DMEDT-d_4 allowed us to reach good agreement with experiment. In Fig. 18d, the arrows indicate chemical shift positions of protons A–C. Using the chemical shifts and coupling constants determined for DMEDT-d_4, we reattempted to analyze the spectrum of DMEDT and successfully reproduced the observation as shown in Fig. 18b.

From the structural similarity between BMTE and DMEDT (cf. Figs. 17 and 19), we have assumed the following relations:

$$ {}^3J_{\mathrm{T}}^{\mathrm{HH}} = {}^3J_{\mathrm{T}}'^{\mathrm{HH}} = {}^3J_{\mathrm{DG}} \tag{30} $$

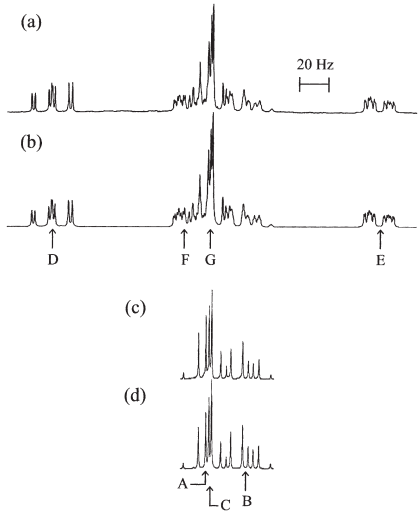

Fig. 18. (a) Observed, and (b) calculated ^{1}H NMR spectra of DMEDT in $CDCl_3$ at 35 °C, and (c) observed, and (d) calculated ^{1}H NMR spectra of DMEDT-d_4 in $CDCl_3$ at 35 °C. The capital letters (A–G) indicate chemical shift positions of the corresponding protons (see Fig. 19). (Reproduced with permission from *Macromolecules*, 2002, **35**, 3748. Copyright 2002 Am. Chem. Soc.)

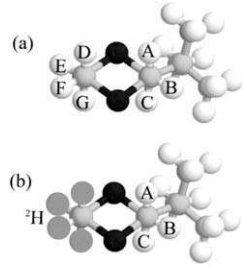

Fig. 19. (a) DMEDT, and (b) 2-(1,1-dimethylethyl)-1,4-dithiane-5,5,6,6-d_4 (DMEDT-d_4). The hydrogen atoms are designated as indicated.

$$^{3}J_{G} = \frac{^{3}J_{DE} + {}^{3}J_{EF} + {}^{3}J_{FG}}{3} \tag{31}$$

$$^{3}J'^{HH}_{G} = \frac{^{3}J_{DE} + {}^{3}J_{FG}}{2} \tag{32}$$

and

$$^{3}J''^{HH}_{G} = {}^{3}J_{EF} \tag{33}$$

In DMEDT, two sulfur atoms are in the gauche position and hence the $^3J_T^{HH}$ and $^3J_G^{HH}$ values cannot be obtained directly from DMEDT. Accordingly, the following assumptions have been adopted: $^3J_T^{HH} = {}^3J_T'^{HH}$ and $^3J_G^{HH} = (^3J_{DE} + {}^3J_{EF} + {}^3J_{FG})/3$.

Substitution of $^3J_{HH}$ and $^3J'_{HH}$ of BMTE (in $CDCl_3$ at 35 °C) and $^3J_T^{HH}$'s and $^3J_G^{HH}$'s of DMEDT (in $CDCl_3$ at 35 °C) into Eqs. (27) and (28) gives $p_t^{CC} = 0.76$ and $p_g^{CC} = 0.40$. However, the sum (1.16) of p_t^{CC} and p_g^{CC} slightly exceeds unity. This discrepancy comes from the fact that the number of equations is larger than that of variables. This problem has been discussed in the NMR analysis for DME and PEO.[44,95–97] In this study, the p_t^{CC} and p_g^{CC} values obtained as above were divided by their sum so as to satisfy Eq. (29). Finally, we obtained $p_t^{CC} = 0.66$ and $p_g^{CC} = 0.34$. The difference in p_η^{CC} between before and after normalization of Eq. (29) is at most 10%. The bond conformations thus evaluated are listed in Table 8.

6.2. ^{13}C NMR from model compounds of PES

Shown in Fig. 20 is a ^{13}C NMR spectrum observed from the methyl carbon of BMTE in C_6D_6 at 15 °C. The signal is largely split into four by direct coupling with methyl protons. In Fig. 20a, one of the quartet is enlarged. On the basis of AA′BB′X spin system, the spectrum was simulated by gNMR. In the calculated spectrum, even small peaks are exactly reproduced. The vicinal coupling constant between the methyl carbon and methylene protons, $^3J_{CH}$, was

Table 8. Bond conformations of BMTE

Medium	Temperature (°C)	p_t^{CC}	p_g^{CC}	p_t^{CS}	p_g^{CS}
NMR					
Benzene	15	0.69	0.31	0.12	0.88
	25	0.68	0.32	0.13	0.87
	35	0.68	0.32	0.14	0.86
	45	0.67	0.33	0.15	0.85
	55	0.67	0.33	0.17	0.83
Chloroform	15	0.67	0.33	0.20	0.80
	25	0.66	0.34	0.22	0.78
	35	0.66	0.34	0.22	0.78
	45	0.65	0.35	0.23	0.77
	55	0.65	0.35	0.26	0.74
Ab initio *MO*[a]					
Gas (B3LYP)	25	0.91	0.09	0.25	0.75
Gas (MP2)	25	0.83	0.17	0.21	0.79

[a]Evaluated from the conformer free energies shown in Table 9. (Reproduced with permission from *Macromolecules*, 2002, **35**, 3748. Copyright 2002 Am. Chem. Soc.)

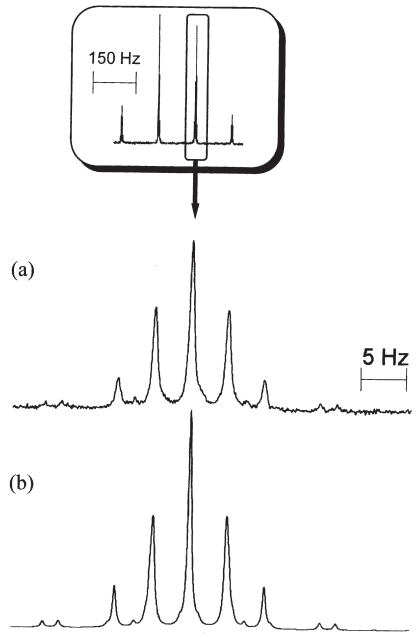

Fig. 20. (a) Observed, and (b) calculated ^{13}C NMR spectra of the methyl carbon of BMTE in C_6D_6 at 15 °C. (Reproduced with permission from *Macromolecules*, 2002, **35**, 3748. Copyright 2002 Am. Chem. Soc.)

evaluated to be 4.60 Hz. The observed $^3J_{CH}$ value, i.e., the average of $^3J_{CH_A}$ and $^3J_{CH_{A'}}$ (Fig. 17b), may be expressed as[44,45]

$$^3J_{CH} = {}^3J_G^{CH} p_t^{CS} + \frac{{}^3J_T^{CH} + {}^3J_G'^{CH}}{2} p_g^{CS} \tag{34}$$

where $^3J_G^{CH}$, $^3J_G'^{CH}$, and $^3J_T^{CH}$ are defined in Fig. 17b, and p_t^{CS} and p_g^{CS} are trans and gauche fractions of the C–S bond. From the definition, it follows that

$$p_t^{CS} + p_g^{CS} = 1 \tag{35}$$

Here, the $^3J_G^{CH}$, and $^3J_T^{CH}$ values obtained from MTT were employed: $^3J_T^{CH} = 7.13$ Hz and $^3J_G^{CH} = {}^3J_G'^{CH} = 2.62$ Hz (for C_6D_6 solution of BMTE); $^3J_T^{CH} = 7.12$ Hz and $^3J_G^{CH} = {}^3J_G'^{CH} = 2.58$ Hz (for the $CDCl_3$ solution). The p_t^{CS} and p_g^{CS} values thus derived are also listed in Table 8.

The trans fraction of the C–C bond, found within a range of 0.65–0.69, slightly decreases with temperature and dielectric constant (ε) of solvent. On the other hand, the C–S bond strongly prefers the gauche conformation; the p_g^{CS} values are 0.74–0.88.

Table 9. Free energies (ΔG_k) of conformers of BMTE and DME, evaluated by *ab initio* MO calculations

k	Conformation	M_k	BMTE			DME			
			Statistical weight[b]	ΔG_k[a] (kcal mol^{-1})		Statistical weight[b]	ΔG_k[a] (kcal mol^{-1})		
				B3LYP[c]	MP2[d]		B3LYP[c]	MP2[d]	CBS-Q[e]
1	t t t	1	1	0.00	0.00	1	0.00	0.00	0.00
2	t t $g^{\pm}$	4	ρ	−0.30	−0.46	ρ	1.34	1.28	1.25
3	t $g^{\pm}$ t	2	σ	1.26	0.90	σ	0.66	0.61	0.75
4	t $g^{\pm}$ $g^{\pm}$	4	$\rho\sigma$	1.26	0.49	$\rho\sigma$	1.47	1.31	1.40
5	t $g^{\pm}$ $g^{\mp}$	4	$\rho\sigma\omega$	1.33	0.77	$\rho\sigma\omega$	0.67	0.30	0.41
6	$g^{\pm}$ t $g^{\pm}$	2	ρ^2	−0.45	−0.81	ρ^2	2.90	2.73	2.55
7	$g^{\pm}$ t $g^{\mp}$	2	$\rho^2\kappa$	−0.68	−1.02	ρ^2	2.67	2.60	2.39
8	$g^{\pm}$ $g^{\pm}$ $g^{\pm}$	2	$\rho^2\sigma\chi$	1.21	0.57	$\rho^2\sigma\chi$	3.47	2.30	2.38
9	$g^{\pm}$ $g^{\pm}$ $g^{\mp}$	4	$\rho^2\sigma\omega$	1.46	0.63	$\rho^2\sigma\omega$	2.45	1.93	1.94
10	$g^{\pm}$ $g^{\mp}$ $g^{\pm}$	2	$\rho^2\sigma\omega^2$	2.00	1.02	$\rho^2\sigma\omega^2$	2.63	1.89	1.49

[a]Relative to the ΔG_k value of the all-trans conformation. At 25 °C and 1 atm.
[b]The statistical weights are illustrated in Fig. 15.
[c]At the B3LYP/6-311+G(3df, 2p)//B3LYP/6-31G(d) level.
[d]At the MP2/6-311+G(3df, 2p)//HF/6-31G(d) level.
[e]By the complete basis set (CBS-Q) method. (Reproduced with permission from *Macromolecules*, 2002, **35**, 3748. Copyright 2002 Am. Chem. Soc.)

6.3. MO calculations, statistical weight matrices, and conformational energies of model compound of PES

Free energies of ten conformers of BMTE, obtained from *ab initio* MO calculations, are listed in Table 9. From the table, the most stable conformations of BMTE are seen to be $g^{\pm}tg^{\mp}$, which have a free energy of $-1.02\,\mathrm{kcal\,mol^{-1}}$ at the MP2/6-311+G(3df, 2p)//HF/6-31G(d) level. Both BMTE and PES are known to adopt this conformation in the crystalline state.[83,84] The MP2 and B3LYP calculations indicate that the $g^{\pm}tg^{\mp}$ conformers have a free energy lower by ca. $0.2\,\mathrm{kcal\,mol^{-1}}$ than that of $g^{\pm}tg^{\pm}$. The $ttg^{\pm}$ and $tg^{\pm}t$ states have ΔG_k values of -0.46 and $0.90\,\mathrm{kcal\,mol^{-1}}$ (MP2), respectively; the C–S and C–C bonds prefer the gauche and trans states, respectively. These results are qualitatively consistent with the above NMR analysis.

In Table 8, bond conformations calculated from the free energies are compared with the NMR experiments. The p_t^{CC} values derived from the MO data are somewhat larger than those from NMR. Because the MO calculations represent gaseous BMTE ($\varepsilon = 1$), the difference comes partly from solvent effect. On the other hand, the p_t^{CS} and p_g^{CS} values obtained from the MO calculations are comparable to those from NMR.

Statistical weight matrices of BMTE were formulated as follows:

$$\mathbf{U}_2 = \begin{pmatrix} 1 & \rho & \rho \\ 0 & 0 & 0 \\ 0 & 0 & 0 \end{pmatrix} \tag{36}$$

$$\mathbf{U}_3 = \begin{pmatrix} 1 & \sigma & \sigma & 0 & 0 & 0 & 0 & 0 & 0 \\ 0 & 0 & 0 & 1 & \sigma & \sigma\omega & 0 & 0 & 0 \\ 0 & 0 & 0 & 0 & 0 & 0 & 1 & \sigma\omega & \sigma \end{pmatrix} \tag{37}$$

and

$$\mathbf{U}_4 = \begin{pmatrix} 1 & \rho & \rho & 0 & 0 & 0 & 0 & 0 & 0 \\ 0 & 0 & 0 & 1 & \rho & \rho\omega & 0 & 0 & 0 \\ 0 & 0 & 0 & 0 & 0 & 0 & 1 & \rho\omega & \rho \\ 1 & \rho & \rho\kappa & 0 & 0 & 0 & 0 & 0 & 0 \\ 0 & 0 & 0 & 1 & \rho\chi & \rho\omega & 0 & 0 & 0 \\ 0 & 0 & 0 & 0 & 0 & 0 & 1 & \rho\omega & \rho \\ 1 & \rho\kappa & \rho & 0 & 0 & 0 & 0 & 0 & 0 \\ 0 & 0 & 0 & 1 & \rho & \rho\omega & 0 & 0 & 0 \\ 0 & 0 & 0 & 0 & 0 & 0 & 1 & \rho\omega & \rho\chi \end{pmatrix} \tag{38}$$

In the (4, 3) and (7, 2) elements of $\mathbf{U}_4$, the third-order interaction, κ, is included. This weight represents the extra stabilization of the $g^{\pm}tg^{\mp}$ states, as stated above.

Conformational energies (E_ξ's) were determined from Eqs. (25) and (26). Then, the temperature T was set to 298.15 K. The E_ξ values thus determined are shown in Table 10. To evaluate the E_ξ values of BMTE and PES experimentally, the five energy parameters, E_ξ ($\xi = \rho$, σ, ω, χ, and κ), were adjusted so as to reproduce 20 bond conformations of BMTE in benzene or chloroform at 15, 25, 35, 45, and 55 °C. Here, $E_{\omega'}$ of PES, reflecting $CH_2 \cdots CH_2$ close contacts occurring in the $g^{\pm}g^{\mp}$ conformations for the C–S/S–C bond pairs (see Fig. 15d), has been assumed to be null. As the initial values of E_ξ's, those obtained from the MP2 free energies were used. The optimization was carried out by the maximum entropy method including the RIS scheme.[98–102] The conformational energies thus obtained are also listed in Table 10.

The MO calculations, representing the gaseous molecules ($\varepsilon = 1$), gave the E_ρ values of -0.24 (B3LYP) and -0.41 kcal mol^{-1} (MP2). The ^{13}C NMR analysis yielded -0.74 and -0.41 kcal mol^{-1} for the benzene ($\varepsilon = 2.28$) and chloroform ($\varepsilon = 4.81$) solutions, respectively. Our NBO analysis on BMTE[31] revealed that the gauche preference of the C–S bond comes from the $n_S \rightarrow \sigma^*_{C-C}$ delocalization, etc. For E_ρ, therefore, no explicit solvent dependence can be found. On the other hand, E_σ tends to decrease with increasing ε: 1.39 (gas, B3LYP), 0.89 (gas, MP2), 0.41 (benzene, NMR), and 0.31 kcal mol^{-1} (chloroform, NMR). This may be because dipole moments formed along the bisector of $\angle$CSC cancel out each other in the all-trans state. Polar solvents enhance the polarity of solute; the E_σ value tends to be reduced in polar solvents.

6.4. MO calculations on model compounds of PEO

Ab initio MO calculations by the CBS-Q[103] as well as B3LYP and MP2 methods were carried out for DME. Differences in ΔG_k's among the three methods were slight, and the most stable conformation was indicated to be all-trans. For gaseous DME, conformer fractions were estimated by electron diffraction (ED),[90] and ^{1}H and ^{13}C NMR vicinal coupling constants[45] were reported. From the latter data, we derived the p_t^{CC}, p_g^{CC}, p_t^{CO}, and p_g^{CO} values of DME at 125 °C. The conformer fractions (f's) and bond conformations, calculated from ΔG_k's, were compared with the experimental data. Consequently, it was found that the ΔG_k values at the MP2 level give the best agreement with the experiments: conformer fractions, $f_{ttt} = 0.20$ (0.13 ± 0.07), $f_{ttg} = 0.08$ (0.03 ± 0.07), $f_{tgt} = 0.13$ (0.23 ± 0.07), $f_{tgg} = 0.54$ (0.53 ± 0.07), and $f_{gtg} = 0.01$ (0.05), and $f_{ggg} = 0.04$ (0.03); bond conformations, $p_t^{CC} = 0.28$ (0.25), $p_g^{CC} = 0.72$ (0.75), $p_t^{CO} = 0.58$ (0.65), and $p_g^{CO} = 0.42$ (0.35), where the values in the parentheses represent the experimental data (f's were obtained from ED and p's from NMR).

Table 10. Conformational energies[a] and configuration-dependent properties[b] of PES (BMTE), DME, and PEO

	BMTE and PES				DME	PEO	
	MO[c]		NMR		MO[c]	NMR and dipole moment	Abe-Mark[e]
	B3LYP	MP2	Benzene	Chloroform	MP2	Nonpolar organic solvent[d]	
E_ρ	−0.24	−0.41	−0.74	−0.41	1.22	1.17	0.9
E_σ	1.39	0.89	0.41	0.31	0.32	−0.25	−0.5
E_ω	0.40	0.45	0.40	0.53	−1.12	−0.79	0.4
$E_{\omega'}$	(0.00)[f]	(0.00)[f]	(0.00)[f]	(0.00)[f]	∞	∞	∞
E_χ	0.30	0.50	0.46	0.59	−0.45	(0.00)[g]	0.0
E_κ	−0.20	−0.19	−0.18	−0.22	–	–	–
$\langle r^2\rangle_0/nl^2$ [h]	3.5	3.1	2.5	2.9	4.5	4.1	5.1
$10^3\, \mathrm{d}\ln\langle r^2\rangle_0/\mathrm{d}T^{\mathrm{h}}$ (K^{-1})	−0.75	−0.89	−0.97	−0.83	−0.17	0.23	0.36
$\langle \mu^2\rangle/nm^2$ [i]	0.13	0.22	0.38	0.44	0.34	0.41	0.49
$10^3\, \mathrm{d}\ln\langle \mu^2\rangle/\mathrm{d}T^{\mathrm{i}}$ (K^{-1})	8.7	6.4	3.8	3.3	2.2	1.9	2.9

[a]In kcal mol^{-1}.

[b]Calculated for the 200 mers.

[c]Based on *ab initio* MO calculations for BMTE or DME at the B3LYP/6-311+G(3df, 2p)//B3LYP/6-31G(d) (B3LYP) and MP2/6-311+G(3df, 2p)//HF/6-31G(d) (MP2) levels.

[d]The conformational energies were determined from NMR vicinal coupling constants of the 1,4-dioxane solution and the dipole moment ratio of the benzene solution. See text.

[e]Reference 11.

[f]On the basis of the MO calculations at the B3LYP/6-311+G(3df, 2p)//B3LYP/6-31G(d) level, the $E_{\omega'}$ value was assumed to be null.

[g]The E_χ value was set to zero.

[h]At 25 °C for PES and 40 °C for PEO.

[i]At 25 °C. (Reproduced with permission from *Macromolecules*, 2002, **35**, 3748. Copyright 2002 Am. Chem. Soc.)

From the MP2 free energies, therefore, the conformational energies were evaluated according to Eqs. (25) and (26). For DME and PEO, the energy parameter, E_κ, which was defined as the energy difference between $g^{\pm}tg^{\mp}$ and $g^{\pm}tg^{\pm}$ states, has not been considered. In Table 10, the conformational energies determined for gaseous DME at the MP2/6-311+G(3df, 2p) level are shown. The E_ρ value of 1.22 kcal mol^{-1} indicates a strong trans preference of the C–O bond. The negative E_ω (-1.12 kcal mol^{-1}) value results from the intramolecular (C–H)$\cdots$O attraction occurring in the $tg^{\pm}g^{\mp}$ conformations, yielding a large p_g^{CC} value of 0.72, although E_σ is positive (0.32 kcal mol^{-1}).

6.5. Configuration-dependent properties of PES and PEO

Bond dipole moments m_{C-X}'s were determined from the MO calculations for BMTE and DME; the m_{C-X} values were optimized so as to minimize the difference between μ^{MO}'s and μ^{BOND}'s, where μ_k^{MO} is the dipole moment of conformer k, obtained from the MO calculations, and μ_k^{BOND} is that calculated as the sum of bond dipole moment vectors. The m_{C-C} value has been assumed to be null. In the optimization for m_{C-X}'s, free energies, dipole moments, and geometrical parameters obtained by the individual MO methods were used. As for free energies of DME, however, only those at the MP2 level were adopted, because they were shown to be the most reliable. The m_{C-S} value was optimized as 1.22 ± 0.02 (B3LYP) or 1.35 ± 0.01 D (MP2), and the m_{C-O} value as 1.18 ± 0.04 (B3LYP), 1.29 ± 0.04 (MP2), or 1.46 ± 0.07 D (CBS-Q). The B3LYP parameters gave a m_{C-S} value close to that (1.21 D) so far used for polysulfides[7,21,22,92] and a m_{C-O} value in agreement with that (1.17–1.19 D) optimized for PPO and poly(tetramethylene oxide).[27] For PMS, we derived a m_{C-S} value of 1.23 ± 0.08 D from μ^{MO}'s at the B3LYP/6-311+G(2d, p)// B3LYP/6-31G(d) level.[30] The MP2 and CBS-Q calculations tend to overestimate the bond dipole moments. Therefore, we have employed m_{C-S} of 1.22 D for PES and m_{C-O} of 1.18 D for PEO.

Statistical weight matrices for bonds a, b, and c in the repeating unit of PES may be expressed as

$$\mathbf{U}_a = \begin{pmatrix} 1 & \rho & \rho & 0 & 0 & 0 & 0 & 0 & 0 \\ 0 & 0 & 0 & 1 & \rho & \rho\omega' & 0 & 0 & 0 \\ 0 & 0 & 0 & 0 & 0 & 0 & 1 & \rho\omega' & \rho \\ 1 & \rho & \rho & 0 & 0 & 0 & 0 & 0 & 0 \\ 0 & 0 & 0 & 1 & \rho & \rho\omega' & 0 & 0 & 0 \\ 0 & 0 & 0 & 0 & 0 & 0 & 1 & \rho\omega' & \rho \\ 1 & \rho & \rho & 0 & 0 & 0 & 0 & 0 & 0 \\ 0 & 0 & 0 & 1 & \rho & \rho\omega' & 0 & 0 & 0 \\ 0 & 0 & 0 & 0 & 0 & 0 & 1 & \rho\omega' & \rho \end{pmatrix} \tag{39}$$

$$\mathbf{U}_b = \begin{pmatrix} 1 & \sigma & \sigma & 0 & 0 & 0 & 0 & 0 & 0 \\ 0 & 0 & 0 & 1 & \sigma & \sigma\omega & 0 & 0 & 0 \\ 0 & 0 & 0 & 0 & 0 & 0 & 1 & \sigma\omega & \sigma \\ 1 & \sigma & \sigma & 0 & 0 & 0 & 0 & 0 & 0 \\ 0 & 0 & 0 & 1 & \sigma & \sigma\omega & 0 & 0 & 0 \\ 0 & 0 & 0 & 0 & 0 & 0 & 1 & \sigma\omega & \sigma \\ 1 & \sigma & \sigma & 0 & 0 & 0 & 0 & 0 & 0 \\ 0 & 0 & 0 & 1 & \sigma & \sigma\omega & 0 & 0 & 0 \\ 0 & 0 & 0 & 0 & 0 & 0 & 1 & \sigma\omega & \sigma \end{pmatrix} \tag{40}$$

and

$$\mathbf{U}_c = \mathbf{U}_4 \tag{41}$$

As described above, ω' has been assumed to be unity for PES (i.e., $E_{\omega'} = 0$). However, because these statistical weight matrices are also used for PEO, ω' is included in $\mathbf{U}_a$. The $\langle r^2\rangle_0/nl^2$ and $\langle\mu^2\rangle/nm^2$ values of unperturbed PES were calculated by the RIS scheme using the statistical weight matrices defined as above. Geometrical parameters at the B3LYP/6-31G(d) level were used in the calculations: bond lengths, $l_{C-S} = 1.839$ Å and $l_{C-C} = 1.528$ Å; bond angles, $\angle CSC = 99.45°$ and $\angle CCS = 109.39°$; dihedral angles, $\phi^{C-S}_{trans} = \phi^{C-C}_{trans} = 0.00°$, $\phi^{C-S}_{gauche^{\pm}} = \pm 104.24°$, and $\phi^{C-C}_{gauche^{\pm}} = \pm 115.04°$. In Table 10, the $\langle r^2\rangle_0/nl^2$ and $\langle\mu^2\rangle/nm^2$ values and their temperature coefficients of PES (degree of polymerization, $x = 200$) at 25 °C are listed for each energy set.

For PEO, a wide range of $\langle r^2\rangle_0/nl^2$ values (4.1–9.7) and a variety of theta conditions have been determined experimentally.[12,104–111] The temperature coefficient, $10^3\, d\ln\langle r^2\rangle_0/dT$, ranges from positive and negative values: 0.23 ± 0.2 (amorphous network at 60 °C),[12] 0.2 ± 0.2 (extrapolated from benzene solution at 35 °C),[112] -1.5 ± 0.5 (1.24 M KOH at 25 °C),[108] and $-0.3\,K^{-1}$ (melt at 130 °C).[110] On the other hand, experimental dipole moment ratios ($\langle\mu^2\rangle/nm^2$) obtained from the benzene solutions at ambient temperature are found within a narrow range of 0.40–0.42.[113–115] Here, the $\langle\mu^2\rangle/nm^2$ values are calibrated with the m_{C-O} value (1.18 D) determined as above. The temperature coefficient, $10^3\, d\ln\langle\mu^2\rangle/dT$, was estimated as $2.6\,K^{-1}$.[114]

Statistical weight matrices of DME and PEO may be obtained by minor modifications of those of BMTE and PES. The $\mathbf{U}_2$ and $\mathbf{U}_3$ matrices of DME and PEO are assumed to have the same formats as those of BMTE, but $\mathbf{U}_4$ and $\mathbf{U}_c$ of DME and PEO do not include the statistical weight κ. The short C–O bond does not allow $g^{\pm}g^{\mp}g^{\pm}$ conformational sequences to exist; therefore, the (6, 8) and (8, 6) elements of $\mathbf{U}_a$, $\mathbf{U}_b$, and $\mathbf{U}_c$ (Eqs. (39)–(41)) of PES must be replaced by zero.

Conformational energies of PEO were determined by a simulation for C–C and C–O bond conformations obtained from ^1H and ^{13}C NMR vicinal coupling constants of PEO in 1,4-dioxane ($\varepsilon = 2.10$) at 40 °C[44] and the dipole

moment ratio (0.41) of PEO in benzene ($\varepsilon = 2.28$).[113–115] This is partly because the NMR coupling constants and dipole moment ratio are free from the excluded volume effect, partly because dielectric constants of these two solvents are close to each other (the results were expected to be little subject to solvent effects). Then, as the initial values, the conformational energies obtained from the MP2 calculations were used, except for E_χ which was set to zero. For comparison, geometrical parameters offered in the previous study[11] were used: bond lengths, $l_{C-O} = 1.43$ Å and $l_{C-C} = 1.53$ Å; bond angles, $\angle COC = \angle CCO = 111.5°$; dihedral angles, $\phi^{C-O}_{trans} = \phi^{C-C}_{trans} = 0.0°$ and $\phi^{C-O}_{gauche^{\pm}} = \phi^{C-C}_{gauche^{\pm}} = \pm 110°$. The conformational energies thus optimized, designated as 'nonpolar organic solvent', are shown in Table 10. The p_t^{CC}, p_g^{CC}, p_t^{CO}, and p_g^{CO} values were obtained as 0.19, 0.81, 0.71, and 0.29, respectively, being in complete agreement with the experimental values. The $\langle r^2\rangle_0/nl^2$, $10^3\,\mathrm{d}\ln\langle r^2\rangle_0/\mathrm{d}T$, and $10^3\,\mathrm{d}\ln\langle\mu^2\rangle/\mathrm{d}T$ values (Table 10) were also calculated from the energy parameters. The $\langle r^2\rangle_0/nl^2$ (4.1) and $10^3\,\mathrm{d}\ln\langle r^2\rangle_0/\mathrm{d}T$ ($0.23\,\mathrm{K}^{-1}$) values agree with those (4.1 and 0.2–$0.23\,\mathrm{K}^{-1}$) estimated experimentally,[12,112] and the $10^3\,\mathrm{d}\ln\langle\mu^2\rangle/\mathrm{d}T$ value ($1.9\,\mathrm{K}^{-1}$) is comparable to the experimental one ($2.6\,\mathrm{K}^{-1}$).[114] The configuration-dependent properties calculated from the energy set of Abe and Mark[11] and the 9×9 statistical weight matrices defined here are also listed in Table 10. The calculated characteristic ratio (5.1) agrees well with that (5.2 ± 0.1) determined by light scattering for a 0.45 M K_2SO_4 aqueous solution at 34.5 °C.[111] On the other hand, the $\langle r^2\rangle_0/nl^2$ value of PES was calculated to be 2.5–2.9 from the experimental energy parameters, indicating the flexibility of PES as compared with PEO and PMS ($\langle r^2\rangle_0/nl^2 = 7.6$).

To investigate the chain length dependence of E_σ of PEO, free energy differences between trans and gauche states of the central C–C bonds of its monomer (DME), trimer, and pentamer were evaluated from MO calculations at the B3LYP/6-311+G(3df, 2p)//B3LYP/6-31G(d) level. The MP2 calculation is too expensive to be applied to the trimer and pentamer. Therefore, the B3LYP method was used instead. The frequency calculations, required for the thermal corrections, were also carried out at the B3LYP/6-31G(d) level. The free energy differences of the monomer, trimer, and pentamer were evaluated to be 0.76, 0.15, and 0.18 kcal mol^{-1}, respectively. The terminal bonds seem to have a larger E_σ than the inner bonds. As described in the previous section, this property was also found for PMO.

From Table 10, it can be seen that E_σ decreases and E_ω increases in the order 'MP2' → 'nonpolar organic solvent' → 'Abe–Mark'. By the MO calculations, the isolated (gaseous) PEO chain was suggested to have an E_σ value smaller than 0.2 kcal mol^{-1}. Polar solvents such as water must further enhance the gauche stability of the C–C bond, because of the resultant dipole moment in the gauche form and attractive polymer–solvent interactions. When the C–C and C–O bonds are, respectively, in the gauche and trans conformations, the O–C–C–O portion acts as an efficient electron donor, as found for crown

ethers. If the Abe–Mark parameters approximately represent PEO in the theta solvent, 0.45 M K_2SO_4 at 34.5 °C,[111] the ions are suggested to reduce the gauche stability of the C–C bond. From NMR vicinal coupling constants of PEO in pure water, the E_σ value was estimated as $-1.2\,\mathrm{kcal\,mol^{-1}}$,[44] being much smaller than $-0.5\,\mathrm{kcal\,mol^{-1}}$ (Abe–Mark).[11] This is probably because the ions compete for the oxygen atom of PEO with water.[116] In the gas phase, the intramolecular (C–H)···O attraction is not disturbed by solvent, and hence the E_ω values is as small as $-1.12\,\mathrm{kcal\,mol^{-1}}$ (for DME by MP2). Polar solvents (and ions), being electron acceptors stronger than the methylene protons of PEO, can capture the oxygen atom of PEO; the E_ω value appears to increase from negative to positive in the order 'MP2' (gas phase) → 'nonpolar organic solvent' → 'Abe–Mark' (0.45 M K_2SO_4).

6.6. (C–H)···O and C–H···S interactions

As has been shown above, the PEO chain adjusts itself to the environment by varying the conformational energies. In particular, E_σ and E_ω are sensitive to solvent. Consequently, PEO is soluble in a variety of solvents including water. On the other hand, the skeletal C–C bond of PPO has a moderate trans preference; the first-order interaction energies, E_α and E_β, for the g^+ and g^- states of isotactic (*R*)-PPO in benzene are 0.5 and $0.8\,\mathrm{kcal\,mol^{-1}}$, respectively (Table 3). In addition, the methyl side chain prevents solvent molecules from approaching the lone pair of PPO. Therefore, PPO is insoluble in water. Conformational energies, E_{ω_1} and E_{ω_2}, of PPO, representing the intramolecular (C–H)···O interactions are kept negative even in comparatively polar solvents such as DMSO ($\varepsilon = 45.0$). The methyl group differentiates PPO from PEO in physicochemical properties.

In $tg^{\pm}g^{\mp}$ conformations of BMTE, no particular close contact between the methyl proton and sulfur atom was found. The distance between sulfur and the nearest methyl proton was evaluated as 2.96 Å from the MO calculations at the HF/6-31G(d) level, being almost equal to the sum (3.0 Å) of van der Waals radii of proton and sulfur. The conformational energy E_ω was determined by MO calculations and NMR experiments to be 0.40–0.53 $\mathrm{kcal\,mol^{-1}}$, and hence the C–H···S interaction is rather repulsive.

7. POLY(PROPYLENE SULFIDE) (PPS)

In the crystalline state, PPS adopts all-trans conformation.[117] Its melting point (53 °C) is much lower than those of PMS (245 °C) and PES (216 °C). In contrast to PMS and PES, PPS is soluble in a number of solvents.[118] Therefore, its configuration-dependent properties such as characteristic ratio[119] and dipole moment ratio[120,121] have been reported. Although PPS has two stereochemical

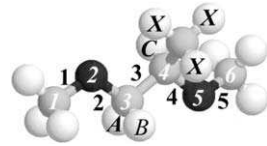

Fig. 21. BMTP, a model compound of PPS. The atoms and bonds are designated as indicated.

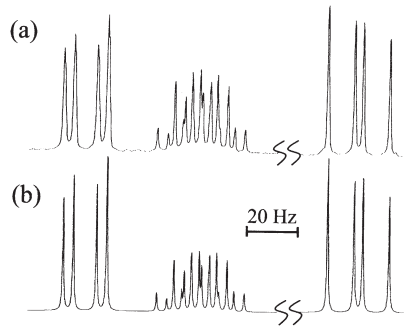

Fig. 22. Methine and methylene part of: (a) observed; and (b) calculated ^{1}H NMR spectra of BMTP in cyclohexane-d_{12} at 26 °C. The ^{1}H NMR parameters obtained from a simulation are as follows: chemical shifts, $\nu_A - \nu_B = 198.39$ Hz, $\nu_A - \nu_C = 45.04$ Hz, and $\nu_A - \nu_X = 734.85$ Hz; coupling constants, $^{2}J_{AB} = -13.22$ Hz, $^{3}J_{AC} = 4.06$ Hz, $^{3}J_{BC} = 9.99$ Hz, and $^{3}J_{CX} = 6.83$ Hz.

arrangements, i.e., (*R*)- and (*S*)-optical isomers, (*R*)-forms are exclusively used as models for isotactic PPS and its model compounds in this section.

In this study, we measured ^{1}H and ^{13}C NMR of a monomeric model compound, 1,2-bis(methylthio)propane (BMTP, $CH_3SCH_2C^*H(CH_3)SCH_3$, Fig. 21) and analyzed vicinal ^{1}H–^{1}H and ^{13}C–^{1}H coupling constants to evaluate bond conformations of the S–C, C–C*, and C*–S bonds individually. *Ab initio* MO calculations on BMTP were carried out to evaluate free energies, atomic charges, and dipole moments of all the possible conformers. The conformational energies of PPS were determined from experimental observations of bond conformations of BMTP, the characteristic ratio of atactic PPS in the Θ state, and dipole moment ratios of atactic and isotactic PPS.

7.1. ^{1}H NMR from model compound

Shown in Fig. 22 are methine and methylene parts of a ^{1}H NMR spectrum observed from BMTP in C_6D_{12} at 26 °C. In previous studies,[122,123] ^{1}H NMR chemical shifts of isotactic PPS were assigned to the methine and methylene protons by comparison with those of poly(propene-2-d_1 sulfide) $[CH_2C^*D(CH_3)S]_x$. Following the assignment, we simulated the ^{1}H NMR

spectra observed from BMTP. The calculated spectrum is also shown in Fig. 22. Vicinal coupling constants, $^3J_{AC}$ and $^3J_{BC}$, were, respectively, obtained as 4.06 and 9.99 Hz (in C_6D_{12} at 26 °C). Similarly, all ^{1}H NMR spectra observed from BMTP were satisfactorily reproduced by the simulations. In the same manner as employed for DMP, bond conformations of the C–C* bond of BMTP were determined from the vicinal ^{1}H–^{1}H coupling constants. Then, the $^3J_T^{HH}$ and $^3J_G^{HH}$ values obtained from DMEDT were used. The bond conformations thus derived are listed in Table 11.

7.2. ^{13}C NMR from model compound

Carbon-13 NMR signals of two methoxy carbons (designated as carbons 1 and 6) of BMTP are largely split into four by direct couplings with the methoxy protons. The signal of carbon 1 is further divided into four by protons A and B, and that of carbon 6 into two by proton C. Fig. 23 shows one of the four quartets from carbon 1 and one of the four doublets from carbon 6 of BMTP in C_6D_{12} at 26 °C. The peak spacings directly give vicinal coupling constants, $^3J_{CH_A}$, $^3J_{CH_B}$, and $^3J_{CH_C}$. The two ^3J values of carbon 1 were assigned to $^3J_{CH_A}$ and $^3J_{CH_B}$ so as to be consistent with MO calculations to be shown later; $p_{g^-}^{SC}$ would be larger than $p_{g^+}^{SC}$, where $p_{g^+}^{SC}$ and $p_{g^-}^{SC}$ are gauche$^+$ and gauche$^-$ fractions of bond 2.

The observed $^3J_{CH_A}$ and $^3J_{CH_B}$ values may be expressed as

$$^3J_{CH_A} = {}^3J_G^{CH} + ({}^3J_T^{CH} - {}^3J_G^{CH})p_{g^+}^{SC} \tag{42}$$

and

$$^3J_{CH_B} = {}^3J_G^{CH} + ({}^3J_T^{CH} - {}^3J_G^{CH})p_{g^-}^{SC} \tag{43}$$

where $^3J_G^{CH}$ and $^3J_T^{CH}$ are, respectively, vicinal coupling constants between carbon and proton in trans and gauche positions, being taken from MTT: $^3J_T^{CH} = 7.13$ Hz and $^3J_G^{CH} = 2.62$ Hz (for the C_6D_{12} and C_6D_6 solutions); $^3J_T^{CH} = 6.92$ Hz and $^3J_G^{CH} = 2.71$ Hz (for the DMSO solution). From the definition of p^{CS}'s, we have

$$p_t^{SC} + p_{g^+}^{SC} + p_{g^-}^{SC} = 1 \tag{44}$$

These bond conformations may be determined from observed $^3J_{CH_A}$ and $^3J_{CH_B}$ values. The observed $^3J_{CH_C}$ value is expressed as

$$^3J_{CH_C} = {}^3J_G^{CH} + ({}^3J_T^{CH} - {}^3J_G^{CH})p_{g^+}^{C^*S} \tag{45}$$

where $p_{g^+}^{C^*S}$ is the gauche$^+$ fraction of bond 4. From Eq. (45), the $p_{g^+}^{C^*S}$ value can be derived, whereas trans and gauche$^-$ fractions ($p_t^{C^*S}$ and $p_{g^-}^{C^*S}$) of bond 4

Table 11. Bond conformations of BMTP and isotactic PPS

Medium	Temperature (°C)	p_t^{CS}	$p_{g^+}^{CS}$	$p_{g^-}^{CS}$	$p_t^{CC^*}$	$p_{g^+}^{CC^*}$	$p_{g^-}^{CC^*}$	$p_t^{C^*S}$	$p_{g^+}^{C^*S}$	$p_{g^-}^{C^*S}$
BMTP										
						NMR				
Gas	150				0.83 ± 0.05	0.10 ± 0.05	0.07 ± 0.05			
Cyclohexane	26.0	0.04	0.34	0.62	0.83	0.13	0.04		0.22	
Benzene	26.0	0.10	0.32	0.58	0.78	0.17	0.05		0.20	
DMSO	25.0	0.12	0.31	0.57	0.72	0.20	0.08		0.14	
						Ab initio MO calculations				
Gas (MP2[a])	150[b]	0.29	0.22	0.49	0.70	0.18	0.12	0.29	0.21	0.50
Gas (B3LYP[c])	150[b]	0.32	0.14	0.54	0.84	0.11	0.05	0.30	0.15	0.55
						RIS simulation				
Set I	26.0	0.12	0.39	0.49	0.77	0.18	0.05	0.52	0.20	0.28
Set II	26.0	0.20	0.36	0.44	0.77	0.18	0.05	0.52	0.22	0.26
Isotactic PPS										
						RIS simulation				
Set I	26.0	0.17	0.36	0.47	0.77	0.19	0.04	0.59	0.12	0.29
Set II	26.0	0.29	0.31	0.40	0.76	0.20	0.04	0.59	0.15	0.26

[a]At the MP2/6-311+G(3df, 2p)//HF/6-31G(d) level.
[b]Calculated from conformer free energies of BMTP at 150 °C and 7.1 atm (estimated as described in Section 2.1).
[c]At the B3LYP/6-311+G(3df, 2p)//HF/6-31G(d) level.

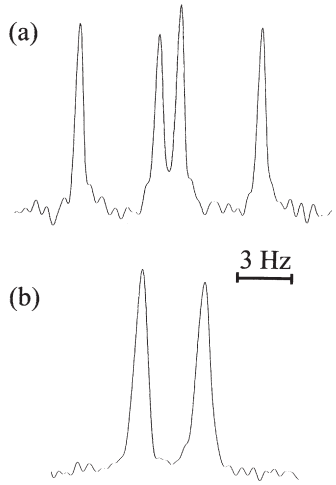

Fig. 23. ^{13}C NMR spectra observed from methoxy carbons: (a) 1; and (b) 6 of BMTP in cyclohexane-d_{12} at 26 °C.

remain indeterminate. The p_{t}^{SC}, $p_{g^+}^{SC}$, $p_{g^-}^{SC}$, and $p_{g^+}^{C^*S}$ values thus evaluated are listed in Table 11.

7.3. MO calculations on model compound

Conformer free energies of BMTP, calculated from *ab initio* MO calculations, are listed in Table 12. The bond conformations calculated from the ΔG_k values are also shown in Table 11.

On the analogy of statistical weight matrices of DMP, those of BMTP were formulated according to the 9×9 matrix scheme.[47,48] The statistical weights are designated so as to correspond to those of DMP and PPO. The geometrical optimization by the MO calculations gave only 19 conformers for DMP (Table 2) but as many as 25 conformers for BMTP (Table 12). This may be due to the difference between the C–O and C–S bond lengths. Thus, two statistical weights (τ and ζ) representing second-order interactions were introduced to $\mathbf{U}_i$'s of BMTP and PPS (see Fig. 24). For DMP and PPO, on the other hand, these parameters were assumed to be zero; that is, $E_\tau = E_\zeta = \infty$. Visual inspection of the molecular model and the above consideration led to the following statistical weight matrices for BMTP:

$$\mathbf{U}_2 = \begin{pmatrix} 1 & \sigma & \sigma \\ 0 & 0 & 0 \\ 0 & 0 & 0 \end{pmatrix} \tag{46}$$

Table 12. Free energies (ΔG_k) of conformers of BMTP, evaluated by *ab initio* MO calculations

k	Conformation	Statistical weight[b]	ΔG_k[a] (kcal mol^{-1})	
			MP2[c]	B3LYP[d]
1	t t t	1	0.00	0.00
2	t t g^+	γ	0.42	0.60
3	t t g^-	δ	−0.46	−0.61
4	t g^+ t	α	0.81	1.17
5	t g^+ g^+	$\alpha\gamma$	0.89	1.76
6	t g^+ g^-	$\alpha\delta\omega_1$	0.99	1.44
7	t g^- t	β	1.20	1.71
8	t g^- g^+	$\beta\gamma\omega_2$	2.15	2.75
9	t g^- g^-	$\beta\delta$	0.72	1.65
10	g^+ t t	$\sigma\tau$	0.63	0.82
11	g^+ t g^+	$\sigma\gamma\tau$	1.05	1.49
12	g^+ t g^-	$\sigma\delta\tau$	0.14	0.42
13	g^+ g^+ t	$\sigma\alpha$	0.83	1.28
14	g^+ g^+ g^+	$\sigma\alpha\gamma\chi$	0.99	2.34
15	g^+ g^+ g^-	$\sigma\alpha\delta\omega_1$	0.78	1.46
16	g^+ g^- t	$\sigma\beta\omega_2$	0.81	1.70
17	g^+ g^- g^-	$\sigma\beta\delta\omega_2$	0.72	1.73
18	g^- t t	σ	−0.55	−0.54
19	g^- t g^+	$\sigma\gamma$	−0.25	0.11
20	g^- t g^-	$\sigma\delta$	−0.96	−0.84
21	g^- g^+ t	$\sigma\alpha\omega_1$	0.71	1.16
22	g^- g^+ g^+	$\sigma\alpha\gamma\omega_1$	1.33	2.02
23	g^- g^- t	$\sigma\beta\tau$	1.91	2.28
24	g^- g^- g^+	$\sigma\beta\gamma\tau\omega_2$	2.75	3.59
25	g^- g^- g^-	$\sigma\beta\delta\tau$	1.39	2.26

[a]Relative to the ΔG_k value of the all-trans conformation. At 25 °C and 1 atm.

[b]The statistical weights correspond to those of DMP and isotactic PPO (see Figs. 2 and 5).

[c]At the MP2/6-311+G(3df, 2p)//HF/6-31G(d) level.

[d]At the B3LYP/6-311+G(3df, 2p)//B3LYP/6-31G(d) level.

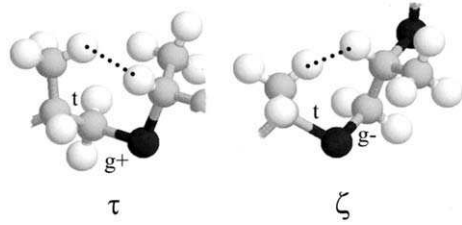

Fig. 24. Second-order intramolecular interactions (κ and ζ) defined for BMTP and PPS.

$$\mathbf{U}_3 = \begin{pmatrix} 1 & \alpha & \beta & 0 & 0 & 0 & 0 & 0 & 0 \\ 0 & 0 & 0 & \tau & \alpha & \beta\omega_2 & 0 & 0 & 0 \\ 0 & 0 & 0 & 0 & 0 & 0 & 1 & \alpha\omega_1 & \beta\tau \end{pmatrix} \tag{47}$$

and

$$\mathbf{U}_4 = \begin{pmatrix} 1 & \gamma & \delta & 0 & 0 & 0 & 0 & 0 & 0 \\ 0 & 0 & 0 & 1 & \gamma & \delta\omega_1 & 0 & 0 & 0 \\ 0 & 0 & 0 & 0 & 0 & 0 & 1 & \gamma\omega_2 & \delta \\ 1 & \gamma & \delta & 0 & 0 & 0 & 0 & 0 & 0 \\ 0 & 0 & 0 & 1 & \gamma\chi & \delta\omega_1 & 0 & 0 & 0 \\ 0 & 0 & 0 & 0 & 0 & 0 & 1 & 0 & \delta \\ 1 & \gamma & \delta & 0 & 0 & 0 & 0 & 0 & 0 \\ 0 & 0 & 0 & 1 & \gamma & 0 & 0 & 0 & 0 \\ 0 & 0 & 0 & 0 & 0 & 0 & 1 & \gamma\omega_2 & \delta \end{pmatrix} \tag{48}$$

On the basis of the above statistical weights, the E_ξ values were determined by minimizing the standard deviation between ΔG_k's and sums of E_ξ's of the conformers (Eqs. (25) and (26)). The temperature T was set to 298.15 K. The conformational energies were determined as shown in Table 13.

7.4. Configuration-dependent properties of PPS

Statistical weight matrices for bonds a (S–C), b (C–C*), and c (C*–S) of the repeating unit of isotactic (*R*)-PPS and those of four linkage types ($R \rightarrow R$, $R \rightarrow S$, $S \rightarrow S$, and $S \rightarrow R$) of atactic PPS were formulated from inspection of the molecular models and $\mathbf{U}_i$'s of PPO (see Appendix A of Ref. 32). The atactic chain was synthesized and its configuration-dependent properties were calculated according to the following procedures: (1) a number is sampled out of a set in which numbers are uniformly distributed between zero and unity. (2) If the number is smaller than or equal to a given value of (*R*)-monomer fraction in a chain, P_R, an (*R*)-unit is added to the propagating end of the polymeric chain. Otherwise, an (*S*)-unit is added. (3) Statistical weight matrices corresponding to the linkage type formed newly ($R \rightarrow R$, $R \rightarrow S$, $S \rightarrow S$, or $S \rightarrow R$) are chosen. The procedures 1–3 are repeated up to a given degree of polymerization. (4) From a series of statistical weight matrices thus arranged, the characteristic ratio $\langle r^2 \rangle_0 / nl^2$ and dipole moment ratio $\langle \mu^2 \rangle / nm^2$ are calculated.

The bond dipole moment $m_{\text{C–S}}$ was estimated from the MO calculations for BMTP; the $m_{\text{C–S}}$ value was optimized so as to minimize the difference between μ_k^{MO}'s and μ_k^{BOND}'s. Then, we employed ΔG_k's at the MP2/6-311+G(3df, 2p) level and μ_k^{MO}'s at the B3LYP/6-311+G(3df, 2p) level. It was assumed that $m_{C\text{–}S} = m_{C^*\text{–}S}$ and $m_{\text{C–C}^*} = 0$. As a result, the $m_{\text{C–S}}$ value was obtained as 1.21 D, being in agreement with that used by Riande *et al.*[7,120,121] and Abe[21,22]

Table 13. Conformational energies[a] of BMTP and PPS

	MO calc		Exptl	
	MP2[b]	B3LYP[c]	Set I[d]	Set II[e]
First-order interaction				
E_α	0.93	1.38	0.55	0.49
E_β	1.19	1.85	1.13	1.18
E_γ	0.30	0.55	0.49	0.43
E_δ	−0.43	−0.48	0.25	0.27
E_σ	−0.52	−0.43	−0.99	−0.60
Second-order interaction				
E_{ω_1}	0.55	0.51	0.64	0.89
E_{ω_2}	0.35	0.51	1.16	0.99
E_τ	1.14	1.30	0.26	0.28
E_ζ[f]			0.35	0.35
Third-order interaction				
E_χ	0.29	0.84	0.38	0.42

[a]In kcal mol^{-1}.

[b]At the MP2/6-311+G(3df, 2p)//HF/6-31G(d) level.

[c]At the B3LYP/6-311+G(3df, 2p)//B3LYP/6-31G(d) level.

[d]Determined from bond conformations of BMTP in benzene at 10, 26, 43, 59, and 75 °C and dipole moment ratios of isotactic and atactic PPS in benzene at 25 °C.

[e]Determined from the bond conformations, the dipole moment ratios, and the characteristic ratio of atactic PPS in the Θ solvent (*n*-hexane (31%) and toluene).

[f]To evaluate the E_ζ value by MO calculations, the geometrical optimizations at the HF/6-31G(d) and B3LYP/6-31G(d) levels were carried out for the tttg$^-$tt conformation of an *RR* dimeric model compound, CH_3S–CH_2–C*H(CH_3)–S–CH_2–C*H(CH_3)–SCH_3, because the E_ζ value may be estimated from the energy difference ($=E_\sigma+E_\zeta$) between the tttg$^-$tt and tttttt states. However, the local minimum was not found. On the other hand, the MM2 calculations gave the potential minimum. In the RIS simulations, the E_ζ value was initially set to zero.

for polysulfides and close to those optimized by us for PMS (1.23 D)[30] and PES (1.22 D) (in Section 6.5).

Conformational energies of PPS were determined by RIS simulations for experimental observations of the following configuration-dependent properties: simulation I, bond conformations of BMTP in benzene at 10, 26, 43, 59, and 75 °C and dipole moment ratios of isotactic and atactic PPS; simulation II, characteristic ratio of atactic PPS in the Θ solvent (*n*-heptane (31%) and toluene)[119] as well as the experimental data used in simulation I. The ten energy parameters E_ξ's ($\xi=\alpha$, β, γ, δ, σ, ω_1, ω_2, τ, ζ, and χ) were optimized by the simplex method[64] for 37 (simulation I) or 38 (simulation II) experimental values. Then, the conformational energies at the MP2 level were adopted as the initial values. The following geometrical parameters were used:[32] bond lengths, $l_{C-C^*}=1.529$ Å and $l_{C-S}=1.818$ Å; bond angles, $\angle CSC=101.60°$, $\angle SCC^*=114.59°$, and $\angle CC^*S=110.23°$; dihedral angles, $\phi^a_t=-2.55°$,$\phi^a_{g^+}=89.09°$, $\phi^a_{g^-}=-101.10°$, $\phi^b_t=10.32°$, $\phi^b_{g^+}=112.40°$, $\phi^b_{g^-}=-114.58°$, $\phi^c_t=-12.87°$,

$\phi^c_{g^+} = 113.96°$, and $\phi^c_{g^-} = -105.60°$. The bond dipole moments, $m_{C–S}$ ($m_{C^*–S}$) and $m_{C–C^*}$, were assumed to be 1.21 and 0 D, respectively. For both isotactic and atactic chains, the degree of polymerization, x, was set to 200. For the atactic chain, P_R was set to 0.5, and 100 chains were generated; the $\langle r^2\rangle_0/nl^2$ and $\langle\mu^2\rangle/nm^2$ values were averaged over the 100 chains. The E_ξ values determined in simulations I and II, designated as sets I and II, respectively, are listed in Table 13. The bond conformations of BMTP and isotactic PPS at 26 °C, calculated from the two sets of energy parameters, are given in Table 11. The calculated characteristic ratio, dipole moment ratio, and their temperature coefficients are as follows: isotactic chain, $\langle r^2\rangle_0/nl^2 = 3.3$ (set I) and 4.0 (set II), $\langle\mu^2\rangle/nm^2 = 0.33$ (set I) and 0.34 (set II) [0.33–0.39],[120] $10^3\, d\ln\langle r^2\rangle_0/dT = 1.0$ (set I) and 0.47 (set II) [-2.8 ± 0.3],[124] and $10^3\, d\ln\langle\mu^2\rangle/dT = 2.2$ (set I) and 2.3 (set II) [2.0 and 2.1];[120] atactic chain, $\langle r^2\rangle_0/nl^2 = 3.2$ (set I) and 3.9 (set II) [4.0],[119] $\langle\mu^2\rangle/nm^2 = 0.38$ (set I) and 0.38 (set II) [0.37–0.44],[120] $10^3\, d\ln\langle r^2\rangle_0/dT = 1.6$ (set I) and 0.87 (set II) [-2.0 ± 0.3[124] and 0.51 ± 0.11[125,126]], and $10^3\, d\ln\langle\mu^2\rangle/dT = 2.9$ (set I) and 2.6 (set II) [0.72–4.0],[121] where the values in the brackets are the corresponding experimental data.

The bond conformations of BMTP and dipole moment ratios and the temperature coefficients of isotactic and atactic PPS were satisfactorily reproduced by simulation I. However, the characteristic ratio of the atactic chain was calculated to be 3.2, being smaller than that (4.0)[119] observed from the Θ solution. On the other hand, simulation II gave good agreement between the calculated and observed $\langle r^2\rangle_0/nl^2$ and $\langle\mu^2\rangle/nm^2$ values but moderate agreement for bond conformations of BMTP. The $10^3\, d\ln\langle r^2\rangle_0/dT$ value estimated from thermoelasticity measurements on networks of atactic PPS is positive, 0.51 ± 0.11,[125,126] close to that (0.87) obtained in simulation II. However, the temperature coefficients obtained from the monomer (cyclic propylene sulfide) solution are negative: -2.8 ± 0.3 (isotactic)[124] and -2.0 ± 0.3 (atactic).[124]

The first-order interaction energies for the C–S and C–C bond of PES are, respectively, −0.74 and +0.41 kcal mol^{-1} (Table 10), thus being comparable to those of PPS. On the other hand, the E_{ω_1} and E_{ω_2} values, representing C–H ··· S close contacts, are larger than E_ω of PES, because the steric repulsions may be increased by the methyl side chain. Interestingly, both E_α and E_β of isotactic PPO (Table 3) are comparable to those of PPS. As shown above, the C–C* bond of PPS strongly prefers the trans state, whereas that of isotactic (*R*)-PPO exhibits a gauche$^+$ preference (the gauche-oxygen effect).[16] This is obviously due to the difference in signs of E_{ω_1} and E_{ω_2}. The intramolecular (C–H) ··· O interactions of PPO are attractive, while the C–H ··· S interactions of PPS are rather repulsive. As found for PES (Table 8), the CH_2–S bond of PPS also shows a gauche stability. In the C*–S bond, however, the trans state is the most stable. The C*–S and S–C bonds, being longer than C*–O and O–C, reduce steric repulsions occurring in the g^+ state of the C*–S bond: E_γ (PPS) = 0.43–0.49 and E_γ (PPO) = 2.97 kcal mol^{-1}. From the above results, it can be stated

that the conformational preferences of PPS are, in general, similar to those of PES but greatly different from those of PPO as found in PES and PEO.

8. CONCLUDING REMARKS

In the crystal, PMO and PMS, respectively, adopt 29/16 and 17/9 helical structures of the all-gauche form,[74,75] which have been shown to be the most stable conformations in the Θ state. Crystallized PES chain is also allowed to take the lowest-energy $g^{\pm}tg^{\mp}$ state in the S–C–C–S bond sequence.[83] The energy minima are ca. -1.4×3 (PMO), -1.05×3 (PMS), and -1.66 (PES) kcal mol^{-1} per three bonds in depth from the level of the all-trans conformation. For PMS and PES, the induced dipole–dipole interactions further stabilize the crystal structure. The melting points are as high as 245 (PMS), 180 (PMO), and 216 °C (PES). Isotactic PPS and PPO, being isomorphous,[117,127] adopt the all-trans form, which is not the most stable conformation in the Θ state. The PEO chain has only a little energy difference between the tgt and ttt forms in the O–C–C–O bonds. For PPS, PPO, and PEO, therefore, disorderings of the chain structure may occur at low temperatures, leading to fusion at 53, 73, and 68 °C, respectively.

Configurational entropies S_{conf}'s of the polymers treated here at the individual melting points, calculated from Eq. (A.8), are listed in Table 14. The melting point is given by $T_m = \Delta H_u / \Delta S_u$, where ΔH_u and ΔS_u are enthalpy and entropy of fusion. The experimental ΔS_u and ΔH_u values,[21,128] so far reported for some of the polymers, are also shown. The entropy of fusion can be broken down into ΔS_{conf} and ΔS_v terms, where ΔS_{conf} is configurational entropy change on melting, defined by $\Delta S_{conf} = S_{conf,a} - S_{conf,c}$, with $S_{conf,a}$ and $S_{conf,c}$ being configurational entropies of amorphous (molten) and crystalline states, respectively. Because $S_{conf,c}$ is null, ΔS_{conf} is equal to $S_{conf,a}$, which is given by Eq. (A.8) using the conformational energies in the Θ state. The entropy change (ΔS_v) due to volume change (ΔV_u) on melting is expressed by $\Delta S_v = (\alpha/\beta)\Delta V_u$, with α and β being the thermal expansion coefficient, compressibility, respectively.[21,129–132] From Table 14, the polysulfides are seen to have larger S_{conf} values than the corresponding polyethers. Since the contribution of ΔS_{conf} to ΔS_u, in general, amounts to 70–80%, the polysulfides probably have larger ΔS_u than the polyethers. Nevertheless, the polysulfides melt at much higher temperatures than the counterparts, except for PPS. This must be ascribed to the difference in ΔH_u: ΔH_u (polysulfide) > H_u (polyether).

As found for PMS, electrons of polysulfides are so flexible as to be redistributed and consequently reduce the S···S repulsion. In the $g^{\pm}tg^{\mp}$ conformations of PES, the charge distribution is arranged so as to enhance favorable intramolecular dipole–dipole interactions. In polysulfides, the electrons behave as if they had intelligence to reduce the ΔH term as much

Table 14. Configurational entropies (S_{conf}'s), entropies (ΔS_u's) and enthalpies (ΔH_u's) of fusion, and melting points (T_m's) of PMO, PMS, PEO, PES, PPO, and PPS

	PMO	PMS	PEO	PES	PPO	PPS
S_{conf}[a] (cal mol^{-1} K^{-1})	2.9	3.4	5.0	6.2	4.0	4.6
ΔS_u (cal mol^{-1} K^{-1})	3.4[b]		6.5[c]	6.9[c]	5.8[c]	
ΔH_u (kcal mol^{-1})			2.2[c]	3.4[c]	2.0[c]	
T_m (°C)	180	245	68	216	73	53

[a]Calculated with Eq. (A.6) from the individual conformational energies.
[b]Reference 128.
[c]Reference 21.

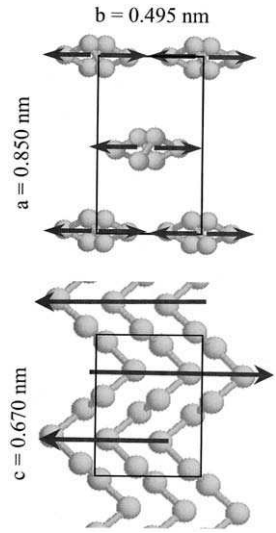

Fig. 25. Crystal structure of PES: an orthorhombic cell with the dimensions shown.[83] The arrows stand for dipole moments, which are canceled out within a chain and between chains. These antiparallel dipole–dipole interactions are expected to stabilize the crystal structure significantly.

as possible, depending on conformation. Thus, it is also expected that such inductive effects arise between the molecular chains. The crystal structure of PES shows the possibility of strong intermolecular dipole–dipole interactions (Fig. 25). Without the intermolecular inductive effects, the melting point would not be so high as 216 °C.

As have been shown so far, the NMR experiments, if combined with *ab initio* MO calculations and the RIS treatments, would become much more powerful techniques for the structural characterization, in particular, the conformational analysis of polymers. Our methodology will be able to be extended to a variety of polymers. However, to understand the structure–property relationship and

actualize molecular designs of polymers, *intermolecular* interactions related to polymers must also be investigated theoretically and experimentally. In such studies, NMR is expected to play a major role.

Acknowledgements

I wish to thank Dr. Robert V. Law of Imperial College, UK and Dr. Akira Kaito, Dr. Shinichi Kinugasa, and Dr. Takashi Yarita of National Institute of Advanced Industrial Science and Technology, Japan for collaboration in this work. Thanks are also due to my graduates and students (Taisuke Iwata, Haruhisa Kato, Yasukazu Kato, Nobuyuki Miura, Yugo Hayashi, Hajime Ohta, Misa Sawanobori, Ikuko Touma, and Hiroki Matoba) of Chiba University for contributions to this series of studies. This work was supported in part by Grant-in-Aid for Science Research (C) (Nos. 11650920 and 14550842) of Japan Society for the Promotion of Science and by the Royal Society, UK.

Note Added in Proof

In connection with discussion in Section 6.5, we have recently evaluated conformational energies of monomeric (DME), trimeric, and pentameric model compounds of PEO by very precise MO calculations at the MP2/6−311++G(3df, 3pd)//HF/6−31G(d) level. The results can be summarized as follows. (1) Since a narrow range (−1.1 to 1.3 kcal mol^{-1}) of E_ω's were obtained for the three model compounds, the strength of the intramolecular (C–H) $\cdots$ O hydrogen bond may be independent of chain length. (2) Even in the gas phase, the central monomeric units of the trimer and pentamer have slightly negative E_σ values (in free energy): trimer, −0.08 (−0.13) kcal mol^{-1}; pentamer, −0.02 (−0.14) kcal mol^{-1}. Here, the values in the parentheses represent the SCF energies. (3) Only the terminal units have positive E_σ values: DME, +0.09 kcal mol^{-1}; trimer, +0.05 kcal mol^{-1}; pentamer, +0.11 kcal mol^{-1}. As described in Section 5.3, this tendency was also found for oligomers of PMO. To our knowledge, this is the first time that negative E_σ values were obtained for ethylene oxides by *ab initio* MO calculations. These results indicate the followings. (1) The PEO chain can adopt the gauche conformation in the C–C bond without aid of the intramolecular hydrogen bond. (2) The helical structure is more stable than the all-trans planar zigzag form.[85,86] The small negative E_σ values suggest that the PEO chain may change the C–C conformation between gauche and trans even in the crystal.[86] (3) The gauche attractive effect exists independently of the hydrogen bonds.

REFERENCES

1. P. J. Flory, *Statistical Mechanics of Chain Molecules*, Interscience, New York, 1969.
2. P. J. Flory, *Principles of Polymer Chemistry*, Cornell University Press, Ithaca, NY, 1953.
3. H.-G. Elias, *Polymer Handbook*, 4th edn, J. Brandrup, E. H. Immergut, and E. A. Grulke, eds., Chap. VII/291, Wiley & Sons, New York, 1999.
4. A. Abe, R. L. Jernigan and P. J. Flory, *J. Am. Chem. Soc.*, 1966, **88**, 631.
5. U. W. Suter and P. J. Flory, *Macromolecules*, 1975, **8**, 765.
6. W. L. Mattice and U. W. Suter, *Conformational Theory of Large Molecules: The Rotational Isomeric State Model in Macromolecular Systems*, Wiley & Sons, New York, 1994.
7. E. Riande and E. Saiz, *Dipole Moments and Birefringence of Polymers*, Prentice Hall, Englewood Cliffs, NJ, 1992.
8. K. Nagai and T. Ishikawa, *Polym. J.*, 1971, **2**, 416.
9. M. Doi, *Polym. J.*, 1970, **3**, 252.
10. P. J. Flory and J. E. Mark, *Makromol. Chem.*, 1964, **75**, 11.
11. A. Abe and J. E. Mark, *J. Am. Chem. Soc.*, 1976, **98**, 6468.
12. J. E. Mark and P. J. Flory, *J. Am. Chem. Soc.*, 1965, **87**, 1415.
13. J. E. Mark and P. J. Flory, *J. Am. Chem. Soc.*, 1966, **88**, 3702.
14. T. Hirano, P. H. Khanh and T. Tsuruta, *Makromol. Chem.*, 1972, **153**, 331.
15. N. Oguni, S. Maeda and H. Tani, *Macromolecules*, 1973, **6**, 459.
16. A. Abe, T. Hirano and T. Tsuruta, *Macromolecules*, 1979, **12**, 1092.
17. E. Juaristi, *Introduction to Stereochemistry and Conformational Analysis*, Wiley & Sons, New York, 1991.
18. E. Juaristi and G. Cuevas, *The Anomeric Effect*, CRC Press, Boca Raton, FL, 1995.
19. W. J. Welsh, J. E. Mark, J. Guzman and E. Riande, *Makromol. Chem.*, 1982, **183**, 2565.
20. J. L. de la Peñ, E. Riande and J. Guzmán, *Macromolecules*, 1985, **18**, 2739.
21. A. Abe, *Macromolecules*, 1980, **13**, 546.
22. A. Abe, *Macromolecules*, 1980, **13**, 541.
23. H. S. Gutowsky, G. C. Belford and P. E. McMahon, *J. Chem. Phys.*, 1962, **36**, 3353.
24. J. B. Foresman and Æ. Frisch, *Exploring Chemistry, with Electronic Structure Methods*, 2nd edn, Gaussian, Inc, Pittsburgh, PA, 1996.
25. Y. Sasanuma, *J. Phys. Chem.*, 1994, **98**, 13486.
26. Y. Sasanuma, *Macromolecules*, 1995, **28**, 8629.
27. R. V. Law and Y. Sasanuma, *Macromolecules*, 1998, **31**, 2335.
28. Y. Sasanuma, T. Iwata, Y. Kato, H. Kato, T. Yarita, S. Kinugasa and R. V. Law, *J. Phys. Chem. A*, 2001, **105**, 3277.
29. R. V. Law and Y. Sasanuma, *J. Chem. Soc., Faraday Trans.*, 1996, **92**, 4885.
30. M. Sawanobori, Y. Sasanuma and A. Kaito, *Macromolecules*, 2001, **34**, 8321.
31. Y. Sasanuma, H. Ohta, I. Touma, H. Matoba, Y. Hayashi and A. Kaito, *Macromolecules*, 2002, **35**, 3748.
32. Y. Sasanuma, Y. Hayashi, H. Matoba, I. Touma, H. Ohta, M. Sawanobori and A. Kaito, *Macromolecules*, 2002, **35**, 8216.
33. P. W. Atkins, *Physical Chemistry*, 6th edn, Oxford University Press, New York, 1998.
34. M. J. Frisch, G. W. Trucks, M. Head-Gordon, P. M. W. Gill, M. W. Wong, J. B. Foresman, B. G. Johnson, H. B. Schlegel, M. A. Robb, E. S. Replogle, R. Gomperts, J. L. Andres, K. Raghavachari, J. S. Binkley, C. Gonzalez, R. L. Martin, D. J. Fox, D. J. Defrees, J. Baker, J. J. P. Stewart and J. A. Pople, GAUSSIAN-92, Revision G.1, Gaussian, Inc., Pittsburgh, PA, 1992.
35. M. J. Frisch, G. W. Trucks, H. B. Schlegel, G. E. Scuseria, M. A. Robb, J. R. Cheeseman, V. G. Zakrzewski, J. A. Montgomery, Jr., R. E. Stratmann, J. C. Burant, S. Dapprich, J. M. Millam, A. D. Daniels, K. N. Kudin, M. C. Strain, O. Farkas, J. Tomasi, V. Barone, M. Cossi, R. Cammi, B. Mennucci, C. Pomelli, C. Adamo, S. Clifford, J. Ochterski, G. A. Petersson, P. Y. Ayala, Q. Cui, K. Morokuma, D. K. Malick, A. D. Rabuck, K. Raghavachari, J. B.

Foresman, J. Cioslowski, J. V. Ortiz, A. G. Baboul, B. B. Stefanov, G. Liu, A. Liashenko, P. Piskorz, I. Komaromi, R. Gomperts, R. L. Martin, D. J. Fox, T. Keith, M. A. Al-Laham, C. Y. Peng, A. Nanayakkara, C. Gonzalez, M. Challacombe, P. M. W. Gill, B. Johnson, W. Chen, M. W. Wong, J. L. Andres, C. Gonzalez, M. Head-Gordon, E. S. Replogle and J. A. Pople, GAUSSIAN-98, Revision A.7, Gaussian, Inc., Pittsburgh, PA, 1998.
36. J. A. Pople, A. P. Scott, M. W. Wong and L. Radom, *Isr. J. Chem.*, 1993, **33**, 345.
37. C. Møller and M. S. Plesset, *Phys. Rev.*, 1934, **46**, 618.
38. B. H. Besler, Merz, K. M., Jr. and P. A. Kollman, *J. Comput. Chem.*, 1990, **11**, 431.
39. U. C. Singh and P. A. Kollman, *J. Comput. Chem.*, 1984, **5**, 129.
40. A. E. Reed, L. A. Curtiss and F. Weinhold, *Chem. Rev.*, 1988, **88**, 899.
41. A. D. Becke, *J. Chem. Phys.*, 1993, **98**, 5648.
42. C. Lee, W. Yang and R. G. Parr, *Phys. Rev. B*, 1988, **37**, 785.
43. M. W. Wong, M. J. Frisch and K. B. Wiberg, *J. Am. Chem. Soc.*, 1991, **113**, 4776.
44. K. Tasaki and A. Abe, *Polym. J.*, 1985, **17**, 641.
45. K. Inomata and A. Abe, *J. Phys. Chem.*, 1992, **17**, 7934.
46. S. Castellano and A. A. Bothner-By, *J. Chem. Phys.*, 1964, **41**, 3863.
47. J. Xu, X. Song, Z. Zhou and D. Yan, *J. Polym. Sci., Polym. Phys. Ed.*, 1991, **29**, 877.
48. X. Wu, J. Jin, L. Zhang and J. Xu, *J. Polym. Sci., Polym. Phys. Ed.*, 1993, **31**, 455.
49. A. Bondi, *J. Phys. Chem.*, 1964, **68**, 441.
50. G. A. Jeffrey, *An Introduction to Hydrogen Bonding*, Oxford University Press, New York, 1997.
51. G. Desiraju and T. Steiner, eds., *The Weak Hydrogen Bond: Applications to Structural Chemistry and Biology*, Oxford University Press, New York, 1999.
52. G. Allen, C. Booth and C. Price, *Polymer*, 1967, **8**, 397.
53. T. Hirano, P. H. Khanh, K. Tsuji, A. Sato, T. Tsuruta, A. Abe, T. Shimozawa, A. Kotera, N. Yamaguchi and S. Kitahara, *Polym. J.*, 1979, **11**, 905.
54. F. Rodriguez, *Principles of Polymer Systems*, 4th edn, Taylor and Francis Publishers, New York, 1996.
55. F. C. Schilling and A. E. Tonelli, *Macromolecules*, 1986, **19**, 1337.
56. F. Heatley, Y. Z. Luo, J. F. Ding, R. H. Mobbs and C. Booth, *Macromolecules*, 1988, **21**, 2713.
57. A. E. Tonelli, *NMR Spectroscopy and Polymer Microstructure: The Conformational Connection*, VCH Publishers, New York, 1989.
58. F. Bovey and P. Mirau, *NMR of Polymers*, Academic Press, New York, 1996.
59. K. Pihlaja and E. Kleinpeter, *Carbon-13 NMR Chemical Shifts in Structural and Stereochemical Analysis*, VCH Publishers, New York, 1994.
60. M. Barfield, *J. Am. Chem. Soc.*, 1995, **117**, 2862.
61. H. C. Chitwood and B. T. Freure, *J. Am Chem. Soc.*, 1946, **68**, 680.
62. T. Yarita, A. Nomura, K. Abe and Y. Takeshita, *J. Chromatogr. A*, 1994, **679**, 329.
63. H. Friebolin, *Basic One- and Two-Dimensional NMR Spectroscopy, Second, Enlarged Edition*, VCH Publishers, New York, 1993.
64. J. A. Nelder and R. Mead, *Comput. J.*, 1965, **7**, 308.
65. J. T. Edward, *Chem. Ind. (London)*, 1955, 1102
66. R. U. Lemieux, A. A. Pavia, J. C. Martin and K. A. Watanabe, *Can. J. Chem.*, 1969, **47**, 4427.
67. C. Altona, C. Knobler and C. Romers, *Acta Crystallogr.*, 1963, **16**, 1217.
68. A. J. Kirby, *The Anomeric Effect and Related Stereoelectronic Effects at Oxygen*, Springer-Verlag, Berlin, 1983.
69. E. L. Eliel and C. A. Giza, *J. Org. Chem.*, 1968, **33**, 3754.
70. F. W. Nadar and E. L. Eliel, *J. Am. Chem. Soc.*, 1970, **92**, 3050.
71. E. Juaristi, J. Tapia and R. Mendez, *Tetrahedron*, 1986, **42**, 1253.
72. A. S. Hay and Y. Ding, *Polymer Data Handbook*, J. E. Mark, ed., Oxford University Press, New York, 1999, 650.
73. M. Iguchi, *Makromol. Chem.*, 1976, **177**, 549.
74. T. Uchida and H. Tadokoro, *J. Polym. Sci., Part A-2: Polym. Phys.*, 1967, **5**, 63.

75. G. Carazzolo and G. Valle, *Makromol. Chem.*, 1966, **90**, 66.
76. J. Lal, *J. Org. Chem.*, 1961, **26**, 971.
77. E. Gipstein, E. Wellisch and O. J. Sweeting, *J. Polym. Sci., Part B: Polym. Lett.*, 1963, **1**, 237.
78. A. Abe, K. Inomata, E. Tanisawa and I. Ando, *J. Mol. Struct.*, 1990, **238**, 315.
79. T. Uchida, Y. Kurita and M. Kubo, *J. Polym. Sci.*, 1956, **19**, 365.
80. L. Pauling, *The Nature of the Chemical Bond and the Structure of Molecules and Crystals: An Introduction to Modern Structural Chemistry*, 3rd edn, Cornell University Press, Ithaca, NY, 1960.
81. Q. W. Yuan, *Polymer Data Handbook*, J. E. Mark, ed., Oxford University Press, New York, 1999, 542.
82. J. Masamoto, *Polymer Data Handbook*, J. E. Mark, ed., Oxford University Press, New York, 1999, 553.
83. Y. Takahashi, H. Tadokoro and Y. Chatani, *J. Macromol. Sci. Phys.*, 1968, **B2**, 361.
84. Y. Yokoyama and Y. Ohashi, *Bull. Chem. Soc. Jpn.*, 1998, **71**, 1565.
85. H. Tadokoro, Y. Chatani, T. Yoshihara, S. Tahara and S. Murahashi, *Makromol. Chem.*, 1964, **73**, 109.
86. Y. Takahashi, I. Sumita and H. Tadokoro, *J. Polym. Sci., Polym. Phys. Ed.*, 1973, **11**, 2113.
87. Y. Yokoyama, H. Uekusa and Y. Ohashi, *Chem. Lett.*, 1996, 443
88. S. Tsuzuki, T. Uchimaru, K. Tanabe and T. Hirano, *J. Phys. Chem.*, 1993, **97**, 1346.
89. R. L. Jaffe, G. D. Smith and D. Y. Yoon, *J. Phys. Chem.*, 1993, **97**, 12745.
90. E. E. Astrup, *Acta Chem. Scand.*, 1979, **A33**, 655.
91. H. Yoshida, I. Kaneko, H. Matsuura, Y. Ogawa and M. Tasumi, *Chem. Phys. Lett.*, 1992, **196**, 601.
92. E. Riande and J. Guzmán, *Macromolecules*, 1981, **14**, 1234.
93. *gNMR, version 4.1*, Cherwell Scientific Ltd., Oxford, UK, 1995.
94. F. J. M. van de Ven, *Multidimensional NMR in Liquids: Basic Principles and Experimental Methods*, VCH Publishers, New York, 1995.
95. T. M. Connor and K. A. McLauchlan, *J. Phys. Chem.*, 1965, **69**, 1888.
96. K. Matsuzaki and H. Ito, *J. Polym. Sci., Polym. Phys. Ed.*, 1974, **12**, 2507.
97. V. Viti, P. L. Indovina, F. Podo, L. R. Radics and G. Némethyl, *Mol. Phys.*, 1974, **27**, 541.
98. B. Buck and V. A. Macaulay, eds., *Maximum Entropy in Action: A Collection of Expository Essays*, Oxford University Press, New York, 1991.
99. S. F. Gull, M. Charter and J. Skilling, *MemSys5 Ver. 1.20*, Maximum Entropy Data Consultants Ltd., Cambridge, England, 1991.
100. A. Suzuki, N. Miura and Y. Sasanuma, *Langmuir*, 2000, **16**, 6317.
101. Y. Sasanuma, *Polym. J.*, 2000, **32**, 883.
102. Y. Sasanuma, *Polym. J.*, 2000, **32**, 890.
103. J. W. Ochterski, G. A. Petersson and Montgomery, J. A., Jr., *J. Chem. Phys.*, 1996, **104**, 2598.
104. D. R. Beech and C. Booth, *J. Polym. Sci., Part A-2*, 1969, **7**, 575.
105. G. Allen, *Proc. R. Soc. London, Ser. A*, 1976, **351**, 381.
106. E. A. Boucher and P. M. Hines, *J. Polym. Sci., Polym. Phys. Ed.*, 1978, **16**, 501.
107. J. Kugler and E. W. Fischer, *Makromol. Chem.*, 1983, **184**, 2325.
108. P. Gregory and M. B. Huglin, *Makromol. Chem.*, 1986, **187**, 1745.
109. N. Vennemann, M. D. Lechner and R. C. Oberthür, *Polymer*, 1987, **28**, 1738.
110. G. D. Smith, D. Y. Yoon, R. L. Jaffe, R. H. Colby, R. Krishnamoorti and L. J. Fetters, *Macromolecules*, 1996, **29**, 3462.
111. S. Kawaguchi, G. Imai, J. Suzuki, A. Miyahara, T. Kitano and K. Ito, *Polymer*, 1997, **38**, 2885.
112. S. Bluestone, J. E. Mark and P. J. Flory, *Macromolecules*, 1974, **7**, 325.
113. C. Rossi and V. Magnasco, *J. Polym. Sci.*, 1962, **58**, 977.
114. K. Bak, G. Elefante and J. E. Mark, *J. Phys. Chem.*, 1967, **71**, 4007.
115. K. M. Kelly, G. D. Patterson and A. E. Tonelli, *Macromolecules*, 1977, **10**, 859.

116. R. D. Lundberg, F. E. Bailey and R. W. Callard, *J. Polym. Sci., Part A-1*, 1966, **4**, 1563.
117. H. Sakakihara, Y. Takahashi, H. Tadokoro, P. Sigwalt and N. Spassky, *Macromolecules*, 1969, **2**, 515.
118. J. Masamoto, *Polymer Data Handbook*, J. E. Mark, ed., Oxford University Press, New York, 1999, 792.
119. D. W. Nash and D. C. Pepper, *Polymer*, 1975, **16**, 105.
120. E. Riande, S. Boileau, P. Hemery and J. E. Mark, *Macromolecules*, 1979, **12**, 702.
121. E. Riande, S. Boileau, P. Hemery and J. E. Mark, *J. Chem. Phys*., 1979, **71**, 4206.
122. K. J. Ivin and M. Navrátil, *J. Polym. Sci., Part B*, 1970, **8**, 51.
123. K. J. Ivin and M. Navrátil, *J. Polym. Sci., Part A-1*, 1971, **9**, 1.
124. R. R. Rahalkar, J. E. Mark, S. Boileau, P. Hemery and E. Riande, *J. Polym. Sci., Polym. Phys. Ed*., 1979, **17**, 1623.
125. R. H. Becker, *M. S. Thesis in Chemistry*, The Polytechnic Institute of Brooklyn, 1967.
126. J. E. Mark, *Rubber Chem. Technol*., 1973, **46**, 593.
127. M. Cesari, G. Perego and W. Marconi, *Makromol. Chem*., 1966, **94**, 194.
128. I. Kirshenbaum, *J. Polym. Sci., Part A*, 1965, **3**, 1869.
129. D. A. Brant, W. G. Miller and P. J. Flory, *J. Mol. Biol*., 1967, **23**, 47.
130. A. E. Tonelli, *J. Chem. Phys*., 1970, **52**, 4749.
131. A. E. Tonelli, *J. Chem. Phys*., 1970, **53**, 4339.
132. J. E. Mark, *J. Chem. Phys*., 1977, **67**, 3300.

Appendix A Calculations of characteristic ratio, dipole moment ratio, and configurational entropy by RIS scheme[1,4,6,47,48]

A Cartesian coordinate system is defined for bond i of a molecule in the following manner: the x-axis is along bond i, the y-axis lies in the plane formed by bonds i and $i-1$ in the direction making a positive projection on bond $i-1$, and the z-axis is set so as to form a right-handed Cartesian frame. Then, the orthogonal axis transformation matrix $\mathbf{T}_i$, which transforms a vector from the ith to $(i-1)$th frame of reference, is expressed as

$$\mathbf{T}_i = \begin{pmatrix} \cos\theta_i & \sin\theta_i & 0 \\ \sin\theta_i \cos\phi_i & -\cos\theta_i \cos\phi_i & \sin\phi_i \\ \sin\theta_i \cos\phi_i & -\cos\theta_i \sin\phi_i & -\cos\phi_i \end{pmatrix} \tag{A.1}$$

where θ_i is the supplement of the bond angle, and ϕ_i is the dihedral angle. The mean square $\langle M^2 \rangle$ of end-to-end distance ($M = r$) or dipole moment ($M = \mu$) is given by

$$\langle M^2 \rangle = 2Z^{-1}\mathbf{J}^*\mathbf{G}_1\mathbf{G}_2\mathbf{G}_3 \cdots (\mathbf{G}_a\mathbf{G}_b \cdots)^{x-1}\mathbf{G}_n\mathbf{J} \tag{A.2}$$

where $\mathbf{J}^* = [100\ldots]$, $\mathbf{J}$ is the column matrix of which elements are all unity, and Z is the partition function, which can be calculated from

$$Z = \mathbf{J}^*\mathbf{U}_2\mathbf{U}_3 \ldots (\mathbf{U}_a\mathbf{U}_b \ldots)^{x-1}\mathbf{U}_{n-1}\mathbf{J} \tag{A.3}$$

The $\mathbf{G}_i$ matrix is defined by

$$\mathbf{G}_i = \begin{pmatrix} \mathbf{U}_i & (\mathbf{U}_i \otimes \overline{\mathbf{m}}^{\mathrm{T}})\|\mathbf{T}\|_i & (m^2/2)\mathbf{U}_i \\ 0 & (\mathbf{U}_i \otimes \mathbf{E}_3)\|\mathbf{T}\|_i & \mathbf{U}_i \otimes \overline{\mathbf{m}} \\ 0 & 0 & \mathbf{U}_i \end{pmatrix} \tag{A.4}$$

where $\otimes$ denotes the direct product, m is the bond length or bond dipole moment, $\mathbf{E}_3$ is the third-order identity matrix, and $\overline{\mathbf{m}}$ is given by

$$\overline{\mathbf{m}} = m \begin{pmatrix} 1 \\ 0 \\ 0 \end{pmatrix} \tag{A.5}$$

The $\|\mathbf{T}\|_i$ matrix is defined as

$$\|\mathbf{T}\|_i = \begin{cases} \tau_i & i = 1 \text{ or } 2 \\ \mathbf{E}_3 \otimes \tau_i & i > 2 \end{cases} \tag{A.6}$$

where

$$\tau_i = \begin{pmatrix} T_{\mathrm{t}} & & 0 \\ & T_{\mathrm{g}^+} & \\ 0 & & T_{\mathrm{g}^-} \end{pmatrix} \tag{A.7}$$

is a pseudo-diagonal matrix formed from the transformation matrices for the t, g^+, and g^- states. The $\mathbf{G}_i$ matrix has a size of $5s \times 5t$, when $\mathbf{U}_i$ is an $s \times t$ matrix.

The configurational entropy per mole of the repeating unit can be calculated from[21,129–132]

$$S_{\mathrm{conf}} = R\left(\ln z + T \frac{\mathrm{d} \ln z}{\mathrm{d}T}\right) \tag{A.8}$$

where z is the configurational partition function per mole of the repeating unit, given by

$$z = Z^{1/n_{\mathrm{r}}} \tag{A.9}$$

with n_{r} being the number of repeating units in a chain. The Z function can be calculated from Eq. (A.3). For the calculations of Eqs. (A.8) and (A.9), however, the statistical weight matrices in Eq. (A.3) must be scaled so that the weight of the lowest-energy conformation is unity.

Appendix B Glossary of symbols and abbreviations

$\otimes$	direct product
B3LYP	Becke's three-parameter functional using the Lee–Yang–Parr correlation functional
BMTE	1,2-bis(methylthio)ethane
BMTP	1,2-bis(methylthio)propane
CBS-Q	complete basis set (Q) method
COSY	correlation spectroscopy
DEPT	distortionless enhancement by polarization transfer
cis-DMDO	*cis*-2,6-dimethyl-1,4-dioxane
DME	1,2-dimethoxyethane
DMEDT	2-(1,1-dimethylethyl)-1,4-dithiane
DMP	1,2-dimethoxypropane
DMSO	dimethyl sulfoxide
$\mathbf{E}_3$	third-order identity matrix
E_ξ	conformational energy for ξ interaction
ED	electron diffraction
f_k	fraction of conformer k
$\mathbf{G}_i$	supermatrix for calculations of mean square moments
ΔG	free energy difference
ΔG_k	free energy of conformer k
ΔH_u	enthalpy of fusion
ΔH_vap	enthalpy of vaporization
HF	Hartree–Fock method
H–H	PPO dimers with H–H linkage
H–T	PPO dimers with H–T linkage
i	bond number
i_C	carbon number
$\mathbf{J}$	column matrix of which elements are all unity
$\mathbf{J}^*$	row matrix defined as $\mathbf{J}^* = [100\ldots]$
$^1J_\mathrm{CH}$	direct coupling constant between carbon and proton
^3J	vicinal coupling constant
$^3J_\mathrm{AC}$	^3J between protons A and C
$^3J_\mathrm{BC}$	^3J between protons B and C
$^3J_\mathrm{CH}$	^3J between carbon and proton
$^3J_\mathrm{G}$	^3J between spins in gauche position
$^3J_\mathrm{G}^\mathrm{CH}$	^3J between carbon and proton in gauche position
$^3J_\mathrm{G}^\mathrm{HH}$, $^3J_\mathrm{G}^{\prime\mathrm{HH}}$, $^3J_\mathrm{G}^{\prime\prime\mathrm{HH}}$	^3J between protons in gauche position
$^3J_\mathrm{HH}$, $^3J'_\mathrm{HH}$	^3J between protons around C–C bond of BMTE
$^3J_\mathrm{T}$	^3J between spins in trans position
$^3J_\mathrm{T}^\mathrm{CH}$	^3J between carbon and proton in trans position
$^3J_\mathrm{T}^\mathrm{HH}$, $^3J_\mathrm{T}^{\prime\mathrm{HH}}$	^3J between protons in trans position
k	conformer number
l	bond length
m	bond dipole moment
$\overline{\mathbf{m}}$	moment column matrix (moment vector)
M_k	multiplicity of conformation k
MO	molecular orbital
MP2	second-order Møller–Plesset correlation theory
MTT	2-methyl-1,3,5-trithiane

n	number of skeletal bonds
$n_{j,\alpha}$	number of nonhydrogen atoms j at α position
$n_{j,\beta}$	number of nonhydrogen atoms j at β position
$n_{j,\gamma}$	number of nonhydrogen atoms j at γ position
$n_{j,\delta}$	number of nonhydrogen atoms j at δ position
NBO	natural bond orbital
n_r	number of repeating units in a chain
n_X	lone pair of X atom
PEO	poly(ethylene oxide)
PES	poly(ethylene sulfide)
PMO	poly(methylene oxide)
PMO-x	x mer of PMO
PMS	poly(methylene sulfide)
PMS-x	x mer of PMS
PO	propylene oxide
PPO	poly(propylene oxide)
PPS	poly(propylene sulfide)
P_R	(R)-unit fraction in an atactic PPS chain
p_η, p_η^{bond}	bond conformation of η state (in the bond, e.g., C–C*, S–C, C–S, or C*–S)
$p_{\eta\eta'}$	fraction of $\eta\eta'$ ($=$tt, tg$^+$, ... or g$^-$g$^-$) conformation
$\langle r^2\rangle_0/nl^2$	characteristic ratio in the Θ state
RIS	rotational isomeric state
RMSE	root-mean-square error
S_{conf}	configurational entropy
ΔS_u	entropy of fusion
SCF	self-consistent field
SCRF	self-consistent reaction field method
SFC	supercritical fluid chromatography
T	absolute temperature
$\|\mathbf{T}\|_i$	supermatrix for $\mathbf{T}_i$
T_{bp}	boiling point
$\mathbf{T}_i$	orthogonal axis transformation matrix
T_m	melting point
T–T	PPO dimers with T–T linkage
$\mathbf{U}_i$	statistical weight matrix of bond i
ΔV_u	volume change on melting
x	degree of polymerization
X	electronegative atom ($=$O or S)
Y	electronegative atom
z	partition function per mole of repeating unit
Z	partition function of a whole chain
α	interaction and statistical weight defined for DMP and PPO or BMTP and PPS; thermal expansion coefficient
A	interaction and statistical weight defined for PPO dimers
β	interaction and statistical weight defined for DMP and PPO or BMTP and PPS; compressibility
B	interaction and statistical weight defined for PPO dimers
γ	interaction and statistical weight defined for DMP and PPO or BMTP and PPS
Γ	interaction and statistical weight defined for PPO dimers

δ	interaction and statistical weight defined for DMP and PPO or BMTP and PPS
Δ	interaction and statistical weight defined for PPO dimers
δ_{i_C}	chemical shift of carbon i_C
$\Delta\delta_{0,i_C}$	chemical shift term of carbon i_C, independent of conformation
$\Delta\delta_{0,\zeta}$	chemical shift term of carbon atom in chemical species ζ (= CH, CH_2, CH_3, or CH_3O), independent of conformation
$\Delta\delta_{\alpha,j}$	chemical shift increment due to atom j at α position
$\Delta\delta_{\beta,j}$	chemical shift increment due to atom j at β position
$\Delta\delta^{\eta}_{\gamma,j}$	chemical shift increment due to atom j at γ position with intervening bond being in η conformation
$\Delta\delta^{\eta\eta'}_{\delta,j}$	chemical shift increment due to atom j at δ position with intervening bonds being in η and η' conformations
ε	dielectric constant
ζ	interaction and statistical weight defined for BMTP and PPS
η	conformation, i.e., t, g^+, or g^-
θ_i	supplement of bond angle of bond i
κ	interaction and statistical weight defined for BMTE and PES
μ	dipole moment
μ^{BOND}	dipole moment calculated from bond dipole moment vectors
μ^{MO}	dipole moment evaluated from MO calculations
$\langle\mu^2\rangle/nm^2$	dipole moment ratio
ξ	intramolecular interaction and statistical weight
ρ	interaction and statistical weight defined for BMTE and PES or DME and PEO
σ	interaction and statistical weight defined for DMP and PPO, PMO-x, PMS-x, BMTE and PES, DME and PEO, or BMTP and PPS
Σ	interaction and statistical weight defined for PPO dimers
$\sigma^*_{\mathrm{C-X}}$	antibonding orbital of C–X bond
τ	interaction and statistical weight defined for BMTP and PPS
τ_i	pseudo-diagonal matrix composed of transformation matrices
ϕ_i	dihedral angle of bond i
$\phi^{\mathrm{bond}}_{\eta}$	dihedral angle of η state of the bond
χ	interaction and statistical weight defined for DMP and PPO, BMTE and PES, DME and PEO, or BMTP and PPS
ω	interaction and statistical weight defined for PMO-x, PMS-x, BMTE and PES, or DME and PEO
ω'	interaction and statistical weight defined for BMTE and PES or DME and PEO
ω_1	interaction and statistical weight defined for DMP and PPO or BMTP and PPS
Ω_1	interaction and statistical weight defined for PPO dimers
ω_2	interaction and statistical weight defined for DMP and PPO or BMTP and PPS
Ω_2	interaction and statistical weight defined for PPO dimers

Index

Note – Page numbers in *italic* type refer to figures and tables.